New Methodology for the Assessment of Decayed Utility Wood Poles Using Ultrasonic Testing

by

Fernando J. Tallavó

A thesis
presented to the University of Waterloo
in fulfilment of the
thesis requirement for the degree of
Doctor of Philosophy
in
Civil Engineering

Waterloo, Ontario, Canada, 2009

I hereby declare that I am the sole author of this thesis. This is a true copy of the thesis, including any required final revisions, as accepted by my examiners.

I understand that my thesis may be made electronically available to the public.

Abstract

Wood is one of the oldest and most common material used in construction. Since the beginning of the electrification in Canada in late 19th-century, wood poles have been widely used to provide structural support to electric transmission and distribution lines. For example, electrical network in Ontario has over 2 millions distribution poles across the province. Wood poles are typically exposed to severe environmental conditions, which cause deterioration due to wood rotting, insect attack, and weathering. The wood deterioration resulting in loss of strength can compromise the structural integrity of poles. Typical life expectancy of wood varies from 35 to 50 years depending on the environmental condition and type of wood.

Electrical distribution infrastructure in Canada is aging. For example, the average age of in-service wood poles in Ontario is estimated to be 29 years with a standard deviation of 15 years. About 300,000 wood poles have been in-service for more than 45 years, which are rapidly reaching to end of expected service life. Different types of non-destructive testing (NDT) methods have been historically used for the condition assessment of wood poles. However, current methods are based on simple concepts that do not consider the variations of wave velocity and wave attenuation in an orthotropic material. The goal of this research investigation is to develop an advanced and reliable NDT technique for in-situ inspection and assessment of wood poles in order to remove unsafe poles from service, extend the service life of sound poles, and support optimum replacement strategies for the renewal of wood pole infrastructure.

The thesis presents a new methodology for condition assessment of wood poles using ultrasonic testing based on theoretical, numerical, and experimental studies. The research covers areas such as signal processing, dynamic characterization, statistical reliability analysis, numerical simulations, and laboratory testing. Wood is modeled as a cylindrical orthotropic material with uncertainties in its elastic and mechanical properties. The arrival time of compressional waves as well as full-waveform analysis are used for an integrated evaluation of wood pole. A simplified model of P-wave propagation in pole cross-sections is developed; which allows to (a) estimate the elastic moduli in the radial and tangential directions by solving the inverse problem, and (b) compute the probability density function of P-wave velocity. Both of these parameters are critical for condition assessment; however, they are not available in the literature because of the complexities associated with modelling wood as an orthotropic material. A new specialized software is developed for (a) general signal processing, (b) non-destructive condition assessment of wood poles, and (c) management of a statistical database for the assessment of wood poles. Based on the proposed methodology, a new clamping device is designed and built for the ultrasonic testing of wood poles in the field.

The basic background for signal processing covering Fourier analysis, frequency response and impulse response functions, and the complex exponential method for dynamic system iden-

tification is reviewed and summarized. The elastic and mechanical properties for most common species of wood used as poles are summarized from the literature, including the main statistical distributions used for their probabilistic characterization. The calibration and basic assumptions for the simulation of wave propagation in orthotropic media using finite element analysis are explained in detail.

Numerical modelling is based on finite element method under plain strain condition. The numerical model is calibrated using theoretical results and validated using experimental results from laboratory testing of a new red pine pole. After calibrating the model, numerical simulations were performed to understand ultrasonic wave propagation in cross-sections of sound and decayed wood poles sections. Results of numerical simulations of ultrasonic wave propagation in pole cross-sections are presented. The effect of a void in the cross section on the ultrasonic measurement is discussed.

A sample of 8 wood pole cross-sections were subjected to laboratory ultrasonic tests. In the testing, a transmitter was placed at four positions around the pole circumference. For each transmitter position, five receivers were used. The transmitter-receiver system was calibrated to evaluate its transfer function and thus eliminate the inherent characteristics of the transmitter-receiver system from the actual measurements. The experimental results of the condition assessment of new and decayed pole samples are presented in the thesis. The effect of a hole in a new pole was studied and the results were compared with the numerical analysis. A blind test is performed on an aged red pine pole. The predicted areas of decay from the ultrasonic measurements are in good agreement with the actual decay observed from dissecting the pole sections.

In summary, the experimental and numerical results presented in this thesis show that the proposed methodology can be successfully applied for condition assessment of in-service wood poles in the electrical network. This method will contribute to cost-effective life cycle management of energy infrastructure as a whole.

Acknowledgements

I am deeply thankful to my supervisors Dr. Giovanni Cascante and Dr. Mahesh D. Pandey for their advises and encouragement received during the conduction of this research. I will always be grateful, again, many thanks.

I would also like to express my gratitude to the Department of Civil and Environmental Engineering for all the support given. In particular, I want to thank to Ken Bowman, Terry Ridgway, and Marguarite Knechtel.

Sincere thanks to John Boldt from Engineering Machine Shops for the building of the UT-Pole prototype and preparation of the wood pole samples; and to Jorge Cruz and Juan Ulloa for their continuous support during the laboratory tests.

I gratefully acknowledgement the financial support for this research provided by Natural Sciences and Engineering Research Council of Canada (NSERC), University Network of Excellence in Nuclear Engineering (UNENE), OCE-Centre for Earth and Environmental Technologies, and Dillon Consulting/ Waterloo Geophysics Inc.

Especially, I want to thank to my wife Rosaiba and my sons Luis Fernando and Juan Andrés their support, comprehension, and infinite love enabled me to complete this thesis.

Dedication

I dedicate this work to my wife Rosaiba, my sons Luis Fernando and Juan Andrés, and to the memory of my parents Ana Mercedes de Tallavó and Luis Alberto Tallavó

Table of Contents

List of Tables

List of Figures

Nomenclature

A	Pulse amplitude
$A(Z)$, $B(Z)$	Polynomial functions
$A(\omega)$	Displacement amplitude as function of frequency
A_d	Dynamic magnification factor
A_f	Transmission factor
Br, Bt	Direction cosines to define the orientation of the local coordinate system RT
COV_x	Coefficient of variation of x
C_k	Free-vibration amplitude
DIA_{θ_r}	Dissimilarity index of the wave transmission computed at θ_r
DIE_{θ_r}	Dissimilarity index of the elastic modulus computed at θ_r
DIV_{θ_r}	Dissimilarity index of the wave velocity computed at θ_r
D_{ij}	Elastic coefficient
ET	Energy of continuous-time periodic signals
E_b	Elastic modulus in green condition
E_l	Elastic modulus in the longitudinal direction
E_n	Elastic modulus in air-dry condition
E_r	Elastic modulus in the radial direction
E_t	Elastic modulus in the tangential direction
$E_{(MC)}$	Elastic modulus as function of moisture content
$E_{(t)}$	Elastic modulus as function of temperature
E_{l_d}	Elastic modulus in the longitudinal direction for dynamic loading
E_{l_s}	Elastic modulus in the longitudinal direction for static loading
E_{r_d}	Elastic modulus in the radial direction for dynamic loading
E_{t_d}	Elastic modulus in the tangential direction for dynamic loading

$F(t)$	Force vector
$F(x)$	Cumulative distribution function
F_d	Dynamic loading factor
F_s	Bending test factor
F_{MCT}	Moisture-temperature factor for the elastic modulus
G_{rt}	Shear modulus in the radial-tangential plane
$H(Z)$	Frequency response function computed as $B(Z)/A(Z)$
H^R_{UT-B}	Frequency response function of the receiver
H^T_{UT-A}	Frequency response function of the transmitter
H^s_{alum}	Frequency response function of the aluminum bar
$H_d(\omega)$	Receptance
$H_{(UT-A/aluminum/UT-B)}$	Frequency response function of the assembly transmitter-aluminum bar-receiver
L	Number of discrete values used to compute $H(Z)$; specimen length
MC	Moisture content
MOE_b	Bending elastic modulus in green condition
MOE_n	Bending elastic modulus in air-dry condition
MP	Apparent fiber saturation point
N	Number of samples used to represent a discrete-time signal
$N(\mu_x, \sigma_x)$	Normal distribution
N_c	Number of cycles
N_m	Number of degrees of freedom
N_p	Model order
N_s	Sample size
ODI_{θ_r}	Overall dissimilarity index computed at θ_r
$P_r(x_r, y_r)$	Receiver position at $x = x_r$ and $y = y_r$
$P_t(x_t, y_t)$	Transmitter position at $x = x_t$ and $y = y_t$
Q_0	Excitation amplitude
RT	Local coordinate system
R^2	Regression coefficient
R_r	Ratio between the elastic moduli in the radial and longitudinal directions
R_t	Ratio between the elastic moduli in the tangential and longitudinal directions
$R_{V_p}(MC, T)$	Moisture-temperature factor for the velocity V_p
S_b	Specific gravities in green condition
S_n	Specific gravities in air-dry condition
T	Signal period; temperature
T_0	Signal duration

T_c	Pulse duration
T_t	Nominal period of the transmitter ($T_t = 1/f_t$)
$U(a,b)$	Uniform distribution
U_r, U_t	Displacement amplitudes in the radial and tangential directions
V	Wave velocity
V_l	Longitudinal wave velocity
V_p	P-wave velocity
V_s	Shear wave velocity
W_1, W_2, W_3	Weight factors
$X(\omega)$	Continuous Fourier transform
XY	Global coordinate system
X_k	Discrete Fourier transform
Z_k	Poles
$[B_e]$	Element strain-displacement matrix
$[C]$	Damping matrix
$[D]$	Elastic matrix
$[K'_e]$	Element stiffness matrix
$[K]$	Stiffness matrix
$[M]$	Mass matrix
$[R_e]$	Element rotation matrix
$[S]$	Compliance matrix
$\Delta\theta$	Angle increment
$\Delta\omega$	Frequency resolution of the Fourier spectrum
Δt	Sampling rate
α, β	Rayleigh damping parameters
α_m	Temperature coefficient
αr, αt	Direction cosines for the displacement vector in local coordinate system
αx, αy	Direction cosines for the displacement vector in global coordinate system
γ_{xy}, γ_{zx}, γ_{zy}	Shear strains
λ	Wavelength
μ_x	Mean value of x
ν_{lr}, ν_{lt}, ν_{rt}	Poisson's ratios
ω_k	Angular frequency
ω_{max}	Maximum angular frequency of the Fourier spectrum
ϕ_k	Phase angle
ρ	Mass density
σ_e^2	Prediction error variance
σ_x	Standard deviation of x
σ_x, σ_y, σ_z	Normal stresses
τ_{yx}, τ_{zx}, τ_{zy}	Shear stresses

θ_r	Receiver angle
ε_x, ε_y, ε_z	Strains
ξ	Damping ratio
a	Minimum value of an Uniform distribution
a_0, a_k, b_k	Fourier coefficients
$a_1, a_2, ..., a_{N_p}$	Coefficients of $A(Z)$
a_r, n_r	Coefficient and exponent used to compute V_p from E_r
ar, at	Direction cosines for a plane wave in local coordinate system
ax, ay	Direction cosines for a plane wave in global coordinate system
b	Maximum value of an Uniform distribution
$b_0, b_1, ..., b_{N_p}$	Coefficients of $B(Z)$
f	Frequency
f_c	Pulse frequency ($f_c = 1/T_c$)
f_t	Nominal frequency of the transmitter
$f_x(x)$	Probability density function of x
h	Finite element size
$h(t)$	Impulse response function
k	Stiffness
k, p	Factors used to define a linear exponential pulse
m	Signal pulse duration ratio; mass
$q(t)$	Nodal displacement vector
r	Frequency ratio
u_x, u_y, u_z	Displacements components
$x(t)$	Continuous time signal
x_n, y_n	Discrete time signals

Abbreviations

AIC	Akaike's information criterion
APE	Average power energy
CDF	Cumulative distribution function
CEM	Complex exponential method
COV	Coefficient of variation
CT	Computed tomography
dB	Decibel
DFT	Discrete Fourier transform
EMC	Equilibrium moisture content
FEA	Finite element analysis
FK	Frequency-wavenumber plot
FRF	Frequency response function
FSP	Fiber saturation point
FT	Fourier transform
IFT	Inverse Fourier transform
IRF	Impulse response function
MCS	Monte Carlo simulations
MDOF	Multi-degree of freedom
MOE	Elastic modulus in bending
MOR	Modulus of rupture
NDE	Non-destructive evaluation
NDT	Non-destructive test
NESC	National Electrical Safety Code
pdf	Probability density function

ppp	Probability paper plots
PVT	Pulse velocity testing
SDOF	Single-degree of freedom

Chapter 1

Introduction

Wood is one of the oldest and most common material used as structural element. It is a valuable engineering material with a high ratio of strength to weight and a remarkable performance as construction material [4, 5]. Since the beginning of electrification in Canada, late 19th-century, wood poles have been used as structural support for electric transmission and distribution lines. The transmission system is a grid of high voltage lines through which electricity travels from the generators to the area where it is needed (transformer stations). On the other hand, the distribution system is a grid that moves the electricity from the transformer stations to where the customers use it. Nowadays, wood poles are still a vital part of the electric and communication network. They are used instead of steel and concrete poles because of [5, 6]

- lower price and installation cost,
- expected service life of 35-50 years,
- easiness to handle, store, and climb,
- low electrical conductivity,
- environmental compatibility, and
- wide availability in Canada.

Wood poles are structures exposed to severe environmental conditions, which can lead to deterioration in the form of decay, insect attack, and weathering. The service life of wood poles depends on the type of wood, preservative treatments, service conditions, and maintenance practices. The average service life of wood poles can vary from 35-50 years, depending on its surrounding environment [7, 8, 9]. The main cause for the replacement of wood poles is deterioration due to decay near to the groundline. Decay in pressure treated Douglas-fir poles after 6 to 18 years in-service has been reported [10].

Ontario has over 2 millions distribution poles across the province. The average age of in-service poles is estimated in 29 years with a standard deviation of 15 years [9]. Approximately, 30% of the wood poles have more than 40 years in-service; and 17%, more than 50 years. To ensure high reliability of electrical distribution network, a large number of aging wood poles must be inspected to ensure that they are in adequate condition to remain in-service.

Wood pole inspection is part of maintenance programs for the detection of hazardous poles and the identification of early stage of decay. Visual inspection is the easiest and lowest cost method for in-situ pole inspection. It is commonly accompanied with others inspection methods such as impacting the pole with a hammer (sound), measuring the penetration resistance with a pointed tool (bore), making an excavation around the base of the pole, and using sonic waves. Wood poles are replaced when the severity of the deterioration has reduced the pole strength at the groundline below the National Electrical Safety Code (NESC) requirements [11]. However, the replacement decision based on visual inspection is subjective and therefore not reliable. It might cause either a premature or a delayed pole replacement. When visual inspection is used in conjunction with sonic waves, the reliability of the inspection method is between 40 and 50%; which is increased by 10% when it is combined with the sound and bore methods [12, 13]. More reliable inspection methods are needed for condition assessment of utility wood poles in-situ.

Ultrasonic testing is a non-destructive test (NDT) that has been used for inspection of wood poles [14]. However, wood pole condition assessment has been based only on the comparison of the measured P-wave velocity (V_p) with a reference value. This simple evaluation cannot be used for the detection of early stages of decay because of the highly variation involved in the calculation of V_p.

The elastic and mechanical properties (elastic moduli, mass density, and Poisson's ratios) present significant variations within the same wood species; therefore, the velocity V_p should be modeled as a random variable. A better understanding of wave propagation considering the orthotropic characteristics and the uncertainty in the elastic and mechanical properties of wood is essential for condition assessment of wood poles.

A new methodology for condition assessment of wood poles using ultrasonic testing is developed. It is based on numerical simulations of wave propagation in a cylindrical orthotropic medium including the uncertainties in the elastic and mechanical properties. The effect of moisture content and temperature on the elastic modulus is considered as well. A simplified method for the analysis of wave propagation in cross-sections of wood poles is developed. This simplified method allows to (a) estimate the elastic moduli in the radial and tangential directions by solving the inverse problem, and (b) compute the probability density function of P-wave velocity This evaluation is performed for four transmitter positions around the cross-section. For each transmitter position, the waveform is measured at five different angles ($\pm 90^\circ$, $\pm 135^\circ$, and

180°) with respect to the transmitter position. P-wave velocities, the elastic moduli in the radial (E_r) and tangential (E_t) directions, wave transmission factors, and the frequency and impulse response functions are obtained from the evaluation. A new specialized software is developed for (a) general signal processing; (b) condition assessment of wood poles; and (c) management of a statistical database for the assessment of wood poles. Based on the proposed methodology, a new clamping device is designed and built for the ultrasonic testing of wood poles in the field. A clamping device prototype is designed and built to perform ultrasonic tests of wood poles in the laboratory as well as in the field.

This thesis is organized as follows. The literature review is presented in Chapter 2. The Chapter 3 summarizes the Fourier analysis and the complex exponential method for identification of dynamic properties; the elastic and mechanical properties of wood as function of moisture content (MC) and temperature; and wave propagation in orthotropic media.

The methodology is described in Chapter 4. A new signal processing program, a new analysis method, and the characterization of ultrasonic transmitters are presented. A clamping device for performing ultrasonic testing of wood poles in-situ. The experimental setups for transmitter/receiver calibration, experimental modal analysis, and ultrasonic testing in wood poles are presented in Chapter 5.

Chapter 6 contains the results from numerical simulations using finite element analysis. Experimental results for new (with and without a hole) and decayed red pine poles are shown and discussed in detail in Chapter 7. Finally, the conclusions are reported in Chapter 8.

Chapter 2

Literature Review

2.1 Chapter Overview

Wood poles are typically exposed to severe environmental conditions, which cause deterioration due to wood rotting, insect attack, and weathering This deterioration is accompanied with loss of strength that reduce the structural integrity of the poles. The early detection of internal deterioration wood poles is vital for the reliability of an electric network.

Non-destructive testing uses non-invasive techniques to evaluate the integrity of a material, component or structure without altering its usefulness [15]. Non-destructive evaluation (NDE) is used to describe measurements that are more quantitative than qualitative. A NDT could be used to determine whether or not a wood pole is decayed, whereas a NDE should also be able to measured the size and location of the decayed area.

NDT was initially applied in wood for grading structural lumber by measurements of elastic parameters such as the elastic modulus in bending (MOE). Data obtained from destructive and non-destructive tests shows that the MOE can be correlated with the modulus of rupture (MOR) [16, 17, 18, 19, 20]. The MOR is an important parameter which is used to determine the remaining strength of a wood pole. In this Chapter, a review of the most common NDT techniques which have been used for condition assessment of wood poles, logs, and standing trees is presented and discussed. Methods such as visual inspection, electrical resistance, X-ray scan, impulse radar, transverse vibration, sonic waves propagation, and ultrasonic waves propagation are reviewed.

2.2 Visual Inspection

Visual inspection is the simplest and lowest cost method used for in-situ pole inspection. This method requires the knowledge of a qualified inspector for pole classification depending of the degree of deterioration observed. Hydro One Networks Inc. currently uses a strategy based on visual inspection for the assessment of transmission wood structures. The result of the inspection is expressed by a rating number from 1 (like new) to 5 (need replacement).

Ho [21] conducted full scale bending tests on 57 Douglas-fir crossarms with more than 35 years of service, from which 23 had rating 4; and the rest, rating 5. The probability that a crossarm with rating 4 may need to be replaced (rating 5) is 30%. The opposite condition has also been reported. McCarthy [22] investigated the reliability and consistency of the current visual inspection techniques. From a sample of 30 crossarms removed from service in Northern Ontario, 63% of the samples were removed prematurely.

Visual inspection is not a reliable method for condition assessment of wood poles because it is subjective and inherently inaccurate. To improve the reliability of visual inspection, it is normally accompanied with sound and bore inspection methods. The sound inspection method involves hitting the pole with a hammer for detecting interior deterioration. Depending of the sound, an experienced inspector could detect decay inside the wood pole. This inspection method continues being subjective because it depends on the level of experience and criterion of the inspector. The bore inspection method measures the penetration resistance with a pointed tool; this method cannot be classified as a non-destructive technique; and it is also non-reliable because the decision of where to introduce the pointed tool depends on the inspector. On the other hand, it is no easy to differentiate between decay and soft textured wood such as for the western red cedar [23].

2.3 Electrical Resistance

Electrical resistance has been used for the detection of internal decay in wood poles [11]. Two probes are inserted in the pole, and an electric current pulse is passed trough the probes. When a pole is decayed, the measured electrical resistance is lower than the corresponding value when the pole is sound. This method is considered as an invasive technique because many holes are required in order to cover different directions in a cross-section. Therefore, it is not suitable for in-situ wood pole inspection.

2.4 X-Ray Scan

X-rays are high-energy electromagnetic waves used to generate detailed images of materials. The attenuation of the X-rays increases with the mass density. The representation of a X-rays scan, known also as computed tomography (CT), is a two-dimensional tomographic imaging that shows how the mass density is distributed.

Schad et al. [24] performed laboratory tests on five logs (three balsam-fir and two white spruce) with different lengths and diameters using X-rays. The CT was able to detect large areas of internal degradation and large voids in logs, but it was not successful for the detection of small pockets of decay.

The main drawbacks of a *CT* scanner are its high cost and its large size. Furthermore, a highly qualified operator is required to perform an X-rays scan in a wood pole. *CT* scanner is mostly used in laboratory environment or in production lines. X-Ray scan is not suitable for the detection of early stage of decay in wood because the loss of mass density is negligible [24].

2.5 Impulse Radar

The impulse radar technique is based on sending and receiving electromagnetic waves, usually in the form of microwaves. The characteristics of electromagnetic waves depend on their wavelength. Gamma rays and X-rays have short wavelengths, whereas radar systems use long wavelengths (0.8 to 10 cm) in the microwave and radio ranges. Radio waves and microwaves tend to reflect better than shorter wavelength radiation, which are absorbed for the material.

A radar system sends an electromagnetic waves using an antenna. When the wave hist an object or boundary with different electromagnetic properties, part of the signal is reflected and received by an antenna. Sound wood has relatively low dielectric constant. Therefore, it is expected that areas of decay (high water content) can generate important reflections. A map of the discontinuities in the material can be created from the relative time delays between the reflections.

The same specimens analyzed by Schad using X-rays scan were also inspected using a 1.2 GHz radar antenna along the length of the log. The radar could detect knots, large areas of decay and large voids in logs. The main drawback of the ground penetration radar is the difficulty in interpreting the results, which are affected by the porosity, water saturation, and salinity [24, 25]. More research on the use of the ground penetration radar for the detection of decay in wood poles is required.

2.6 Transverse Vibration

The transverse vibration technique has been used to estimate the dynamic elastic modulus in bending. This method is based on the equation of the fundamental flexural mode of a beam. This technique can be use either in the laboratory or in-situ for testing wood poles. In the laboratory, the pole is simply supported on the nodal points (Fig. 2.1(a)) and excited in the transversal direction using a hammer or shaker. For a homogeneous and isotropic material, the nodal points are at $0.224L$ from the ends, where L is the length of the specimen. When the pole presents noticeable defects or decayed areas, the nodal points are not at $0.224L$. In this case, it is recommendable to test the pole as a free-free supported beam (Fig. 2.1(b)).

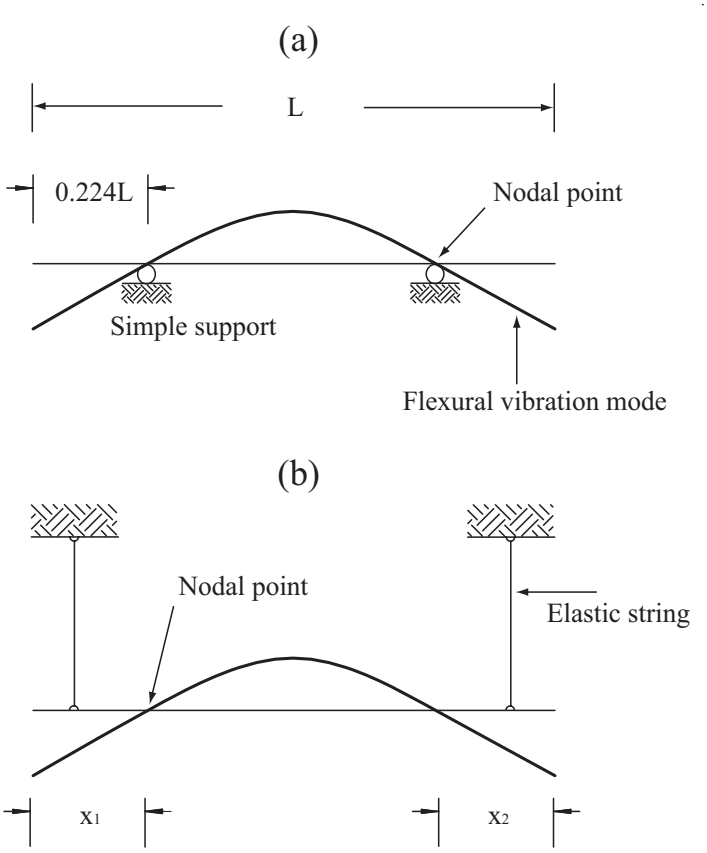

Figure 2.1: Simply supported (a) and free-free supported (b) beams

In-situ, transverse vibrations are induced by hitting the pole with a hammer and recording the pole response (time signals) at different positions from the groundline. The resonant frequency is obtained from the magnitude spectra computed from the time signals. The dynamic elastic modulus is estimated from a mathematical model of a cantilever beam. Franklin et al. [26] patented a method for testing wood poles in-situ based on measurement of the resonant frequency.

Yang et al. [27] used modal analysis to detect some defects such as knots and grain deviations in wood. Both the resonant frequency and the mode shape were used in the analysis. The mode shape of flexural vibration was determined by the transfer function method. It was compared with the theoretical mode shape for a uniform material. Yang et al. found that the mode shape of wood beams with defects is different from the theoretical one, especially close to the defect.

The dynamic elastic modulus measured from transverse vibrations represents an average value for a pole. This average is not sensitive to detect local defects inside wood poles [16].

2.7 Sonic Waves

Sonic testing is one of the most popular NDT methods used in wood to measure wave velocities [28]. A sonic wave is induced in the pole by hitting it with a hammer.

Accelerometers are used to measured the first arrival time as well as the waveform propagating trough the pole [11]. The sonic wave velocity is computed as the radial distance between the accelerometers divided by the arrival time. The dynamic elastic modulus from the one-dimensional wave equation is given by

$$E = \rho \cdot V^2 \tag{2.1}$$

where ρ is the mass density and V is the sonic wave velocity. The sonic wave velocity has been used to predict the MOR. A decrease of 30% in wave velocity respect with the expected value for sound poles implies 50% loss in strength, and 50% of decrease in wave velocity indicates that the wood is severely rotten [29].

Wang et al. [30] carried out an extensive testing in standing trees in Alaska using sonic wave technique for evaluating the elastic modulus in the longitudinal direction. The dynamic elastic modulus was computed using the one-dimensional wave equation. The results were compared with dynamic and static elastic moduli obtained in the laboratory from samples extracted from the trees. The coefficient of correlation between the wave velocities measured in the field and in the laboratory was $R^2 = 0.83$. The regression coefficient between the dynamic and the static elastic moduli in bending was $R^2 = 0.91$.

Halabe et al. [31] conducted an experimental program on green and dry southern pine to examine the relationships between the dynamic and static elastic moduli. The dynamic elastic modulus was obtained from sonic wave velocity as well as by transverse vibration measurements. The regression coefficients at green and dry conditions were 0.73 and 0.74, respectively. The wave velocity and the elastic modulus were greater for air-dry condition than for green condition

because of changes in moisture content.

Full-waveform analysis has also been used for condition assessment of wood. Magnitude spectra [32] and circumferential mode shapes [33] are determined from the waveforms. For the first case, decay in wood is determined from the attenuation of the high frequencies; whereas for the second one, decay is determined by changes in the circumferential resonant frequency.

Tomography imaging is a technique for detecting contrasting features in the medium using electromagnetic or mechanical waves. Tomography imaging using mechanical waves has been used for detection of tunnels in the ground and cracks on concrete block [34]. Rust [35] presented a new device for detecting cracks, cavities, and decay of standing trees. It is based on the simultaneous measurement of the wave transmission times by several sensors arranged around the tree (4 to 32 sensors). The sonic waves are induced by hitting every sensor with a small hammer and taking simultaneously measurements of arrival time of the wave on the others. Assuming a straight raypath model and a discrete model of the medium, the field velocity inside the wood is estimated using inversion techniques.

Waterborne preservatives can react with cellulose and other organic constituents of wood and modify its mechanical properties. Their effects are particularly important when high concentration of preservative is applied at high temperature and high pressure [16]. DeGroot and Lauret [10] found that treatment with waterborne salts have almost no effect on wave velocity. Wood poles are usually penetrated with preservatives between 37 to 61 mm.

The main drawback of using sonic waves propagation for in-situ pole inspection is the wavelength generated by the hammer. For the detection of an anomaly (decayed area in wood poles) using sonic wave techniques, the wavelength has to be smaller than the size of the anomaly. The wavelength (λ) is related with frequency (f) and wave velocity (V) by $\lambda = V/f$. The expected P-wave velocity in the radial direction of red pine poles is 1683 $\frac{m}{s}$ (Fig. 4.46). For a decayed area of 6 cm, the frequency has to be greater or equal to 28 kHz. This frequency cannot be generated by a hammer hitting the pole. From tests performed in the laboratory, the maximum frequency generated by using a hammer is about 2 kHz. The minimum wavelength would be 84 cm, which is greater than the maximum pole diameter used in transmission lines. Therefore, sonic wave propagation cannot detect a small area of decay in wood poles; and thereby, the use of ultrasonic testing is recommended.

2.8 Ultrasonic Waves

Ultrasonic waves have been used as a non-destructive test for the condition assessment of wood poles in-service [14]. This technique uses the transmission of high-frequency waves into the wood. In general, a transmitter and a receiver are used in a transillumination configuration (op-

posite faces of the specimen) to measured the first arrival of compressional waves (V_p). The velocity V_p is then computed as the distance between the transducers divided by the first arrival time. The condition assessment is performed by comparing the measured velocity V_p with a referential value that depends on the wood specie [36].

Emerson [37] conducted ultrasonic inspection technique for identifying incipient decay in large bridge timbers. The ultrasonic tests were able to identify the presence of moderate to advanced decay. Incipient decay conditions were detected from the attenuation of the wave propagation.

Nicolotti et al. [25] performed NDT on two plane trees. They used ultrasonic waves, electrical resistance, sonic waves, and ground-penetrating radar. The ultrasonic method showed the best results in detecting decayed areas with 15% of mass loss. Martinis et al. [38] reported a 5 cm anomaly resolution with ultrasonic measurements.

The main drawback of ultrasonic testing is the high attenuation of the wave propagation, particularly when the wood is decayed. Therefore, the right selection of ultrasonic transducers, waveform acquisition system, and signal processing methods are fundamental for using ultrasonic testing in wood poles. On the other hand, cylindrical orthotropic conditions and the variability in elastic and mechanical properties have to be considered for condition assessment of wood poles.

2.9 Chapter Summary

The main non-destructive tests for condition assessment of wood poles, logs, and standing tress are presented. Although visual inspection is the simplest and lowest cost method used for in-situ pole inspection, it is not a reliable method for condition assessment of wood poles because it is subjective and inherently inaccurate. The electric resistance method is not suitable for the detection of decay pockets in wood poles because many drill holes are required to cover a section. This method can be cataloged as an invasive technique.

The main drawbacks of X-ray scan are its high cost and highly qualified operator required. For this reason, the X-ray scan is mostly used in laboratory environment. X-ray scan measures the loss of mass density. Therefore, it is not suitable to detect early stage of decay in wood where loss of mass density is negligible.

The ground penetration radar generates many false positive peaks. Its use is limited because of the difficulty in interpreting the results. The porosity, water saturation and salinity affect the results of this method. The transverse vibration technique is not precise enough to detect internal deterioration in wood poles.

Although sonic testing is one of the most popular NDT methods used in wood, it is not

a reliable method because of the large wavelength involved in the evaluation; which is often greater than the wood pole diameter.

Ultrasonic testing has the required characteristics for condition assessment of wood poles in-situ: (a) it is easy to use and non-invasive technique, (b) ultrasonic waves are directly related with elastic properties, (d) a cross-section can be evaluated in an easy way, and (e) wavelengths of ultrasonic waves are small enough for the detection of a decay area of 6 cm diameter. However, until now this technique has not been reliable for in-situ pole inspection because: (a) of the high attenuation of ultrasonic waves, (b) only the first arrival of the compressional wave is considered (P-wave velocity), and (c) the P-wave velocity is modeled as a determinist variable. For using ultrasonic testing as a reliable technique for condition assessment of wood poles the following issues should be addressed: (a) characterization of ultrasonic transducers, (b) use of full-waveform analysis, (c) wood poles modeled as cylindrical orthotropic material, (d) consideration of the effect of temperature and moisture content on the mechanical properties, and (e) modelling of the mechanical properties as random variables.

Chapter 3

Theoretical Background

3.1 Chapter Overview

The mathematical tools required for condition assessment of wood poles using ultrasonic testing is reviewed next. Specifically Fourier analysis, frequency response and impulse response functions, and the complex exponential method are summarized. The elastic and mechanical properties for the most common wood species used as poles are presented, including their main statistical distributions. Wave propagation in orthotropic media and the numerical method of finite element analysis are reviewed in details. Finally, the characteristics of transducers used in ultrasonic testing are presented.

3.2 Fourier Analysis

Any periodic function can be represented by the Fourier series as a superposition of sine and cosine functions [39]. Given a time signal $x(t)$ with period T, its representation as Fourier series is expressed by

$$x(t) = a_0 + \sum_{k=1}^{\infty} a_k \cos(\omega_k t) + b_k \sin(\omega_k t) \tag{3.1}$$

The coefficients a_0, a_k and b_k are calculated by

$$a_0 = \frac{1}{T}\int_0^T x(t)dt,\ a_k = \frac{2}{T}\int_0^T x(t)\cos(\omega_k t)dt,\ b_k = \frac{2}{T}\int_0^T x(t)\sin(\omega_k t)dt \tag{3.2}$$

The coefficient a_0 represents the average or mean value of $x(t)$, whereas the coefficients a_k and b_k represent the projection of $x(t)$ on sine and cosine functions of argument $\phi_k = \omega_k t$, respectively. The angular frequency is $\omega_k = k\Delta\omega$, where $\Delta\omega = 2\pi/T$. Sine and cosine functions can be expressed using the Euler's equation [40]

$$\cos(\phi) = \frac{e^{j\phi} + e^{-j\phi}}{2}, \quad \sin(\phi) = \frac{e^{j\phi} - e^{-j\phi}}{2i} \tag{3.3}$$

where j is the complex unit ($(j)^2 = -1$). Equation (3.1) can be written as

$$x(t) = a_0 + \sum_{k=1}^{\infty} a_k\left(\frac{e^{j\omega_k t} + e^{-j\omega_k t}}{2}\right) + b_k\left(\frac{e^{j\omega_k t} - e^{-j\omega_k t}}{2j}\right) \tag{3.4}$$

regrouping terms

$$x(t) = a_0 + \sum_{k=1}^{\infty} \frac{a_k - jb_k}{2} e^{j\omega_k t} + \frac{a_k + jb_k}{2} e^{-j\omega_k t} \tag{3.5}$$

The term $(a_k - jb_k)/2$ is the complex conjugate of $(a_k + jb_k)/2$, by which eqn. (3.5) becomes

$$x(t) = \sum_{k=-\infty}^{\infty} X_k e^{j\omega_k t} \tag{3.6}$$

where

$$X_k = \frac{1}{2}(a_k - j\,b_k) = \frac{1}{T}\int_0^T x(t)\, e^{-j\omega_k t} dt \tag{3.7}$$

Fourier series are applicable only to periodic functions, but they can be extended to non-periodic functions. In the limit, when the period T tends to infinity, ω_k becomes a continuous variable, the discrete coefficients X_k become a continuous function of ω, and the summation is replaced by an integral. Equations (3.6) and (3.7) are then represented as [41]

$$x(t) = \frac{1}{2\pi}\int_{-\infty}^{+\infty} X(\omega)\, e^{j\omega t}\, d\omega \tag{3.8}$$

$$X(\omega) = \int_{-\infty}^{+\infty} x(t)\, e^{-j\omega t} dt \tag{3.9}$$

Equations (3.8) and (3.9) are known as the Fourier transform pairs. For digital signal processing, the time history is given in discrete form (x_n, $n = 1,2,3...N$). The discrete Fourier transform (DFT) pairs are therefore represented by

$$x_n = \sum_{k=1}^{N} X_k\, e^{i\frac{2\pi}{N}(n-1)(k-1)} \tag{3.10}$$

$$X_k = \frac{1}{N} \sum_{n=1}^{N} x_n\, e^{-i\frac{2\pi}{N}(n-1)(k-1)} \tag{3.11}$$

The energy of continuous-time periodic signals (ET) is given by the area under the squared signal as

$$ET = \int_0^T f(t)^2\, dt \tag{3.12}$$

while the average power energy (APE) is defined as the energy per unit of time, this is

$$\text{APE} = \frac{1}{T} \int_0^T f(t)^2\, dt \tag{3.13}$$

According to the Parseval's theorem [42], the energy computed from the time and frequency domains is the same and given by

$$\frac{1}{T} \int_0^T f(t)^2\, dt = X_0^2 + 2 \sum_{k=1}^{\infty} |X_k|^2 = \frac{1}{2}[a_0^2 + \sum_{k=1}^{\infty} (a_k^2 + b_k^2)] \tag{3.14}$$

3.3 Frequency and Impulse Response Functions

The frequency response function (FRF) for a single-degree of freedom (SDOF) linear system is defined as the ratio between the harmonic response (output) and the harmonic excitation force (input) [43]. The equation of motion for a SDOF system with viscous damping and subjected to

a harmonic force is given by [44]

$$m\ddot{x}(t) + 2\xi\sqrt{mk}\dot{x}(t) + kx(t) = Q_0 e^{j\omega t} \tag{3.15}$$

where m = mass,
k = stiffness,
ξ = damping ratio,
ω = angular frequency of the excitation,
$\ddot{x}(t)$ = acceleration response,
$\dot{x}(t)$ = velocity response,
$x(t)$ = displacement response, and
Q_0 = excitation amplitude.

If a SDOF system is subjected to a harmonic excitation force, it responds with the same frequency but with amplitude and phase given by the system. Therefore,

$$x(t) = A(\omega)\, e^{j(\omega t - \phi)} \tag{3.16}$$

$$\dot{x}(t) = j\omega A(\omega)\, e^{j(\omega t - \phi)} \tag{3.17}$$

$$\ddot{x}(t) = -\omega^2 A(\omega)\, e^{j(\omega t - \phi)} \tag{3.18}$$

where $A(\omega)$ and ϕ are the displacement amplitude and phase of the system as function of the angular frequency ω. Replacing eqns. (3.16), (3.17), and (3.18) in eqn. (3.15) and solving for $A(\omega)$

$$A(\omega) = \frac{Q_0}{(-m\omega^2 + k) + j2\xi\sqrt{mk}\,\omega} \tag{3.19}$$

The FRF or transfer function is the ratio between the SDOF response and the excitation. There are various ways of presenting the FRF depending of the parameter used to characterize the

dynamic response of the SDOF. When the displacement is the selected response parameter, the FRF is called receptance and given as

$$H_d(\omega) = \frac{A(\omega)}{Q_0} = \frac{1}{(-m\,\omega^2 + k) + j2\xi\sqrt{m\,k}\,\omega} \tag{3.20}$$

$H_d(\omega)$ is independent of the excitation and a complex function, containing both magnitude and phase information. The magnitude of $H_d(\omega)$ can be represented as

$$|H_d(r)| = \frac{1}{K\sqrt{1 + r^4 - r^2(4\xi^2 - 2)}} \tag{3.21}$$

where $r = \omega/\omega_o$, and $\omega_o^2 = k/m$. Figure 3.1 shows the FRF of a SDOF system for damping ratios of $\xi = 0.05$, $\xi = 0.1$, and $\xi = 0.2$. When the frequency ratio is $r = 1$ ($\omega_0 = \omega$), there is a condition of resonance. The width and amplitude of the FRF at the resonant frequency is governed by the damping ratio. The dynamic magnification factor (A_d) is defined as the ratio between the amplitudes at resonant condition ($r = 1$) and in a static condition ($r = 0$). For typical values of structural damping ($\xi < 0.10$), the dynamic magnification factor can be computed as $A_d = 1/(2\xi)$.

The FRF characterizes completely the dynamic system of a SDOF; therefore, the resonant frequency, the mass, the stiffness, and the damping ratio can be computed from the $H_d(r)$ [44]. The damping ratio can be determined from the dynamic magnification factor as $\xi = 1/(2A_d)$. It can also be determined by the band-width method. In this case, $\xi = (\omega_2 - \omega_1)/(\omega_2 + \omega_1) = \Delta_r/2$ where ω_1 and ω_2 are the frequencies at which the magnitude of the FRF is equal to $A_d/\sqrt{2}$ as shown in Fig. 3.1.

Other types of excitations such as random and transient can also be used to compute the FRF [45]. The discrete Fourier transform (DFT) is used when the input and the output are discrete-time signals. In this case, the resolution and maximum frequency of the Fourier spectrum ($\Delta\omega$ and ω_{max}) are related with the duration of the signal (T_0) and the number of discrete values (N) by

$$\omega_{max} = \frac{\pi\,(N-1)}{T_0} \tag{3.22}$$

$$\Delta\omega = \frac{2\pi}{T_0} \tag{3.23}$$

The inverse Fourier transform of the FRF is known as the impulse response function (IRF). The IRF is a function in time and represents the response of a linear system to an unit impulse excitation with initial conditions equal to zero. The IRF, denoted by $h(t)$, is given by

$$h(t) = \frac{1}{2\pi}\int_{-\infty}^{\infty} H(\omega)\, e^{j\omega t}\, d\omega \tag{3.24}$$

The FRF and the IRF of a linear time invariant system contain the same information; therefore, dynamic properties of a mechanical system can be determined from the free vibration response due to an impulse excitation.

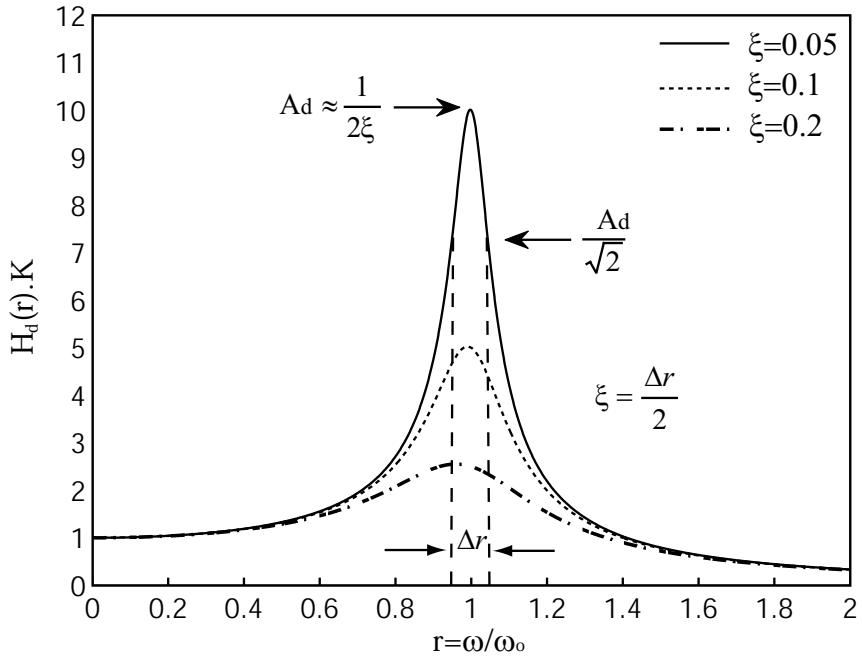

Figure 3.1: Frequency response function for a SDOF system

3.4 Complex Exponential Method

The complex exponential method (CEM) is a technique used to model transient signals as a linear sum of complex exponential functions. The CEM was developed in 1795 by Gaspard Riche, Baron de Prony, in order to explain the expansion of various gases [46]. The main advantage of the CEM with respect to Fourier analysis is the representation of transient time signals as a summation of exponential functions instead of continuous sinusoidal functions. This type of representation allows: a) direct calculation of damping ratios, and b) an increased resolution in frequency domain because the frequencies of the exponential functions are estimated in time domain. Even though the CEM provides accurate results for analysis of transient signals, the presence of noise affects the results [47]. Therefore, signal processing for noise reduction is recommended.

The CEM has been used for identification of the IRF of mechanical systems [48], characterization of waveform distortions in power systems [49], analysis of non-stationary signals [50], and in other applications where time signals can be represented as a sum of damped sinusoids.

The dynamic response in free vibration of a mechanical system with multi-degree of freedom (MDOF) is represented in discrete form as

$$y_n = \sum_{k=1}^{N_m} C_k \, e^{-\xi_k \omega_k (n\Delta t)} \cos(\omega_k (n\Delta t) + \phi_k) \tag{3.25}$$

where y_n is the system response given as acceleration, velocity, or displacement; C_k, ξ_k, ω_k, and ϕ_k are the amplitude, damping ratio, angular frequency, and phase angle, respectively; Δt is the sampling rate; N_m is the number of degrees of freedom; and $n = 0, 1, 2, ...N-1$ with N being the number of discrete values used to represent the signal. Equation (3.25) can also be expressed as a sum of exponential functions

$$y_n = \sum_{k=1}^{N_p} \hat{C}_k Z_k^n \tag{3.26}$$

where N_p is the order of the model, and Z_k is

$$Z_k = e^{(-\xi_k + j)\,\omega_k \Delta t} \tag{3.27}$$

Taking natural logarithm, the following relationships for the angular frequency (ω_k) and the

damping ratio (ξ_k) are obtained

$$\omega_k = \frac{1}{\Delta t} imag(ln(Z_k)) \tag{3.28}$$

and

$$\xi_k = -\frac{real(ln(Z_k))}{imag(ln(Z_k))} \tag{3.29}$$

If eqn. (3.25) represents the IRF of a MDOF system, the FRF is given by the Z-transform as

$$H(Z) = \frac{B(Z)}{A(Z)} = \sum_{n=1}^{L} y_n Z^{-n} \tag{3.30}$$

where $B(Z)$ and $A(Z)$ are polynomial functions, and L is the number of values of y_n used to compute $H(Z)$. The order of the numerator is equal to the order of the denominator in most practical cases. Equation (3.30) can be expanded in terms of real coefficients a_i and b_i as

$$b_0 + b_1 Z^{-1} + ... + b_{N_p} Z^{-N_p} = (y_0 + y_1 Z^{-1} + ... + y_L Z^{-L})(1 + a_1 Z^{-1} + ... + a_{N_p} Z^{-N_p}) \tag{3.31}$$

$b_0, b_1, ..., b_{N_p}$ and $a_1, a_2, ..., a_{N_p}$ are the coefficients of the polynomials $B(Z)$ and $A(Z)$, respectively. Since the coefficients $b_1, b_2, ..., b_{N_p}$ and $a_1, a_2, ..., a_{N_p}$ are real, the poles and zeros of $H(Z)$ occur in complex conjugate pairs. Equating powers of Z on each side eqn. (3.31), the following

set of equations are obtained

$$
\begin{aligned}
b_0 &= y_0 \\
b_1 &= y_1 + y_0\, a_1 \\
b_2 &= y_2 + y_1\, a_1 + y_0\, a_2 \\
&\cdot \\
&\cdot \\
b_{N_p} &= y_{N_p} + y_{(N_p-1)}\, a_1 + \ldots + y_0\, a_{N_p} \\
0 &= y_{(N_p+1)} + y_{N_p}\, a_1 + \ldots + y_1\, a_{N_p} \\
&\cdot \\
&\cdot \\
0 &= y_L + y_{(L-1)}\, a_1 + \ldots + y_{(L-N_P)}\, a_{N_p}
\end{aligned}
\tag{3.32}
$$

Equation (3.32) can be written in matrix form $\tilde{y} = \bar{Y}\,\tilde{a}$, which can be partitioned into two parts. The lower partition is given by

$$
\begin{Bmatrix} -y_{(N_p+1)} \\ -y_{(N_p+2)} \\ \cdot \\ \cdot \\ \cdot \\ -y_L \end{Bmatrix}
=
\begin{bmatrix} y_{N_p} & y_{(N_p-1)} & \cdot & \cdot & \cdot & y_1 \\ y_{(N_p+1)} & y_{N_p} & \cdot & \cdot & \cdot & y_2 \\ \cdot & & & & & \\ \cdot & & & & & \\ \cdot & & & & & \\ y_{(L-1)} & y_{(L-2)} & \cdot & \cdot & \cdot & y_{(L-N_p)} \end{bmatrix}
\begin{Bmatrix} a_1 \\ a_2 \\ \cdot \\ \cdot \\ \cdot \\ a_{N_p} \end{Bmatrix}
\tag{3.33}
$$

The resulting system of equations is underdetermined if L is smaller than $2N_p$, and it is overdetermined if L is greater than $2N_p$. In both cases, the measurement matrix $\bar{Y}$ is not square. The coefficients a_i can be evaluated by using the least-square method or from the pseudo-inverse of $\bar{Y}$ as [41]

$$
\tilde{a} = [(\bar{Y}^T \cdot \bar{Y})^{-1} \cdot \bar{Y}^T] \cdot \tilde{y} \tag{3.34}
$$

Once the coefficients a_i are determined, the coefficients Z_k, which represent the poles of the system, are obtained as

$$
Z_k = roots[A(Z)] = 1 + a_1\, Z^{-1} + \ldots + a_{N_p}\, Z^{-N_p} \tag{3.35}
$$

The coefficients Z_k are used to compute the angular frequencies (ω_k) and damping ratios (ξ_k) (eqns. (3.28) and (3.29)). The coefficients b_i are obtained substituting the coefficients a_i into the top partition of eqn. (3.32). The coefficients $\hat{C}_k$ are determined by solving the system of equations defined by eqn. (3.26). The coefficients $\hat{C}_k$ are complex numbers since the coefficients Z_k are complex (eqn. (3.27)). Finally, the FRF is computed from eqn. (3.30).

The choice of the appropriate order of the model is one of the most critical aspects of any parametric methods [51]. There is not a single theory for the determination of the optimum model order. If a low model order is selected, the computed FRF has insufficient resolution; on the other hand, a high model order can yield false peaks in the FRF. Most of the criteria available to determine the model order are based on the residual sum of square errors between the original and curve-fitted signals. The widely used Akaike's information criterion (AIC) is based on minimizing the log-likelihood of the prediction error variance as a function of the model order [51]. The error function is assumed to follow a Normal distribution with parameters $N(0,\sigma_e^2)$. The AIC of the least square fit for a regression model is given as

$$\text{AIC} = ln(\sigma_e^2) + \frac{2N}{N_p} \tag{3.36}$$

where N is the number of data points used in the modelling, N_p is the model order, and σ_e^2 is the prediction error variance computed from

$$\sigma_e^2 = \frac{1}{N}\sum_{i=1}^{N}(y_i - \hat{y}_i)^2 \tag{3.37}$$

where y_i and $\hat{y}_i$ are the actual and predicted values of the signal. The AIC criterion includes two main components: one takes into account the prediction error variance (fitting); and the other one, the deviation of the estimated coefficients $\hat{a}_i$ from their true values (complexity of the model). The first component decreases whereas the second one increases when the model order N_p increases. Therefore, there is an optimum value for N_p such that AIC is minimum.

3.5 Mechanical Properties of Wood

Water has an important effect on the mechanical properties of wood. It may be present as bound water and as free water. Bound water is within the cell walls, it affects volume changes associated with changes in moisture content (MC). Free water is in the cell cavities. The fiber saturation point (FSP) is the MC at which the free water has been removed from the wood cavities, but

the cell walls are still 100% saturated. The FSP varies depending of the wood specie; in average, FSP=28% [52]. Air-dry condition corresponds to $MC = 12\%$; whereas for green condition, $MC \geq FSP$. Moisture content values higher than the FSP have no effect on the mechanical properties.

In this section, the mechanical properties of mass density, elastic modulus, and Poisson's ratio are presented for wood species commonly used in utility poles. The mechanical properties are given for air-dry and green conditions. The main environmental factors affecting the elastic modulus are also presented.

3.5.1 Mass density

Table 3.1 shows average values of specific gravities for air-dry and green conditions of the main species of wood used in utility poles. The specific gravities for air-dry (S_n) and green (S_b) conditions are computed using the ovendry weight and the volumes in air-dry and green conditions, respectively. For $MC <$FSP, wood swells as MC increases and shrinks when MC decreases; thus, $S_b < S_n$. The specific gravity for green condition is typically 2 to 10% smaller than for air-dry condition.

The mass density as function of MC can be estimated by [53]

$$\rho_{(MC)} = \frac{1000\, S_b\, (1 + \frac{MC}{100})}{1 - (\frac{30-MC}{30})\, 0.265\, S_b} \tag{3.38}$$

3.5.2 Elastic modulus

The elastic modulus in the longitudinal direction depends on the state of stress condition (compression E_l or bending MOE) and the type of loading (static or dynamic). In general, E_l is 10% to 20% greater than MOE [2, 1, 16, 54]. On the other hand, E_l is greater than the elastic moduli in the radial (E_r) and tangential (E_t) directions; E_r is in average 40% greater than E_t [55, 1]; thus, $E_l > MOE > E_r > E_t$. The elastic modulus measured from dynamic tests is 5% to 15% greater than the measured value from static methods [56, 57, 17, 16].

Table 3.2 shows mean values of MOE for the main species of wood used in utility poles. The MOE values for green condition are between 10% and 20% smaller than the corresponding values in air-dry condition.

Experimental values for the elastic moduli E_r and E_t are not available in the literature for most wood species. Estimated values of E_r and E_t are given as fractions of E_l; typical values are summarized in Table 3.3 [2]. The ratio E_r/E_l varies from 0.068 for Douglas-fir to 0.102

Table 3.1: Specific gravities for wood species commonly used in utility poles [1, 2]

Softwood	Air-dry condition S_n	Green condition S_b
Eastern white cedar	0.30	0.30
Western red Cedar	0.34	0.31
Douglas-fir	0.49	0.45
Western larch	0.58	0.55
Tamarack	0.51	0.48
Red pine	0.46	0.41
Jack pine	0.44	0.42
Lodgepole pine	0.41	0.40

Table 3.2: Elastic modulus in static bending (*MOE*) for wood species commonly used in utility poles [1, 2]

Softwood	Air-dry condition *MOE* (GPa)	Green condition *MOE* (GPa)
Eastern white cedar	4.38	3.55
Western red Cedar	8.27	7.24
Douglas-fir	13.5	11.10
Western larch	14.3	11.40
Tamarack	9.38	8.55
Red pine	9.45	7.38
Jack pine	10.2	8.07
Lodgepole pine	10.9	8.76

Table 3.3: Elastic ratios in air-dry condition ($MC = 12\%$) for the most common wood species used in utility poles [2]

Softwood	$\frac{E_t}{E_l}$	$\frac{E_r}{E_l}$	$\frac{G_{rt}}{E_l}$
Eastern White cedar	0.05	0.07	0.018
Western Red Cedar	0.055	0.081	0.005
Douglas-fir	0.05	0.068	0.007
Western larch	0.065	0.079	0.007
Tamarack	0.057	0.086	0.008
Red pine	0.044	0.088	0.011
Jack pine	0.052	0.085	0.007
Lodgepole pine	0.068	0.102	0.005

for lodgepole pine; whereas that E_t/E_l varies from 0.044 for red pine to 0.068 for lodgepole pine. The shear modulus in a cross-section is typically between 0.5% and 2% of the longitudinal modulus E_l (Table 3.3).

3.5.3 Poisson's ratio

Isotropic materials are characterized by a single value of Poisson's ratio; however, orthotropic materials require six Poisson's ratios. Only three of them are independent when the symmetry of the stiffness matrix is considered. The relationships between elastic moduli and Poisson's ratios are given by [58]:

$$\frac{\nu_{lr}}{E_l} = \frac{\nu_{rl}}{E_r}, \qquad \frac{\nu_{lt}}{E_l} = \frac{\nu_{tl}}{E_t}, \qquad \frac{\nu_{rt}}{E_r} = \frac{\nu_{tr}}{E_t} \tag{3.39}$$

where ν_{lr} is given by the ratio of the radial strain to the longitudinal strain. The Poisson's ratio is an important parameter for the calculation of strains. However, its experimental determination is difficult. Average values of Poisson's ratios determined from static tests for some wood species are given in Table 3.4. The Poisson's ratios ν_{lr} and ν_{lt} are in average 0.34; whereas Poisson's ratios in the radial-tangential plane (ν_{rt}) is about 0.43.

Table 3.4: Poisson's ratios for wood species commonly used in utility poles [2]

Softwood	ν_{lr}	ν_{lt}	ν_{rt}
Eastern white cedar	0.337	0.340	0.458
Red Cedar	0.378	0.296	0.484
Douglas-fir	0.292	0.449	0.390
Western larch	0.355	0.276	0.389
Red pine	0.347	0.315	0.408
Lodgepole pine	0.316	0.347	0.469

3.5.4 Environmental factors affecting the elastic modulus

Wood poles in-service are exposed to changes in *MC* and temperature which affect the elastic modulus.

Moisture Content

The effect of *MC* on the dynamic and static elastic moduli is similar [59]. The elastic modulus for $MC \leq FSP$ can be computed as

$$E_{(MC)} = E_n \left(\frac{E_n}{E_b}\right)^{\frac{12-MC}{MP-12}} \tag{3.40}$$

where E_n and E_b are the elastic moduli in air-dry and green conditions, respectively; and MP is the apparent fiber saturation point. The MP value is determined by the interception of the curves representing the elastic modulus above and below the FSP. In general, a value of $MP = 25$ can be assumed [2].

Wood is a hygroscopic material by which it absorbs water from the surrounding environment until an equilibrium condition is reached. The equilibrium moisture content (EMC) is then defined as the *MC* at which the wood is neither gaining nor losing moisture. The *MC* below to the FSP is a function of both the relative humidity and temperature of the surrounding air. Figure 3.2 shows the *MC* as function of the relative humidity for a temperature of 20 $^{\circ}C$ [3]

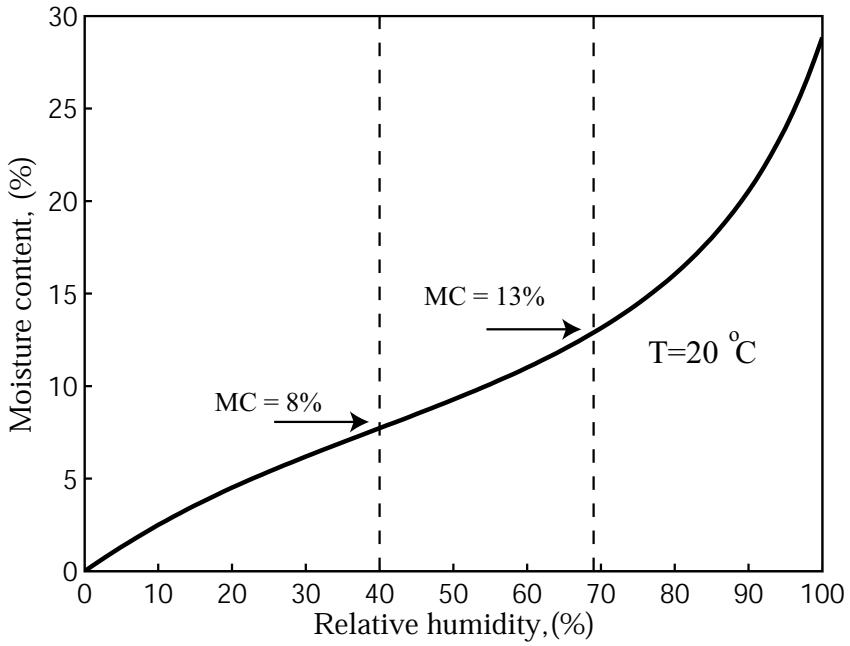

Figure 3.2: Relationship between moisture content and relative humidity for a temperature of 20 $^{\circ}C$ [3]

Table 3.5: Temperature effect on the elastic modulus at various moisture conditions [2]

E	Moisture content (%)	Relative change from 20 $^{\circ}C$ at -50 $^{\circ}C$	+50 $^{\circ}C$
Longitudinal	0	+11	-6
	12	+17	-7
	$\geq$FSP	+50	-
Radial	6	-	-20
	12	-	-35
	$\geq$ 20	-	-38

Temperature

Temperature also affects the elastic modulus in wood poles. The elastic modulus decreases at temperatures above normal room temperature ($T \simeq 20^{\circ}C$) and increases when the temperature is below it [55]. Table 3.5 presents the relative changes on the elastic modulus with respect to the referential value at $20^{\circ}C$, perpendicular and longitudinal directions, for different moisture content and temperatures of $-50^{\circ}C$ and $+50^{\circ}C$. When the temperature increases from $20^{\circ}C$ to $50^{\circ}C$, the reduction in the elastic modulus is smaller than 10%.

The MC plays an important role in the effect of temperature on the elastic modulus. For $MC = 0\%$, the relationship between elastic modulus and temperature is linear. The linearity is lost as the MC increases [60]. The following relationship has been proposed to evaluate the effect of the temperature within the range 20 to 65 $^{\circ}C$ on the elastic modulus.

$$E_{(t_2)} = E_{(t_1)} \left[1 - (t_2 - t_1)\, \alpha_m\right] \tag{3.41}$$

where $E_{(t_2)}$ and $E_{(t_1)}$ are the elastic moduli at the temperatures $T = t_2$ and $T = t_1$, respectively; α_m is a coefficient that varies with MC from $\alpha_m = 0.0004$ for $MC = 0\%$ to $\alpha_m = 0.0035$ for $MC = 24\%$ [61].

3.6 Decay of Wood

Wood is a raw material composed of cellulose, lignin, hemicelluloses, and minor amounts of extraneous materials (5% to 10%) contained in a cellular structure. Variations in the characteristics and volume of these components and differences in the cellular structure make wood heavy or light, stiff or flexible, and hard or soft [62].

The incidence and development of decay depends heavily on the temperature and MC. Decay generally requires a wood moisture content equal or greater than FSP (about 30%) and temperatures between 10°C and 43°C [63, 64]. In general, a decayed wood is less dense than a sound one, and it may be extremely light in an advanced stage of decay. Thereby, the loss in dry weight expressed as a percentage of the original dry weight is a measure to express the amount of decay. However, the loss of weight in early stage of decay is negligible even when the reduction on the elastic modulus could reach 30%.

There are basically three types of decay produced by fungi: soft-decay, white-decay, and brown-decay.

Soft-decay fungi are capable of degrading cellulose and hemicellulose and may partially digest lignin. Soft-decay fungi are particularly prevalent at early stages of wood decay and in conditions of high moisture and increased nitrogen content. Wood affected by soft-decay may appear wet, spongy, or pitted.

White-decay fungi are capable of degrading all the major components of wood (cellulose, hemicellulose, and lignin). The simultaneous decomposition causes wood to become progressively more fragile over time. However, wood does not fracture across the grain, does not shrink or collapse, and retains its outward dimensions. White-decay fungi commonly occur on hardwoods.

Brown-decay fungi are also capable of degrading cellulose and hemicellulose but are unable to digest the lignin component of wood. In this case, the lignin remains intact and appears as a brown colour.The wood can fracture across the grain, shrink, collapse, and be crushed into powder. Brown-decay fungi are of particular importance because they preferentially attack coniferous such as pine species [65].

Brown-decay fungi are characterized by their extensive capacity to digest cellulose. The early detection of brown-decay is important because it can cause a rapid failure of the wood structure. Clausen and Kartal [66] compared different methods in laboratory to detect brown-decay in early stages in southern yellow pine blocks. The maximum compressive strength and elastic modulus in blocks exposed to the fungus for 2 weeks were reduced 21% and 13%, whereas the reduction in weight was only 3%. Further studies highlighted that undetectable mass losses can produce up to 40% of loss in strength [65]. Wood decay caused by brown-decay is characterized by four stages:

Incipient decay: changes in colour and texture might occur in this stage

Intermediate decay: obvious changes in colour and texture occur, although the wood appears to be sound

Advanced decay: the wood darkens before turning brown because of accumulation of lignin residues

Heavy decay: the material is degraded in cubical pieces with little residual strength

Wood poles are structural elements which are partially embedded in the ground. Therefore, decay in wood poles is likely produced by two factors: a) because of wet underground condition; and b) because the soil acts as a source of fungi. The main cause for the replacement of wood poles is deterioration due to decay near to the groundline [7, 8]. As soon as wood is partially decayed, it absorbs water faster than when it is sound.

A heavy stage of brown decay at the centre of a wood pole section is shown in Fig. 3.3(a). Cubic pieces characteristic of brown decay are clearly identified. Figure 3.3(b) shows a heavy stage of brown decay with a circumferential shape. In this figure, the depth of the preservative around the pole is shown. Radial cracks are visible on both wood pole sections. Radial cracks may be the initial cause of internal decay because they allow the penetration of moisture into the wood.

The elastic and mechanical properties vary within the same specie of wood under the same conditions of *MC* and temperature. Therefore, for condition assessment of wood poles, the elastic and mechanical properties should be modeled as random variables.

(a) Decay at the centre of the pole section (b) Circumferential decay inside the pole section

Figure 3.3: Advanced stage of brown decay in wood poles

3.7 Statistical Distributions

The probability density function (pdf) characterizes the probability for random variables; its area between two values x_1 and x_2 of the random variable gives the probability of x being within the interval. The pdf is commonly characterized by two parameters: the expected or mean value and the second moment about the mean value (variance).

The Normal and Weibull probability distributions have been used to describe statistically the elastic modulus and the modulus of rupture [67, 68, 69]. In this section, the definitions of Normal, Log-Normal, Weibull, and Uniform probability distributions are presented. Finally, the paper probability plot is used to determine which probability distributions fits better the experimental data.

3.7.1 Normal distribution

The Normal distribution is the best known and most widely used probability distribution; its pdf is given by [9]

$$f_x(x) = \frac{1}{\sigma_x\sqrt{2\pi}} e^{-\frac{1}{2}(\frac{x-\mu_x}{\sigma_x})^2} \tag{3.42}$$

where μ_x and σ_x are the mean and the standard deviation. The Normal distribution is represented

as $N(\mu_x, \sigma_x)$. The coefficient of variation (COV) is defined as

$$COV_x = \frac{\sigma_x}{\mu_x} \tag{3.43}$$

3.7.2 Log-Normal distribution

The Log-Normal distribution is defined only for positive values of the random variable; therefore, it has been used to represent data for mechanical properties for which negative values have no meaning. The pdf for the Log-Normal distribution is

$$f_x(x) = \frac{1}{\sqrt{2\pi}\zeta_x} e^{-\frac{1}{2}[\frac{ln(x)-\lambda_x}{\zeta_x}]^2} \tag{3.44}$$

where $\zeta_x =$ location parameter, and
$\lambda_x =$ alternative parameter, e^{λ_x} is the scale parameter.

The mean and standard deviation values are given by

$$\mu_x = e^{(\lambda+\frac{1}{2}\zeta^2)} \tag{3.45}$$

$$\sigma_x = \sqrt{e^{(2\lambda+\zeta^2)}\,(e^{\zeta^2}-1)} \tag{3.46}$$

3.7.3 Weibull distribution

The Weibull distribution is a continuous distribution which has been used for reliability engineering [9]. The Weibull pdf is given by

$$f_x(x) = \frac{\gamma}{\alpha}(\frac{x-\upsilon}{\alpha})^{\gamma-1} e^{-(\frac{x-\upsilon}{\alpha})^{\gamma}} \tag{3.47}$$

where $\upsilon =$ location parameter,
$\alpha =$ scale parameter, and
$\gamma =$ shape parameter.

The mean and standard deviation values are given by

$$\mu_x = \upsilon + \alpha \cdot \Gamma[1+\frac{1}{\gamma}] \tag{3.48}$$

$$\sigma_x = \alpha\sqrt{\Gamma[1+\frac{2}{\gamma}] - \Gamma[1+\frac{1}{\gamma}]^2} \tag{3.49}$$

where $\Gamma =$ gamma function evaluated at the values of $[1+\frac{1}{\gamma}]$ and $[1+\frac{2}{\gamma}]$

3.7.4 Uniform distribution

In the Uniform distribution ($U(a,b)$) all the values have the same probability. The Uniform distribution is used in this work to characterize the variability of the Poisson's and elastic ratios; its pdf is

$$f_x(x) = \frac{1}{b-a} \tag{3.50}$$

where a and b represent the minimum and maximum values of the distribution, respectively. The mean value and standard deviation are computed from

$$\mu_x = \frac{(a+b)}{2} \quad and \quad \sigma_x = \frac{(b-a)}{\sqrt{12}} \tag{3.51}$$

The parameters a and b can be expressed as function of the COV_x and the μ_x by

$$a = (\frac{2 - COV_x\sqrt{12}}{2})\,\mu_x \tag{3.52}$$

$$b = (\frac{2 + COV_x\sqrt{12}}{2})\,\mu_x \tag{3.53}$$

For $a > 0$ and $b \geq a$, eqns. (3.52) and (3.53) yield

$$0 \leq COV_{(x)} < 0.58 \tag{3.54}$$

3.7.5 Probability paper plots

Probability paper plots (ppp) are used to determine the best-fitting distribution for an experimental data. The cumulative distribution function (CDF) is defined as

$$F(x) = \int f_x(x)dx \tag{3.55}$$

The scale of the ppp is selected such as a linear relationship between the random variable and the corresponding cumulative distributions is produced. The linearity of the experimental data for a given probability distribution is measured by the correlation coefficient. A value close to one means that the distribution can model the variability of the experimental data. The parameters of the distribution as well as the mean and the standard deviation can be determined from the ppp. Detailed explanations of ppp for different probability distributions can be found in the literature (*e.g.*,[9]).

3.8 Wave Propagation in Orthotropic Media

This section presents the equations of motion for an orthogonally anisotropic medium. These equations are not valid for wood poles because their orthotropic properties are cylindrical. However in a following section (4.6), a simplified method of analysis (Vp-COM) is presented which is based on the solution of a plane waves propagating in an infinite orthogonally anisotropic medium. This assumption is used even for small radius wood pole by reducing the size of the discretization. The assumption is later validated comparing the predicted wavefronts and wave velocities with numerical simulations.

Figure 3.4 shows stresses and displacements in an infinitesimal cubic element. The global axes Z, X, and Y are represented in cartesian coordinates. Applying Newton's second law to the infinitesimal cubic (body-force components taken as zero), the following differential equations are obtained

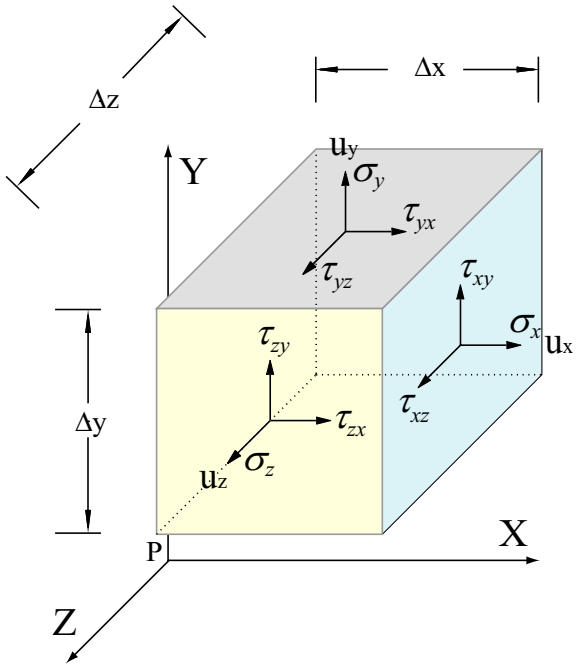

Figure 3.4: Stresses and displacements in an infinitesimal cubic element

$$\frac{\partial \sigma_x}{\partial x} + \frac{\partial \tau_{yx}}{\partial y} + \frac{\partial \tau_{zx}}{\partial z} = \rho \frac{\partial^2 u_x}{\partial t^2} \tag{3.56a}$$

$$\frac{\partial \tau_{xy}}{\partial x} + \frac{\partial \sigma_y}{\partial y} + \frac{\partial \tau_{zy}}{\partial z} = \rho \frac{\partial^2 u_y}{\partial t^2} \tag{3.56b}$$

$$\frac{\partial \tau_{xz}}{\partial x} + \frac{\partial \tau_{yz}}{\partial y} + \frac{\partial \sigma_z}{\partial z} = \rho \frac{\partial^2 u_z}{\partial t^2} \tag{3.56c}$$

The equations of compatibility between displacements and strains are

$$\varepsilon_x = \frac{\partial u_x}{\partial x}, \qquad \varepsilon_y = \frac{\partial u_y}{\partial y}, \qquad \varepsilon_z = \frac{\partial u_z}{\partial z} \tag{3.57a}$$

$$\varepsilon_{xy} = \frac{1}{2}\left(\frac{\partial u_y}{\partial x} + \frac{\partial u_x}{\partial y}\right), \qquad \varepsilon_{zx} = \frac{1}{2}\left(\frac{\partial u_x}{\partial z} + \frac{\partial u_z}{\partial x}\right), \qquad \varepsilon_{zy} = \frac{1}{2}\left(\frac{\partial u_y}{\partial z} + \frac{\partial u_z}{\partial y}\right) \tag{3.57b}$$

On the other hand, the constitutive equations between stress and strain can be expressed by [58]

$$\begin{Bmatrix} \sigma_x \\ \sigma_y \\ \sigma_z \\ \tau_{xy} \\ \tau_{zx} \\ \tau_{zy} \end{Bmatrix} = \begin{bmatrix} D_{11} & D_{12} & D_{13} & 0 & 0 & 0 \\ D_{21} & D_{22} & D_{23} & 0 & 0 & 0 \\ D_{31} & D_{32} & D_{33} & 0 & 0 & 0 \\ 0 & 0 & 0 & D_{44} & 0 & 0 \\ 0 & 0 & 0 & 0 & D_{55} & 0 \\ 0 & 0 & 0 & 0 & 0 & D_{66} \end{bmatrix} \begin{Bmatrix} \frac{\partial u_x}{\partial x} \\ \frac{\partial u_y}{\partial y} \\ \frac{\partial u_z}{\partial z} \\ \frac{\partial u_x}{\partial y} + \frac{\partial u_y}{\partial x} \\ \frac{\partial u_x}{\partial z} + \frac{\partial u_z}{\partial x} \\ \frac{\partial u_y}{\partial z} + \frac{\partial u_z}{\partial y} \end{Bmatrix} \tag{3.58}$$

where D_{ij} are elastic coefficients. The terms related with shear strains in eqn. (3.58) represent the engineering shear strains [70]. The engineering shear strain in the X-Y plane is $\gamma_{xy} = \varepsilon_{xy} + \varepsilon_{yx} = 2\varepsilon_{xy}$. For plain strain analysis in the X-Y plane, the following conditions apply [16]

$$\frac{\partial u_z}{\partial z} = 0, \qquad \frac{\partial u_z}{\partial x} + \frac{\partial u_x}{\partial z} = 0, \qquad \frac{\partial u_z}{\partial y} + \frac{\partial u_y}{\partial z} = 0 \tag{3.59}$$

therefore

$$\sigma_l = D_{31} \frac{\partial u_x}{\partial x} + D_{32} \frac{\partial u_y}{\partial y} \tag{3.60}$$

In this case, eqns. (3.56) and (3.58) can be simplified as

$$\frac{\partial \sigma_x}{\partial x} + \frac{\partial \tau_{yx}}{\partial y} = \rho \frac{\partial^2 u_x}{\partial t^2} \tag{3.61a}$$

$$\frac{\partial \tau_{xy}}{\partial x} + \frac{\partial \sigma_y}{\partial y} = \rho \frac{\partial^2 u_y}{\partial t^2} \tag{3.61b}$$

and

$$\begin{Bmatrix} \sigma_x \\ \sigma_y \\ \tau_{yx} \end{Bmatrix} = \begin{bmatrix} D_{11} & D_{12} & 0 \\ D_{21} & D_{22} & 0 \\ 0 & 0 & D_{33} \end{bmatrix} \begin{Bmatrix} \frac{\partial u_x}{\partial x} \\ \frac{\partial u_y}{\partial y} \\ \frac{\partial u_x}{\partial y} + \frac{\partial u_y}{\partial x} \end{Bmatrix} \tag{3.62}$$

Substituting eqn. (3.62) in eqn. (3.61) yields the wave equations

$$D_{11}\frac{\partial^2 u_x}{\partial x^2}+D_{12}\frac{\partial^2 u_y}{\partial y \partial x}+D_{33}(\frac{\partial^2 u_x}{\partial y^2}+\frac{\partial^2 u_y}{\partial x \partial y})=\rho\frac{\partial^2 u_x}{\partial t^2} \tag{3.63a}$$

$$D_{21}\frac{\partial^2 u_x}{\partial y \partial x}+D_{22}\frac{\partial^2 u_y}{\partial y^2}+D_{33}(\frac{\partial^2 u_x}{\partial y \partial x}+\frac{\partial^2 u_y}{\partial x^2})=\rho\frac{\partial^2 u_y}{\partial t^2} \tag{3.63b}$$

A plane wave solution is assumed as [71]

$$u_x(t)=U_x e^{jk(a_x\cdot x+a_y\cdot y-V\cdot t)}, \qquad u_y(t)=U_y e^{jk(a_x\cdot x+a_y\cdot y-V\cdot t)} \tag{3.64}$$

where U_x = displacement amplitude in X direction,
U_y = displacement amplitude in Y direction,
k = wave number,
V = wave velocity, and
a_x, a_y = direction cosines of a plane wave respect to the X and Y directions, respectively.

Taking the respective derivatives of u_x and u_y, substituting in eqn. (3.63), and expressing the equations in matrix form, it is obtained that

$$\begin{bmatrix} \Gamma_{11}-\rho V^2 & \Gamma_{12} \\ \Gamma_{21} & \Gamma_{22}-\rho V^2 \end{bmatrix} \begin{Bmatrix} U_x \\ U_y \end{Bmatrix} = \begin{Bmatrix} 0 \\ 0 \end{Bmatrix} \tag{3.65}$$

where Γ_{11} = $D_{11}a_x^2+D_{33}a_y^2$,
Γ_{12} = $\Gamma_{21}=(D_{33}+D_{12})a_x a_y$, and
Γ_{22} = $D_{22}a_y^2+D_{33}a_x^2$.

A nontrivial solution of eqn. (3.65) is possible only if

$$det\begin{bmatrix} \Gamma_{11}-\rho V^2 & \Gamma_{12} \\ \Gamma_{21} & \Gamma_{22}-\rho V^2 \end{bmatrix}=0 \tag{3.66}$$

by which

$$(\Gamma_{11}-\rho V^2)(\Gamma_{22}-\rho V^2)-\Gamma_{12}^2=0 \tag{3.67}$$

The solution of the equation of second order in the wave velocity V is

$$V^2 = \frac{\Gamma_{11} + \Gamma_{22} \pm \sqrt{(\Gamma_{11} - \Gamma_{22})^2 + 4\Gamma_{12}^2}}{2\rho} \tag{3.68}$$

For an isotropic case, the higher velocity corresponds to a wave that has particle motion in the same direction as the propagating wave front (longitudinal or compressional wave with velocity V_p). The smaller velocity corresponds to a wave that has particle motion perpendicular to the direction of the propagating wave front (transversal or shear wave with velocity V_s). For an orthotropic material however, the particle motions for the longitudinal and transversal waves are usually not parallel and orthogonal to the propagating wave front; thus, they are call quasi-longitudinal or quasi-transverse waves. Compressional waves generate volumetric changes; whereas shear waves do not.

The elastic coefficients for orthotropic materials are computed as the inverse of the compliance matrix ($[D] = [S]^{-1}$). For plain strain conditions, the compliance matrix is given by

$$S = \begin{bmatrix} \frac{1}{E_x} & \frac{-\nu_{yx}}{E_y} & \frac{-\nu_{zx}}{E_z} \\ \frac{-\nu_{xy}}{E_x} & \frac{1}{E_y} & \frac{-\nu_{zy}}{E_z} \\ \frac{-\nu_{xz}}{E_x} & \frac{-\nu_{yz}}{E_y} & \frac{1}{G_{xy}} \end{bmatrix} \tag{3.69}$$

by symmetry of the compliance matrix

$$\frac{\nu_{yx}}{E_y} = \frac{\nu_{xy}}{E_x}, \qquad \frac{\nu_{zx}}{E_z} = \frac{\nu_{xz}}{E_x}, \qquad \frac{\nu_{zy}}{E_z} = \frac{\nu_{yz}}{E_y} \tag{3.70}$$

and the elastic coefficients D_{ij} are then

$$D_0 = E_x E_z - \nu_{zx}^2 E_x^2 - \nu_{xy}^2 E_y E_z - 2\,\nu_{xy}\,\nu_{zx}\,\nu_{zy}\,E_y E_x - \nu_{zy}^2 E_y E_x \tag{3.71a}$$

$$D_{11} = \frac{(E_z - \nu_{zx}^2 E_x)\,E_x E_y}{D_0} \tag{3.71b}$$

$$D_{12} = D_{21} = \frac{(\nu_{xy} E_z + \nu_{zx}\,\nu_{zy} E_x)\,E_x E_y}{D_0} \tag{3.71c}$$

$$D_{22} = \frac{(E_z - \nu_{zy}^2 E_y)\,E_x^2}{D_0} \tag{3.71d}$$

$$D_{33} = G_{xy} \tag{3.71e}$$

For $E_z = E_x = E_y = E$, $\nu_{xy} = \nu_{zx} = \nu_{zy} = \nu$, and $G_{xy} = E/[2\,(1+\nu)]$, the elastic coefficients given by eqn. (3.71) take the following form

$$D_{11} = \frac{E\,(1-\nu)}{(1+\nu)\,(1-2\nu)} = M \qquad : \textit{constraint modulus} \tag{3.72a}$$

$$D_{12} = D_{21} = \frac{E\,\nu}{(1+\nu)\,(1-2\nu)} = \lambda \quad : \textit{Lame's constant} \tag{3.72b}$$

$$D_{22} = \frac{E\,(1-\nu)}{(1+\nu)\,(1-2\nu)} = M \tag{3.72c}$$

$$D_{33} = \frac{E}{2(1+\nu)} = G \qquad : \textit{shear modulus} \tag{3.72d}$$

which correspond with the elastic coefficients for an isotropic material [72].

3.9 Finite Element Analysis

Wave propagation in wood pole cross-sections as cylindrical orthotropic material under plain strain conditions is modeled by finite element analysis because there is not a closed-form solution. Finite elements of four nodes are used for modelling the continuous as shown in Fig. 3.5. Two degree of freedom (displacements) are defined at each node.

The vertical and horizontal displacements are restricted for point A to avoid rigid-body motion in the plane. In addition, the measured displacements at the centre of the transmitter (D(t)) are used as support displacements in vertical direction. The reaction in the horizontal direction (Rx) is zero because of the symmetry of the problem. There are not boundary conditions for the simplified method Vp-COM (infinite space); because this method is only used to compute the first arrival of compressional waves at different receiver locations. A local coordinate system coincident with the radial and tangential directions ($R'T'$) is defined at each element. The stiffness matrix for the element ($[K_e']$) in local coordinate system is computed

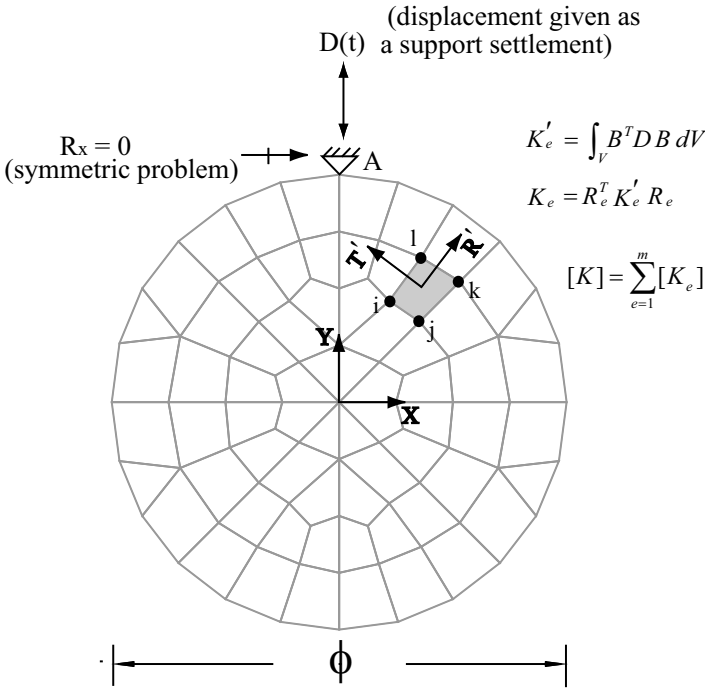

Figure 3.5: Discrete model of a wood pole cross-section using finite elements (ANSYS®)

by [72]

$$[K'_e] = \int_V [B_e]^T [D_e][B_e] dV \tag{3.73}$$

where $B_e =$ strain-displacement relationship for the element which depends of the shape functions [72], and

$D_e =$ elasticity matrix, eqn. (3.71).

The stiffness matrix of the element $[K'_e]$ is converted to global coordinate system by means of the rotation matrix $[R_e]$

$$[K_e] = [R_e^T][K'_e][R_e] \tag{3.74}$$

The assembly of the stiffness matrix of the structure is obtained by adding the contribution of all the elements to the corresponding degree of freedom. The assembly process is commonly represented as

$$[K] = \sum_{e=1}^{m} [K_e] \tag{3.75}$$

Once the stiffness matrix is obtained, the next step is to solve the matrix differential equation given by

$$[M]\ddot{q}(t) + [C]\dot{q}(t) + [K]q(t) = F(t) \tag{3.76}$$

where M = mass matrix,
C = damping matrix,
$\ddot{q}(t)$ = nodal acceleration vector,
$\dot{q}(t)$ = nodal velocity vector,
$q(t)$ = nodal displacement vector, and
$F(t)$ = applied force vector.

The matrix $[M]$ is a lumped mass matrix; therefore, it is a diagonal matrix. The matrix $[C]$ is the damping matrix. It is assumed that $[C]$ is a linear combination of stiffness and mass matrices (Rayleigh damping model), given as [44]

$$[C] = \alpha[M] + \beta[K] \tag{3.77}$$

The parameters α, and β are determined from measurements of two damping ratios at two resonant frequencies. The force vector $F(t)$ is the transmitter response to a one-cycle sine excitation of 50 kHz. This force is applied in vertical direction at the top of the section as shown in Fig. 3.5.

The Newmark time integration is used to solve for the unknown displacements at each node [73, 44]. This method express the response of velocity and displacement at one time step in terms of the values at these quantities in the previous step plus an integral expression. The Newmark parameters are chosen such that the solution is unconditionally stable. Therefore, the time step is selected to provide a satisfactory representation of the dynamic response of an ultrasonic transmitter of 50 kHz as nominal frequency.

The finite element size is defined from a convergence test selecting as parameter the P-wave velocity. The selected finite element size is the value for which the P-wave velocity does not change with the refining of the mesh [74]. The convergence test is based only on the first arrival of the compressional waveform. Therefore, a frequency-wavenumber plot (FK) is also computed for visualization of wave propagation as function of frequency and wavenumber.

3.10 Ultrasonic Transducers

Transducers are a critical component of ultrasonic testing for condition assessment of wood poles. They use a piezoelectric element to convert electrical signals into wave energy (transmitter) and viceversa (receiver). Transmitter and receiver are typically used in a transillumination configuration (opposite faces of the specimen).

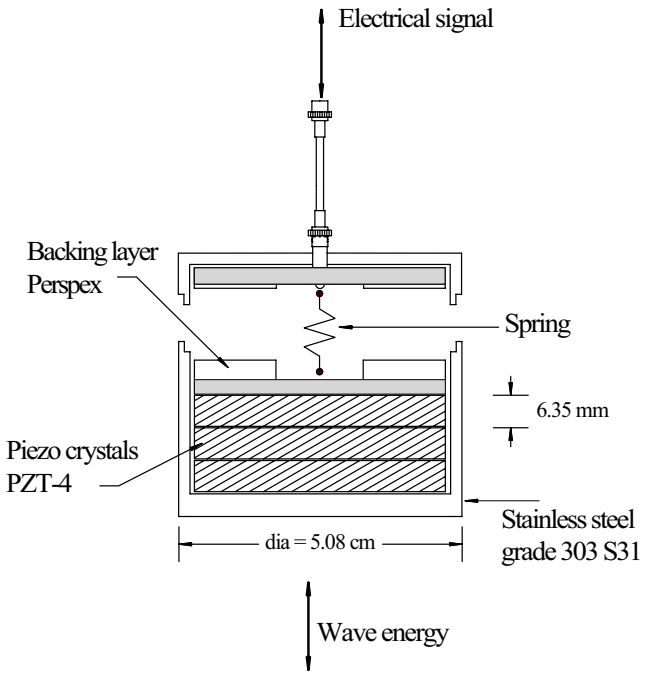

Figure 3.6: Schematic configuration of an ultrasonic transducer

An ultrasonic transducer is characterized by its nominal frequency and the frequency response bandwidth. The nominal frequency, which defines the capability to detect small discontinuities, depends on the thickness of the piezoelectric crystal. A thin piezoelectric disk vibrates with a wavelength that is twice its thickness. On the other hand, the frequency response bandwidth depends of the damping ratio. Highly damped transducers respond to frequencies above and below the nominal frequency. A broad frequency range response (high damping) characterizes transducers with high resolution or ability to generate sharp pulses. Whereas, transducers with small damping exhibits a narrow frequency range with low resolution.

A schematic representation of the ultrasonic transducer used for the condition assessment of wood poles is illustrated in Fig. 3.6. It has three piezoelectric crystals PZT-4 of 6.35 mm thick. The bottom crystal is in direct contact with the inside of the bottom face of the housing, which is stainless steel grade 303-S31. The backing layer is a perspex plate with two disc springs back-to-back to compress the crystal stack. The backing layer controls the vibration of the transducer by absorbing the energy transmitted from the back face of the piezoelectric crystal. The acoustic impedance for the elements PZT-4, stainless steel, and perspex are 34.5×10^5, 45.55×10^5, and 3.06×10^5 $g/cm^3\,s$, respectively. The transmitter is 5.08 cm diameter and has a nominal frequency of 50 kHz.

3.11 Chapter Summary

The theoretical background supporting the new methodology for condition assessment of wood poles is presented. Fourier analysis and the frequency response function are used to analyze the signals in

frequency domain, whereas the CEM and the impulse response function are used for time domain analysis. The CEM can be used successfully for ultrasonic transducer characterization. Mean values and coefficients of variation for elastic properties of wood, finite element analysis, and wave propagation in orthotropic media in cartesian coordinates are presented.

Chapter 4

New NDT Methodology

4.1 Chapter Overview

Wood poles in a frame of a 115 kV transmission line and a 44 kV distribution line are shown in Fig. 4.1. The condition of these poles using ultrasonic testing is commonly performed by monitoring the change in the compressional wave velocity (V_p). This type of evaluation is not always reliable because wood is an orthotropic material; and it is not isotropic as assumed in existing evaluation techniques. A better understanding of wave propagation in a cylindrical orthotropic medium considering the uncertainty in the mechanical properties is essential for condition assessment of wood poles using ultrasonic testing.

In this chapter, a new methodology for condition assessment of wood poles using ultrasonic testing is presented. The new methodology includes advances in the areas of signal processing, dynamic characterization, statistical analysis, numerical simulations, and laboratory testing. Wood is modeled as a cylindrical orthotropic material with uncertainties in its elastic and mechanical properties. The arrival time of compressional waves as well as full-waveform analysis are used for an integrated evaluation of wood pole. A simplified model of P-wave propagation in pole cross-sections is developed; which allows to (a) estimate the elastic moduli in the radial and tangential directions by solving the inverse problem, and (b) compute the probability density function of P-wave velocity. Both of these parameters are critical for condition assessment; however, they are not available in the literature because of the complexities associated with modelling wood as an orthotropic material.

A new specialized software is developed for (a) general signal processing; (b) non-destructive condition assessment of wood poles; and (c) management of a statistical database for the assessment of wood poles. Based on the proposed methodology, a new clamping device is designed and built for the ultrasonic testing of wood poles in the field.

(a) 115 kV transmission line

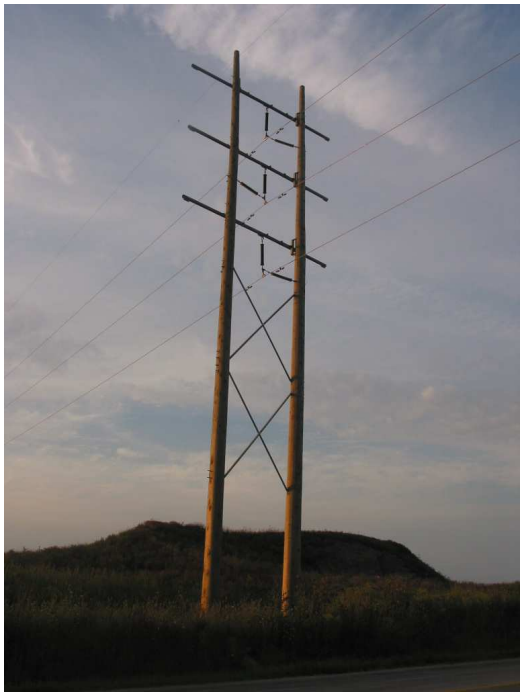

(b) 44 kV distribution line

Figure 4.1: Transmission and distribution electrical lines

4.2 New Signal Processing Software (WPNDTool-Box)

WPNDTool-Box is a specialized software developed for (a) general signal processing, (b) non-destructive condition assessment of wood poles, and (c) management of a statistical database for the assessment of wood poles. WPNDTool-Box is written in Matlab 7.04 and includes modules for file management, pre-processing, processing, probability analysis, P-wave propagation in a cylindrical orthotropic medium (Vp-COM), and condition assessment (SCA-WP). Figure 4.2 shows the main window of WPNDTool-Box. The description of the functions in each module is presented in Fig. 4.3.

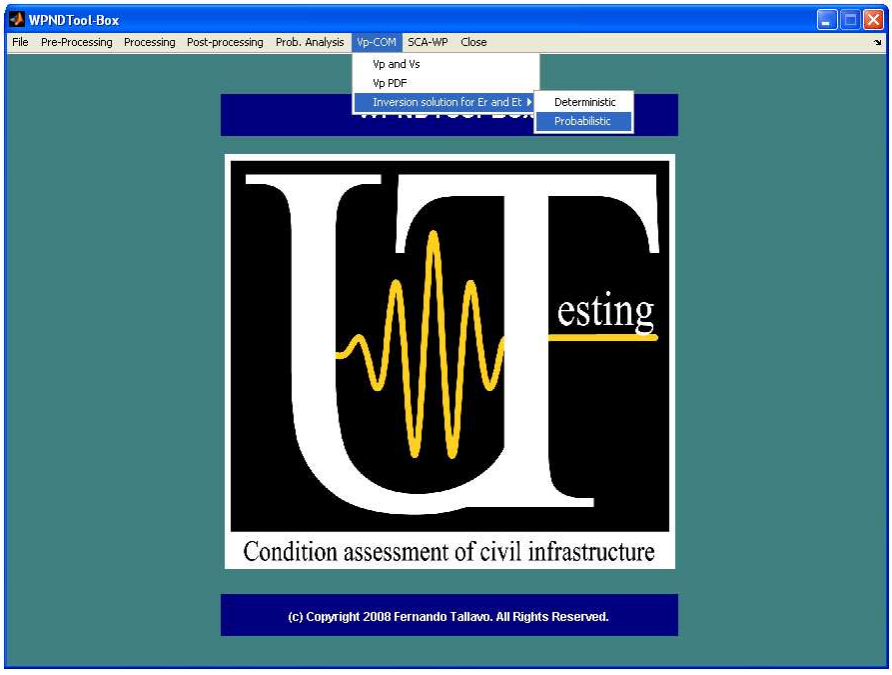

Figure 4.2: WPNDTool-Box: new computer program for data processing and analysis of ultrasonic tests

The file management module converts ascii (.txt) and SG2 (.sg2) files to Matlab format (.mat). The conversion from Matlab file to ascii is also included. The data is organized in vectors containing information of the discrete time signals. The sampling rate is constant for all the signals. WPNDTool-Box can be used to process a total of 99 time signals for each test; input signals are called $y_{01}, y_{02}, y_{03}, ...y_{99}$.

The pre-processing module contains functions for signal conditioning. This module includes low-pass, high-pass, band-pass, and band-stop digital filters; signal denoising using the wavelet transform; single and double integration in time domain; time windowing; and time domain interpolation.

The processing module includes functions for the calculation of the arrival time using the Hilbert transform and the cross-correlation function, the CEM for dynamic characterization, Fourier analysis, the discrete and continuous wavelet transform, the Cepstrum transform, an the frequency response and impulse response functions. The one-dimensional Fourier analysis includes the magnitude and phase

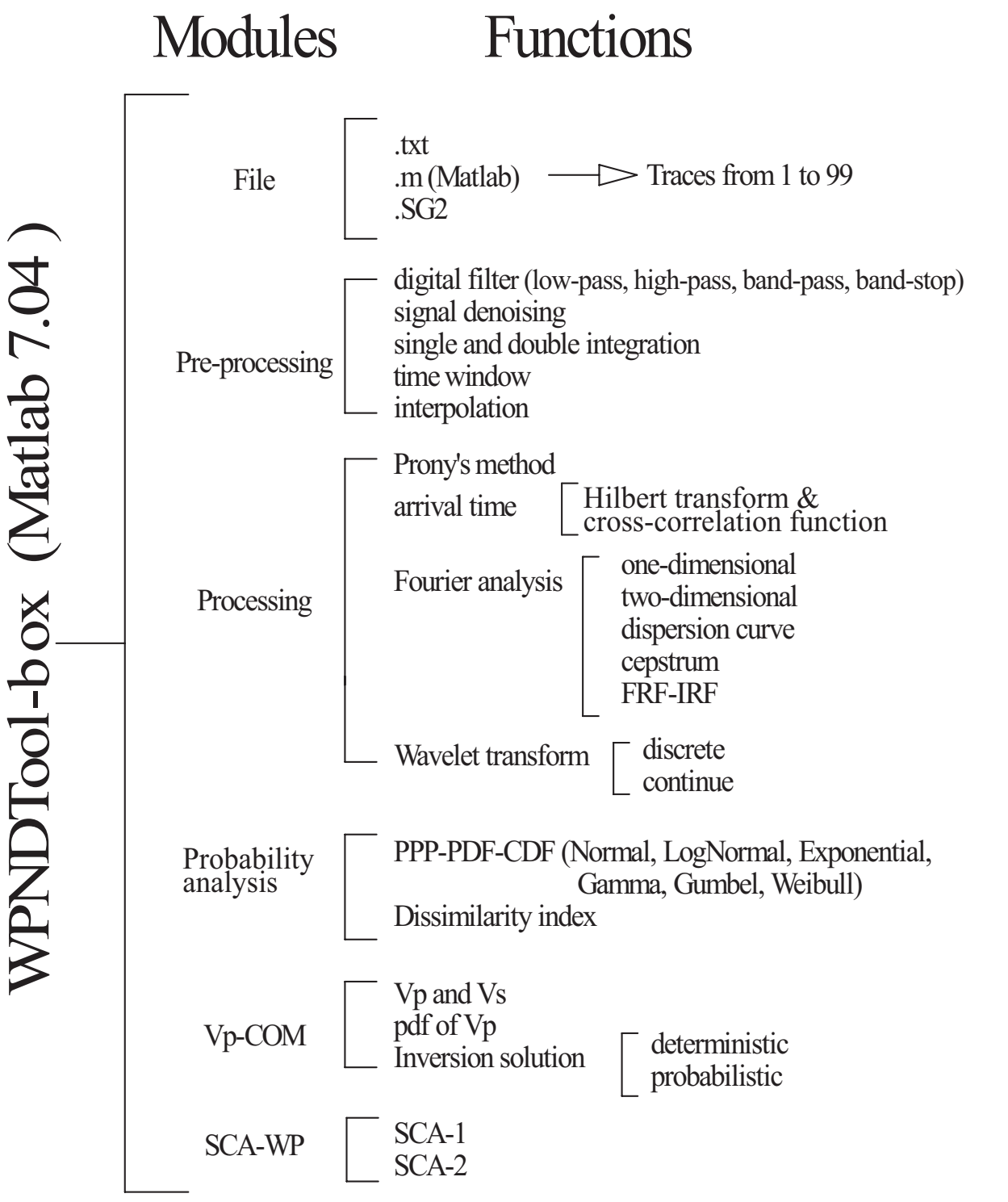

Figure 4.3: WPNDTool-Box: modules and functions

spectrum, unwrapped phase, real and imaginary components, and the damping ratio computed from the power spectral function using the band-width method. The two-dimensional Fourier analysis includes the FK plot and the computation of the dispersion curve.

The statistical distributions Normal, Log-normal with two and three parameters, Exponential with one and two parameters, Gamma with two and three parameters, Gumbel, and Weibull with two and three parameters are included in the statistical module. This module also computes the dissimilarity index between two probability density functions.

The Vp-COM module includes a new simplified method of analysis for the propagation of P-waves and S-waves wood pole cross-sections. The medium is modeled as cylindrical orthotropic under plain strain conditions. The elastic and mechanical properties for most common species of wood are included in a data base for air-dry and green conditions. The mechanical properties can be also defined by the user. The analysis can be performed for any temperature and moisture content below to the fiber saturation point. This module computes three main parameters: (a) V_p and V_s velocities, (b) the pdf of the velocity V_p, and (c) the elastic moduli E_r and E_t by solving the inverse problem. The inversion can be performed assuming either a deterministic value or a probability function for the mass density.

The condition assessment of wood poles is included in the SCA-WP module. The assessment of a wood pole is based on the dissimilarity indexes computed for V_p, elastic moduli E_r and E_t, and wave transmission factors. The results are presented for receivers located at three different angles from the source or transmitter $\theta_r = \pm 90^\circ$, $\theta_r = \pm 135^\circ$, and $\theta_r = 180^\circ$. The computation of the frequency response and impulse response functions are also incorporated in this module. The function SCA-2 performs an integral assessment of the wood pole including a histogram of the overall dissimilarity index. The program detects automatically the location of an anomaly inside the pole and gives a range of values for the elastic moduli E_r and E_t.

4.3 UT-Pole Prototype

UT-Pole prototype is a device designed and built to perform ultrasonic tests in wood pole cross-sections. Figure 4.4 shows the main characteristics of the UT-Pole device. The frame is made of steel and has a triangular shape; which is fixed to the pole by two small supports. The ultrasonic transducer is pressed against the pole by a precision bolt and two bars of 6 mm of diameter. An array of eight UT-Pole devices can be set as shown in Fig. 4.4. The UT-Pole device has four main characteristics: a) is practically isolated from the cross-section being testing and from the transducers, b) can be rotated 180 degrees to perform ultrasonic testing at the groundline of wood poles, c) can control the pressure applied to the transducers, and d) can be used for calibration of the transmitter/receiver system. Figure 4.5 illustrates the UT-Pole device during an ultrasonic test of a red pine pole.

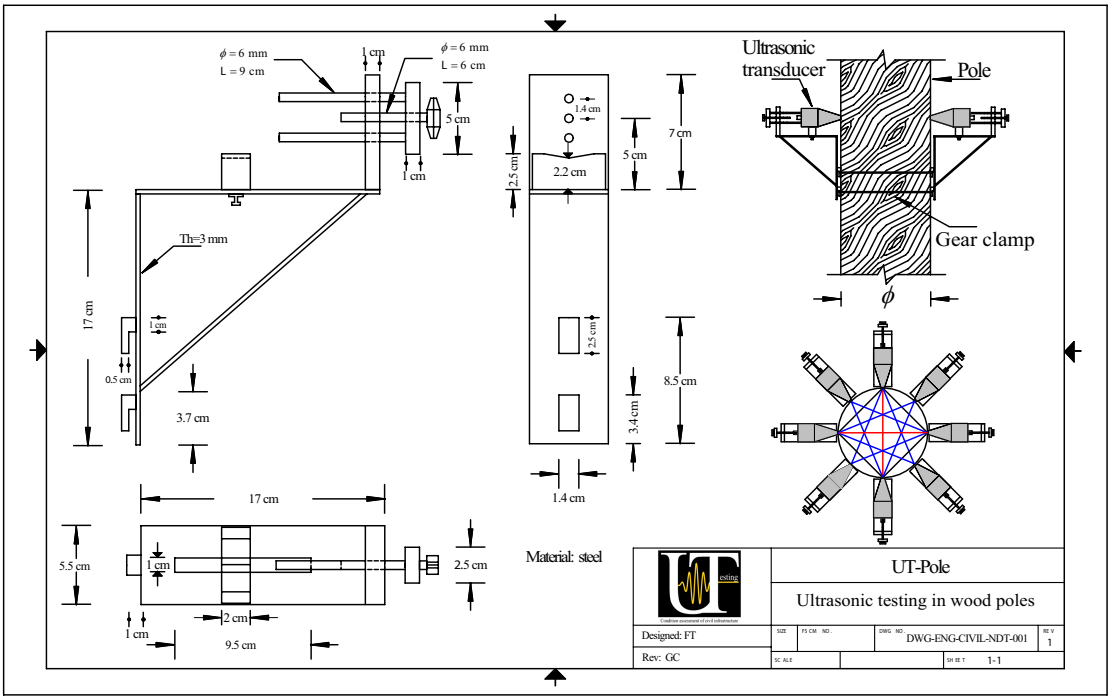

Figure 4.4: UT-Pole design

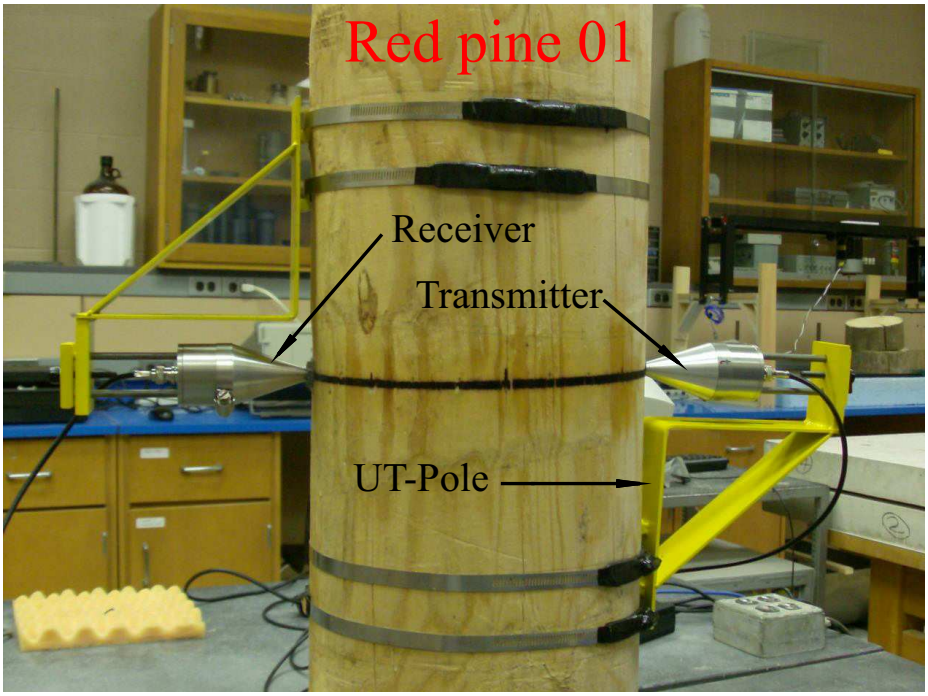

Figure 4.5: UT-Pole prototype

4.4 Ultrasonic Source Characterization

The main characteristics of the ultrasonic waves generated by a transmitter depend on the characteristics of the transmitter and the excitation electrical pulses. In this section, six different types of electrical pulses are analyzed in the frequency domain. The closed-form solution for the Fourier series representation of each pulse is presented. These pulses are later used as excitation for ultrasonic transmitters and their effects on the response of the transmitter are examined.

4.4.1 Transmitter excitation

Square and linear-exponential pulses are commonly used for excitation of ultrasonic transmitters, but other pulses can be used as well. Figure 4.6 shows six different excitations pulses, where T_c and T_0 are the duration of the pulse and the total duration of the signal, respectively. The Fourier series coefficients a_k and b_k for each type of pulse are computed using eqn. (3.2). These coefficients are summarized in Table 4.1. For a square wave, the Fourier series coefficients are only given for the cases of one and three cycles. The derived equations for sine, sawtooth, and triangle waves are general and can be used to compute the Fourier series coefficients for any number of cycles. For the case of the sine wave, the equations given in Table 4.1 can be used also to compute the Fourier coefficients for half a cycle ($N_c = 0.5$).

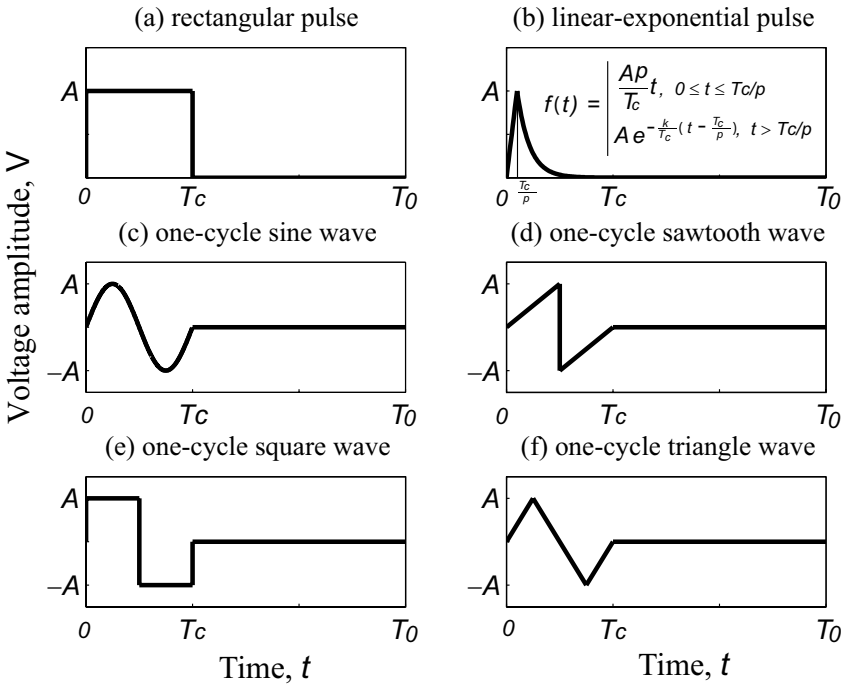

Figure 4.6: Electrical pulses used as excitation of ultrasonic transmitters (p and k are parameters for the linear-exponential pulse)

Table 4.1: Fourier series coefficients for electrical pulses used as excitation of ultrasonic transmitters

Excitation type	a_k and b_k Fourier coefficients
Sine	$a_0 = \frac{A}{2m\pi}[-\cos(2m\pi RN_c)+1]$ $a_k = \begin{cases} \frac{A}{2\pi}[-\frac{\cos(2\pi RN_c(m+k))}{m+k} - \frac{\cos(2\pi RN_c(m-k))}{m-k} + \frac{1}{m+k} + \frac{1}{m-k}] & \text{for } k \neq m \\ \frac{A}{2m\pi}[\sin(2m\pi RN_c] & \text{for } k = m \end{cases}$ $b_k = \begin{cases} \frac{A}{2\pi}[\frac{\sin(2\pi RN_c(m-k))}{m-k} - \frac{\sin(2\pi RN_c(m+k))}{m+k}] & \text{for } k \neq m \\ \frac{A}{2m\pi}[-\sin(2\pi mRN_c)\cos(2\pi mRN_c)+2\pi mRN_c] & \text{for } k = m \end{cases}$
Square pulse	$a_0 = \frac{A}{m}$ $a_k = \frac{A}{m}\sin(\frac{2\pi k}{m})$ $b_k = \frac{A}{m}[-\cos(\frac{2\pi k}{m})+1]$
One-cycle square	$a_k = \frac{A}{\pi k}[2\sin(\frac{\pi k}{m}) - \sin(\frac{2\pi k}{m})]$ $b_k = \frac{A}{\pi k}[-2\cos(\frac{\pi k}{m}) + \cos(\frac{2\pi k}{m})+1]$
Three-cycle square	$a_k = \frac{A}{\pi k}[2\sin(\frac{\pi k}{m}) - 2\sin(\frac{2\pi k}{m}) + 2\sin(\frac{3\pi k}{m}) - 2\sin(\frac{4\pi k}{m}) + 2\sin(\frac{5\pi k}{m}) - \sin(\frac{6\pi k}{m})]$ $b_k = \frac{A}{\pi k}[-2\cos(\frac{\pi k}{m}) + 2\cos(\frac{2\pi k}{m}) - 2\cos(\frac{3\pi k}{m}) + 2\cos(\frac{4\pi k}{m}) - 2\cos(\frac{5\pi k}{m}) + \cos(\frac{6\pi k}{m}+1)]$
Sawtooth	$a_k = \frac{Am}{\pi^2 k^2}[\sum_{i=1}^{N_c} \frac{2\pi k}{m}\sin(\frac{\pi k}{m}(2i-1)) + \cos(\frac{2\pi k}{m}i) - \cos(\frac{2\pi k}{m}(i-1))]$ $b_k = \frac{Am}{\pi^2 k^2}[\sum_{i=1}^{N_c} -\frac{2\pi k}{m}\cos(\frac{\pi k}{m}(2i-1)) + \sin(\frac{2\pi k}{m}i) - \sin(\frac{2\pi k}{m}(i-1))]$
Triangle	$a_k = \frac{2Am}{\pi^2 k^2}[\sum_{i=1}^{N_c} 2\cos(\frac{2\pi k}{m}(i-\frac{3}{4})) - 2\cos(\frac{2\pi k}{m}(i-\frac{1}{4})) + \cos(\frac{2\pi k}{m}i) - \cos((i-1)\frac{2\pi k}{m})]$ $b_k = \frac{2Am}{\pi^2 k^2}[\sum_{i=1}^{N_c} 2\sin(\frac{2\pi k}{m}(i-\frac{3}{4})) - 2\sin(\frac{2\pi k}{m}(i-\frac{1}{4})) + \sin(\frac{2\pi k}{m}i) - \sin((i-1)\frac{2\pi k}{m})]$
Linear-exponential pulse	$a_0 = \frac{A}{m}[\frac{1}{2p} - \frac{e^{-\frac{k(mp-1)}{p}}-1}{k}]$ $a_k = Am[\frac{1}{2\pi^2 k^2}(\cos(\frac{2\pi k}{mp})p + \frac{2\pi k}{m}\sin(\frac{2\pi k}{mp}) - p) - \frac{2}{k^2m^2+4\pi^2k^2}(k(e^{-\frac{k(mp-1)}{p}} - \cos(\frac{2\pi k}{mp})) + \frac{2\pi k}{m}\sin(\frac{2\pi k}{mp}))]$ $b_k = Am[\frac{1}{2\pi^2 k^2}(\sin(\frac{2\pi k}{mp})p - \frac{2\pi k}{m}\cos(\frac{2\pi k}{mp})) - \frac{2}{k^2m^2+4\pi^2k^2}(\frac{2\pi k}{m}(e^{-\frac{k(mp-1)}{p}} - \cos(\frac{2\pi k}{m})) - k\sin(\frac{2\pi k}{m}))]$

A = maximum pulse amplitude, N_c =number of cycles, T_c = pulse duration, T_0 = pulse duration including zero padding, $m = \frac{T_0}{T_c}$, $R = \frac{1}{m}$, k and p are factors to define the linear exponential pulse

Table 4.2: Energy (ET) for electrical pulses used as excitation signals for ultrasonic transducers

Signal	$ET = \int_0^{T_c} f(t)^2 dt$
Sine	$\frac{A^2}{2} T_c N_c$
Square	$A^2 T_c N_c$
Sawtooth	$\frac{A^2}{3} T_c N_c$
Triangle	$\frac{A^2}{3} T_c N_c$
Square pulse	$A^2 T_c$
Linear-exponential pulse	$A^2 [\frac{1}{3p} + \frac{1}{2k}(1 - e^{-2k\frac{(p-1)}{p}})] T_c$

A = pulse amplitude, T_c = pulse duration, N_c = number of cycles, k = factor to define the residual amplitude of a linear-exponential pulse at $t = T_c$, and p = factor to define the starting time for the exponential part of the pulse

The energy for each type of pulse (eqn. (3.12)) is presented in Table 4.2. The energy for the sine and sawtooth pulses is one half and one third of the energy of the square pulse, respectively. The sawtooth and triangle pulses have the same energy. A square pulse and a one-cycle square pulse, with the same pulse width (T_c), have also the same energy. For a linear-exponential pulse, the energy depends on two parameters, p and k, which define the shape of the pulse. For example, an exponential pulse with a residual amplitude of 0.03% at $t = T_c$ ($p \to \infty$, and $k = 8$) has 6% of the energy corresponding to a square pulse with the same width T_c.

The power spectrum for each pulse is computed from the Fourier series coefficients. The power spectra for square and linear-exponential pulses are shown in Fig. 4.7. The frequency values are normalized with respect to the frequency of the pulse f_c. The power spectrum amplitudes are normalized by the factor $(m/A)^2$ where $m = T_0/T_c$. The total area of the normalized power spectrum is equal to the signal energy divided by the factor $A^2 T_c$. Therefore, the power spectrum shape is independent of the ratio $m = T_0/T_c$, the maximum pulse amplitude A, and the frequency of the pulse $f_c = 1/T_c$.

The power spectrum of the square pulse has the maximum magnitude when $f = 0$ (Fig. 4.7) and decays with frequency (practically zero for $f/f_c > 5$). The spectrum is also zero at frequencies multiple of f_c. Figure 4.8 shows the normalized transmitter amplitude response (assuming a SDOF) as function of the frequency ratio f_t/f_c, where $f_t = 1/T_t$ is the nominal frequency of the transmitter and $f_c = 1/T_c$ is the frequency of a square pulse. The maximum transmitter response is obtained when the width of a square pulse (T_c) is equal to one half of the nominal period of the transmitter (T_t).

The power spectrum for a linear-exponential pulse ($p = k = 8.5$, Fig. 4.7) shows a decay of 3dB (30%) in magnitude at $f = f_c$ with respect to the maximum spectrum magnitude at $f = 0$. The vibration amplitude of a transmitter excited with a square pulse is almost one order of magnitude greater than the corresponding response when a linear-exponential pulse of the same amplitude is used.

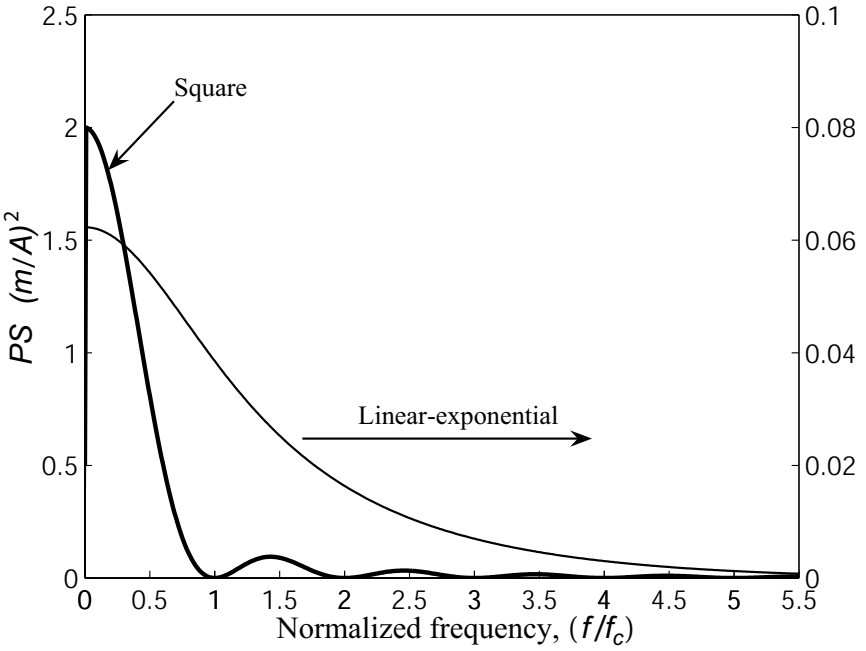

Figure 4.7: Normalized power spectra for square and linear-exponential pulses

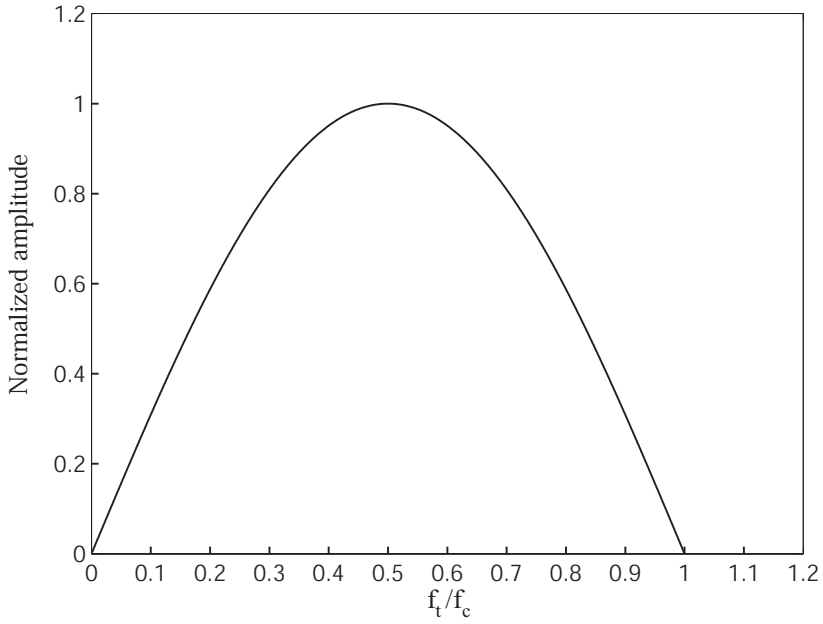

Figure 4.8: Normalized transmitter amplitude response as function of the ratio f_t/f_c, where f_t is the transmitter nominal frequency, and f_c is the frequency of a square pulse

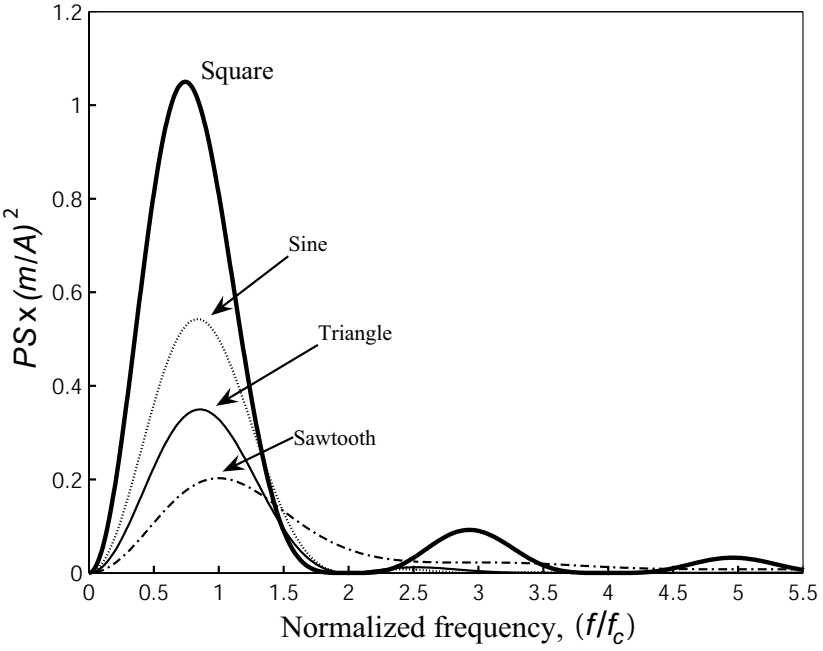

Figure 4.9: Normalized power spectra for a one-cycle square, sine, triangle, and sawtooth pulses

The power spectra for a one-cycle square, sine, triangle, and sawtooth pulses are presented in Fig. 4.9. These spectra have zero magnitude at $f = 0$ and maximum magnitude at normalized frequencies $f/f_c =$ 0.74, 0.84, 0.86, and 1.0, respectively. The magnitude ratios between the square and sine pulses is 1.94; whereas for the square and triangle pulses, the ratio is 3. These ratios are practically the same as the ratios of the total energies computed in time domain (Table 4.2). Even though the sawtooth and triangle pulses have the same total energy, the sawtooth pulse exhibits the smallest maximum spectral magnitude (the maximum spectral amplitude ratio between the square and sawtooth pulses is 5.2). Thus, the maximum response of a transmitter is obtained using a square pulse with frequency $f = f_t/0.74$.

The power spectra for three-cycle pulses are presented in Fig. 4.10. The energy concentrates at the frequency f_c. There are secondary peaks at normalized frequencies $f/f_c = 0.17$, 0.52 and 1.5 of f_c, but their amplitudes are smaller than the main peak. The spectrum of the sawtooth pulse has also peaks at frequency multiples of f_c ($n = 2,3,4...$), whereas the square pulse shows peaks at $n = 3,5,7...$ In comparison with the spectra for a one-cycle pulses, the energy at the frequency f_c for a three-cycle square, sine, triangle, and sawtooth pulses is 7.2, 8.4, 8.5, and 9 times greater, respectively. These energy ratios are higher than the computed values in time domain (ratio 3:1) because 50% of the energy is concentrated in a narrow frequency band ($0.9f_c$ to $1.1f_c$) for three-cycle pulses; whereas for one-cycle pulses, only 18% of the energy is concentrated in this frequency bandwidth.

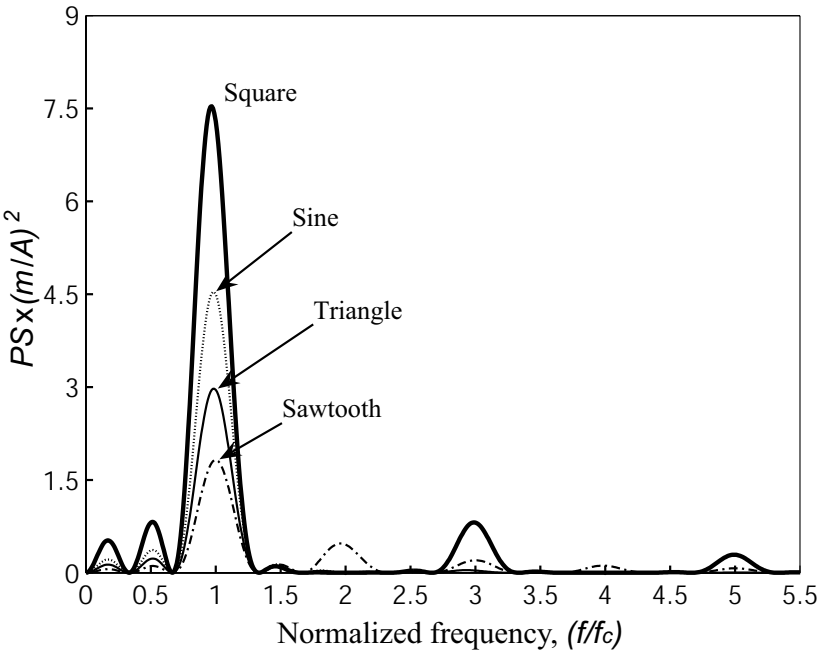

Figure 4.10: Normalized power spectra for a three-cycle square, sine, triangle, and sawtooth pulses

4.4.2 Transmitter response

The characterization of an ultrasonic transmitter is obtained from its dynamic response to different electrical pulses of 50 kHz. The characteristics of the transducers are given in Section 3.10. A piezoelectric accelerometer (PCB 352A60) is used to measure the response of the transmitter.

The measurements are taken at five different positions on the circular section of the transmitter: at the center, at the edges, and at a quarter of the diameter from the centre to the edge. The response of the accelerometer is analyzed using the AIC criterion (eqn. (3.36)), and the CEM is used to identify the main frequencies, damping ratios, amplitudes, and phase angles of the transmitter response. The transmitter response is also given in terms of velocity and displacement by integrating the acceleration signals. The computed displacements at the five different locations are used to calculate the actual deformation of the circular face of the transmitter caused by different electrical pulses.

Figure 4.11 shows the experimental setup used for the characterization of the ultrasonic transmitter. The piezoelectric accelerometer is attached on the face of the transmitter using the Loctite adhesive 454. The calibration data sheet of the accelerometer shows a flat response up to 70 kHz (0.94 dB of deviation at 60 kHz). The accelerometer's weight and measurement range to full scale are 5.678 gr and ± 500 g, respectively.

The ultrasonic transmitter is excited with different types of electrical pulses as shown in Fig. 4.6 (linear-exponential, a one-cycle and three-cycle sinusoidal, square, sawtooth, and triangle). The frequency and amplitude for one-cycle and three-cycle pulses are 50 kHz and 150 V, respectively. The electrical

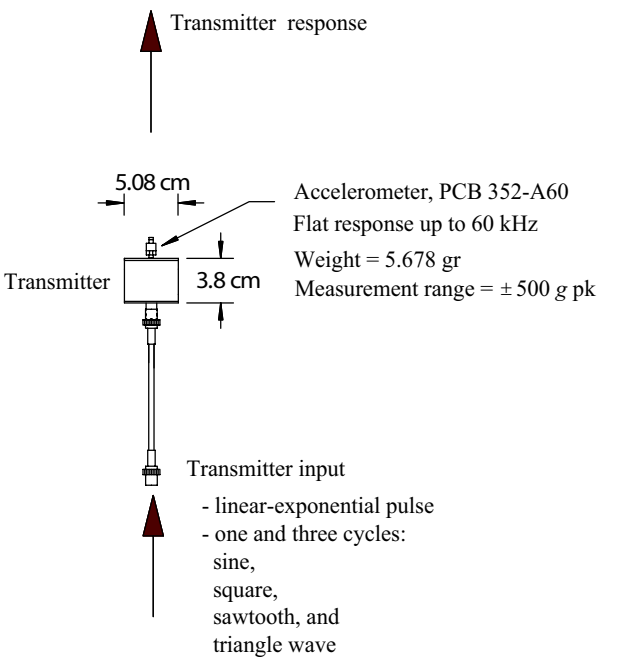

Figure 4.11: Ultrasonic transducer

pulses are generated using a pulse generator (Physical Acoustic, model μDisp/NB-16), and the response of the accelerometer is stored in a computer using a data acquisition system with 1 MHz sampling rate (Wavebook^{TM}, model 516E).

Time histories and Fourier spectra of acceleration, velocity, and displacement at the centre of the transmitter are presented in Fig. 4.12. The maximum amplitudes of acceleration, velocity, and displacement are 185 g, 0.6 cm/s, and 3.18×10^{-5} mm, respectively. The Fourier spectra show three main frequencies at 25.4 kHz, 36.6 kHz, and 49.8 kHz; the latter is the nominal frequency of the transmitter. Reflections of the initial pulse are observed from the velocity and displacement time histories.

The complex Cepstrum transform is a signal processing technique used for identification of reflections in a signal [75]. The complex Cepstrum of a signal $x(t)$ is given by

$$\hat{x(t)} = \mathrm{IFT}(ln(\mathrm{FT}(x(t)))) \tag{4.1}$$

where FT and IFT are the Fourier transform and its inverse, respectively. The Cepstrum transform for the time history of velocity is presented in Fig. 4.13. Reflections can be clearly observed with a period of 41 μs. This period corresponds to a frequency of 24.4 kHz. This frequency is not only present in Fig. 4.12, but also it is almost half of the nominal frequency of the transmitter (49.8 kHz). Hence, it is likely that the observed reflections are produced at the interface between the piezoelectric element (PZT-4) and the backing layer (perspex).

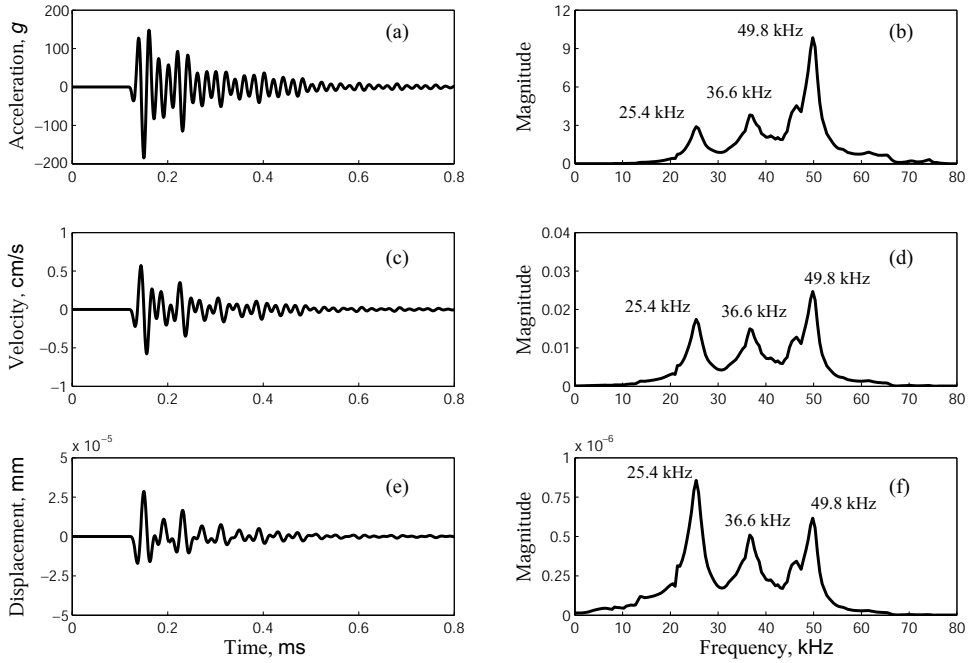

Figure 4.12: Measured time histories and corresponding Fourier spectra at the centre of the transmitter for a one-cycle sine pulse excitation of 50 kHz in terms of acceleration (a, b), velocity (c, d) and displacement (e, f)

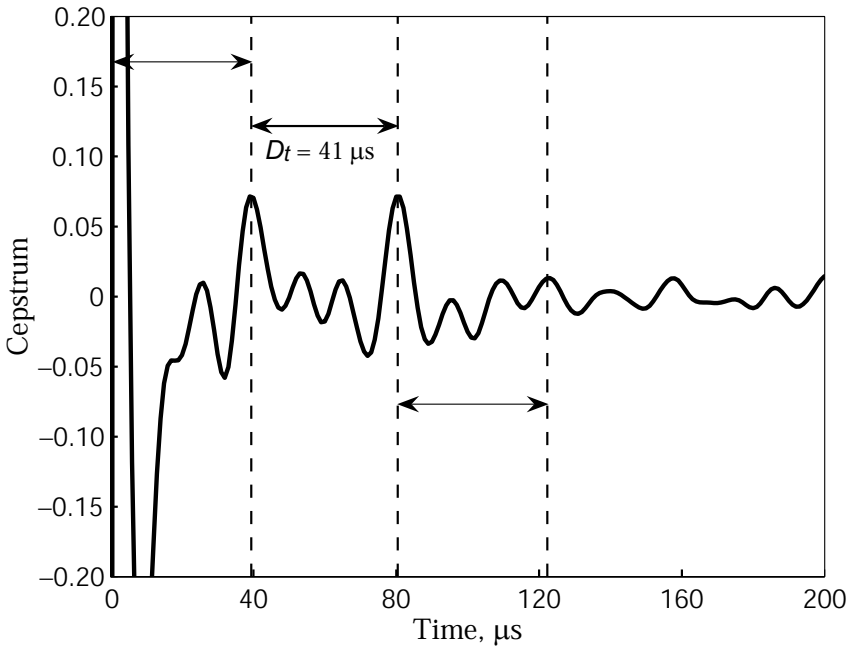

Figure 4.13: Cepstrum transform

The dynamic response of the transmitter subjected to a three-cycle sinusoidal pulse is shown in Fig. 4.14. The signal amplitude increases during the first three cycles, and shows a free vibration behaviour after. The Fourier spectra show main frequencies at 25.4 kHz and 36.6 kHz as in the case of one-cycle pulses (Fig. 4.12) but attenuated, whereas the amplitude at 49.8 kHz is amplified by a factor of 2.7 in agreement with the energy calculations in time domain (Table 4.2).

The acceleration and velocity power spectra at the centre of the transmitter for different electrical pulse excitations are shown in Figs. 4.15(a) and 4.15(b), respectively. For the main frequency (49.8 kHz), the square pulse shows the greatest amplitude followed by sine, triangle, and sawtooth pulses. These results are in agreement with the theoretical power spectra shown in Fig. 4.9.

Resonant frequencies and damping ratios

The results obtained using the CEM for a one-cycle and three-cycle sinusoidal, square, sawtooth, and triangle pulses are summarized in Table 4.3. In general, four complex exponentials are required to model the transmitter response according to the AIC criterion (eqn. (3.36)). For each exponential, the amplitude, frequency, damping ratio, and phase angle are presented. The ratio between the mean square error and the mean square value is presented as an index to evaluate the goodness of the curve-fitting.

The main frequencies obtained from the CEM (for one-cycle and three-cycle pulses) are compared with the main frequencies from the Fourier spectra (Table 4.4). In general, the resonant frequencies obtained from the CEM are on average, 4% smaller than the corresponding frequencies obtained from the Fourier spectra.

The damping ratio can be computed from the power spectrum curve using the bandwidth method (half-power) [76]. The bandwidth method is applicable for moderately damped systems without modal interference. Figure 4.16 shows the response power spectrum for a one-cycle sinusoidal pulse of 50 kHz. The computed damping ratio is 1.97% which is 23% greater than the damping ratio obtained using the CEM ($\xi = 1.6\%$).

The CEM has two main advantages with respect to Fourier analysis: a) resonant frequencies are computed directly from the time domain data; therefore, they are not affected by spectral resolution, and b) damping ratios and mode shapes can be more readily obtained. Figure 4.17 shows the measured and curve-fitted time signals using the CEM for one-cycle and three-cycle sinusoidal excitations. For a one-cycle sinusoidal pulse, the transmitter response is completely defined by four exponentials, whereas three exponentials are required to model the transmitter response when excited with a three-cycle sinusoidal pulse.

The measured signals at the edges and at the quarters on the transmitter face are also analyzed using the CEM. Measurements are taken at each location for different electrical excitation pulses. The mean values and coefficients of variation for the main frequency and damping ratio are shown in Table 4.5. The main frequencies obtained at the quarter and at the edge of the transmitter diameter are up to 3% smaller than the frequencies measured at the center. The damping

Table 4.3: Dynamic response parameters of the transmitter obtained by the CEM for different electrical pulses

Excitation type	Cycles	$\hat{C}_k$ (g)	f_k [1] (kHz)	$\xi_k \times 100$ $(\%)$	ϕ_k $(degrees)$	CE [2]
Sine wave	1	36.2	20.7	9.7	64.1	0.054
		84.1	35.2	11.8	-119.4	
		92.8	**49.0**	**1.6**	**32.3**	
		56.4	62.7	6.6	-143.6	
	3	23.2	23.2	9.8	-69.4	0.060
		316.0	**48.8**	**1.9**	**-27.8**	
		332.4	55.0	8.2	-177.3	
Square wave	1	63.2	21.0	11.7	59.8	0.045
		147.3	34.4	16.9	-125.2	
		118.4	**49.0**	**1.8**	**28.3**	
		61.9	60.8	6.9	-165.5	
	3	33.8	23.7	4.3	87.6	0.040
		63.1	37.5	8.7	52.2	
		426.7	**48.9**	**1.8**	**-23.1**	
		364.2	55.9	6.9	-160.5	
Sawtooth wave	1	19.4	20.8	9.6	50.8	0.066
		40.7	35.6	10.4	-145.2	
		59.9	**49.2**	**1.6**	**-7.2**	
		45.8	64.6	7.5	-179.0	
	3	16.4	22.3	8.1	57.4	0.020
		14.7	34.7	5.1	47.1	
		80.1	46.2	6.1	-158.5	
		191.3	**49.2**	**1.7**	**2.7**	
		90.7	58.8	5.2	-140.2	
Triangle wave	1	33.6	21.2	12.0	43.2	0.080
		62.7	35.8	13.5	-155.1	
		78.6	**49.1**	**1.8**	**-25.7**	
		46.4	64.2	7.4	-155.8	
	3	**224.2**	**49.2**	**1.5**	**-2.1**	0.068
		172.3	56.4	7.0	-173.6	

[1] $f_k = \frac{2\pi}{\omega_k}$

[2] CE : coefficient of error = $\frac{\Sigma(y_n - y_p)^2}{\Sigma(y_n)^2}$

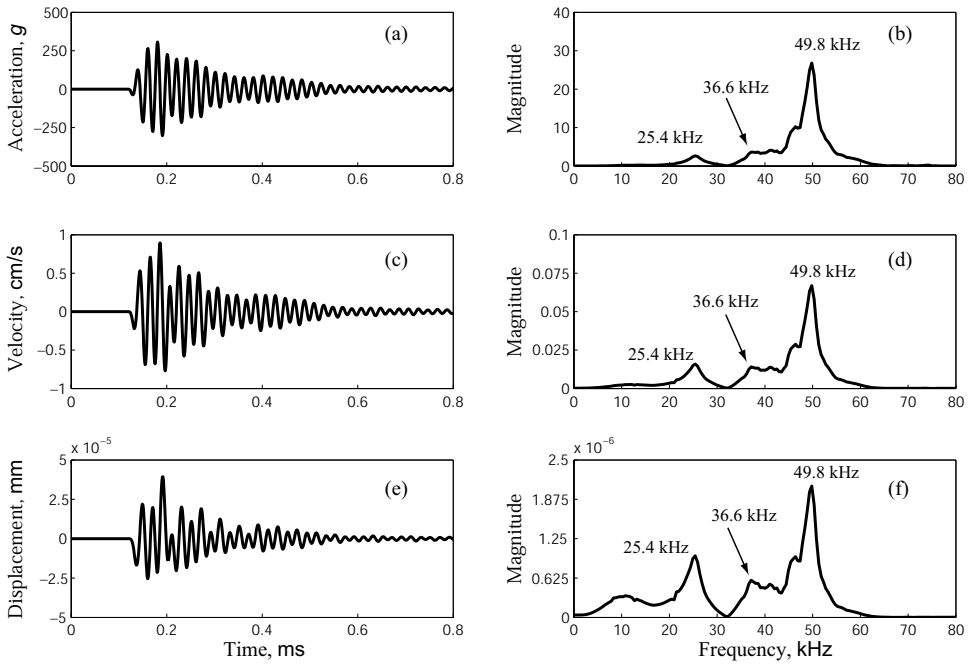

Figure 4.14: Measured time histories and corresponding Fourier spectra at the centre of the transmitter for a three-cycle sine pulse excitation of 50 kHz in terms of acceleration (a, b), velocity (c, d) and displacement (e, f)

Table 4.4: Main vibration frequencies obtained from the discrete Fourier spectra and the CEM for one-cycle and three-cycle electrical pulses

Excitation type	Frequencies, kHz									
	One-cycle						Three-cycle			
	DFT			CEM			DFT		CEM	
sine	25.4	36.6	49.8	20.7	35.2	49.0	25.4	49.8	23.2	48.8
square	25.4	36.9	49.8	21	34.4	49.0	25.4	49.8	23.7	48.9
sawtooth	25.4	36.9	49.8	20.8	35.6	49.2	25.5	49.8	22.3	49.2
triangle	25.4	36.9	49.8	21.2	35.8	49.1	25.4	49.8	—	49.2

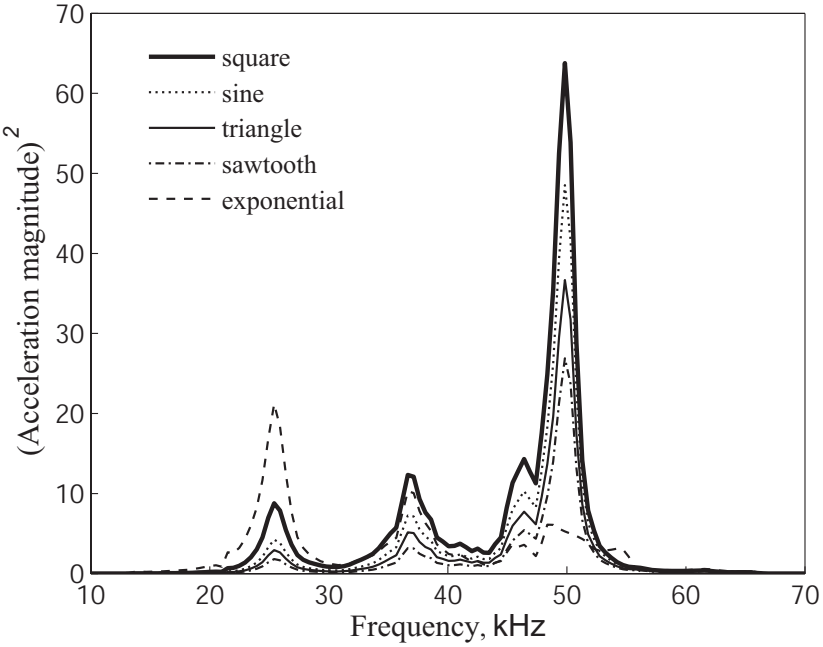

(a) Acceleration

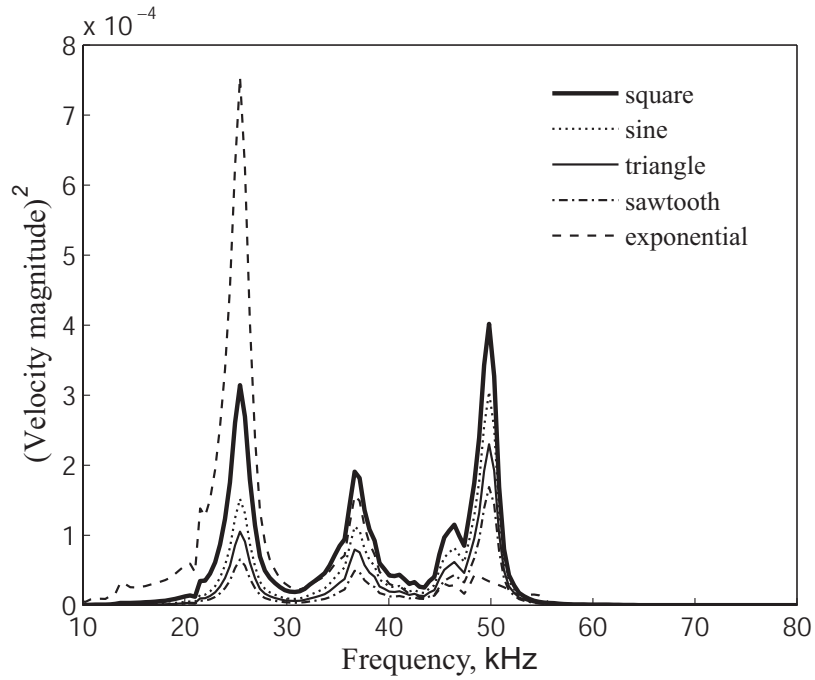

(b) Velocity

Figure 4.15: Acceleration and velocity power spectra at the centre of the transmitter for different one-cycle electrical pulse excitations

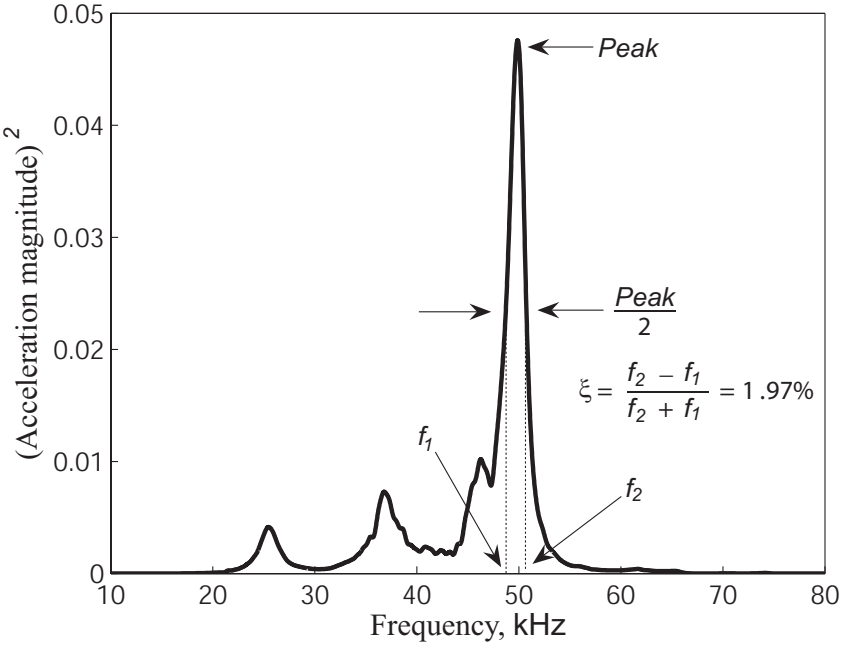

Figure 4.16: Damping ratio computed from the power spectrum using the band-width method (a one-cycle of sine pulse excitation of 50 kHz)

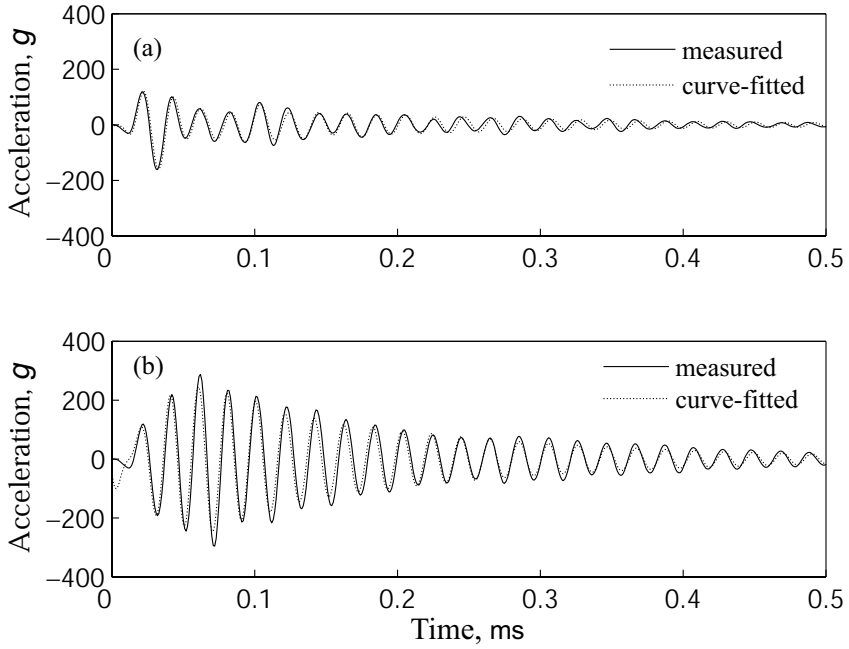

Figure 4.17: Typical time histories at the centre of the transmitter for a one-cycle (a) and three-cycle (b) sine excitation of 50 kHz

ratios are up to 47% larger. The decrease in frequency and increase of damping are likely caused by the effect of the accelerometer's mass on the vibration of the transducer face.

Table 4.5: Resonant frequencies and damping ratios measured at different points on the face of the transmitter (all pulses with one and three cycle measurements)

Location	Main Frequency (kHz)		Damping ratio (%)	
	mean value	COV	mean value	COV
centre	49.1	0.003	1.7	0.08
quarter	48.6	0.002	1.8	0.12
edge	47.9	0.010	2.5	0.31

Vibration mode

The vibration mode of an ultrasonic transmitter is important for numerical simulations of wave propagation; which require the dynamic characterization of the excitation source.

The vibration mode of the transmitter is determined from acceleration measurements at five positions on the transmitter face (centre, edges, and at the quarters). The acceleration signals are integrated twice to obtain displacements. The vibration mode of the transmitter for a one-cycle sinusoidal pulse is presented in Fig. 4.18. The position measured with respect to the centre of the transmitter is normalized with the transmitter diameter; hence, the values ± 1 and ± 0.5 correspond to the positions at the edges and quarters of the transmitter face, respectively After the arrival of the initial pulse ($t > 75\ \mu s$), the transmitter presents a vibration similar to the second flexural mode of a piezoelectric disk. A similar vibration mode is found using different electrical excitation pulses (a one-cycle square, sawtooth, and triangle).

Lee et al. [77] deduced a closed-form solution for the free vibration of piezoelectric circular disks. For a piezoelectric disk with 2.54 cm diameter and 0.113 cm thickness, the fundamental flexural mode (simple curvature in bending) has a resonant frequency of 11 kHz. The second flexural mode has a resonant frequency of 43 kHz. The measured vibration mode (Fig. 4.18) is similar to the second flexural mode reported by Lee et al.

4.5 Transmitter/Receiver Characterization

In this section, measurements of the FRF and the IRF for the transmitter/receiver system are presented. The transmitter/receiver system includes two ultrasonic transducers denominated UT-

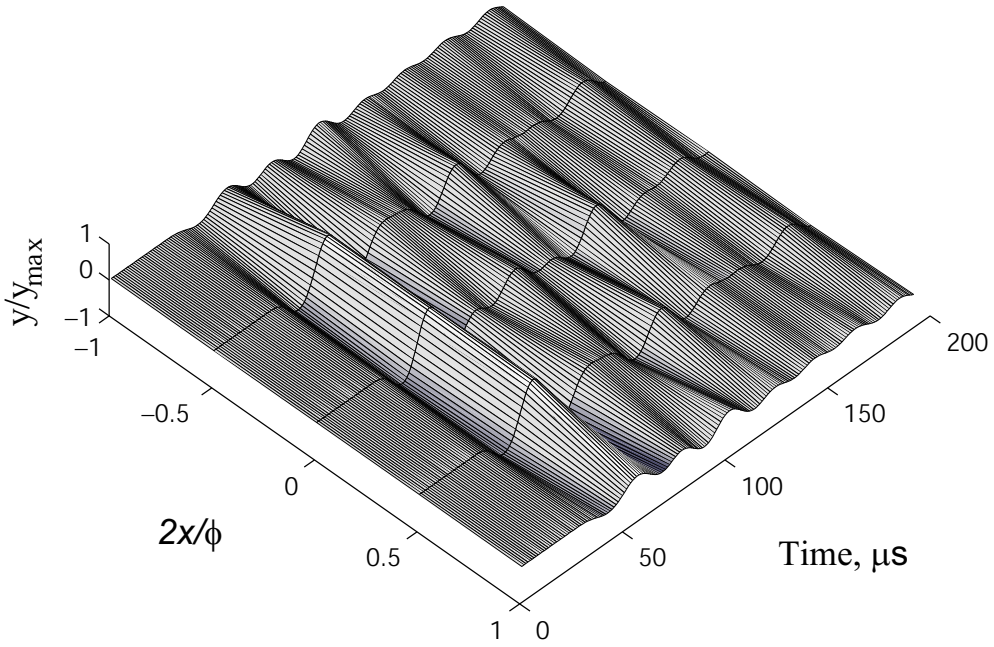

Figure 4.18: Typical vibration mode of the transmitter for a one-cycle sine pulse excitation of 50 kHz

A and UT-B and the BNC cables. Both transducers can be used as transmitter and as receiver and are similar to the transducer presented in Section 4.4.

An aluminum cone is attached to the transducers to reduce the area of contact from 5.08 cm to 1 cm as shown in Fig. 4.19. The height of the coupling cone is 6.3 cm, and it is glued to the transducers using Loctite adhesive 454. The aluminum cone allows the coupling of the transducers with a wood pole (curved surface). A sine sweep wave(constant amplitude and frequency content from 30 to 70 kHz) is used as excitation to measure the FRF and IRF of the transmitter/receiver system (Fig. 5.2(a)).

Figure 4.20(a) shows the the FRFs of the transmitter/receiver system for excitation amplitudes of of 5, 10, and 20 volts. The system response is linear respect to the excitation amplitude. Five main frequencies can be distinguished (28.8, 33.9, 44.5, 48.9, and 52.9 kHz). The resonant frequencies of 28.8, 33.9, and 48.9 kHz are similar to the resonant frequencies for a transmitter without coupling cone (maximum difference of 13%). The magnitudes at 28.8 and 33.9 kHz are larger than the corresponding value at the nominal frequency of the transducer (48.9 kHz). The units of the FRF are voltage response per voltage excitation (V_{output}/V_{input}), whereas the magnitude spectra shown in Figs. 4.14(b), 4.14(d), and 4.14(f) are given in units of acceleration, velocity, and displacement, respectively. The FRF shows also two frequencies which are not observed in the transmitter response without the coupling cone (44.5 and 52.9 kHz). The coupling

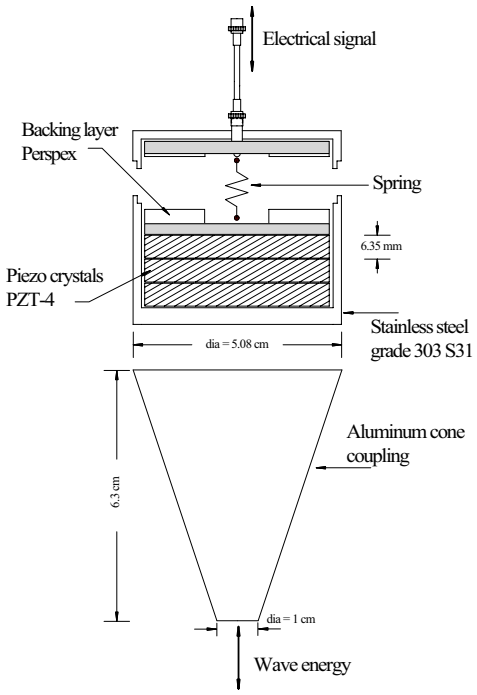

Figure 4.19: Schematic configuration of an ultrasonic transducer with a coupling aluminum cone

cone modifies the response of the transducer because the transducer face is restricted to vibrate freely. This effect is greater when two transducers with coupling cones are in a face-to-face contact. The IRF is presented in Fig. 4.20(b). The IRF shows the delay of the transmitter/receiver system.

The transmitter and receiver are interchanged to verify the linearity of the system. Figure 4.21 shows the FRFs for the cases when UT-A and UT-B are used as transmitter and receiver, respectively; and viceversa. The response of the transmitter/receiver system to three cycles sine wave of 50 kHz is presented in Fig. 4.22. The excitation input $x(t)$ is determined from

$$x(t) = ifft(\frac{S(\omega)}{H_{xs}(\omega)}) \tag{4.2}$$

where $S(\omega) =$ discrete Fourier transform of the time response $s(t)$, and
$H_{xs}(\omega) =$ FRF of the transmitter/receiver system.

The dynamic properties of the transmitter/receiver system are determined from the IRF by using the CEM. A total of eleven vibration modes are identified; the amplitude, resonant frequency, damping ratio, and the phase angle are presented in Table 4.6 for each vibration mode. The damping ratios for the frequencies of 28.8, 33.9, 44.5, 48.9, and 52.9 kHz are 3.0, 2.7, 1.1,

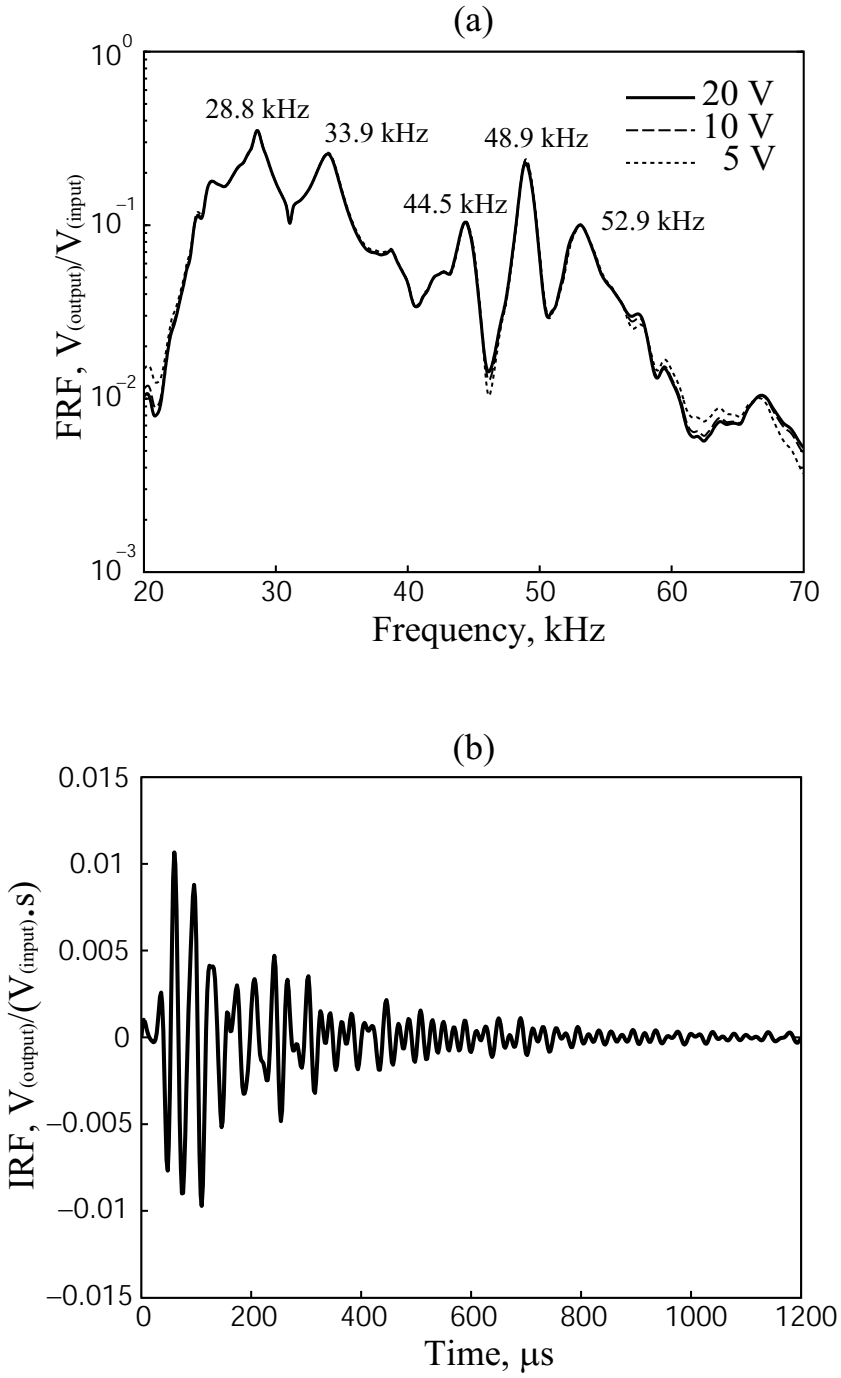

Figure 4.20: FRFs of the transmitter/receiver system for different excitation voltages (a), and IRF of the transmitter/receiver system (b)

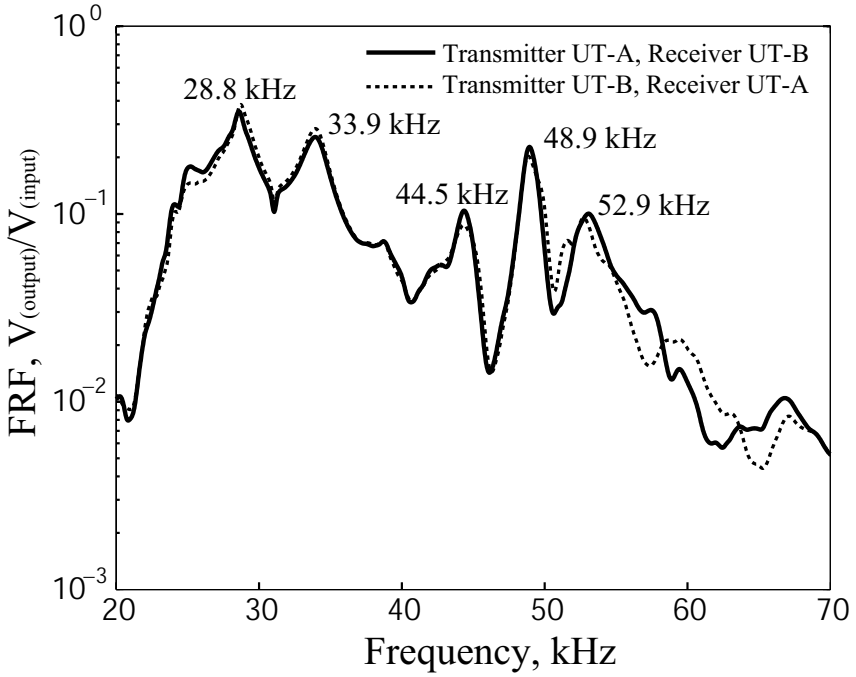

Figure 4.21: FRFs of UT-A/UT-B and UT-B/UT-A systems

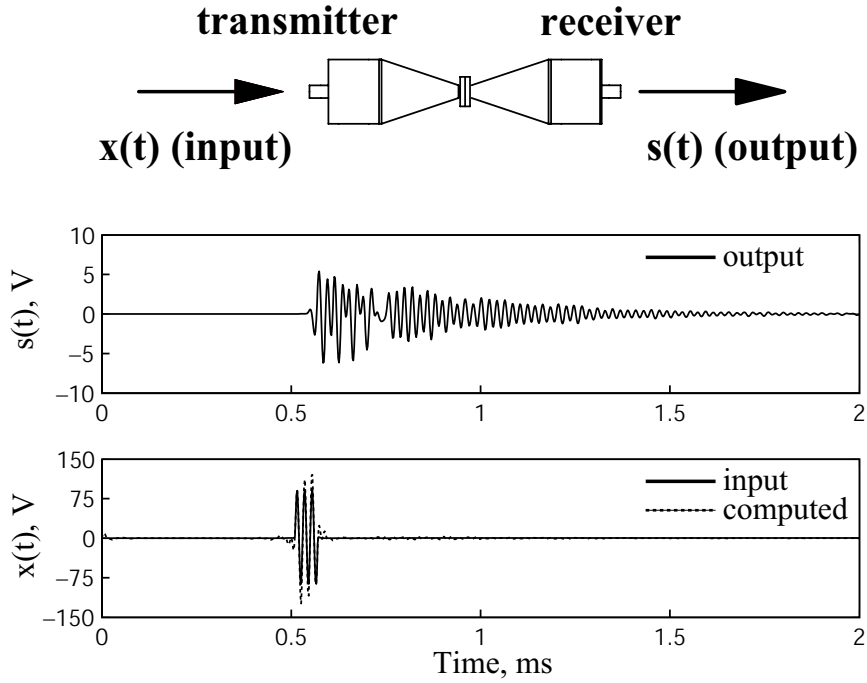

Figure 4.22: Transmitter/receiver system response for a three-cycle sine excitation of 50 kHz

Table 4.6: Dynamic parameters of the transmitter/receiver system

Mode	Frequency (kHz)	Normalized amplitude(*)	Phase (degrees)	Damping ratio (%)
1	24.6	0.69	-62.3	4.7
2	27.8	1.00	177.8	14.5
3	28.8	0.96	72.2	3.0
4	33.9	0.80	-54.5	2.7
5	39.0	0.06	179.7	1.7
6	44.5	0.17	99.71	1.1
7	48.9	0.22	55.274	0.5
8	52.9	0.21	-38.6	1.2
9	56.1	0.48	147.8	3.9
10	58.2	0.22	-44.6	2.2
11	66.8	0.06	113.5	2.5

(*) amplitudes normalized to 0.0074 $V_{output}/(V_{input} \cdot s)$

0.5, and 1.2%, respectively. In general, the damping ratio decreases with frequency.

4.5.1 Application examples

The main application of the transmitter/receiver characterization is the estimation of the mechanical properties such as resonant frequency and damping ratio of laboratory specimens using ultrasonic testing. In this section, laboratory and numerical experiments are conducted to determine the FRFs of a calibration aluminum bar and a cemented sand specimen.

Dynamic characterization of a calibration aluminum bar

The transducers UT-A and UT-B are used as transmitter and the receiver to compute the FRF of a simply supported aluminum bar. The transducers are coupled at the ends of the bar using vacuum grease as couplant. A sine sweep function is used to excite the transmitter. The frequency of the sine sweep varies from 30 kHz to 70 kHz in 3.5 ms. Figure 4.23 shows the experimental setup for ultrasonic testing of an aluminum bar. The transducers UT-A and UT-B are used as

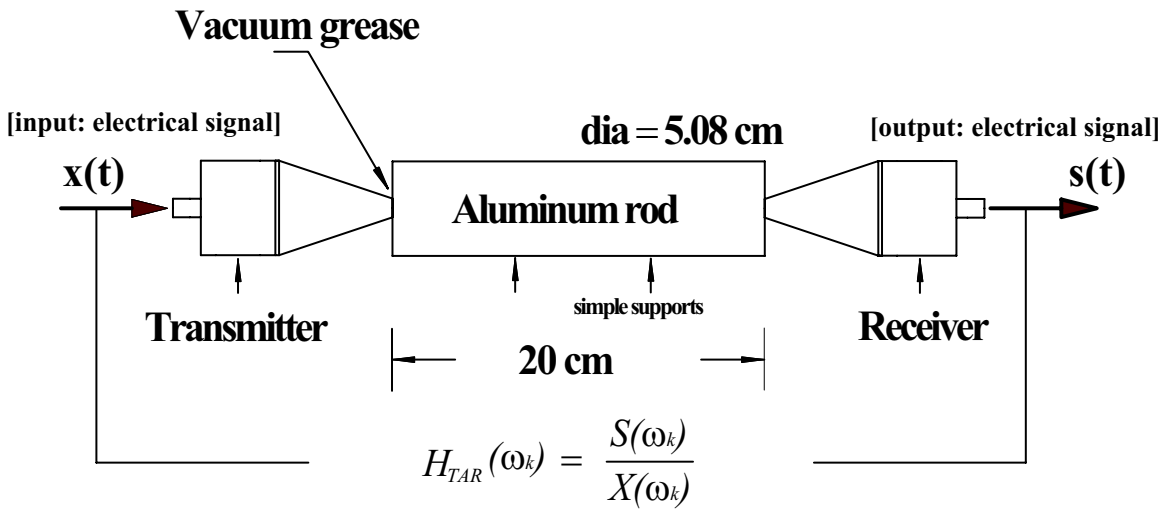

Figure 4.23: Experimental setup for the estimation of the FRF of an aluminum bar in the frequency range 30-70 kHz using ultrasonic testing

the transmitter and the receiver, respectively. The calibration aluminum bar (AL 2024 T4) has a diameter and length of $\phi = 5.08$ cm and $L = 20$ cm. The bar weights 1.1207 kg (mass density $\rho = 2765\ kg/m^3$). Prior to the ultrasonic test, the compressional wave velocity of the aluminum bar is determined using the pulse velocity testing (PVT) method ($V_p = 6337 m/s$). The wave velocity reported for this material is $V_l = 6370 m/s$ [78]. The FRF of the aluminum bar (H^s_{alum}) is computed as

$$H^s_{alum} = \frac{H_{(UT-A/aluminum/UT-B)}}{H^T_{UT-A} \cdot H^R_{UT-B}} \tag{4.3}$$

where $H_{(UT-A/aluminum/UT-B)}$ = FRF of the assembly,
H^T_{UT-A} = FRF of the transmitter UT-A, and
H^R_{UT-B} = FRF of the receiver UT-B.

Figure 4.24 shows the FRF and IRF for the aluminum bar. Five main frequencies are observed. In order to verified the experimental results, the FRF is also computed interchanging the transducers (transmitter UT-B, receiver UT-A). The computed FRF shows an excellent match with a maximum difference of 10%. The denominator in eqn. (4.3) is obtained from the previous measurements (Fig. 4.21)

The measured FRF and the curve-fitted one using the CEM are shown in Fig. 4.25. The predicted FRF matches well the measured one. The dynamic parameters of amplitude, damping ratio, angle phase, and resonant frequency for each vibration mode are computed using the CEM and are summarized in Table 4.7. The damping ratio for the main frequency ($f_0 = 65.6$ kHz) is

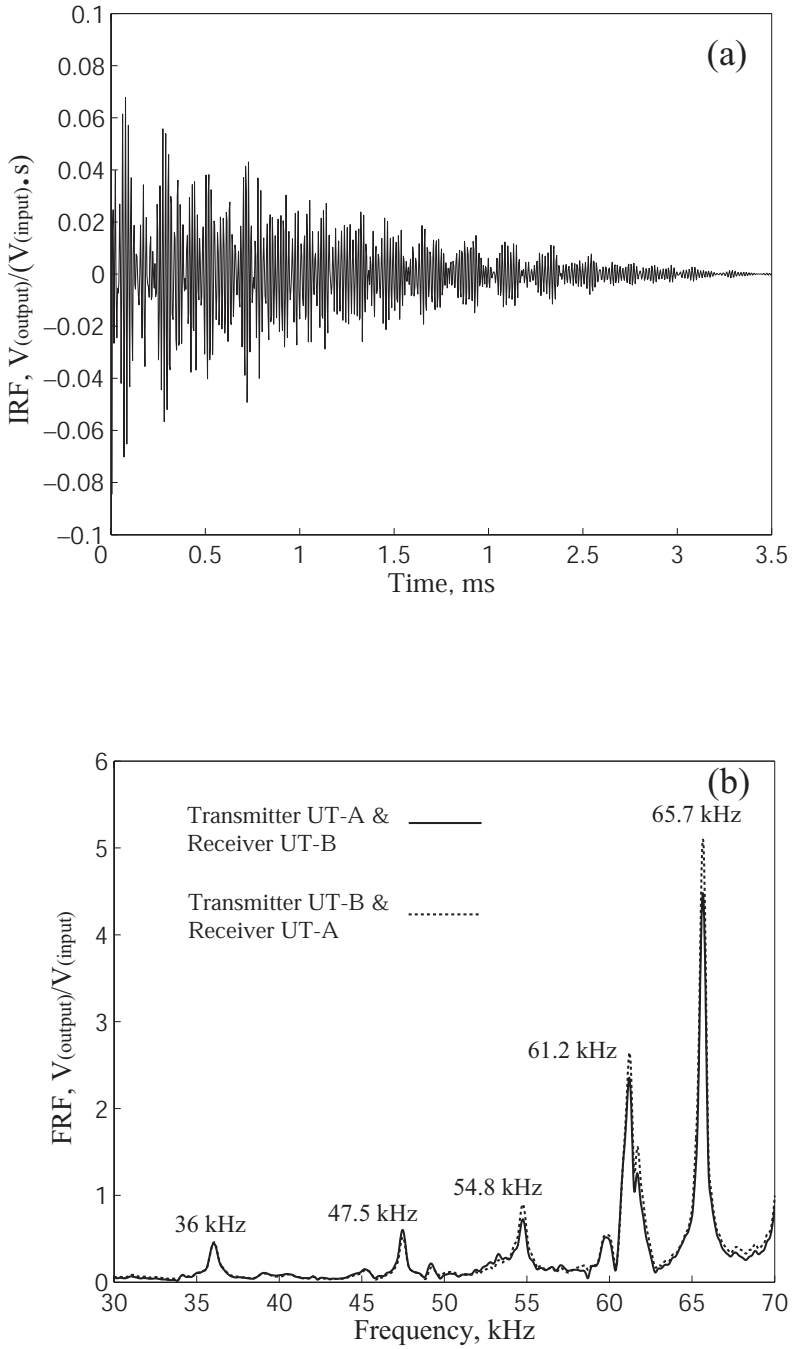

Figure 4.24: IRF (a) and FRF (b) of the aluminum bar in the frequency range 30-70 kHz

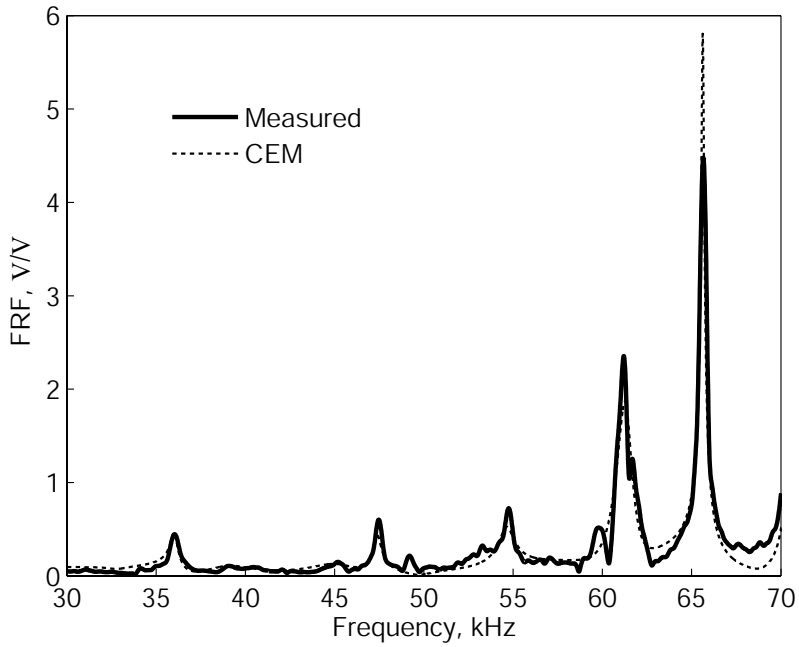

Figure 4.25: FRF of the aluminum bar in the frequency range 30-70 kHz obtained by the CEM

Table 4.7: Dynamic parameters of the aluminum bar in the frequency range 30-70 kHz

Main Frequencies			Normalized amplitude(*)	Phase	Damping ratio
Measured (kHz)	Computed (kHz)	Difference (%)		(degrees)	(%)
36.0	36.0	0	0.08	134.8	0.5
47.5	47.4	0.2	0.08	120.6	0.4
54.8	54.6	0.4	0.21	-39.7	0.8
61.2	61.3	0.2	1.00	173.2	0.6
65.7	65.6	0.2	0.48	76.25	0.1

(*) amplitudes normalized to 0.0048 $V_{output}/(V_{input} \cdot s)$

0.1%. This low damping ratio is characteristic for aluminum; which as damping ratios in the order of 0.04% [79].

Numerical simulations are performed to determine the theoretical FRF of the aluminum bar. The objective of the simulations is to confirm the main frequencies obtained from the measured

FRF (Table 4.7). The magnitudes of the theoretical and measured FRF's are expected to be different because of the difficulties in modelling the energy dissipation mechanisms. A simplified model to determine the resonant frequencies as well as one and two-dimensional finite element analysis of wave propagation are presented next.

Simplified model

The aluminum bar can be modeled as one-dimensional element with free-free ends and excited longitudinally with a compressional acoustic wave. The resonant frequencies for the first four vibration modes are $f_1 = V_l/(2L)$, $f_2 = V_l/L$, $f_3 = 3V_l/(2L)$, and $f_4 = 2V_l/L$. The wave velocity (V), the frequency (f) and the wavelength (λ) are related by

$$f = \frac{V}{\lambda} \tag{4.4}$$

The fundamental vibration mode corresponds to a half wave length; then, the first resonant frequency is $f_1 = V_l/(2L) = 15.8$ kHz. The second vibration mode has one wavelength, $f_2 = 2f_1 = 31.6$ kHz. The wavelength and resonant frequency for the third vibration mode are $\lambda_3 = 2L/3$ and $f_3 = 3f_1 = 47.7$ kHz. Finally, the fourth vibration mode has $\lambda_4 = L/2$ and $f_4 = 4f_1 = 63.2$ kHz. Only the second, third, and fourth vibration modes have frequencies in the frequency range of the ultrasonic system used.

The resonant frequencies of 31.6, 47.7, and 63.2 kHz are close to the resonant frequencies obtained from the measured FRF (36, 47.5, and 65.7 kHz). However, the simplified model cannot explain the frequencies of 54.8 and 61.2 kHz.

One-dimensional wave propagation

A finite element structural analysis program (SAP2000 [80]) is used to model the wave propagation in the aluminum bar. The main characteristics of the model are presented in Fig. 4.26. A total of 20 finite elements (frame type) are used. One end of the bar is fixed in the transverse and rotational directions but it is allowed to move in the longitudinal direction. The imposed excitation to the aluminum bar corresponds to the measured acceleration response of the ultrasonic transmitter when it is subjected to a sine sweep function (Fig. 5.2(a)). The damping is modeled as Rayleigh damping using the values measured experimentally. The absolute acceleration time history response is computed at the other end of the bar. The theoretical FRF of the bar is then computed as the ratio between the response ($Y(\omega)$) and the excitation ($X(\omega)$).

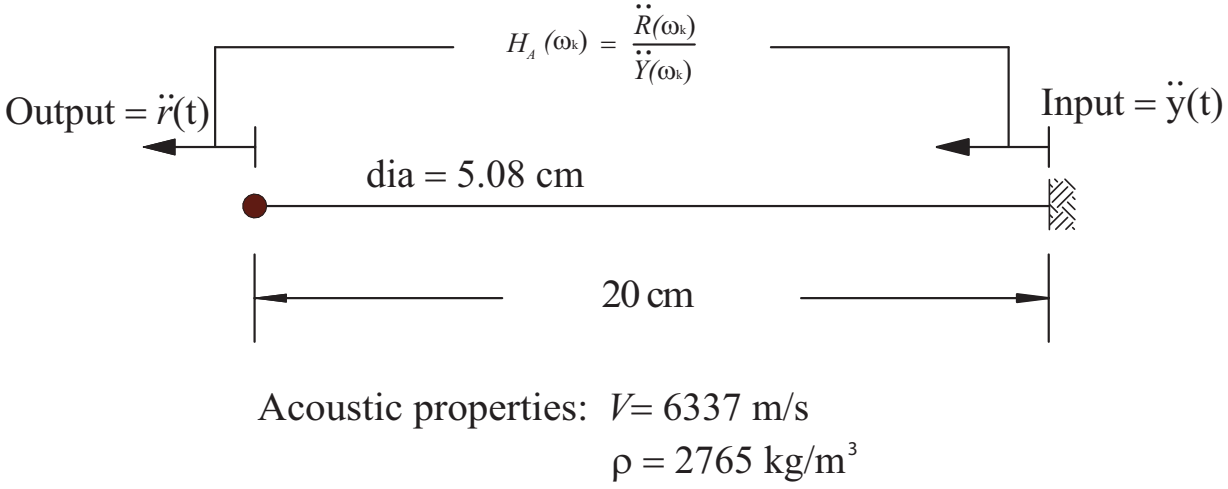

Figure 4.26: One-dimensional model of wave propagation in an aluminum bar

The computed FRF is shown in Fig. 4.27. Three resonant frequencies of 43, 47.5, and 61.1 kHz are clearly observed. The damping ratio for three modes are 0.5%, 0.4%, and 0.1%, respectively, which correspond to the measured values using the CEM. These resonant frequencies are similar to the values obtained from the mode shapes for free-free boundary condition (differences less than 8%). The computed magnitudes of the FRF follow the measured trend (increasing with frequency) and the amplitude for the main frequency ($f_0 = 61.1$ kHz) is in the same order of the measured one. However, the one-dimensional model can only predict three frequencies from the five determined experimentally.

Two-dimensional axisymmetric wave propagation

A finite element program (ANSYS® Academic Research 11.0 [73]) is used to model the aluminum bar. Four-node axisymmetric elements with two degrees of freedom at each node are used. The mass density and longitudinal wave velocity are the same used for the one-dimensional model. The Poisson's ratio for the aluminum is 0.30 [81]. The damping is modeled by a Rayleigh model adjusted with experimental values of damping ratios computed using the CEM (Fig. 4.28). The size of the finite element is 0.2 cm and the sampling rate $\triangle t = 0.5\ \mu s$. One end of the aluminum bar is subjected to the measured displacement time history at the centre of the section. The acceleration time history is integrated twice to obtain displacement. The displacement response is computed at the other end of the bar.

The FRF is shown in Fig. 4.29. The amplitude is given in decibels (dB) to enhance the details. Five resonant frequencies at 33.8, 46.5, 55.7, 61.9, and 66.7 kHz are clearly observed. These frequencies are similar to the measured values. Table 4.8 compares the resonant frequencies

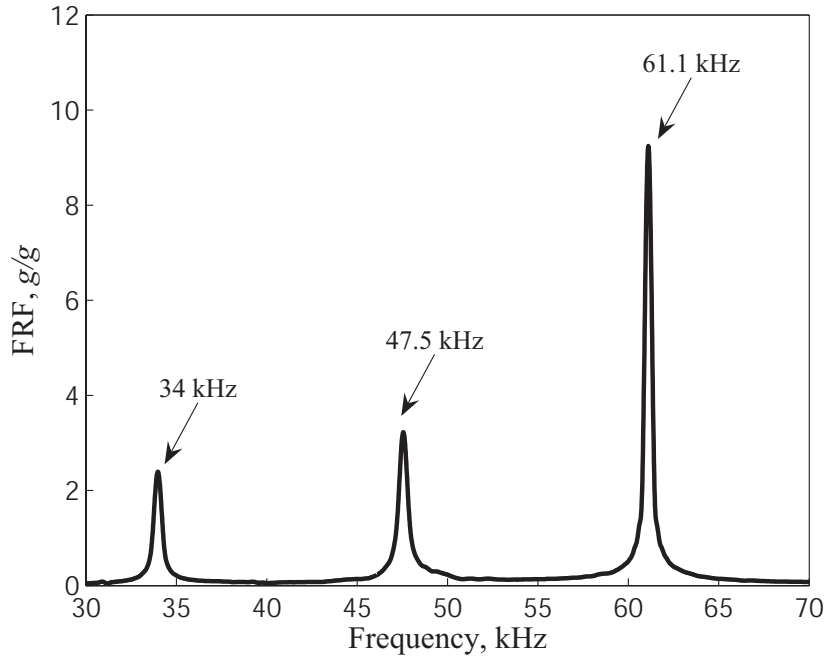

Figure 4.27: FRF of the aluminum bar in the frequency range 30-70 kHz obtained from the one-dimensional wave propagation model

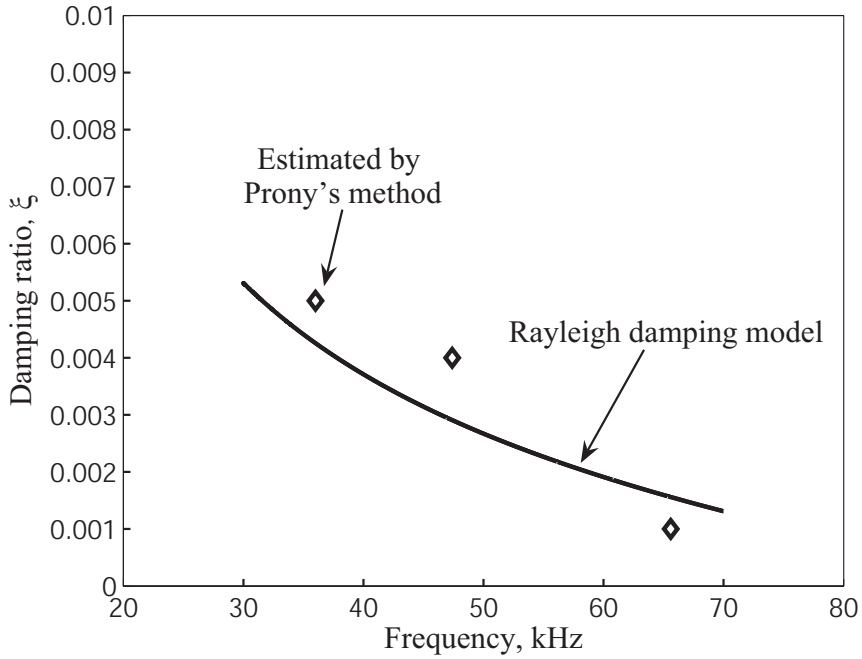

Figure 4.28: Rayleigh damping model used for two-dimensional wave propagation in an aluminum bar

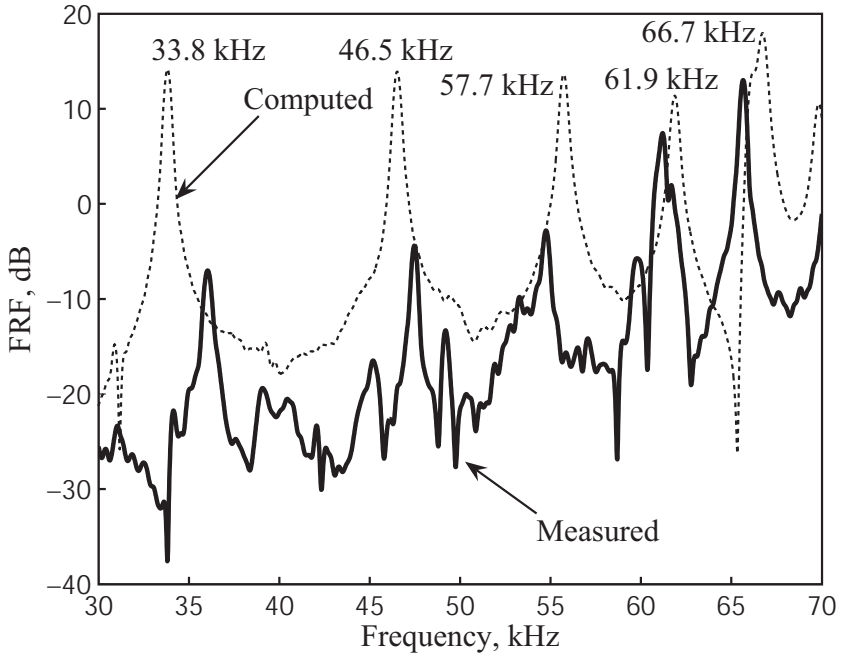

Figure 4.29: Comparison of the measured FRF of the aluminum bar with the computed one from two-dimensional wave propagation

Table 4.8: Resonant frequencies of the aluminum bar in the frequency range 30-70 kHz: measured and computed using a two-dimensional wave propagation model

	Main Frequencies		
Mode	Measured (kHz)	Computed (kHz)	Difference (%)
1	36	33.8	6.5
2	47.5	46.5	2
3	54.8	55.7	1.6
4	61.2	61.9	1.1
5	65.7	66.7	1.5

measured and computed (3% difference in average). Unlike one-dimensional wave propagation model, the axisymmetric model can detect extensional vibration modes in radial direction of the aluminum bar.

Dynamic characterization of a cemented sand specimen

The ultrasonic testing setup for a cylindrical cemented sand specimen (5% cement content) is shown in Fig. 4.30 ($L = 13.696$ cm, $\phi = 7.51$ cm, and $\rho = 1.83\ g/cm^3$). The calibrated ultrasonic transducers UT-A and UT-B are used as transmitter and as receiver, respectively. The transducers are located at each side of the specimen providing the only two points of support for the specimen by applying a constant pressure. Vacuum grease is used for coupling the transducers and the soil specimen.

First, the P-wave velocity of the specimen is measured using two high-frequency transducers (Panametrics U-100, 1 MHz). The first arrival is determined using a digital oscilloscope with a resolution of 0.1 μs. The pulse-receiver system is calibrated using an aluminum bar. In Fig. 4.31(a), the trigger pulse and the measured signal waveform are shown. The arrival time is 54.2 $\mu s \pm 0.1\ \mu s$ corresponding to $V_p = 2527$ m/s.

The pulse-velocity measurement using the 50 kHz transducers (UT-A and UT-A) is shown in Fig. 4.31(b). The inherent time delay for the transmitter/receiver system is 34 $\mu s \pm 2\ \mu s$; which is measured from the IRF of the system in the face-to-face configuration (Fig. 5.1(b)). Therefore, the first arrival time is 90-34=56 $\mu s \pm 4\ \mu s$ (3% greater than the value obtained with the 1 MHz transducers).

The FRF of the cemented sand specimen is computed by removing the effect of the trasnmitter/receiver system from the measured response. Resonant frequencies and damping ratios are determined from the IRF using the CEM. For the resonant frequency of 54.6 kHz, the damping ratio is 0.4%, which is in agreement with damping ratios measured on cemented sands by Khan et al. [82] using the spectral amplitudes method. The measured resonant frequency corresponds to the sixth mode of vibration of the specimen, according to the simplified model presented before ($f_0 = (2527\ m/s)/(L/3) = 55.4\ kHz$). The frequency response function computed using the CEM is practically identical to the measured one as shown in Fig. 4.32.

4.6 New Analysis Method (Vp-COM)

Figures 4.33(a) and 4.33(b) show the microstructure and a cross-section of a red pine pole. A cylindrical coordinate system with the origin at the pith of the wood is defined. In this figure, the rings produced by seasonal growing of wood are clearly observed. The cells of early wood are larger and have thinner walls than those produced of late wood. The material properties are defined for three orthogonal axes corresponding with the longitudinal (L), radial (R), and tangential (T) directions. The orientation for two of the orthogonal axes (radial and tangential directions) changes with the receiver location θ_r. Therefore, unlike for an orthogonally anisotropic medium,

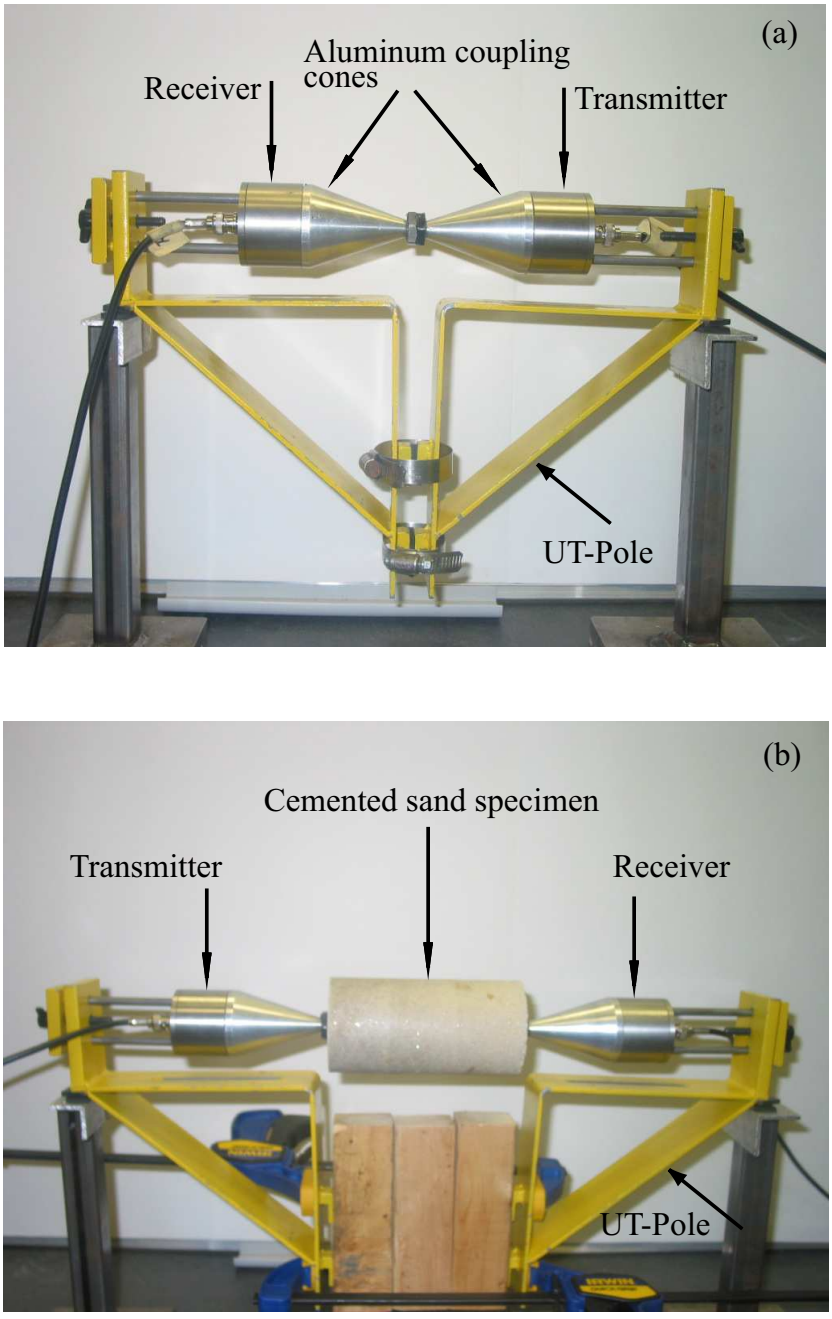

Figure 4.30: Experimental setup for ultrasonic testing of a cemented sand specimen: (a) transmitter/receiver system, (b) transmitter-specimen-receiver system

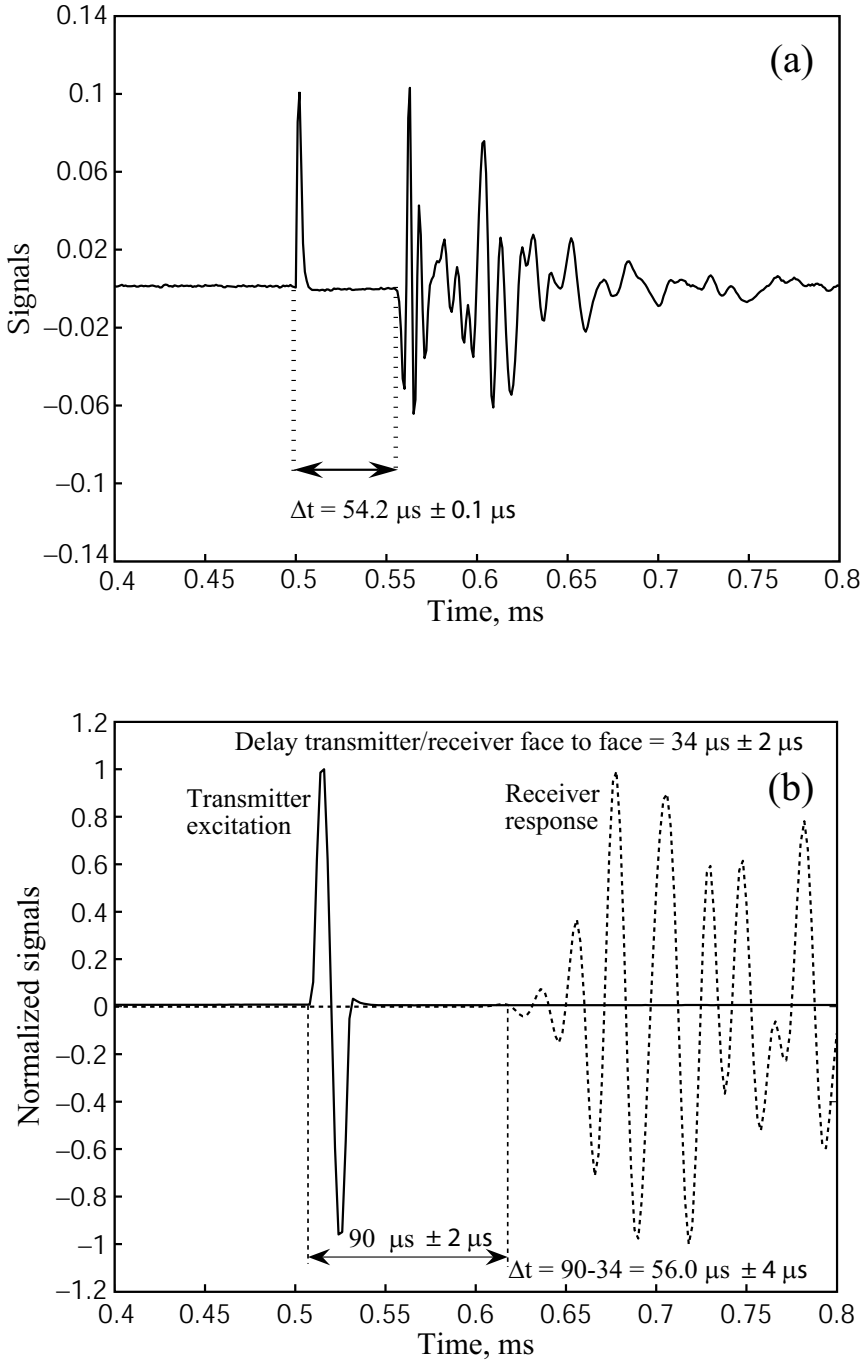

Figure 4.31: First arrival of the compressional wave: (a) 1 MHz transducers, (b) 50 kHz transducers

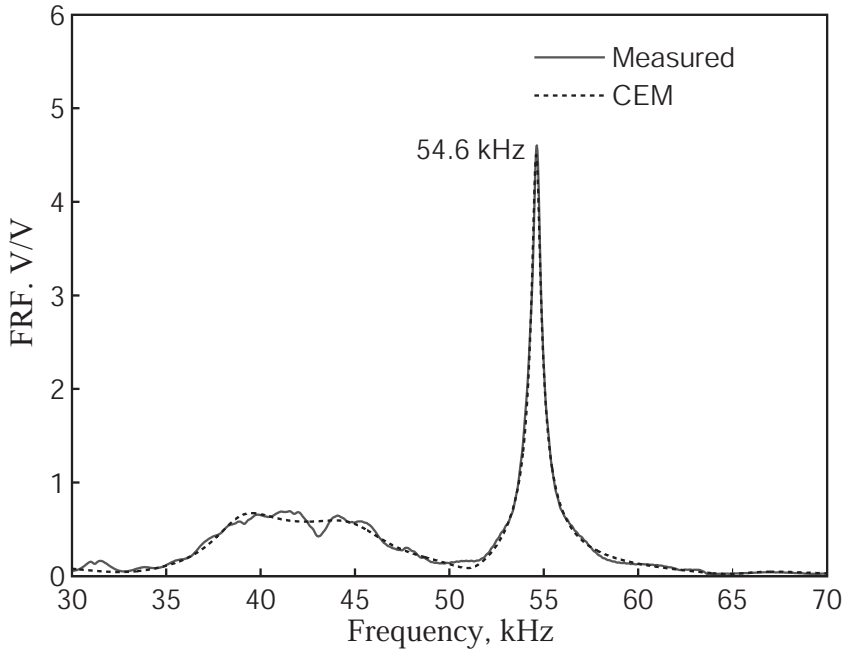

Figure 4.32: FRF of the cemented sand specimen in the frequency range 20-70 kHZ (measured and computed using the CEM

the raypaths of the compressional wave are no straight lines.

A semi-analytical solution for two-dimensional, cylindrically orthotropic, elastic infinite medium excited by an impulsive force is presented by Payton [83]. However, the corresponding closed-form solution for a finite circular medium does not exist; thus, the problem of wave propagation in cross-sections of wood poles has been solved by numerical methods [84].

The modulus of elasticity in the longitudinal direction is about an order of magnitude greater than the moduli in radial and tangential directions. For ultrasound tests in the radial direction of wood poles, most of the energy is concentrated in the cross-section [85]. Hence, plain strain conditions can be used for modelling wave propagation in cross-sections of wood poles.

A simplified method for the analysis of wave propagation (P-waves and S-waves) in a cross-section of a wood pole (plain strain conditions) considering a cylindrical orthotropic material is presented. The main assumptions are a) the cylindrical orthotropic medium is infinite (no boundary reflections), b) the solutions for the wave propagation in an orthogonally anisotropic medium are used to approximate in small cylindrical element the wave propagation in a cylindrical orthotropic medium, and c) the propagation of plane waves until they reach an artificial boundary representing the pole diameter (Fig. 4.34). A global coordinate system (XY) is defined at the centre of the cross-section.

A plane wave propagating trough the medium with direction cosines ax and ay is assumed.

(a)

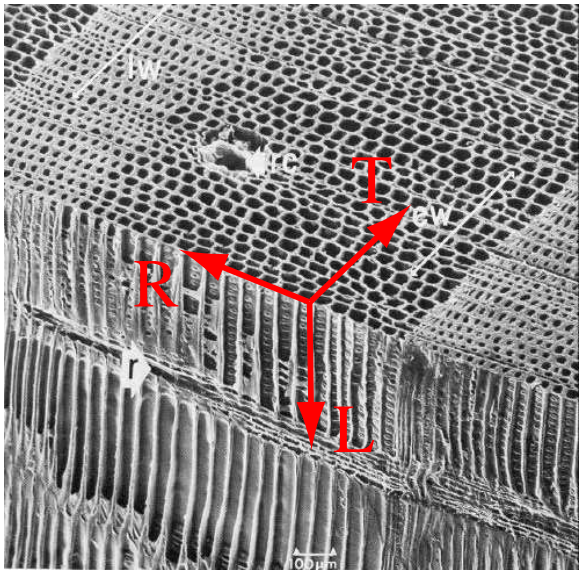

(b)

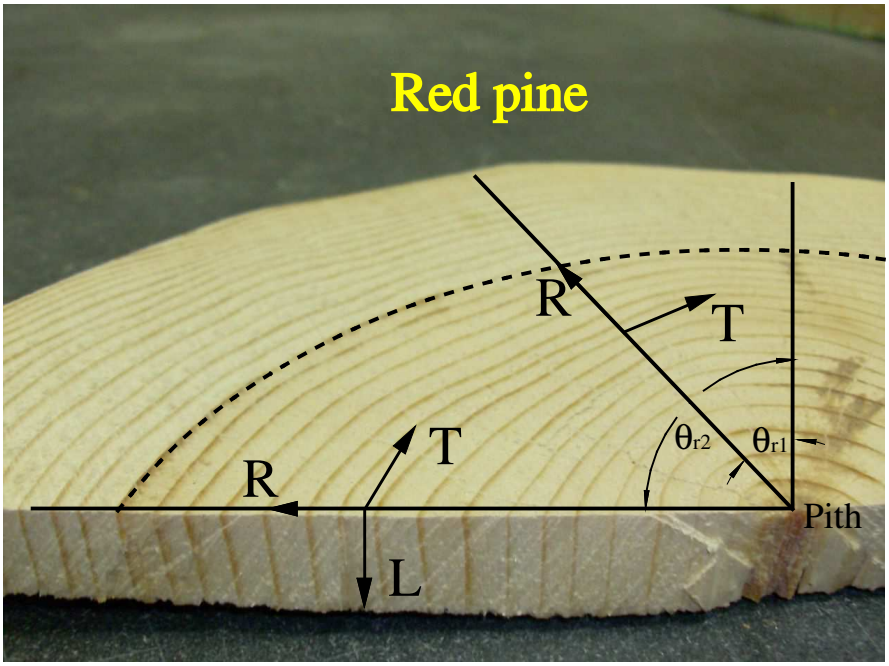

Figure 4.33: Microstructure (a) and Cross-section (b) of a red pine pole

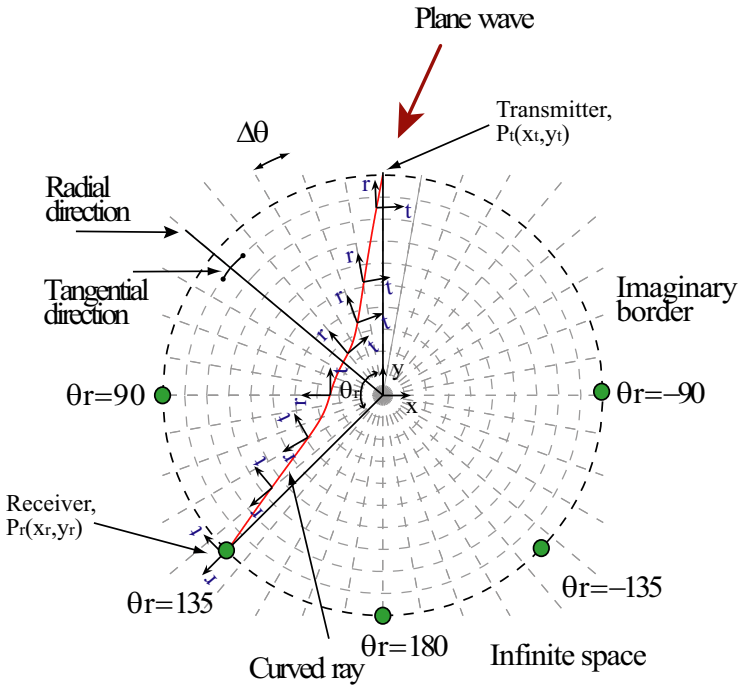

Figure 4.34: 2D cylindrical orthotropic model used for the Vp-COM method

The curved raypath is computed from two points belonging to the imaginary border: one corresponds to the transmitter $P_t(x_t, y_t)$ with coordinates $x_t = 0$ and $y_t = R$; and the other one, to the receiver $P_r(x_r, y_r)$. The direction cosines are changed until the raypath reaches a given receiver. This procedure should converge because in theory rays are generated in all by a point source in a continuum. The error function was defined in terms of the difference in location between the receiver and the final arrival of the raypath. However after numerous simulations, it was found that the minimum error always corresponds to the direction cosines defined by the straight line between the transmitter and the receiver because of the symmetry of the problem.

The receiver location angle (θ_r) is the angle between the transmitter and the receiver. It is positive in the counterclockwise direction; the receiver located at $\theta_r = 180^\circ$ means that the receiver is diametrally opposite to the transmitter. The receiver location angle is subdivided in n values such that the angle increment ($\Delta\theta = \theta_r/n$) is small enough to model the curved raypath. A local coordinate system (RT) coincident with the radial and tangential directions is defined at each angle increment.

The direction cosines ax and ay of the straight line between the transmitter and the receiver are

$$ax = \frac{x_r - x_t}{\sqrt{(x_r - x_t)^2 + (y_r - y_t)^2}}, \quad ay = \frac{y_r - y_t}{\sqrt{(x_r - x_t)^2 + (y_r - y_t)^2}} \tag{4.5}$$

The transmitter position defines the first point of the raypath ($P_1(0,R)$). The global and local coordinate systems are coincident at this point. The velocity V_p and displacement amplitudes U_r and U_t are computed from eqns. (3.68) and (3.65). The direction cosines αr and αt of the displacement vector are computed as

$$\alpha r = \frac{Ur}{\sqrt{Ut^2 + Ur^2}}, \quad \alpha t = \frac{Ut}{\sqrt{Ut^2 + Ur^2}} \tag{4.6}$$

to draw a straight line starting in the point P_1 and with direction defined by the direction cosines αr and αt. The next point $P_2(x_2, y_2)$ is determined by the intersection of this line with the radial ray at $\Delta\theta$. The direction cosines of the plane wave in local coordinate system at P_2 are computed by

$$ar = ay \cdot Bt_1 - ax \cdot Br_1, \quad at = ax \cdot Bt_1 + ay \cdot Br_1 \tag{4.7}$$

where Bt_1 and Br_1 are the direction cosines used to define the orientation of the local coordinate system. The velocity V_p and displacement amplitudes U_r and U_t are computed from eqns. (3.68) and (3.65). The displacements U_r and U_t are given in local coordinate system, thus the direction cosines αr and αt of the displacement vector are computed as

$$\alpha r = \frac{Ur}{\sqrt{Ut^2 + Ur^2}}, \quad \alpha t = \frac{Ut}{\sqrt{Ut^2 + Ur^2}} \tag{4.8}$$

The direction cosines αr and αt are transformed to global coordinates system by

$$\alpha x = Bt_1 \cdot \alpha t - Br_1 \cdot \alpha r, \quad \alpha y = Bt_1 \cdot \alpha r + Br_1 \cdot \alpha t \tag{4.9}$$

Figure 4.35 shows a simplified diagram to illustrate the global and local axes, the plane wave direction, and the displacement vector at the point P_2. In this figure, the following angles are shown:

- β_{TX} = angle of the local axis T respect to the global axis X,
- θ_x = angle of the plane wave respect to the global axis X,
- θ_t = angle of the local axis T respect to the direction of the plane wave,

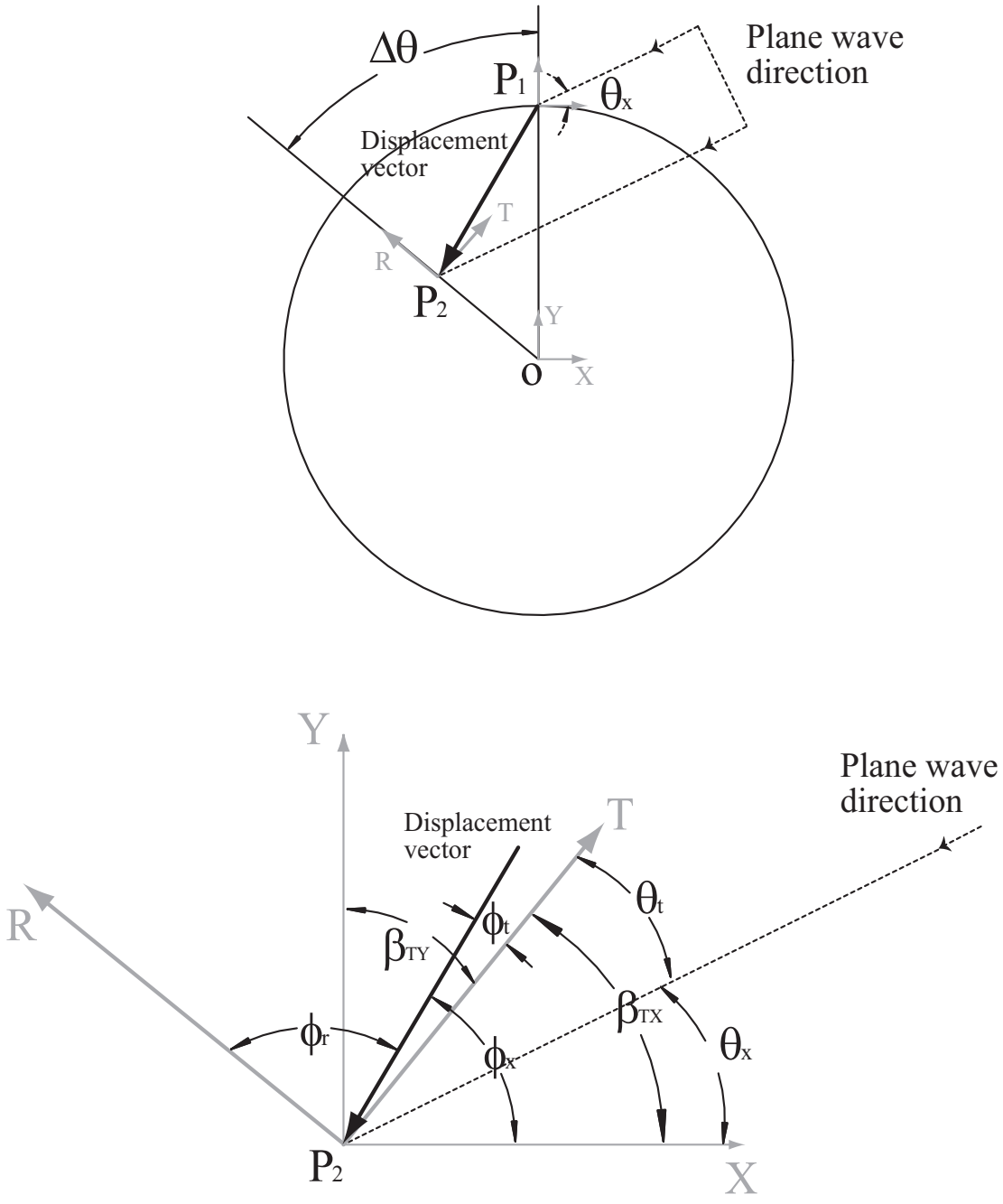

Figure 4.35: Schematic representation showing the global and local axes, the plane wave direction, and the displacement vector at the point P_2

- ϕ_t = angle of the displacement vector respect to the local axis T,
- ϕ_x = angle of the displacement vector respect to the global axis X,
- ϕ_r = angle of the displacement vector respect to the local axis R, and
- β_{TY} = angle of the local axis T respect to the global axis Y.

The direction cosine of the vector displacement respect to the global axis X is given as

$$\alpha x = \cos(\phi_x) = \cos(\beta_{TX} + \phi_t) = \cos(\beta_{TX}) \cdot \cos(\phi_t) - \sin(\beta_{TX}) \cdot \sin(\phi_t) \tag{4.10}$$

but

$$\cos(\beta_{TX}) = Bt_1, \text{ and } \cos(\phi_t) = \alpha t \tag{4.11}$$

on the other hand,

$$\phi_t + \phi_r = 90^\circ, \text{ and } \beta_{TX} + \beta_{TY} = 90^\circ \tag{4.12}$$

by which

$$\sin(\phi_t) = \cos(\phi_r) = \alpha r, \text{ and } \sin(\beta_{TX}) = \cos(\beta_{TY}) = Br_1 \tag{4.13}$$

therefore, eqn. (4.10) becomes in

$$\alpha x = Bt_1 \cdot \alpha t - Br_1 \cdot \alpha r \tag{4.14}$$

A similar procedure can be used to derive the other direction cosines. The problem of P-wave propagation continues by drawing a straight line starting in the point P_2 and with direction defined by the direction cosines αx and αy. The next point $P_3(x_3, y_3)$ is determined by the intersection of this line with the radial ray at $2\Delta\theta$. The direction cosines of the plane wave in local coordinate

system at P_3 are computed by

$$ar = ay \cdot Bt_2 - ax \cdot Br_2, \quad at = ax \cdot Bt_2 + ay \cdot Br_2 \tag{4.15}$$

where Bt_2 and Br_2 are the direction cosines used to define the orientation of the local coordinate system. The P-wave velocity and displacement amplitudes are again computed from eqns. (3.68) and (3.65). The direction cosines of the displacement vector αr and αt are computed as

$$\alpha r = \frac{Ur}{\sqrt{Ut^2 + Ur^2}}, \quad \alpha t = \frac{Ut}{\sqrt{Ut^2 + Ur^2}} \tag{4.16}$$

in global coordinates system, the direction cosines of the displacement vector are given by

$$\alpha x = Bt_2 \cdot \alpha t - Br_2 \cdot \alpha r, \quad \alpha y = Bt_2 \cdot \alpha r + Br_2 \cdot \alpha t \tag{4.17}$$

a line is drew starting in the third location point (P_3) and with direction defined by the direction cosines αx and αy. The next location point of the curved raypath ($P_4(x_4, y_4)$) is determined by the intersection of this line with the radial ray at $3\Delta\theta$. This procedure is repeated until that the curved raypath defined by the points P_i reaches the imaginary border.

Typical results of the velocity V_p as well as the raypaths obtained from the Vp-COM method for the receivers located at $\theta_r = 90°$, $\theta_r = 135°$, and $\theta_r = 180°$ are presented in Fig. 4.36. The velocity V_p at $\theta_r = 180°$ is 20% greater than the V_p at $\theta_r = 90°$ because the material is cylindrical orthotropic ($E_r/E_t = 1.4$). The raypaths for the receivers located at $\theta_r = 90°$ and $\theta_r = 135°$ are curved with a major effect for the receiver located at $\theta_r = 135°$.

The instantaneous wave velocities V_p and V_s along the curved raypath for the receiver located at $\theta_r = 135°$ are shown in Fig. 4.37. The maximum value of the instantaneous P-wave velocity occurs at $\theta = 0°$ and $\theta_r = 135°$ ($V_p = 1561$ m/s). The minimum values are at $\theta = 32°$ and $\theta = 103°$ ($V_p = 1329$ m/s). A relative maximum value at $\theta = 67.5°$ is also observed ($V_p = 1421$ m/s). The shear velocity is maximum at $\theta = 25.7°$ and $\theta = 109.3°$ ($V_s = 873$ m/s) and minimum at $\theta = 67.5°$ ($V_s = 479.5$ m/s). The instantaneous V_p and V_s curves are symmetrical respect the angle of $\theta = 67.5°$. The ratio between the maximum and minimum values is smaller for V_p than for V_s (1.17 v.s 1.82).

Figure 4.38 shows the cumulative travel time vs. the cumulative travel distance for the P-wave. The relationship is linear; therefore, the P-wave velocity computed as distance divided by time is constant along the curved raypath ($V_p = 1463$ m/s). On the other hand, this velocity is

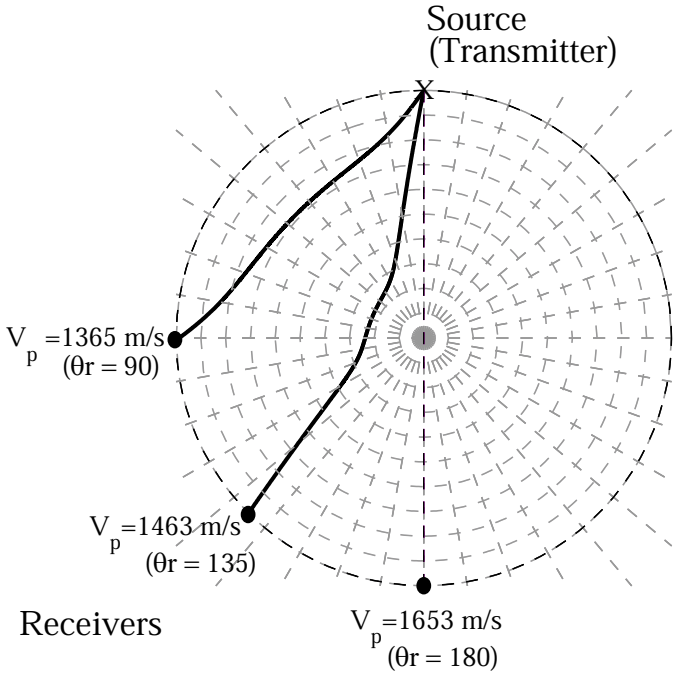

Figure 4.36: Typical results of V_p and curved raypaths obtained by the simplified method of analysis (Vp-COM) for the receivers located at $\theta_r = 90°$, $\theta_r = 135°$, and $\theta_r = 180°$

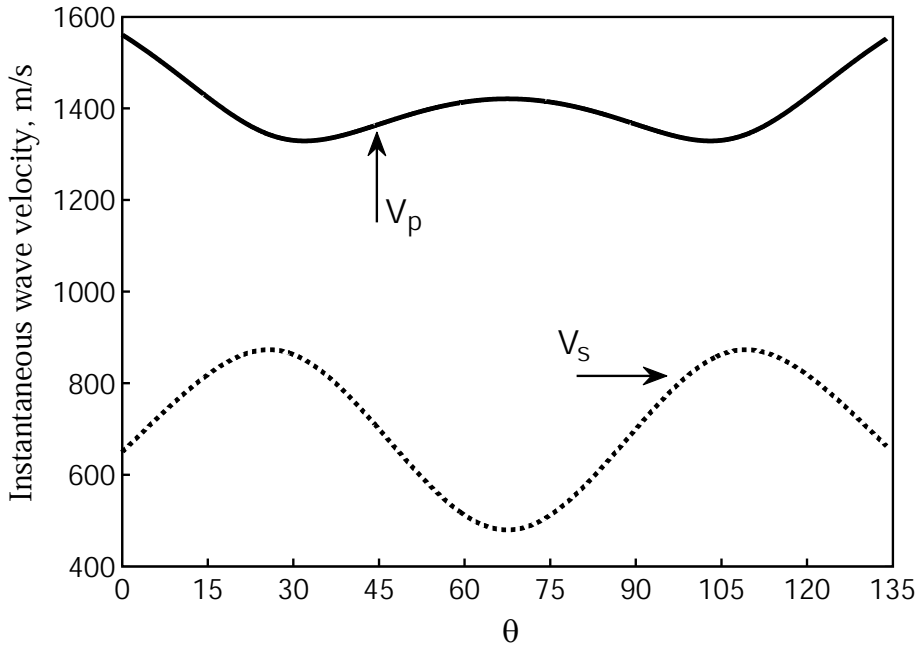

Figure 4.37: Typical results of velocities V_p and V_s along the curved raypath for the receiver located at $\theta_r = 135°$

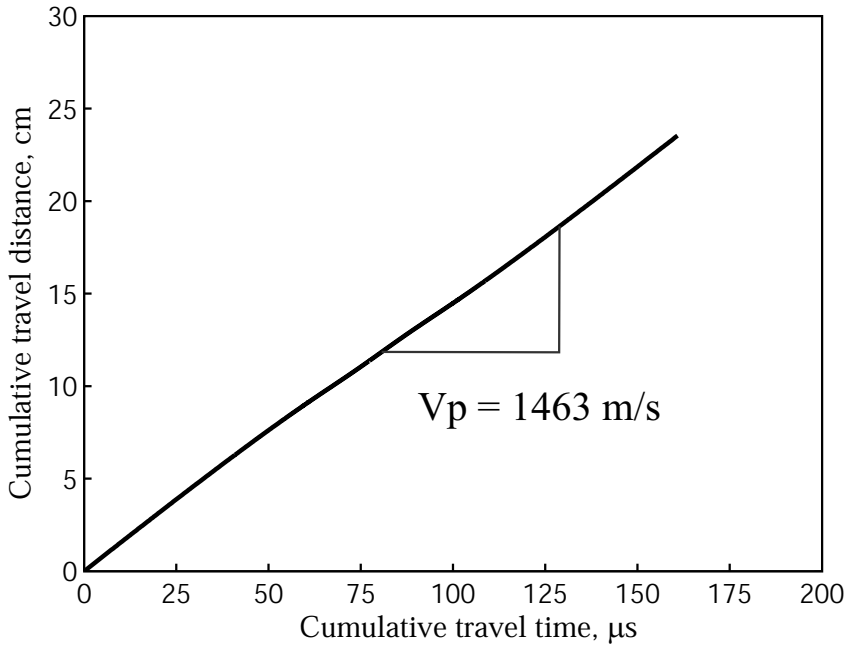

Figure 4.38: Cumulative travel time vs. cumulative travel displacement of V_p along the curved raypath for the receiver located at $\theta_r = 135^\circ$

only 2% greater than the value computed assuming linear ray theory.

The V_p wavefront at 50 and 100 μs is presented in Fig. 4.39. The wavefront shows a triangular shape before reaching the centre of the section. After the centre, the wavefront start taking a circular shape at the centre. This behaviour is characteristic of wave propagation in cylindrical orthotropic media [84, 83]. In Appendix A, the Matlab program of the Vp-COM method is listed.

Vp-COM method validation

Numerical simulations by finite elements of wave propagation in a pole cross-section of 25 cm diameter are performed. The material is cylindrical orthotropic and plain strain conditions are considered. The displacement response of an ultrasonic transmitter excited with a one-cycle sine wave of 50 kHz is used as dynamic excitation for the numerical simulations.

A total of 62 simulations (different values for the elastic moduli and mass density) are carried out to compute the P-wave velocity for the receivers located at $\theta_r = 90^\circ$, $\theta_r = 135^\circ$, and $\theta_r = 180^\circ$. The mean sample value for the elastic moduli in the longitudinal, radial, and tangential directions are 17.8, 1.2, and 0.89 GPa, respectively. The mean sample value for the mass density is 489 kg/m^3. The coefficients of variation for the elastic moduli and mass density are $COV_E = 0.24$ and $COV_\rho = 0.12$. The Poisson's ratios for the tangential-radial, longitudinal- radial, and longitudinal-tangential planes are $\nu_{rt} = 0.39$, $\nu_{lr} = 0.229$, and $\nu_{lt} = 0.229$. These are representative values

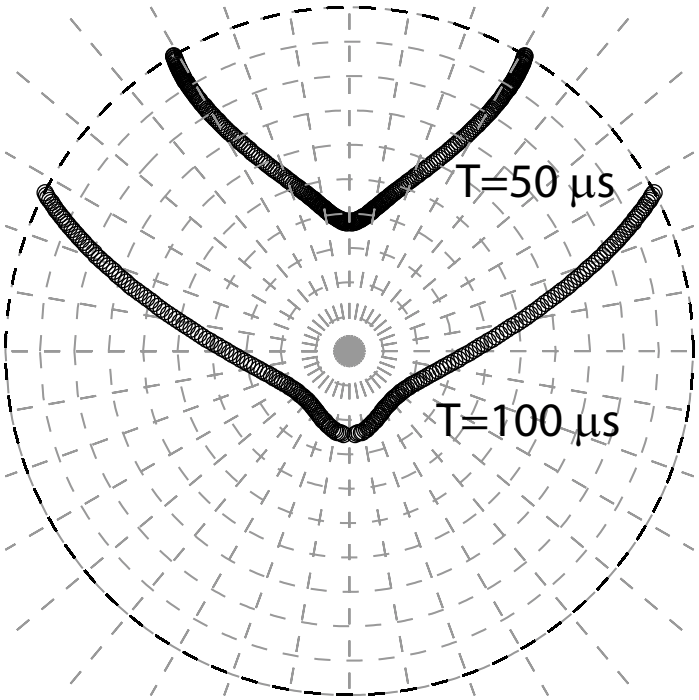

Figure 4.39: Wavefront of the velocity V_p at 50 and 100 μs obtained by the Vp-COM method for a cylindrical orthotropic model

for Douglas-fir.

Four nodes finite elements with two degrees of freedom at each node (translations in x and y directions) are used to model the continuous. The damping matrix $[C]$ is assumed to follow a Rayleigh damping [44]. The sampling rate is $\Delta t = 1\mu s$ which represents 20 points in time of a signal with a frequency of 50 kHz. The finite element size is $h = 0.4$ cm (Section 6.2).

Figure 4.40 shows the velocities V_p computed using finite element analysis (FEA) and the Vp-COM method. For the comparison of the results, the assumption of linear ray for computing the velocity V_p using the Vp-COM method is used. The velocity V_p varies from 1100 m/s to 2150 m/s. The maximum difference between the results obtained using the Vp-COM method and FEA is smaller than 3%.

The Vp-COM method is also able to model the condition of wave propagation in an isotropic medium. In this simple case, three parameters are required to compute the velocity V_p according to the following equation [44]

$$V_p = \sqrt{\frac{E\,(1-\nu)}{\rho\,(1+\nu)\,(1-2\nu)}} \tag{4.18}$$

For $E = 1$ GPa, $\nu = 0.2$, and $\rho = 500\ kg/m^3$, the P-wave velocity is $V_p = 1491$ m/s. The

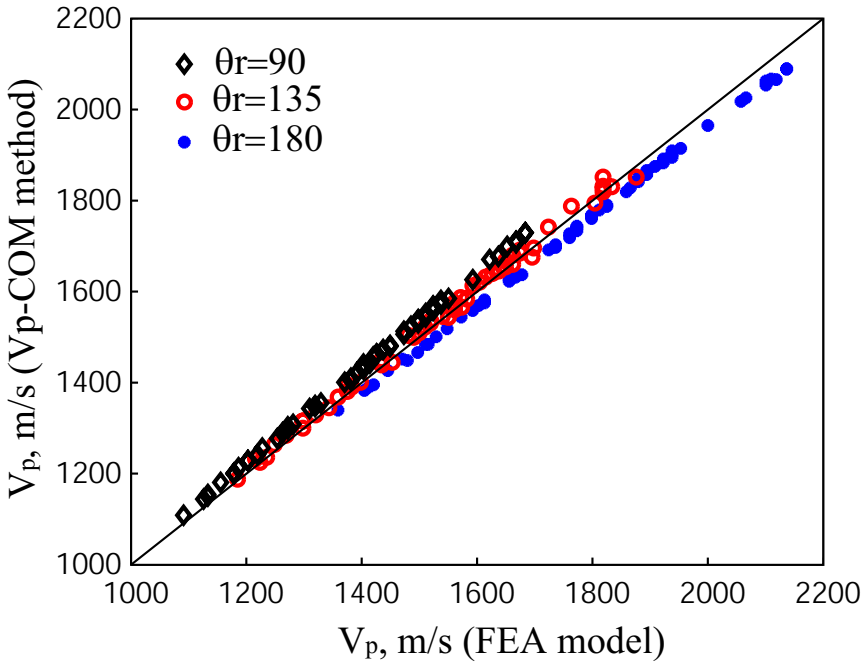

Figure 4.40: Comparison of the velocities V_p computed from the Vp-COM method and from FEA

results obtained using the Vp-COM method are presented in Fig. 4.41. As expected, the same value of V_p is obtained for the receivers located at $\theta_r = 90°$, $\theta_r = 135°$, and $\theta_r = 180°$. The path rays are linear, and the V_p wavefront at 50 and 100 μs is circular for the isotropic medium.

The instantaneous velocities V_p and V_s along the raypath are shown in Fig. 4.42. The velocities V_p and V_s are constant along the raypath. The ratio P-wave to shear wave velocities is $V_p/V_s = 1.633$. The velocities V_p and V_s are related by the Poisson's ratio as [86]

$$\frac{V_p}{V_s} = \sqrt{\frac{2(1-\nu)}{1-2\nu}} \tag{4.19}$$

For $\nu = 0.2$, the ratio $V_p/V_s = 1.633$, which is the same value obtained with the Vp-COM method.

4.6.1 Application examples

Two application examples are presented to illustrate the application of the Vp-COM method. The first one is the estimation of the pdf of the velocity V_p in a cross-section of a red pine pole. The second one is the determination of the elastic moduli in the radial and tangential directions from arrival times of compressional waves at different receiver locations. The elastic moduli are obtained by solving the inverse problem. These examples cannot be solved using finite element

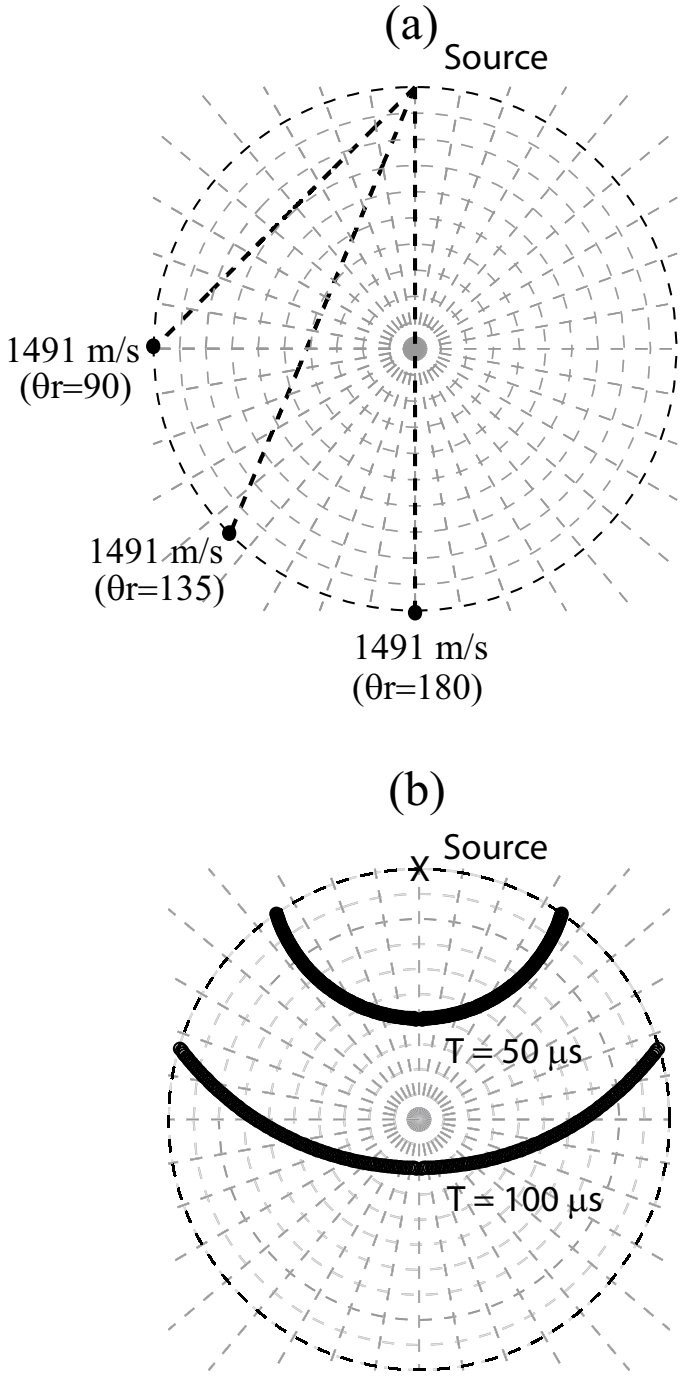

Figure 4.41: Typical result of the Vp-COM method for the velocity V_p (a) and wavefront at 50 and 100 μs (b) for an isotropic medium

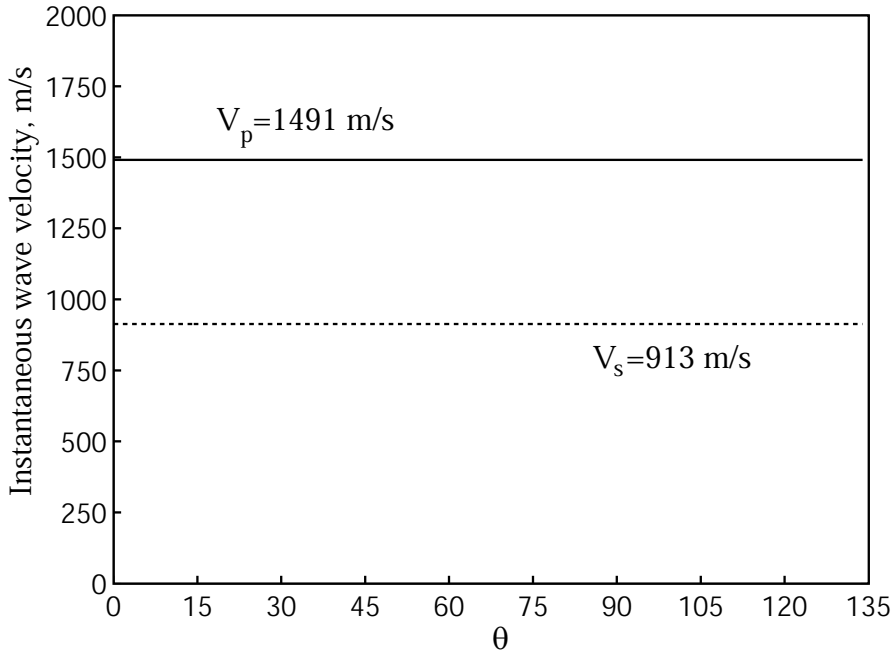

Figure 4.42: Typical results of velocities V_p and V_s along the curved raypath for the receiver located at $\theta_r = 135^\circ$

analysis because of time limitation in the number of simulations.

Estimation of the pdf of the velocity V_p

The nomenclature E_{i_j} is used to represent the elastic modulus. The sub-index i represents the direction (l=longitudinal, r=radial, t=tangential); and the sub-index j, the type of load (d=dynamic, s=static). The elastic modulus in the longitudinal direction for static loading E_{l_s} can be expressed as

$$E_{l_s} = (MOE) \cdot F_s \cdot F_{MCT} \tag{4.20}$$

where F_s is the correction factor for bending test, and F_{MCT} is a factor that considers the temperature and moisture content. F_s can be assumed equal to 1.1 (Sub-section 3.5.2). From eqns. (3.40) and (3.41) is obtained that

$$F_{MCT} = \left(\frac{MOE_n}{MOE_b}\right)^{-\left(\frac{MC-12}{MP-12}\right)} [1 - (t-20)\,\alpha] \tag{4.21}$$

where MOE_n and MOE_b are elastic moduli in air-dry and green conditions, respectively. The dynamic elastic modulus E_{l_d} can be represented as

$$E_{l_d} = E_{l_s} \cdot F_d \tag{4.22}$$

where F_d is the dynamic factor; which takes values between 1.1 and 1.2 (Sub-section 3.5.2). The methodology for the computation of the pdf of the velocity V_p in a cross-section is presented for the receivers located at $\theta_r = 90°$, $\theta_r = 135°$, and $\theta_r = 180°$. The P-wave velocity can be functionally expressed as

$$V_p^2 = f(\rho, E_{l_d}, E_{r_d}, E_{t_d}, \nu_{lr}, \nu_{lt}, \nu_{rt}) \tag{4.23}$$

The dynamic elastic moduli E_{r_d} and E_{t_d} are commonly expressed as fractions R_r and R_t of E_{l_d} by

$$E_{r_d} = R_r \cdot E_{l_d}, \quad \textit{and} \quad E_{t_d} = R_t \cdot E_{l_d} \tag{4.24}$$

In eqns. (4.23) and (4.24), the variables ρ, E_{l_d}, R_r, R_t, and ν_{rt} are modeled as random variables. The elastic moduli and mass density are assumed to be independent random variables because of the lack of information in the literature. The Normal and Weibull probability density functions have been used to describe statistically the elastic modulus [67, 68]. On the other hand, the elastic modulus has been correlated with the specific gravity as a power function of the specific gravity $E = aS^b$ [2, 16]. However, the specific gravity and elastic modulus cannot be defined as independent and dependent variables because a and b are not constant coefficients ($COV \approx 0.17$ for a and b) [87]. Therefore, the elastic modulus and mass density could be modeled as independent random variables. The Normal distribution is selected to represent the pdf of E_{l_d} and ρ avoiding negative values of these variables in the simulations. A uniform distribution is assumed for the random variables R_r, R_t, and ν_{rt} because of the lack of information in the available literature.

The pdf of V_p is computed for seven different cases as shown in Table 4.9. The base case corresponds to the calculation of V_p for the mean values of each random variable given in Tables 3.1, 3.2, 3.3, and 3.4. For case (a), only the mass density is considered as a random variable. The elastic moduli E_{l_d}, E_{r_d} and E_{t_d} are modeled as random variables for case (b), but E_{r_d} and E_{t_d} are dependent variables. The elastic ratios R_r and R_t and the Poisson's ratio ν_{rt} are modeled as

Table 4.9: Cases used to compute the pdf of the velocity V_p

Case	V_p as function of random and deterministic variables
(base)	$V_p^2 = f[\mu_\rho, \mu_{E_{l_d}}, \mu_{R_r}, \mu_{R_t}, \mu_{\nu_{lr}}, \mu_{\nu_{lt}}, \mu_{\nu_{rt}}]$
(a)	$V_p^2 = f[N(\mu_\rho, \sigma_\rho), \mu_{E_{l_d}}, \mu_{R_r}, \mu_{R_t}, \mu_{\nu_{lr}}, \mu_{\nu_{lt}}, \mu_{\nu_{rt}}]$
(b)	$V_p^2 = f[\mu_\rho, N(\mu_{E_{l_d}}, \sigma_{E_{l_d}}), \mu_{R_r}, \mu_{R_t}, \mu_{\nu_{lr}}, \mu_{\nu_{lt}}, \mu_{\nu_{rt}}]$
(c)	$V_p^2 = f[\mu_\rho, \mu_{E_{l_d}}, U(a_{R_r}, b_{R_r}), \mu_{R_t}, \mu_{\nu_{lr}}, \mu_{\nu_{lt}}, \mu_{\nu_{rt}}]$
(d)	$V_p^2 = f[\mu_\rho, \mu_{E_{l_d}}, \mu_{R_r}, U(a_{R_t}, b_{R_t}), \mu_{\nu_{lr}}, \mu_{\nu_{lt}}, \mu_{\nu_{rt}}]$
(e)	$V_p^2 = f[\mu_\rho, \mu_{E_{l_d}}, \mu_{R_r}, \mu_{R_t}, \mu_{\nu_{lr}}, \mu_{\nu_{lt}}, U(a_{\nu_{tr}}, b_{\nu_{rt}})]$
(f)	$V_p^2 = f[N(\mu_\rho, \sigma_\rho), N(\mu_{E_{l_d}}, \sigma_{E_{l_d}}), \mu_{R_r}, \mu_{R_t}, \mu_{\nu_{lr}}, \mu_{\nu_{lt}}, \mu_{\nu_{rt}}]$
(g)	$V_p^2 = f[N(\mu_\rho, \sigma_\rho), N(\mu_{E_{l_d}}, \sigma_{E_{l_d}}), U(a_{R_r}, b_{R_r}), U(a_{R_t}, b_{R_t}), \nu_{lr}, \nu_{lt}, U(a_{\nu_{rt}}, b_{\nu_{rt}})]$

random variables for cases (c), (d), and (e), respectively. The variables ρ, E_{l_d}, R_r, and R_t are modeled as random variables for case (f); and finally, for the case (g), ρ, E_{l_d}, R_r, R_t, and ν_{rt} are considered as random variables.

The methodology for the calculation of the pdf of the velocity V_p is demonstrated here using the mechanical properties of red pine; their mean values as well as the coefficients of variation are shown in Table 4.10. Typical values of moisture content and temperature are assumed as with $MC = 20\%$ and $T = 20\ ^\circ C$. The selected coefficients of variation for ρ and E_{l_d} are widely supported from experimental data published in the literature [21, 2, 16, 88]. The coefficients of variation for the elastic ratios (R_r and R_t) and for the Poisson's ratio (ν_{rt}) are assumed equal to 0.10 because of lack of experimental data in this area.

If the random variables R_r and E_{l_d} are independent, the mean value of E_{r_d} is [9]

$$\mu_{E_{r_d}} = \mu_{R_r} \cdot \mu_{E_{l_d}} \tag{4.25}$$

and the coefficient of variation

$$COV_{(E_{r_d})} = \sqrt{COV^2_{(E_{l_d})}\,(1 + COV^2_{(R_r)}) + COV^2_{(R_r)}} \tag{4.26}$$

Table 4.10: Mean values and COVs for mechanical properties of red pine used to compute the pdf of V_p

Mechanical property	Mean value	COV
Mass density, ρ ($\frac{kgm}{m^3}$)	491.2	0.12
Elastic modulus, MOE_n (GPa)	9.45	0.22
Elastic ratio, R_r	0.088	0.10
Elastic ratio, R_t	0.044	0.10
Poisson's ratio, ν_{lr}	0.347	0.0
Poisson's ratio, ν_{lt}	0.315	0.0
Poisson's ratio, ν_{rt}	0.408	0.10

where $COV_{(E_{l_d})}$ and $COV_{(R_r)}$ are the coefficients of variation of the variables E_{l_d} and R_r, respectively. As expected, $COV_{(E_{r_d})} = COV_{(E_{l_d})}$ when $COV_{(R_r)} = 0$. For this condition, the elastic modulus E_{r_d} follows the same statistical distribution of E_{l_d}.

For the selected values of $COV_{(R_r)} = 0.1$ and $COV_{(E_{l_d})} = 0.22$, the computed value of $COV_{(E_{r_d})} = 0.243$ (eqn. (4.26)). This value is 10% larger than the coefficient of variation of E_{l_d}.

The Poisson's ratios for the longitudinal-radial and longitudinal-tangential planes ν_{lr} and ν_{lr} are considered deterministic variables because they have not significant influence on the results since the wave energy is mostly concentrated in the cross-section plane as in a plain strain problem. The minimum an maximum values of ν_{rt} (Uniform distribution) for $COV_{(\nu_{rt})} = 0.1$, are given by eqns. (3.52) and (3.53) as $0.83\,\mu_{\nu_{rt}}$ and $1.17\,\mu_{\nu_{rt}}$, respectively. Then, the Poisson's ratio ν_{rt} varies from 0.34 to 0.48 for red pine. Whereas the corresponding Poisson's ratio ν_{tr} takes values from 0.125 to 0.34 ($\nu_{tr} = (R_t/R_r)\,\nu_{rt}$).

Monte Carlo simulations (MCS) are used to estimate the pdf of the velocity V_p by sampling sets of random numbers for each statistical distribution and estimating the velocity V_p from the Vp-COM method. With the increase in the number of simulations, the result from the MCS converges to a closed form solution. The MCS is always subject to sampling error because the number of simulation is not infinite.

The required sample size depends on the precision selected for the statistical distribution. For normally distributed data, the sample size depends on the lower exclusion limit, the confidence level, the coefficient of variation, and the allowable error. For 5% exclusion limits, 95% con-

fidence level, and $COV = 0.22$, the required sample size is 320 for an allowable error of 5% [89].

Figure 4.43 shows histograms of P-wave velocity normalized by the sample mean and the sample standard deviation values $(V_p - \mu)/\sigma$ for the receiver located at $\theta_r = 180°$. The histogram is computed for 30, 320, 3000, 30000, 60000, and 90000 samples using the Vp-COM method and MCS. The simulations correspond to the case (g) where the velocity V_p is function of five independent random variables. The histogram is not well defined for a sample size of $N_s = 30$ neither about the sample mean value nor the tails of the distribution. Although the histogram is well defined about the mean value for a sample size $N_s = 320$, the simulated V_p values are between plus/minus three standard deviations respect the sample mean value. Simulations with a sample size of $N_s = 60000$ can model the tails of the distribution $(-5 \leq (V_p - \mu)/\sigma \leq 5)$. The histogram obtained for $N_s = 90000$ is similar to the corresponding for $Ns = 60000$. Based on these results, the number of simulations to compute the pdf of the velocity V_p for the cases (f) and (g), which have two and five independent random variables, is selected as $N_s = 60000$. For cases (a), (b), (c), (d), and (e) with one random variable, the number of simulations is selected as $N_s = 10000$. Statistical tests are performed to determine the probability distribution that best fit the simulated data. The probability distributions used are Normal, Log-Normal, Gamma, Gumbel, and Weibull [9].

The P-wave velocities and raypaths for the base case (Table 4.9) computed ($\theta_r = 90°$, $\theta_r = 135°$, and $\theta_r = 180°$) using the Vp-COM method are shown in Fig. 4.44. The velocity V_p at $\theta_r = 180°$ is 27% greater than the V_p at $\theta_r = 90°$. The variation of V_p with the receiver location angle is linear. Another important feature obtained from the Vp-COM method is the prediction of the curved raypath for the velocity V_p (Fig. 4.44).

In Table 4.11, the results for the calculated mean values and coefficients of variation for the different cases (Table 4.9) are presented. The mean values for all the cases studied are similar to the corresponding values for the deterministic case (less than 2% difference). For case (a), $COV_{V_p} = 0.062$ for all the receiver location angles because the mass density is not affected by the anisotropy of the material. When only one random variable is considered (cases (b) to (e)), the maximum coefficient of variation is obtained for case (b) ($COV_{V_p} = 0.11$) because E_l is the random variable with the maximum COV.

For the cases (c), the coefficient of variation at $\theta_r = 90°$ is $COV_{V_p} = 0.011$, which increases to $COV_{V_p} = 0.041$ and $COV_{V_p} = 0.046$ for the receivers located at $\theta_r = 135°$ and $\theta_r = 180°$, respectively. Likewise, the coefficient of variation for case (d) is $COV_{V_p} = 0.033$ at $\theta_r = 90°$ and practically zero at $\theta_r = 180°$. The effect on the velocity V_p is smaller than 2% for case (e). The coefficient of variation for case (f) at $\theta_r = 90°$ is $COV_{V_p} = 0.117$, increasing to $COV_{V_p} = 0.127$ and $COV_{V_p} = 0.13$ for the receivers located at $\theta_r = 135°$ and $\theta_r = 180°$, respectively. Finally, the

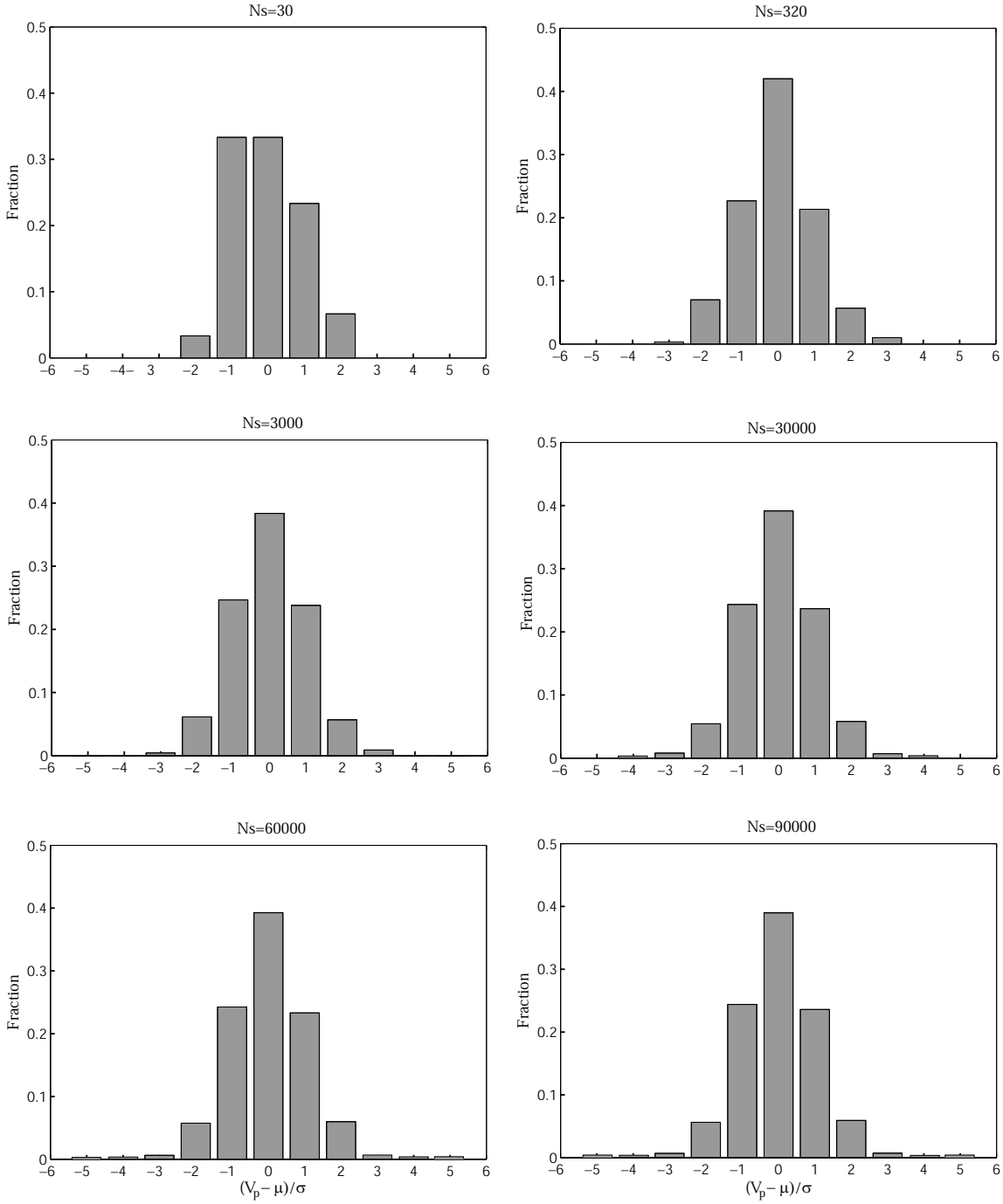

Figure 4.43: Histogram of $(V_p - \mu)/\sigma$ for different sample sizes ($\theta_r = 180°$, case (g))

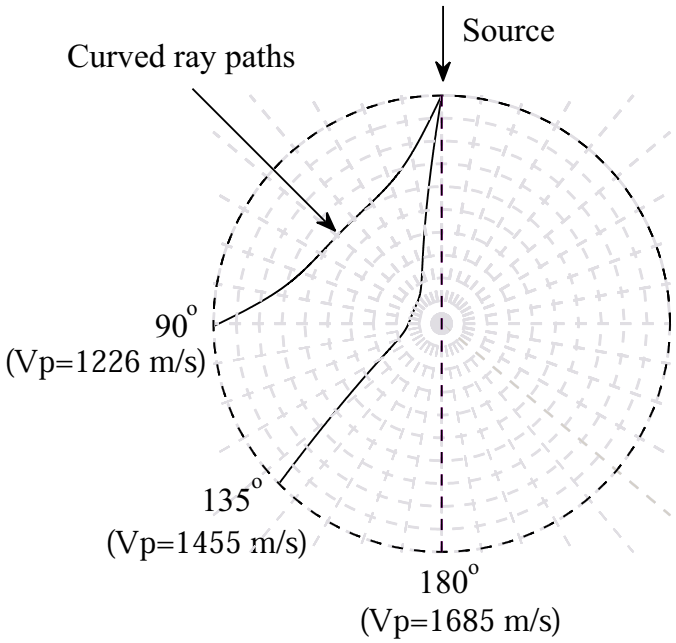

Figure 4.44: Velocity V_p at different receiver location angles: deterministic case (Table 4.9)

coefficient of variation for case (g) at $\theta_r = 180°$ is $COV = 0.137$, which represents 5% increase with respect to case (f). In general, the elastic modulus E_{r_d} shows a greater influence on V_p than the elastic modulus E_{t_d}.

Mean values and COVs of the velocity Vp for the different cases using the Vp-COM method and assuming air-dry conditions

For the simple model of one-dimensional wave propagation, the relationship between the velocity V_p, mass density, and dynamic elastic modulus in the radial direction is given as

$$V_p = \sqrt{\frac{E_{r_d}}{\rho}} \tag{4.27}$$

Assuming that ρ and E_{r_d} follow a Normal distribution with parameters $N(\mu_\rho, \sigma_\rho)$ and $N(\mu_{E_{r_d}}, \sigma_{E_{r_d}})$, the mean value and coefficient of variation obtained using three terms of the Taylor series [9] can be expressed as

$$\mu^2_{V_p} = \frac{\mu_{E_{r_d}}}{\mu_\rho}\left[1 + \frac{COV^2_{E_{r_d}}}{8} - \frac{COV^2_\rho}{8}\right] \tag{4.28}$$

Table 4.11: Mean values and COVs of the velocity V_p for the different cases using the Vp-COM method and assuming air-dry conditions

Case	Number of simulations	Receiver location angles $\theta_r = 90°$		$\theta_r = 135°$		$\theta_r = 180°$	
		μ_x (m/s)	COV_x	μ_x (m/s)	COV_x	μ_x (m/s)	COV_x
(base)	1	1226	0	1455	0	1685	0
(a)	10000	1233	0.062	1463	0.062	1694	0.062
(b)	10000	1220	0.10	1446	0.11	1673	0.11
(c)	10000	1228	0.011	1456	0.041	1683	0.046
(d)	10000	1227	0.033	1456	0.028	1685	0.005
(e)	10000	1227	0.014	1456	0.009	1686	0.01
(f)	60000	1227	0.117	1454	0.127	1683	0.130
(g)	60000	1231	0.122	1458	0.133	1683	0.137

$$COV^2_{(V_p)} = \frac{2\,(COV^2_{(E_{r_d})} + COV^2_{(\rho)})}{8 + COV^2_{(E_{r_d})} - COV^2_{(\rho)}} \tag{4.29}$$

where $\mu_{E_{r_d}}$, μ_ρ, $COV_{(E_{r_d})}$ and $COV_{(\rho)}$ are the mean values and coefficients of variation of E_{r_d} and ρ, respectively. For $\mu_{E_{r_d}} = 9.45 \times 0.088 \times 1.1 \times 1.2 = 1.1\ GPa$, $\mu_\rho = 491.2\ kg/m^3$, $COV_{(E)} = 0.22$, and $COV_{(\rho)} = 0.12$, eqns. (4.28) and (4.29) predict that $\mu_{V_p} = 1500\ m/s$ and $COV_{(V_p)} = 0.125$. Although the coefficients of variation are similar (4% difference), the mean value of the velocity V_p obtained from one-dimensional model is 12% smaller than the computed value using an orthotropic model.

The probability paper plot (PPP) is used to verify the assumed probability distribution of a given data set. Among the probability distributions Normal, Log-Normal, Gamma, Gumbel, and Weibull, the Normal distribution represents the best-fitting probability distribution for the general case (g). Figure 4.45 shows a typical PPP for the receiver located at $\theta_r = 180°$. A linear relationship ($R^2 = 0.99$) is observed between the random variable (V_p) and the standard normal

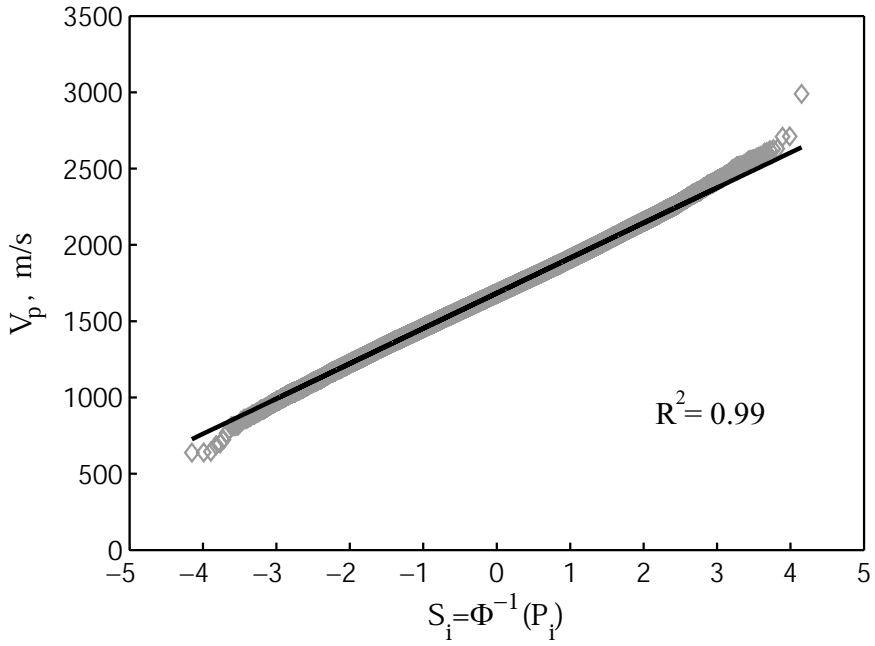

Figure 4.45: Normal probability paper plot for case (g), receiver located at $\theta_r = 180^\circ$ (red pine, $MC = 20\%$, $T = 20\ ^\circ C$)

variable; which indicates that the V_p data follows a Normal distribution.

The pdfs of V_p for case (g) at locations $\theta_r = 90^\circ$, $\theta_r = 135^\circ$, and $\theta_r = 180^\circ$ are shown in Fig. 4.46. The mean value and mean value plus/minus one standard deviation as function of the receiver location angle are presented in Fig. 4.47; which shows a linear trend. In this figure, experimental data of the velocity V_p measured for new and aged red pines using ultrasonic testing is also included. Ultrasonic transducers with nominal frequency of 50 kHz are used to measure the V_p for the receivers located at $\theta_r = 90^\circ$, $\theta_r = 135^\circ$, and $\theta_r = 180^\circ$ on four new red pines; and for the receiver located at $\theta_r = 180^\circ$ on 18 aged red pine poles (sound), a typical experimental setup is shown in Fig. 4.48(a).

Experimental values and numerical simulation results using the Vp-COM method and MCS for the receiver located at $\theta_r = 180^\circ$ are in good agreement. For the receivers located at $\theta_r = 90^\circ$ and $\theta_r = 135^\circ$, the measured velocities V_p are concentrated at the mean value plus/minus one standard deviation. Experimental values of the velocity V_p measured at different receiver location angles are used to calibrate the expected value obtained from the simulations.

The values of V_p from the 60000 simulations for the receivers located at $\theta_r = 90^\circ$, $\theta_r = 135^\circ$, and $\theta_r = 180^\circ$ as well as the simulated values of E_{r_d} are sorted in increasing order and plotted in Fig. 4.49. As expected, the same value of E_{r_d} is obtained for the mean values of the velocity V_p for the receivers located at $\theta_r = 90^\circ$, $\theta_r = 135^\circ$, and $\theta_r = 180^\circ$ because the elastic moduli (E_r, E_t)

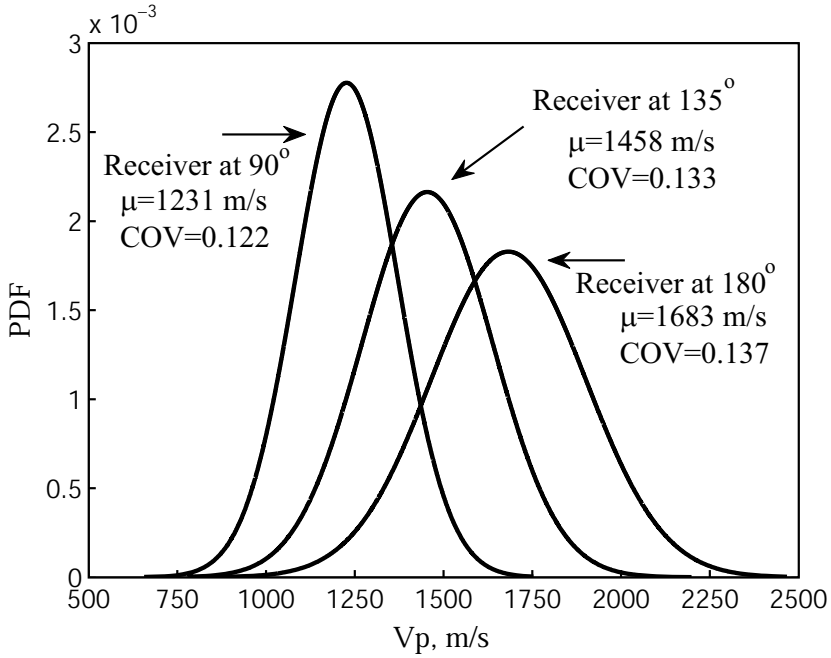

Figure 4.46: Probability density function of the velocity V_p for case (g) (red pine, $MC = 20\%$, $T = 20\ ^{\circ}C$)

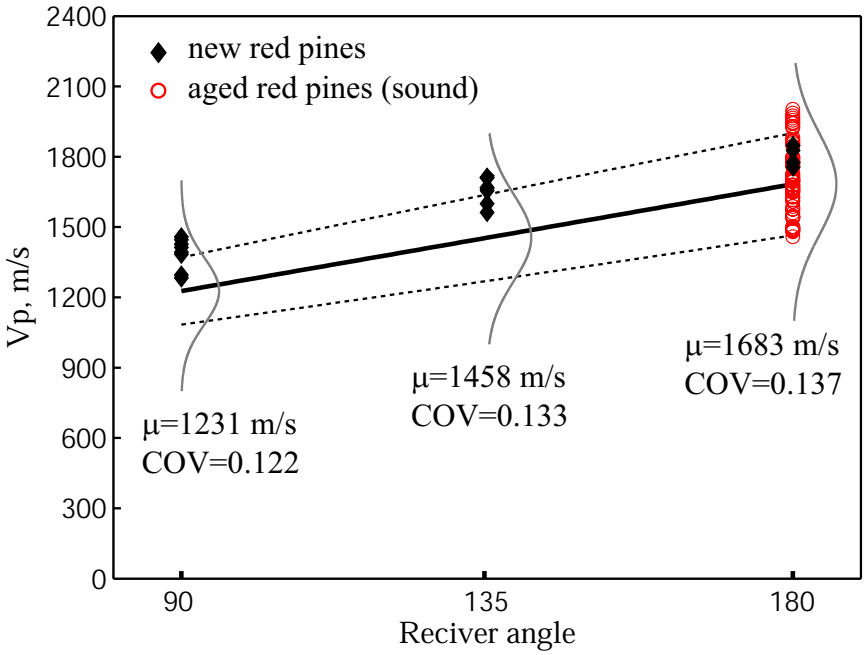

Figure 4.47: Mean value and mean value plus/minus one standard deviation of the velocity Vp for the receivers located at $\theta_r = 90^{\circ}$, $\theta_r = 135^{\circ}$, and $\theta_r = 180^{\circ}$ (red pine, $MC = 20\%$, $T = 20\ ^{\circ}C$)

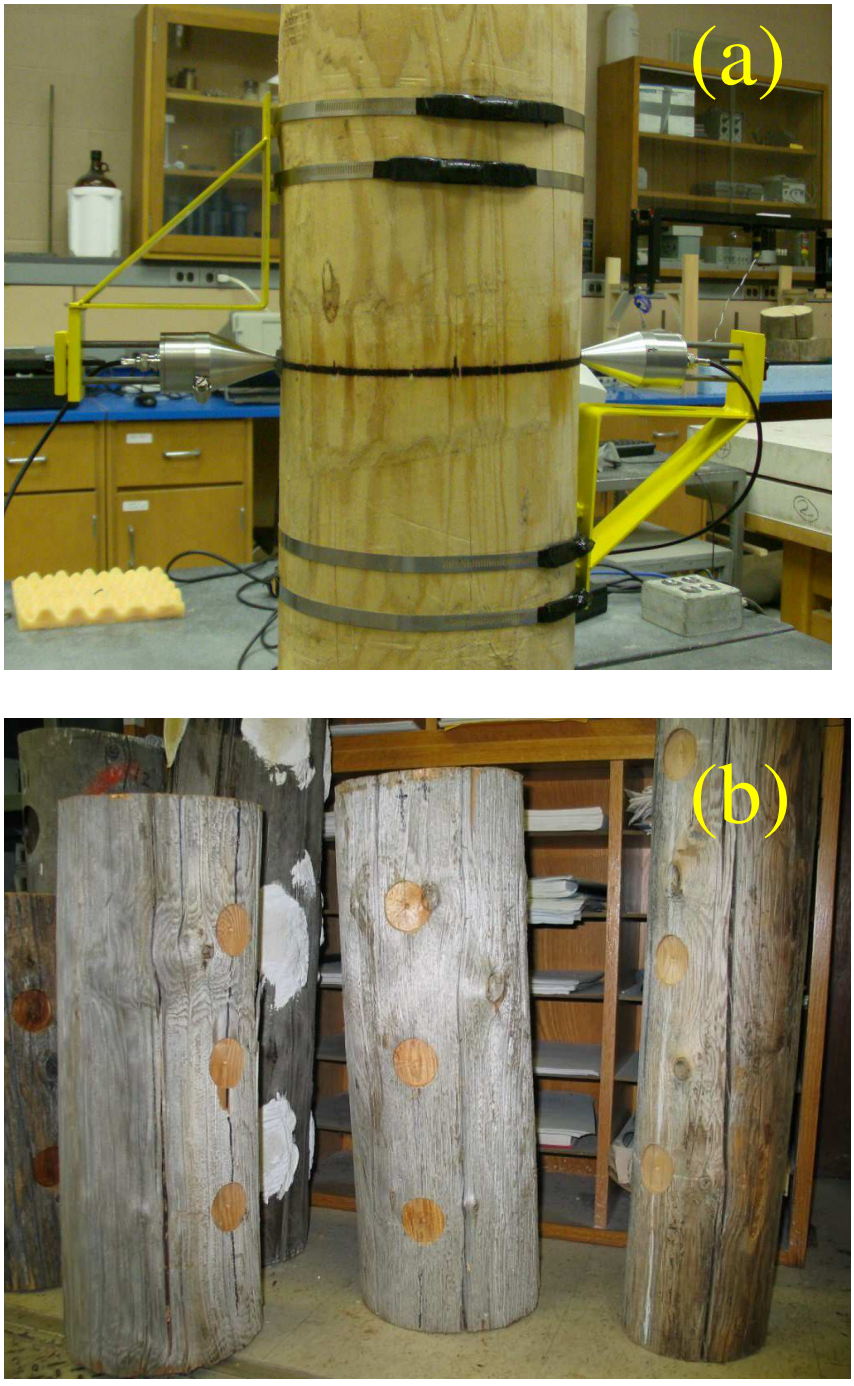

Figure 4.48: Ultrasonic tests in cross-sections of red pine poles: a) new red pine, b) aged red pines (sound)

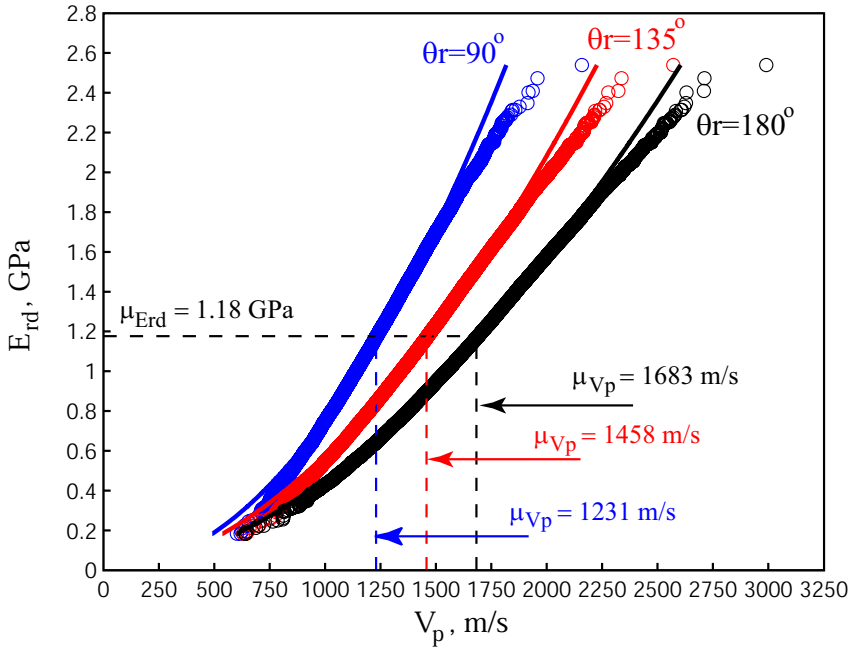

Figure 4.49: Correlation between V_p and E_{r_d} for the receivers located at $\theta_r = 90°$, $\theta_r = 135°$, and $\theta_r = 180°$ (red pine, $MC = 20\%$, $T = 20\ ^\circ C$)

are assumed constant in a cross-section. The computed value of E_{r_d} corresponds to the assumed mean value. The velocity V_p and the elastic modulus E_{r_d} can be related by

$$V_p = a_r \cdot E_{r_d}^{n_r} \tag{4.30}$$

where the coefficient a_r and the exponent n_r are obtained by curve-fitting the data of V_p and E_{r_d} (solid lines in Fig. 4.49). Table 4.12 shows the coefficients a_r and n_r obtained for the different receiver location angles as well as the corresponding regression coefficients. Both coefficient increase with the receiver angle. In general, the exponent n_r is close to the theoretical value for one-dimensional equation given by eqn. (4.27) (maximum 6% of difference). Equation (4.30) can be used to estimate E_{r_d} for a given value of V_p for different receiver location angles.

Figure 4.50 illustrates the expected effect of moisture content and temperature on the mean value of the velocity V_p for red pine pole computed using the Vp-COM method. Moisture content varies from 5 to 28%, and temperature from 0 to 40 $^\circ C$. The mean value of the velocity V_p is normalized by the corresponding value for $MC = 12\%$ and $T = 20\ ^\circ C$. The moisture-temperature factor defined as ($R_{V_p(MC,T)} = \mu_{V_p}(MC,T)/\mu_{V_p}(12,20)$) decreases linearly with MC and T. The

Table 4.12: Coefficients a_r and n_r for the receivers located at $\theta_r = 90°$, $\theta_r = 135°$, and $\theta_r = 180°$ (red pine poles)

Receiver location angle	a_r	n_r	R-squared
$\theta_r = 90°$	1143.85	0.497	0.9954
$\theta_r = 135°$	1345.37	0.540	0.9971
$\theta_r = 180°$	1548.91	0.557	0.9982

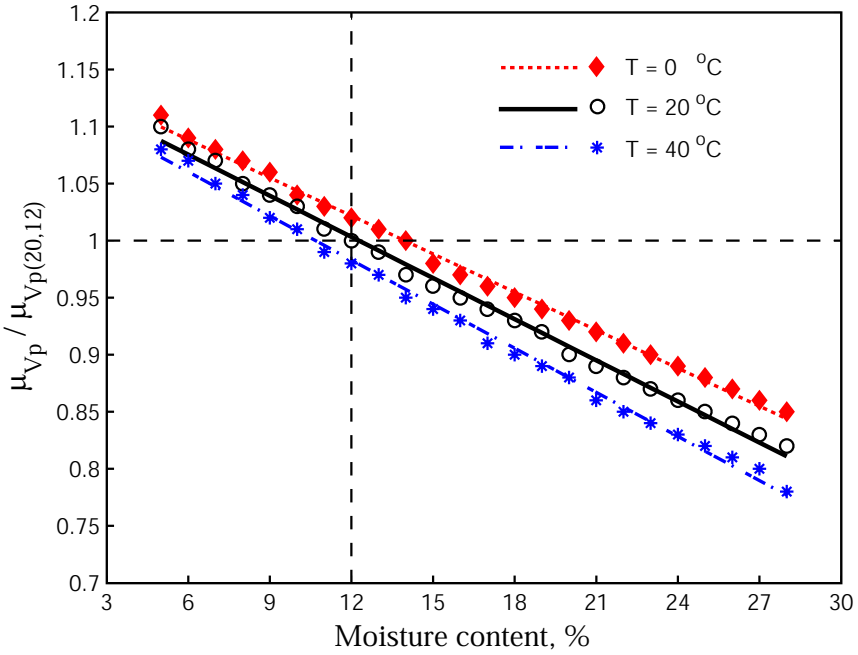

Figure 4.50: Effect of moisture content and temperature in the mean value of the velocity V_p for the receiver located at $\theta_r = 180°$ (red pine, $MC = 20\%$, $T = 20\ ^\circ C$)

moisture-temperature factor is represented by the following equation

$$R_{V_p}(MC,T) = (-0.000045\,T - 0.0111)\,MC - 0.0004\,T + 1.152 \tag{4.31}$$

The probability density functions of wave velocity shown in Fig. 4.46 for the receivers located at $\theta_r = 90°$, $\theta_r = 135°$, and $\theta_r = 180°$ can be computed for any moisture content and temperature values by using eqn. (4.31).

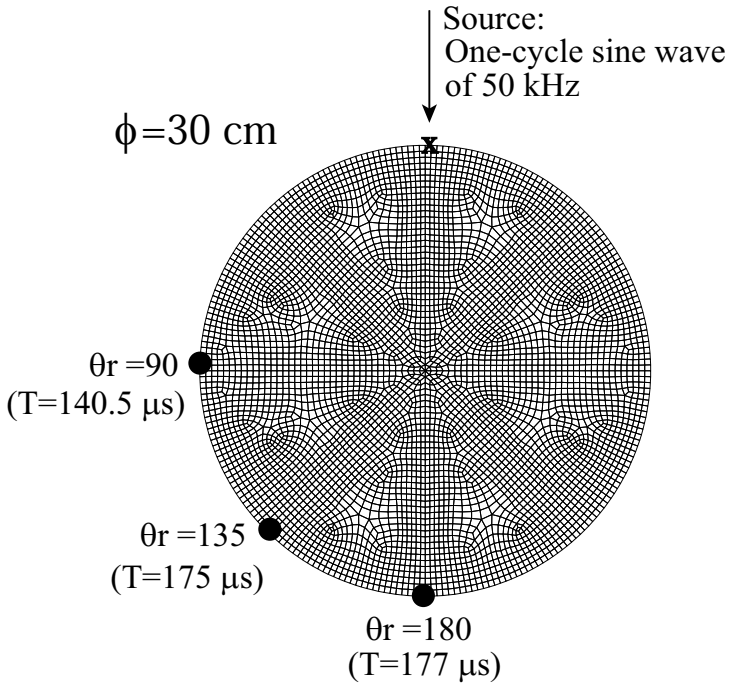

Figure 4.51: Numerical model by finite element analysis

Estimation of E_r and E_t from ultrasonic testing

Another important application of the Vp-COM method is the estimation of the elastic moduli in the radial and tangential directions from measurements of arrival times of the velocity V_p. The elastic moduli are computed by solving the inverse problem. Values of mass density and Poisson's ratios reported in the literature are assumed for a given specie of wood.

Figure 4.51 shows the finite element model used for the simulation of ultrasonic wave propagation in a cross-section of red pine pole. The section is 30 cm diameter; the response of an ultrasonic transmitter excited with a one-cycle sine wave of 50 kHz (Fig. 6.9) is used as source. The elastic moduli for the longitudinal, radial, and tangential directions are $E_l = 7.8$ GPa, $E_r = 1.09$ GPa, and $E_t = 0.91$ GPa, respectively. The mass density is $\rho = 460\ kg/m^3$; and the Poisson's ratios are $\nu_{rt} = 0.408$, $\nu_{lt} = 0.347$, and $\nu_{rt} = 0.315$. Arrival times of P-waves are shown in the figure for the receivers located at $\theta_r = 90^\circ$, $\theta_r = 135^\circ$, and $\theta_r = 180^\circ$.

The elastic moduli are computed from the arrival times by solving the inverse problem. The required input data are the wood specie (red pine) and the arrival times at $\theta_r = 90^\circ$ ($T = 140.5\ \mu s$), $\theta_r = 135^\circ$ ($T = 175\ \mu s$), and $\theta_r = 180^\circ$ ($T = 177\ \mu s$). The mass density and the Poisson's ratios for red pine are obtained from Tables 3.1 and 3.4.

For the inversion of the elastic moduli of a wood pole, it is assumed that they are in a the region $R(Er, Et)$ defined by $E_i \leq E_r \leq E_j$ and $E_i \leq E_t \leq E_k$. The region $R(Er, Et)$ is discretized

using a uniform grid (Fig. 4.52(a)); which is refined using a convergence test. For each combination of E_r and E_t, the arrival times are computed at each receiver location. The mean square relative error (MSRE) between the computed and the measured arrival times is calculated. The values of E_r and E_t that produce the minimum error (MSRE) are selected as the best values to describe the results obtained from ultrasonic test. The total number of simulations for a given grid is

$$N_{si} = (\frac{E_j - E_i}{\Delta E_r} + 1)(\frac{E_k - E_i}{\Delta E_t} + 1) \tag{4.32}$$

where ΔE_r and ΔE_t are the increments for the elastic moduli E_r and E_t, respectively. Figure 4.52(b) shows the convergence test of the ratio E_r/E_t as function of the number of simulation N_{si}. The 2D cartesian region is defined by 0.2 GPa $\leq E_r \leq$ 2 GPa and 0.2 GPa $\leq E_t \leq$ 2 GPa. The ratio E_r/E_t converges to the theoretical value when the modulus mesh is refined.

Figure 4.53(a) illustrates the solution of the inverse problem for $N_{si} = 30000$. The abscissa axis represents the elastic modulus E_r; whereas the ordinate axis, the mean square relative error (MSRE) of arrival times. Each curve in this figure corresponds to a value of E_t from the modulus mesh. The elastic moduli E_r and E_t for the tested cross-section are the corresponding values for the minimum error (MSRE). For the case shown in Fig. 4.53(a), $\widehat{E_r} = 1.11$ GPa and $\widehat{E_t} = 0.93$ GPa. The maximum difference between the theoretical and estimated elastic moduli is less than 2%. Arrival times computed using the Vp-COM method and finite element analysis are show in Fig. 4.53 (b). The match between them is excellent. If a statistical distribution for the mass density is assumed, statistical distributions for E_r and E_t are then obtained as a result.

4.7 New Statistical Characterization Features

Condition assessment of wood pole cross-sections using ultrasonic testing is based on features extracted from the first arrival of compressions wave and the full waveforms. From the arrival times, the V_p and the elastic moduli E_r and E_t are extracted; whereas wave transmission factors, the frequency response and impulse response functions are obtained from the full waveform analysis. Numerical simulation results are calibrated with experimental data obtained on a red pine pole.

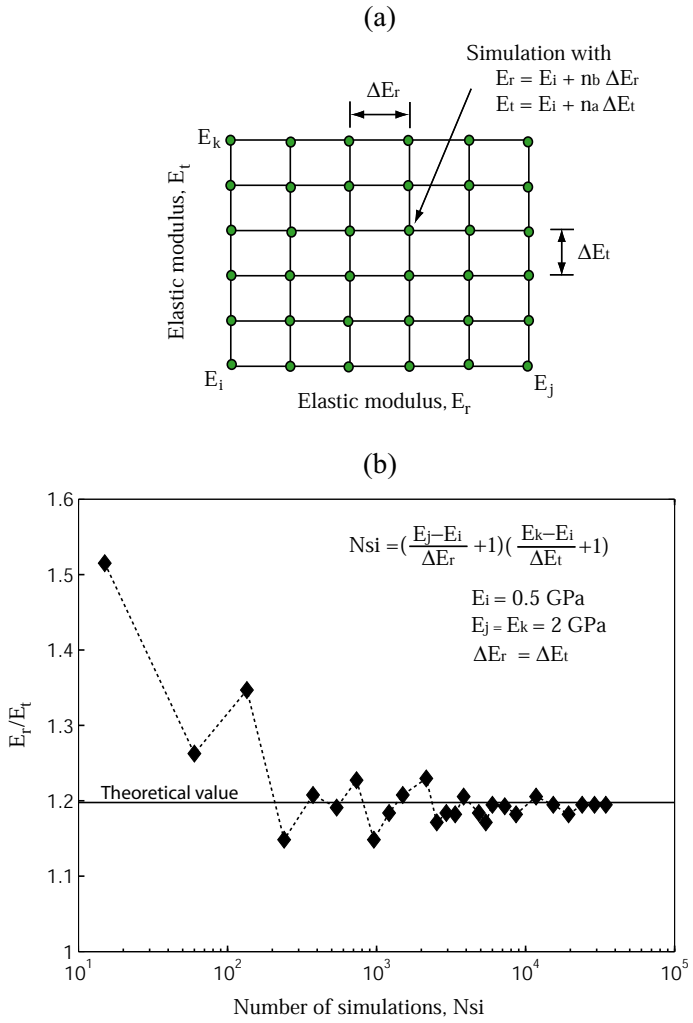

Figure 4.52: Discretization of the region of elastic moduli E_r and E_t (a) and convergence test (b)

4.7.1 P-wave velocity

The mean value and mean value plus/minus one standard deviation of V_p as function of the receiver location angle are presented in Fig. 4.54. The mean value of the velocity V_p (solid line) corresponds to the straight line shown in Fig. 4.47 adjusted with measured values of V_p on new and sound red pine poles.

For the receiver located at $\theta_r = 180°$, 78 measurements of V_p in red pine poles (70 aged and 8 new) are used to adjust the mean value obtained from numerical simulations. For the receivers located at $\theta_r = 135°$ and at $\theta_r = 90°$, the theoretical mean values are adjusted using 16 measurements of V_p on new red pine poles.

The variation of the mean value of the velocity V_p respect the receiver location angle is not linear as in the numerical tests because of several factors: a) wood is not a perfectly homogeneous

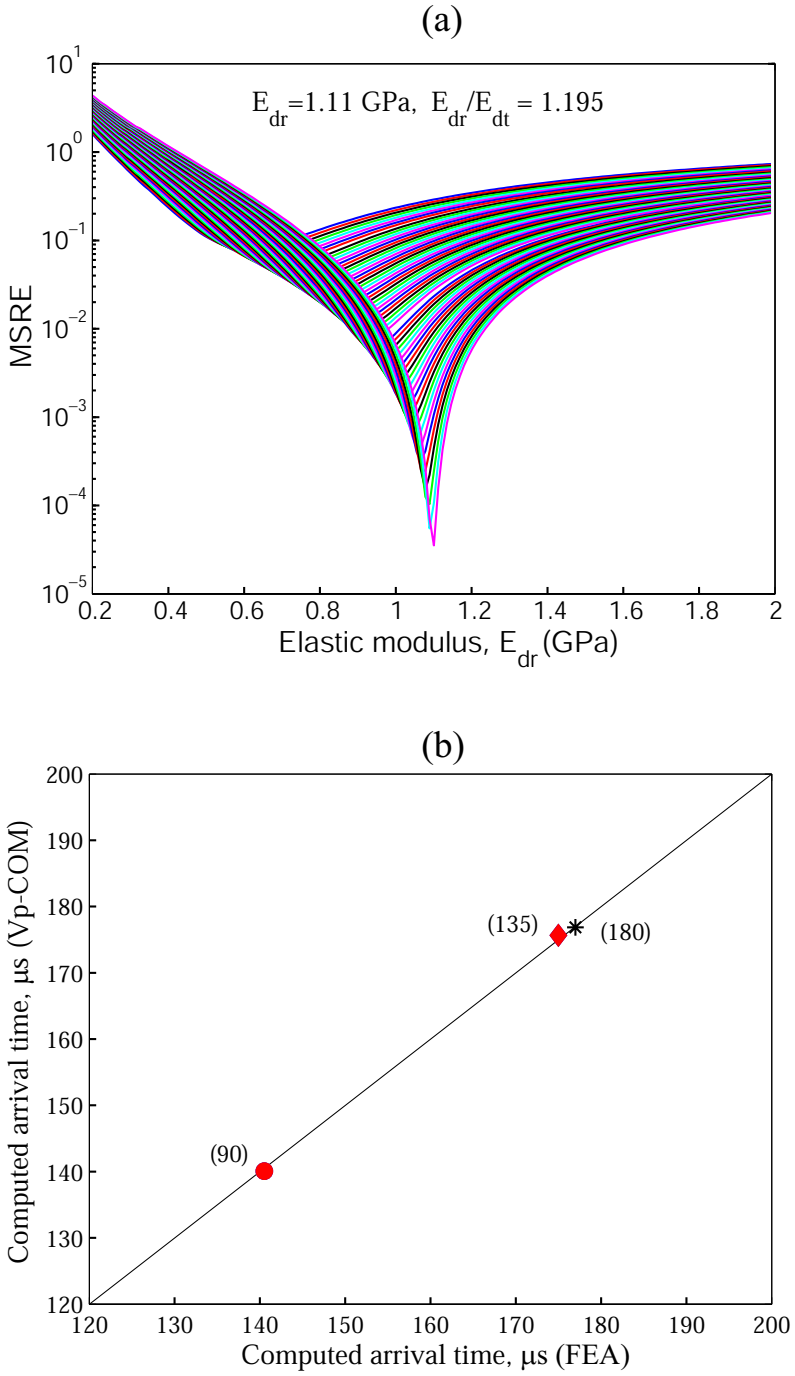

Figure 4.53: Elastic moduli E_{dr} and E_{dt} estimated by solving the inverse problem using the Vp-COM method (a), arrival times computed from finite element analysis and the Vp-COM method (b)

material, b) cross-sections of wood poles are not perfectly circular, and c) the pith is not located exactly at the centre of the section. The mean velocity for the receivers located at $\theta_r = 90°$, $\theta_r = 135°$, and $\theta_r = 180°$ are clearly given in figure. They are 14%, 15%, and 1% larger than the corresponding values from the numerical simulations (Fig. 4.47). The P-wave curve computed for the receivers located at positive angles ($\theta_r = 90°$, $\theta_r = 135°$, and $\theta_r = 180°$) is called "velocity V_p curve-left side". The "velocity V_p curve-right side" is computed for the receivers located at negative angles ($\theta_r = -90°$, $\theta_r = -135°$, and $\theta_r = 180°$).

The condition assessment of a red pine pole is based on the dissimilarity index of velocity (DIV_{θ_r}). The definition of the dissimilarity index is similar to the reliability index used in la literature [9]. The DIV_{θ_r} is given by

$$DIV_{\theta_r} = \frac{(V_p)_{\theta_r} - (\mu_{V_p})_{\theta_r}}{(\sigma_{V_p})_{\theta_r}} \tag{4.33}$$

where $(V_p)_{\theta_r}$ = the velocity V_p measured on a red pine pole for the receiver located at θ_r,
$(\mu_{V_p})_{\theta_r}$ = mean value of the velocity V_p for the receiver located at θ_r (sound red pine poles), and
$(\sigma_{V_p})_{\theta_r}$ = standard deviation of the velocity V_p for sound red pine poles, receiver located at θ_r (sound red pine poles).

The dissimilarity index for a given receiver at an angle θ_r represents the number of standard deviations by which the measured V_p differs from the expected value for a sound pole. This index is useful for condition assessment of wood poles because it considers the statistical variability of the velocity V_p.

4.7.2 Elastic modulus

The elastic modulus of wood is used in the design of wood poles. The elastic modulus is proportional with the square of the velocity V_p; therefore, the elastic modulus is more sensitive than the velocity V_p for detecting deterioration in wood poles. The elastic moduli determined from ultrasonic tests are used to estimate the wood pole response to design loads. Similar to the velocity V_p, the dissimilarity index of the elastic modulus DIE_{θ_r} is defined as

$$DIE_{\theta_r} = \frac{(E_r)_{\theta_r} - (\mu_{E_r})_{\theta_r}}{(\sigma_{E_r})_{\theta_r}} \tag{4.34}$$

where $(E_r)_{\theta_r}$ = elastic modulus for the receiver located at θ_r computed from eqn. (4.30) for the

measured velocity V_p (red pine pole),

$(\mu_{E_r})_{\theta_r}$ = mean value of E_r for the receiver located at θ_r (sound red pine pole), and

$(\sigma_{E_r})_{\theta_r}$ = standard deviation of E_r for the receiver located at θ_r (sound red pine pole).

Figure 4.55 shows the pdf of the elastic modulus E_r normalized by the mean value and the standard deviation. The probability that the elastic modulus in the radial direction for a sound wood pole is smaller or equal than the expected value is $P[(E_r - \mu_{E_r})/\sigma_{E_r} \leq -n]$, where $n = 0, 1, 2, ...$ The probability that E_r is smaller than the expected value minus one standard deviation ($n = 1$) is $P[(E_r - \mu_{E_r})/\sigma_{E_r} \leq -1] = 0.158$. For $n = 2$, $P[(E_r - \mu_{E_r})/\sigma_{E_r} \leq -2] = 0.023$; and $P[(E_r - \mu_{E_r})/\sigma_{E_r} \leq -3] = 0.001$ when $n = 3$.

4.7.3 Transmission factor

The P-wave velocity and the elastic modulus are computed from the first arrival of the compressional wave; whereas, the information contained in the full waveform is ignored. For an integral assessment, the transmission factor between the receiver and the transmitter is introduced as an additional parameter that requires a full waveform analysis. The transmission factor is the reciprocal of the attenuation factor. The transmission factor is computed in frequency domain from the FRF as

$$A_f = \frac{\int_{f_i}^{f_f} (FRF)\, df}{f_f - f_i} \tag{4.35}$$

where f_i and f_f are the selected frequency range for the computation of A_f. Figure 4.56 shows the transmission curves for the receivers located at $\theta_r = 90°$, $\theta_r = 135°$, and $\theta_r = 180°$. The transmission factors are obtained from numerical simulations of wave propagation in cross-sections of red pine poles with diameters between 20 to 50 cm. The numerical results are validated with experimental values. The coefficients of variation for the receivers located at $\theta_r = 90°$, $\theta_r = 135°$, and $\theta_r = 180°$ are 0.47, 0.257, and 0.276, respectively. The expected value plus/minus one standard deviation are also shown in Fig. 4.56. The dissimilarity index of wave transmission is given by

$$DIA_{\theta_r} = \frac{(A_f)_{\theta_r} - (\mu_{A_f})_{\theta_r}}{(\sigma_{A_f})_{\theta_r}} \tag{4.36}$$

where $(A_f)_{\theta_r}$ = measured wave transmission in the frequency range $f_f - f_i$ for the receiver located at θ_r,

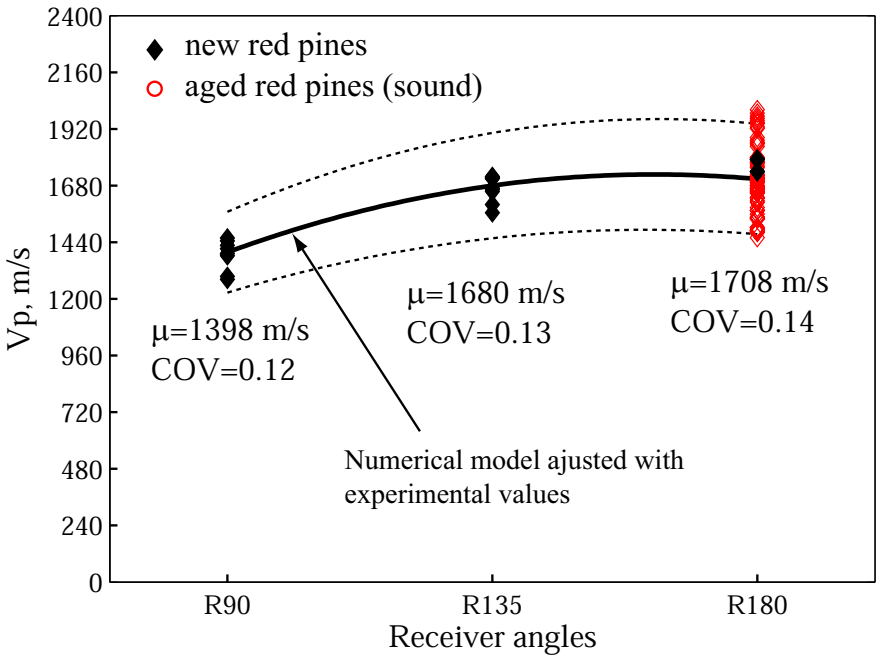

Figure 4.54: Velocity V_p feature (red pine, $MC = 20\%$, $T = 20\ ^{\circ}C$)

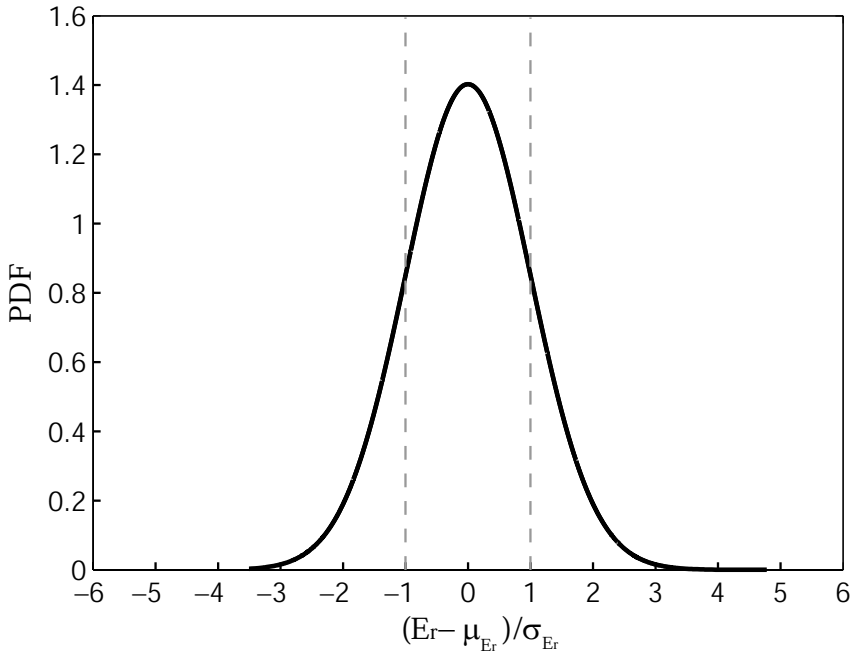

Figure 4.55: Elastic modulus feature (red pine, $MC = 20\%$, $T = 20\ ^{\circ}C$)

$(\mu_{A_f})_{\theta_r}$ = expected wave transmission in the frequency range $f_f - f_i$ for the receiver located at θ_r, and

$(\sigma_{A_f})_{\theta_r}$ = standard deviation of the predicted wave transmission in the frequency range $f_f - f_i$ for the receiver located at θ_r.

4.7.4 Other features

The FRF (frequency domain) and the IRF (time domain) are used to validate the condition assessment of wood poles based on velocities V_p, elastic moduli, and the transmission factors. Typical magnitude spectra for the receivers located at $\theta_r = 90°$, $\theta_r = 135°$, and $\theta_r = 180°$ are presented in Fig. 4.57. The magnitude spectra is computed in the frequency range 30-70 kHz.

Figure 4.58 shows typical IRFs for the receivers located at $\theta_r = \pm 90°$, $\theta_r = \pm 135°$, and $\theta_r = 180°$. The first arrival and the variation of wave transmission with time can be extracted from the IRF. The wave propagation in wood poles can be determined for any arbitrary dynamic excitation from the IRF (in the frequency range 30-70 kHz). This particularity allows the analysis both the transient and the steady state responses.

4.8 Overall dissimilarity index

The overall dissimilarity index (ODI_{θ_r}) for the receiver located at θ_r is defined as

$$ODI_{\theta_r} = DIV_{\theta_r} \cdot W_1 + DIE_{\theta_r} \cdot W_2 + DIA_{\theta_r} \cdot W_3 \tag{4.37}$$

where DIV_{θ_r} = dissimilarity index of the velocity V_p for the receiver located at θ_r,

DIE_{θ_r} = dissimilarity index of elastic modulus for the receiver located at θ_r, and

DIA_{θ_r} = dissimilarity index of transmission factor for the receiver located at θ_r.

The weight factors are function of the coefficients of variation such as $W_1 + W_2 + W_3 = 1$. They are defined as

$$W_1 = \frac{1}{1 + \frac{COV_V}{COV_E} + \frac{COV_V}{COV_A}} \tag{4.38}$$

$$W_2 = \frac{1}{1 + \frac{COV_E}{COV_V} + \frac{COV_E}{COV_A}} \tag{4.39}$$

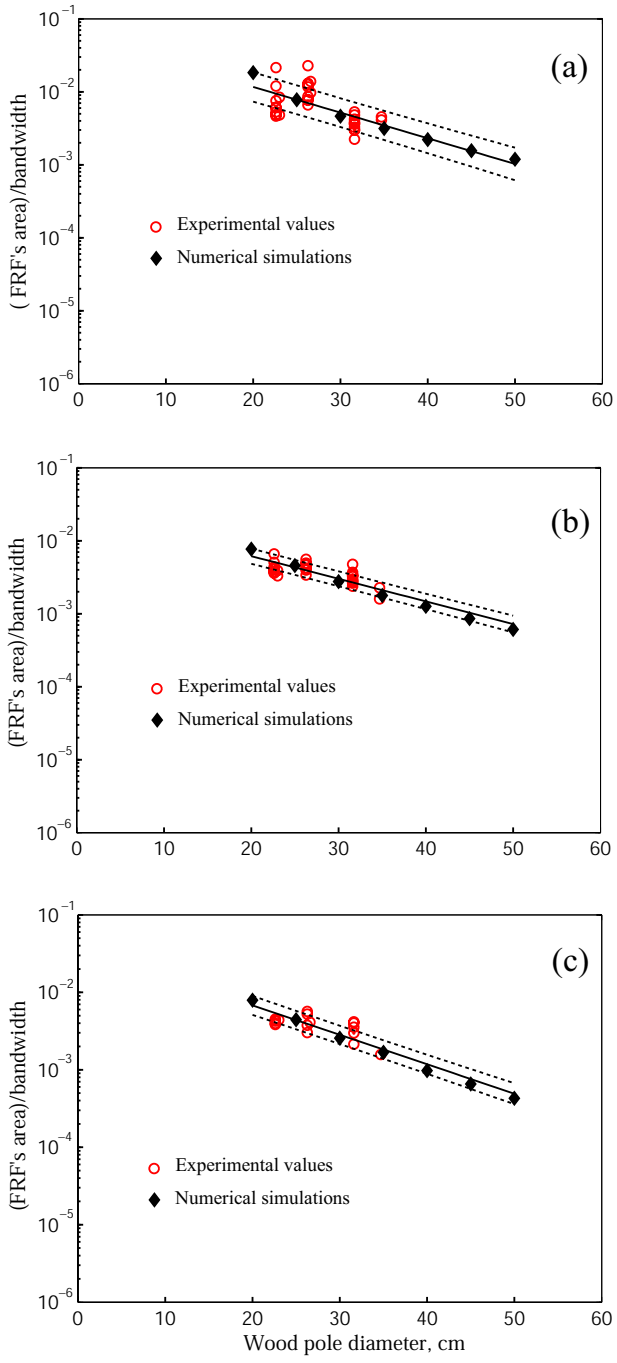

Figure 4.56: Wave transmission feature for the receivers located at $\theta_r = 90°$ (a), $\theta_r = 135°$ (b), and $\theta_r = 180°$ (c)

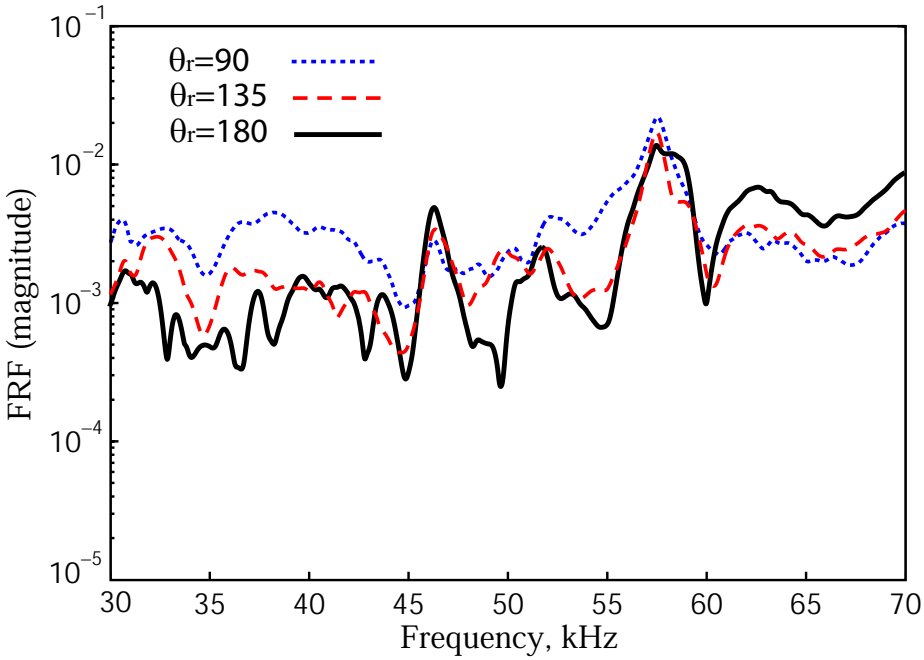

Figure 4.57: FRF magnitude

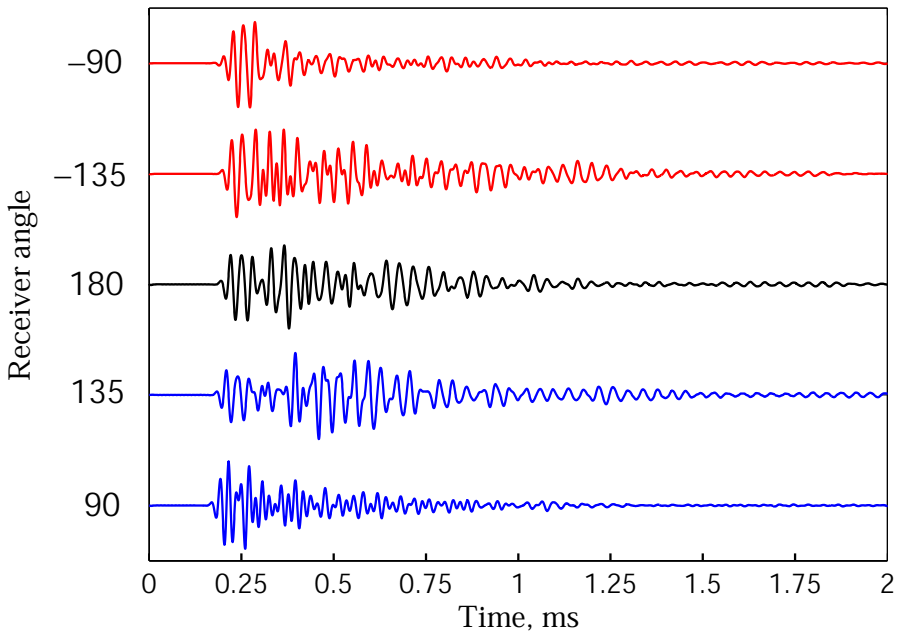

Figure 4.58: Impulse response function feature

$$W_3 = \frac{1}{1 + \frac{COV_A}{COV_V} + \frac{COV_A}{COV_E}} \tag{4.40}$$

where COV_V = coefficient of variation of the velocity V_p,
COV_E = coefficient of variation of the elastic modulus, and
COV_A = coefficient of variation of the transmission factor.

4.9 Chapter Summary

A new methodology for condition assessment of wood poles using ultrasonic testing is presented. The areas of ultrasonic wave propagation in a cylindrical orthotropic medium, specialized signal processing, numerical simulations, statistical analysis, and ultrasonic transducer characterizations are implemented and developed in a methodology to perform an integral evaluation of wood poles.

The UT-Pole device is designed and built specifically for in-situ testing of wood poles. The device is easy to install, versatile (can be used at the groundline), and isolated from the cross-section being analyzed.

WPNDTool-Box is a new software developed for processing and analysis of signals. It is designed in modules and contains all the required functions for pre-processing, processing, and post-processing signals from ultrasonic testing in wood poles. WPNDTool box has more than 10000 lines in Matlab code.

The simplified Vp-COM method developed to study propagation of P-waves in cross-sections of wood poles considering the medium as cylindrical orthotropic under plain strain conditions. The Vp-COM method can be used to determine the probability density function of the velocity V_p modelling the mechanical properties as random variables with practically no limit for the number of simulations. The Vp-COM method can also be used to estimate the elastic moduli in the radial and tangential directions by solving the inverse problem.

Chapter 5

Experimental Setups

5.1 Chapter Overview

Experimental setup is set up the way as an experiment is carried out. Ultrasonic testing of wood pole requires the use of transducers, waveform generator, acquisition system, and coupling conditions; therefore, experimental setups are needed to fully describe the test. On the other hand, experimental setups allow to reproduce the experiment under the same conditions. In this chapter, experimental setups for the calibration of ultrasonic transducers, modal analysis, and ultrasonic testing of wood pole cross-sections are presented.

5.2 Ultrasonic Transducer Calibration

The experimental setup for the evaluation of the FRF and IFR for an ultrasonic transmitter/receiver system is shown in Fig. 5.1.

1. Equipment and materials

    - two 50 kHz ultrasonic transducers (CNSFarnel UTR50kHZ),
    - two aluminum coupling cones,
    - vacuum grease,
    - waveform generator (Physical Acoustic ARB1410),
    - waveform amplifier,
    - waveform acquisition system with 1 MHz sampling rate (WaveBook 516E),
    - UT-Pole device, and

- specialized computer software for analysis and processing of signals (WPNDToolBox).

2. Procedure

- The aluminum cone is glued to the transducers (transmitter and receiver) using the Loctite adhesive 454.
- The transmitter-receiver assembly is made using the UT-Pole device as shown in Figs. 5.1 and 4.30(a). A thin layer of vacuum grease is used as couplant between the transmitter and receiver.
- The transmitter is excited with a sweep sine function $x(t)$ with frequency range 30-70 kHz and constant amplitude (Fig. 5.2(a)). A typical response of the transmitter/receiver system $s(t)$ is shown in Fig. 5.2(b); the resonant frequencies can be observed as peaks defined by the growing and decaying of the signal.
- The FRF for the transmitter/receiver system ($H_{sx}(\omega)$) is computed from

$$H_{sx}(\omega) = \frac{S(\omega)}{X(\omega)} \tag{5.1}$$

  $S(\omega)$ and $X(\omega)$ are the discrete Fourier transform of the excitation $x(t)$ and the response $s(t)$, respectively. $H_{sx}(\omega)$ is given in units of voltage response per voltage excitation (V_{output}/V_{input}).
- The IRF is computed as the inverse discrete Fourier transform of the FRF ($h(t) = ifft(H_{sx})$).
- The dynamic parameters of the system are obtained from the IRF using the CEM. For each vibration mode, the amplitude, resonant frequency, phase angle, and damping ratio are computed.

5.3 Experimental Modal Analysis

The experimental setup for the flexural modal analysis of a wood pole is presented in Fig. 5.3.

1. Equipment and materials

- electromagnetic shaker (ET-126B),
- piezoelectric accelerometer (Dytran 3066A3),

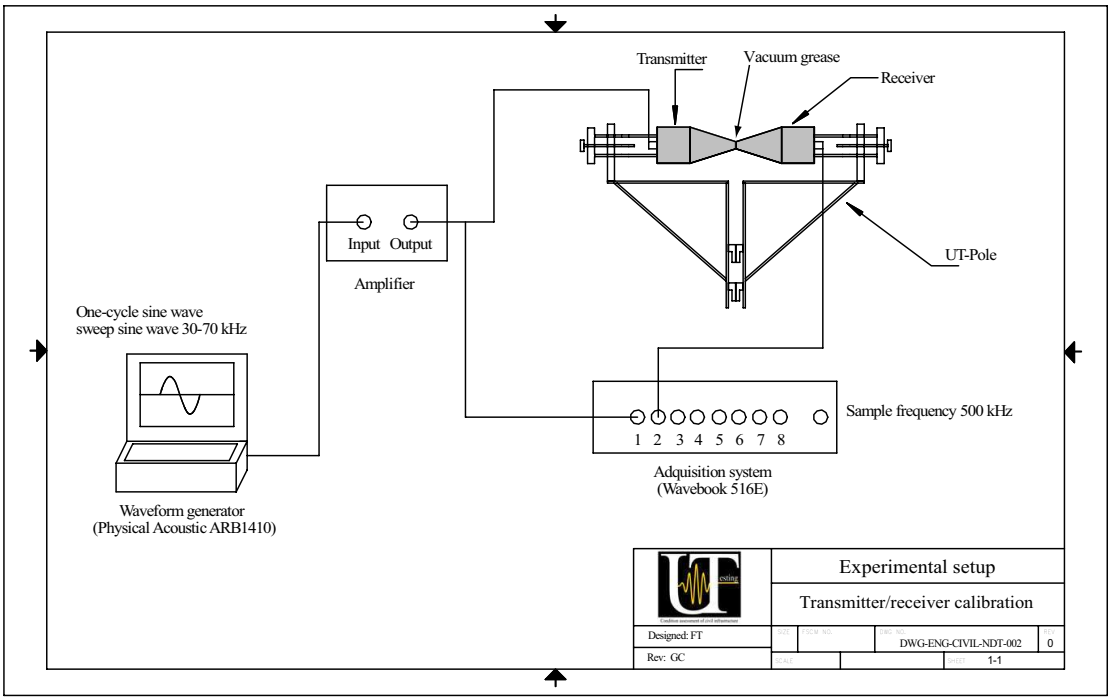

Figure 5.1: Experimental setup for calibration of ultrasonic transducers

- dynamic signal analyzer (HP 35670 A),
- amplifier, and
- simple support system.

2. Procedure

   - The wood pole is sustained at $L/4$ of the ends using the simple support system, being L the length of the pole sample.
   - The accelerometer #2 is set at one end of the pole (point i); and the accelerometer #1, on the shaker (point j).
   - The electro magnetic shaker and the accelerometer are connected to the dynamic signal analyzer as shown in Fig. 5.3. Select the central frequency of the dynamic analyzer to

$$f = \frac{3.6}{L^2}\sqrt{\frac{EI}{\rho A}} \tag{5.2}$$

$L =$ pole length,
$A =$ pole area,
$E =$ estimated elastic modulus in the longitudinal direction,

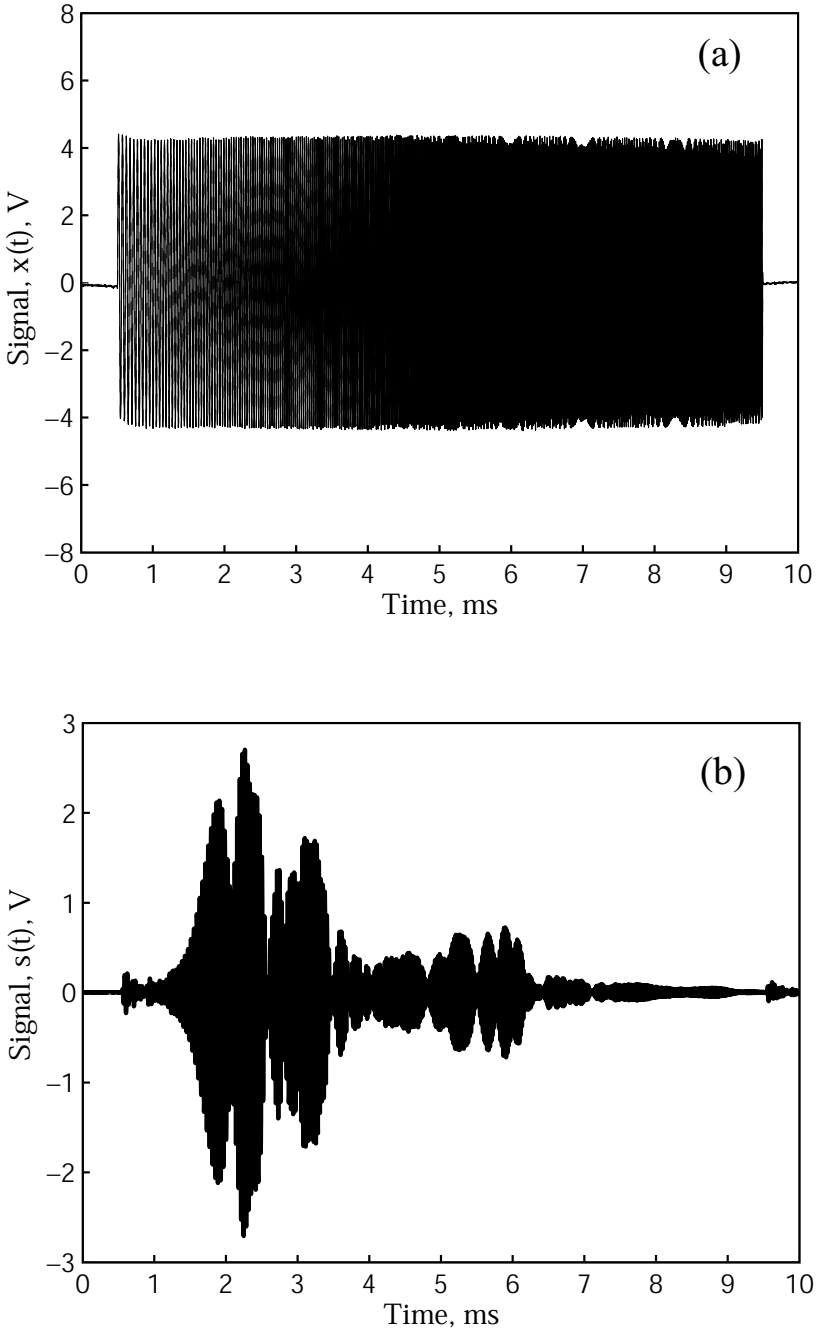

Figure 5.2: Sweep sine excitation (a), transmitter/receiver response to sweep sine excitation (b)

ρ = mass density, and
I = inertia moment.

where f is the fundamental frequency of a free-free beam [90]. The record length have to be long enough to allow the signal decay toward zero.

- The electromagnetic shaker can be placed at $L/2$ or at one end of the pole to excite the fundamental vibration mode in bending.
- A random signal is used as excitation of the electromagnetic shaker.
- The FRF H_{ji} is computed as the Fourier transform of the response (accelerometer #2) divided by the Fourier transform of the excitation (accelerometer #1)
- The FRFs are averaged, the amplitude, resonant frequency and the phase angle are obtained for the main peak.
- The accelerometer #2 is moved 5 cm toward the far end of the pole.
- The same procedure is used to compute the FRF (amplitude, resonant frequency, and phase angle) for this new location.
- Once the length of the pole has been cover, the mode shape for the resonant frequency is drew using the amplitudes and phase angles.
- As verification procedure, the experimental mode shape should correspond with the fundamental flexural vibration mode of a beam with two simple supports, and the nodes have to be close at $L/4$ from the pole ends.
- The shaker is placed on the other end to compute the H_{ij} (frequency response function on j when the shaker is placed on i). For a system is linear, $H_{ij} = H_{ji}$.

5.4 Ultrasonic Testing in Wood Pole Cross-sections

The nomenclature used for ultrasonic testing in a cross-section of wood poles is shown in Fig. 5.4. A global reference system is defined for the transmitter and receiver locations. The reference system is defined by the cardinal points A, B, C, and D corresponding to the northern, western, eastern, and southern directions, respectively. In this way, the transmitter position is defined by an azimuth measured counterclockwise from the cardinal point A. Once the transmitter position is set, five receivers are defined for the receivers located at $\theta_r = \pm 90°$, $\theta_r = \pm 135°$, and $\theta_r = 180°$. The receiver location angle (θ_r) is the angle between the transmitter and the receiver. The receiver location angle is positive in the counterclockwise direction. The experimental setup for ultrasonic testing in a cross-section of wood poles using two ultrasonic transducers (transmitter and receiver) is presented in Fig. 5.5.

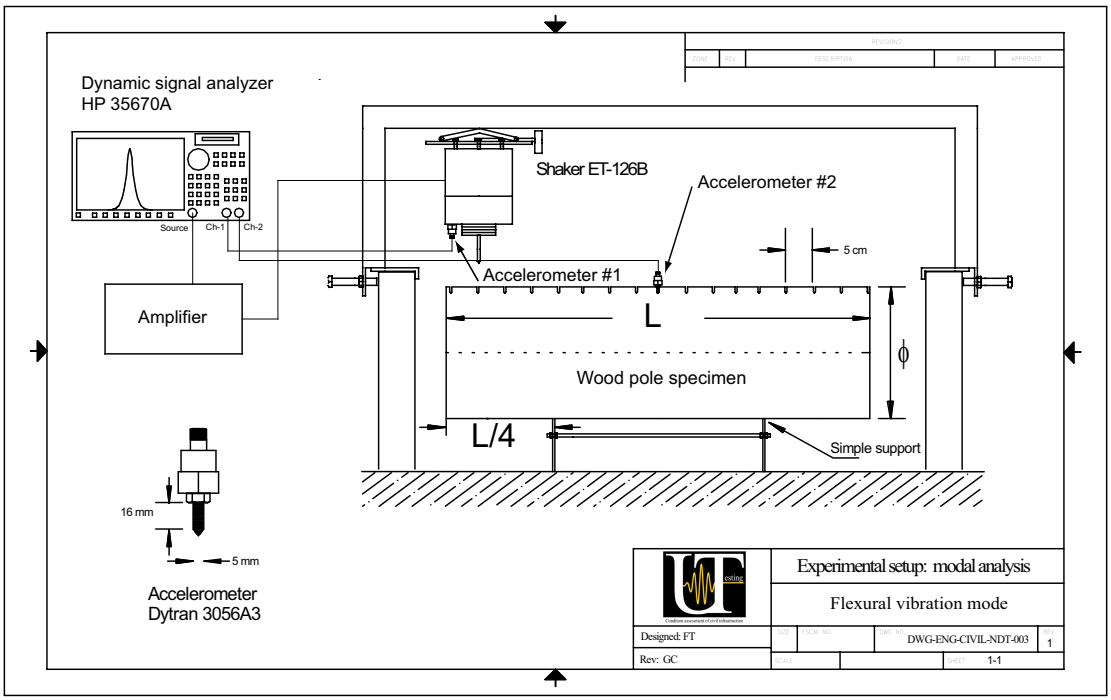

Figure 5.3: Experimental setup for flexural modal analysis

1. Equipment and materials

   - two 50 kHz ultrasonic transducers (CNSFarnel UTR50kHZ),
   - two aluminum coupling cones,
   - vacuum grease,
   - waveform generator (Physical Acoustic ARB1410),
   - waveform amplifier,
   - waveform acquisition system with 1 MHz sampling rate (WaveBook 516E),
   - UT-Pole device, and
   - specialized computer software for analysis and processing of signals (WPNDTool-Box).

2. Procedure

   - The positions of the transmitter (source) and the receiver are defined on the pole. The receivers are set at $\theta_r = \pm 90^\circ$, $\theta_r = \pm 135^\circ$, and $\theta_r = 180^\circ$ respect to the source position.
   - The transmitter and receiver are fixed to the wood pole using the UT-Pole device. The couplant between the transducers and the pole is a thin layer of vacuum grease.

- The receiver is connected to channel #2 of the acquisition system; and the transmitter to the amplifier output. The amplifier input is connected to channel #1 of the acquisition system, whereas the input of the amplifier is connected to the waveform generator.
- The transmitter is excited with a sweep sine wave using the waveform generator with the following parameters: frequency range 30-70 kHz, amplitude of 10 V, length record 12 ms.
- Ten waveforms are recorded. Then, the transmitter and receiver cables are interchanged and ten waveforms are recorder in the inverse direction.
- The waveform generator is set for a one-cycle sine wave of 50 kHz with an amplitude of 10 V.
- Ten waveforms are then recorded, the transducer cables are again interchanged and recorder ten more waveforms.
- The receiver is changed to a new receiver location angle and the procedure is repeated.
- Finally, the recorded data is processed and analyzed using WPNDTool-Box.

This procedure can be easily extended for an array of eight transducers for four positions of the transmitter, but only six transducers are used for each transmitter location (one for the transmitter and five for the receivers).

5.5 Chapter Summary

Experimental setups for the calibration of ultrasonic transducers, modal analysis, and ultrasonic testing of wood pole cross-sections are presented. These experimental setups allow to perform ultrasonic tests in wood pole cross-sections and modal analysis for the characterization of the flexural vibration mode of a wood poles sample (resonant frequency and damping ratio).

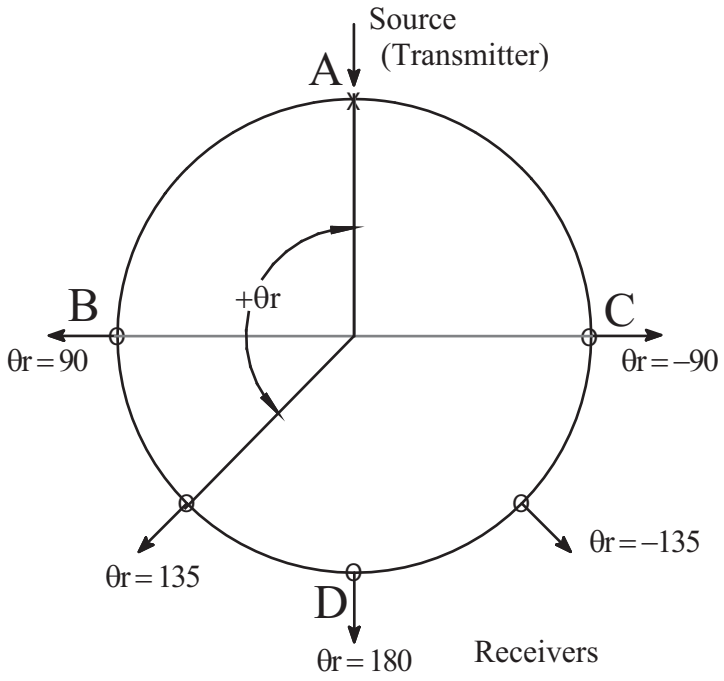

Figure 5.4: Nomenclature used for ultrasonic testing in a cross-section of wood poles

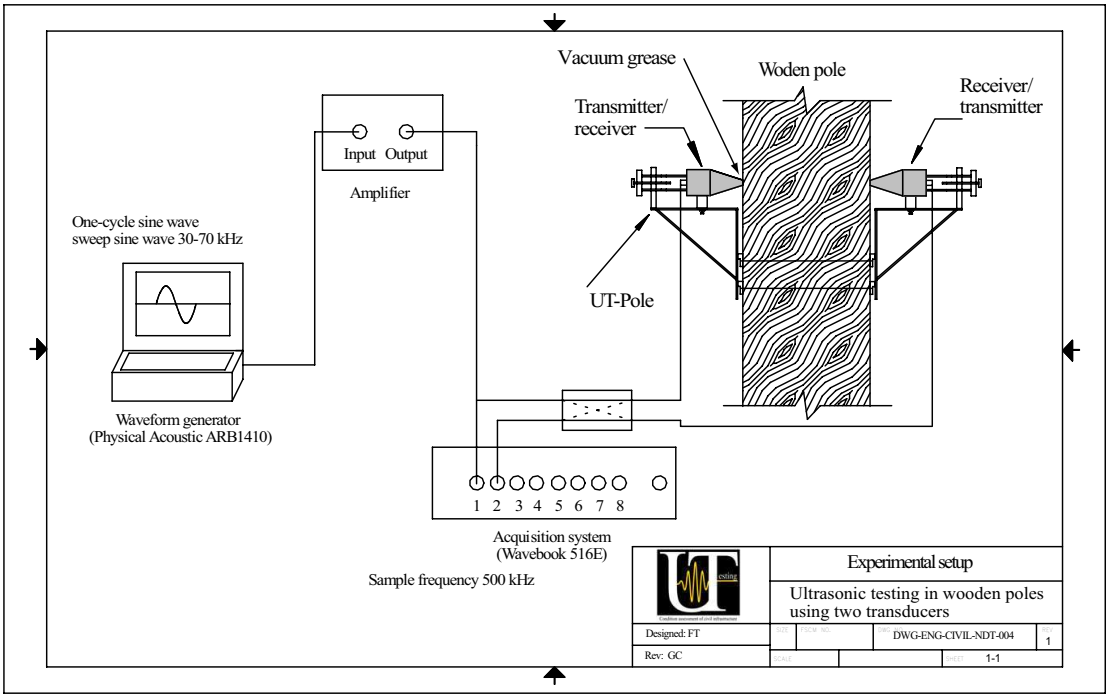

Figure 5.5: Experimental setup for ultrasonic testing in a cross-section of wood poles

Chapter 6

Numerical Simulation Results

6.1 Chapter Overview

Numerical results of ultrasonic wave propagations in cross-sections of red pine poles are presented in this chapter. The cross-section is modeled by finite elements under plain strain conditions considering the wood as an orthotropic material. The dynamic excitation used for the numerical simulations is the measured displacement response of an ultrasonic transmitter of 50 kHz. A Rayleigh damping model, adjusted with measured values of damping ratio, is used to characterize the wood attenuation. The elastic moduli in the longitudinal (E_l), radial (E_r), and tangential (E_t) directions are determined from experimental tests: E_l, from experimental modal analysis; whereas E_r and E_t, from ultrasonic tests (Vp-COM method in Section 4.6). A convergence test for the arrival time is performed to determine the optimum finite element size, which is confirmed with the FK plot. Once the elastic and mechanical properties have been defined, the numerical model is validated using experimental results of ultrasonic testing in a red pine pole. Finally, results of condition assessment in the cross-section of a new red pine pole with and without a centric hole, and a decayed red pine pole are presented.

6.2 Finite Element Characteristics and Model Calibration

6.2.1 Plain strain conditions

Numerical simulations by finite elements are performed to validate the hypothesis of plain strain conditions for ultrasonic wave propagation in cross-sections of wood poles. The numerical model represents a section in the longitudinal-radial plane. The selected elastic and mechanical properties correspond to Douglas-fir specie in air-dry condition (Tables 3.1, 3.2, 3.3, and 3.4). The ratio

between the elastic moduli in the longitudinal and radial directions is $E_l/E_r = 14.7$. Figure 6.1(a) shows the numerical model of an ultrasonic testing in the longitudinal-radial plane. The displacement field at $t = 100\ \mu s$ is presented in Fig. 6.1(b). The wavefront is polarized in the radial direction because of the high anisotropy ratio of the material. The strain in the longitudinal direction is an order of magnitude smaller than the strain in the radial direction. Hence, plain strain conditions can be assumed to study ultrasonic wave propagation in a cross-section of wood poles.

6.2.2 Homogeneous material assumption

Wave propagation in wood is controlled by the properties and orientation of the fiber as well as the geometry of the element [91]. In addition, wood is an orthotropic material with imperfections in its structure, which make the simulations of wave propagation a complex task. In this work, the wood is considered homogeneous. This hypotheses and the assumption of plain strain conditions have been previously used for wave propagation in cross-sections of wood poles [84].

Ultrasonic transducers with a nominal frequency of 50 kHz are commonly used in ultrasonic tests of wood poles. The wavelength of compressional waves corresponding with this frequency and for a typical velocity of $V_p = 1500$ m/s is $\lambda = 3$ cm. This wavelength is at less an order of magnitude greater than the macroscopical elements present in the wood structure (including radial and circumferential cracks, and rings produced by seasonal growing of wood). In consequence, the hypothesis of homogeneous material is considered acceptable for this work.

6.2.3 Finite element characteristics

Four nodes finite elements with two degrees of freedom per node (translations in x and y directions) are used. The time sampling rate is $\Delta t = 1\mu s$, which represents 20 points per cycle at the frequency of 50 kHz. The finite element size is determined from a convergence test for an isotropic material. Figure 6.2 shows the convergence for the P-wave arrival time at $\theta_r = 180^\circ$ for different element sizes. The solution converges to the closed form solution from elasticity theory; the selected element size is $h = 0.4$ cm.

Once the finite element size is selected, numerical simulations of wave propagation in a cross-section of a wood pole are carried out to evaluate the propagation of P-waves. The numerical model represents a circular section of 30 cm diameter. The material is isotropic with $\rho = 460$ kg/m^3, $E = 1.09$ GPa, and $\nu = 0$. The excitation pulse is a one-cycle sinusoidal displacement of 50 kHz applied in the vertical direction at the top of the cross-section. The P-wave velocity is computed from $V_p = \sqrt{E/\rho}$, $V_p = 1539.6$ m/s. Figure 6.3 shows the time history and frequency-wavenumber (FK) plots for the displacements along the radial direction from the source to the centre of the section. The group velocity from Fig. 6.3(a) is equal to $V_g = 1581$ m/s. The P-wave

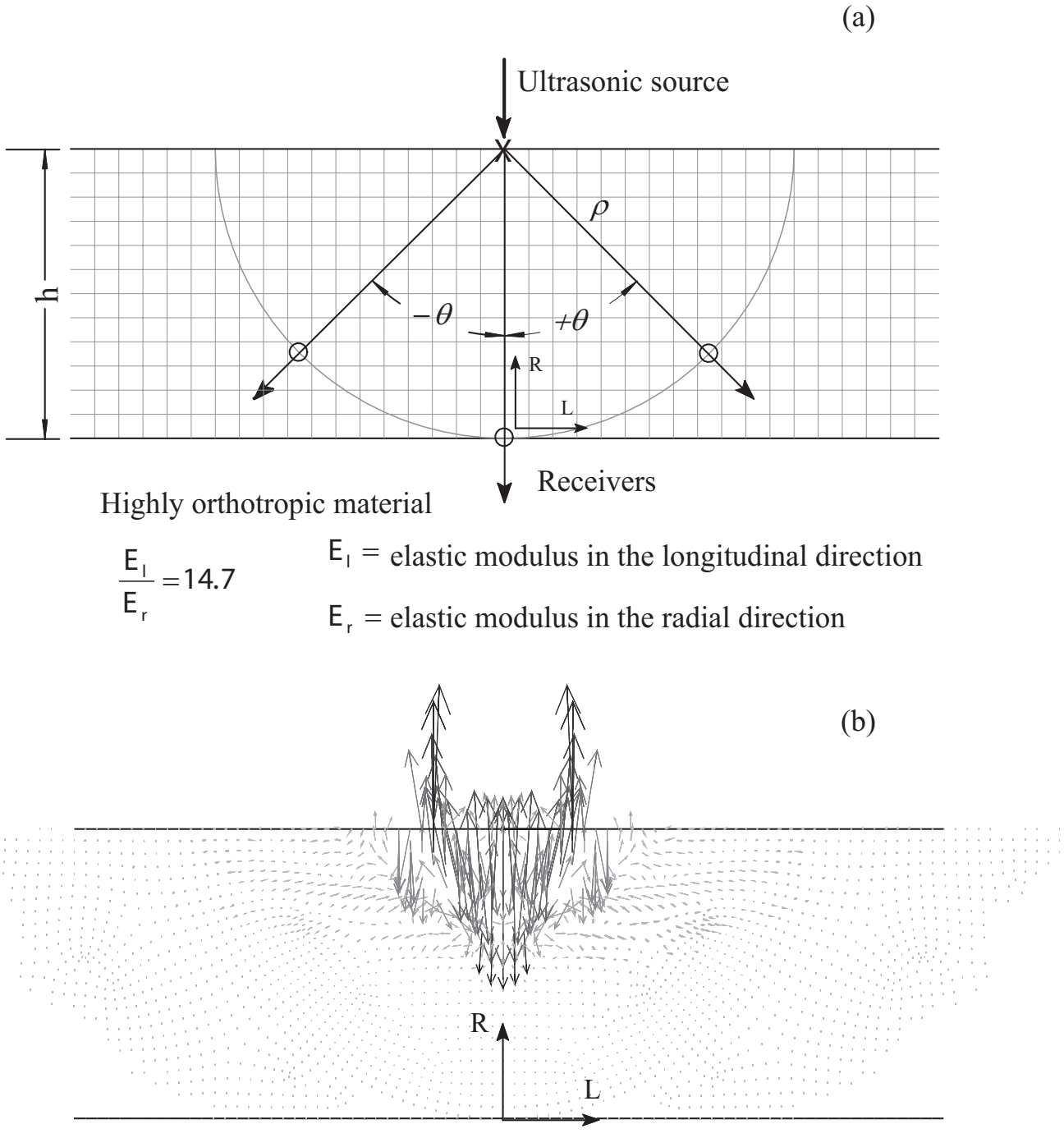

Figure 6.1: Ultrasonic wave propagation in the longitudinal-radial plane for an impulse source applied in the radial direction: (a) numerical model, (b) wave propagation at 100 μs

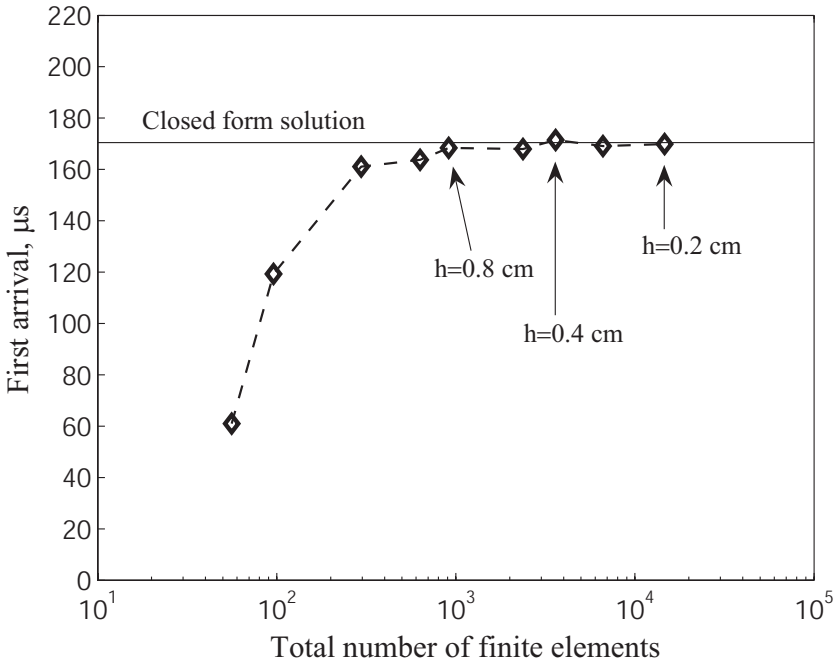

Figure 6.2: Convergence test for the first arrival of the compressional wave (velocity V_p)

energy is clearly observed in Fig. 6.3(b) for frequencies from 10 to 74 kHz with $V_p = 1540$ m/s. The corresponding wavelengths ($k = 2\pi\lambda$, λ =wavelength) are between 2.0 cm ($f = 74$ kHz) and 15.4 cm ($f = 10$ kHz). The element size $h = 0.4$ is therefore small enough to represent more than five points per wavelength, thus to study wave propagation in wood poles with an ultrasonic transmitter of nominal frequency $f_0 = 50$ kHz.

6.2.4 Damping ratio

The damping matrix is assumed to be proportional to a combination of the mass and the stiffness matrices ($[C] = \alpha[M] + \beta[K]$); which is known as Rayleigh damping. The CEM is used to measure damping ratios from ultrasonic tests preformed on a sound red pine. Damping ratios of 3.8, 3.3, and 2.6% are obtained for frequencies of 45.9, 52.4, and 55.9 kHz, respectively. These damping ratios are used to evaluate the parameters α and β such that the mean square error between the measured and curve-fitted damping values is minimum. Figure 6.4 shows the Rayleigh damping model in the frequency range from 20 to 60 kHz as well as the measured values. The damping curve mainly follows a mass-proportional damping because the damping is inversely proportional to frequency.

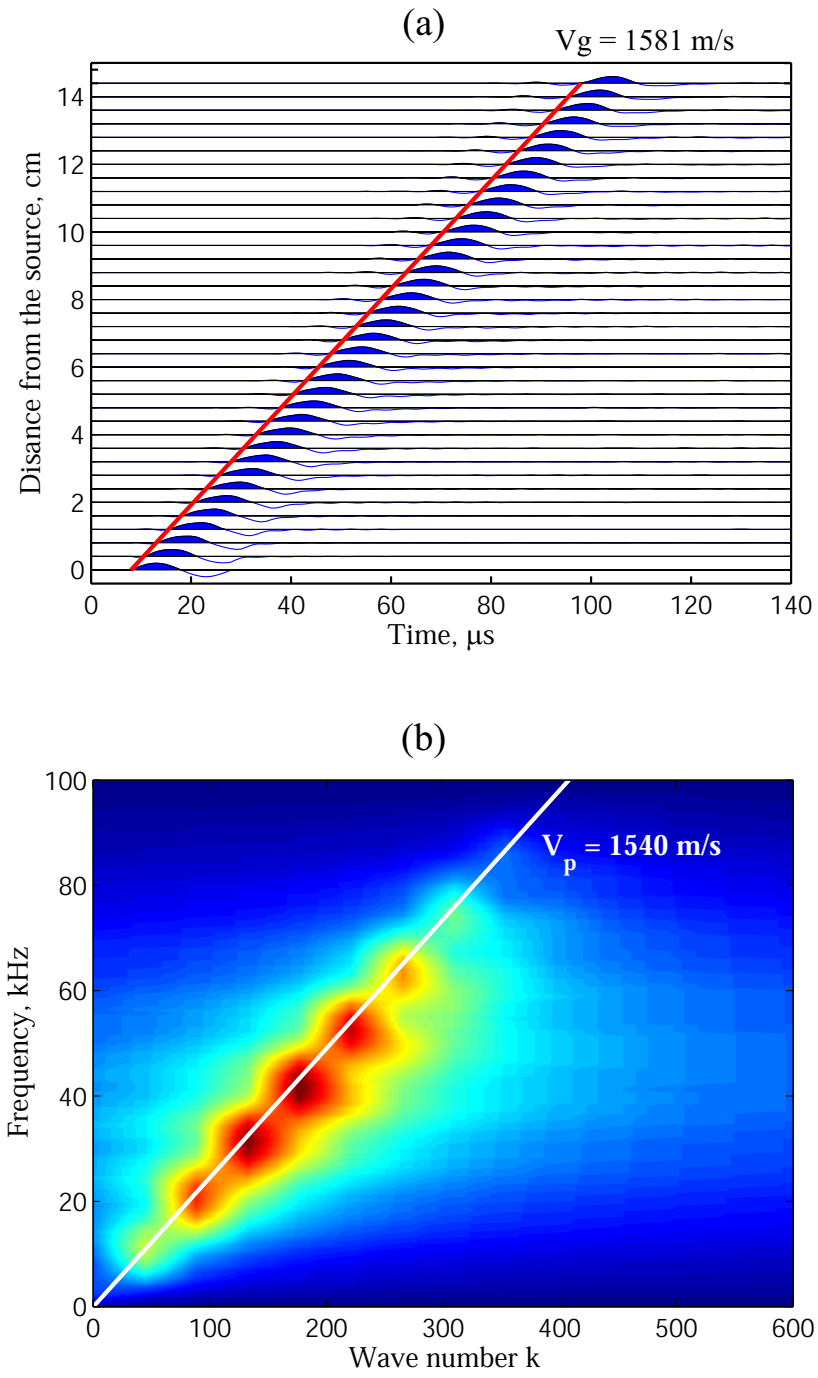

Figure 6.3: Displacement time histories (a) and the FK plot (b) in the radial direction

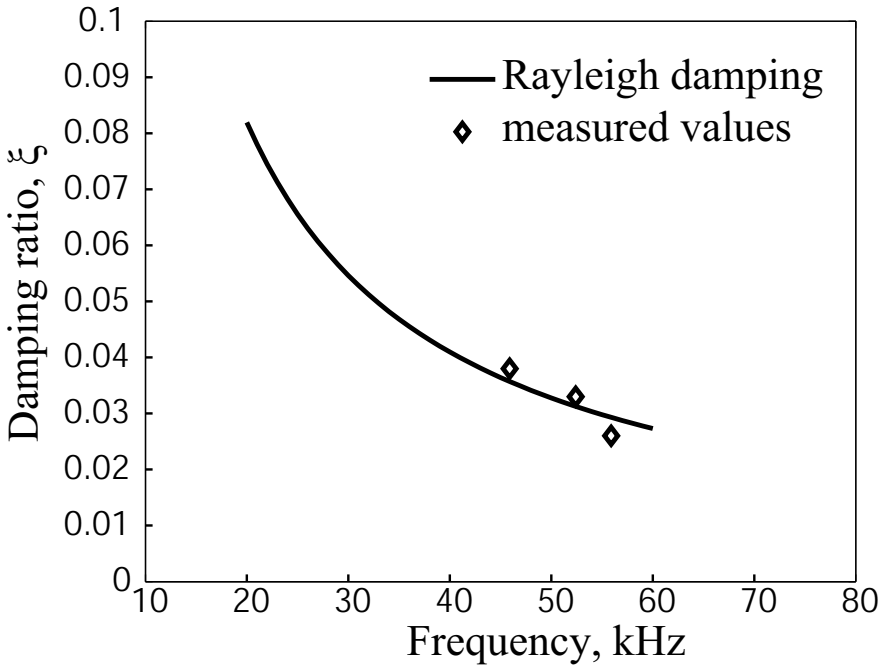

Figure 6.4: Rayleigh damping model

6.2.5 Poisson's ratio

Figure 6.5(a) shows measured time histories on the surface of a pine pole cross-section; and in Fig. 6.5(b), the corresponding surface wave phase velocity. The measured P-wave and surface wave velocities are $V_p = 1897$ m/s and $V_r = 360$ m/s, respectively. The higher velocity in the dispersion curve (Fig. 6.5(b)) is likely associated with higher propagation modes. Poisson's ratio of $\nu = 0.48$ is obtained from the values of V_p and V_r assuming an isotropic model [86]. This value is similar to the Poisson's ratios shown in Table 3.4 for pine species in the radial-tangential plane (maximum difference of 18%). A value of $\mu_{rt} = 0.408$ corresponding to red pine is therefore used for numerical simulations of ultrasonic wave propagation in pole cross-sections.

6.2.6 Elastic modulus

Once the damping model and Poisson's ratio are defined, the next step is to define the elastic moduli in the longitudinal, radial, and tangential directions.

Experimental modal analysis is performed to determine the resonant frequency of the fundamental vibration mode in bending of a specimen. Figure 6.6 shows the experimental setup for modal analysis of a wood pole specimen. The pole specimen is red pine with a diameter of $\phi = 27.1$ cm and length of $L = 85.8$ cm. The pole is simple supported at $L/4$ from the ends. An electromagnetic shaker with flat response up to 10 kHz is used to apply a random excitation in

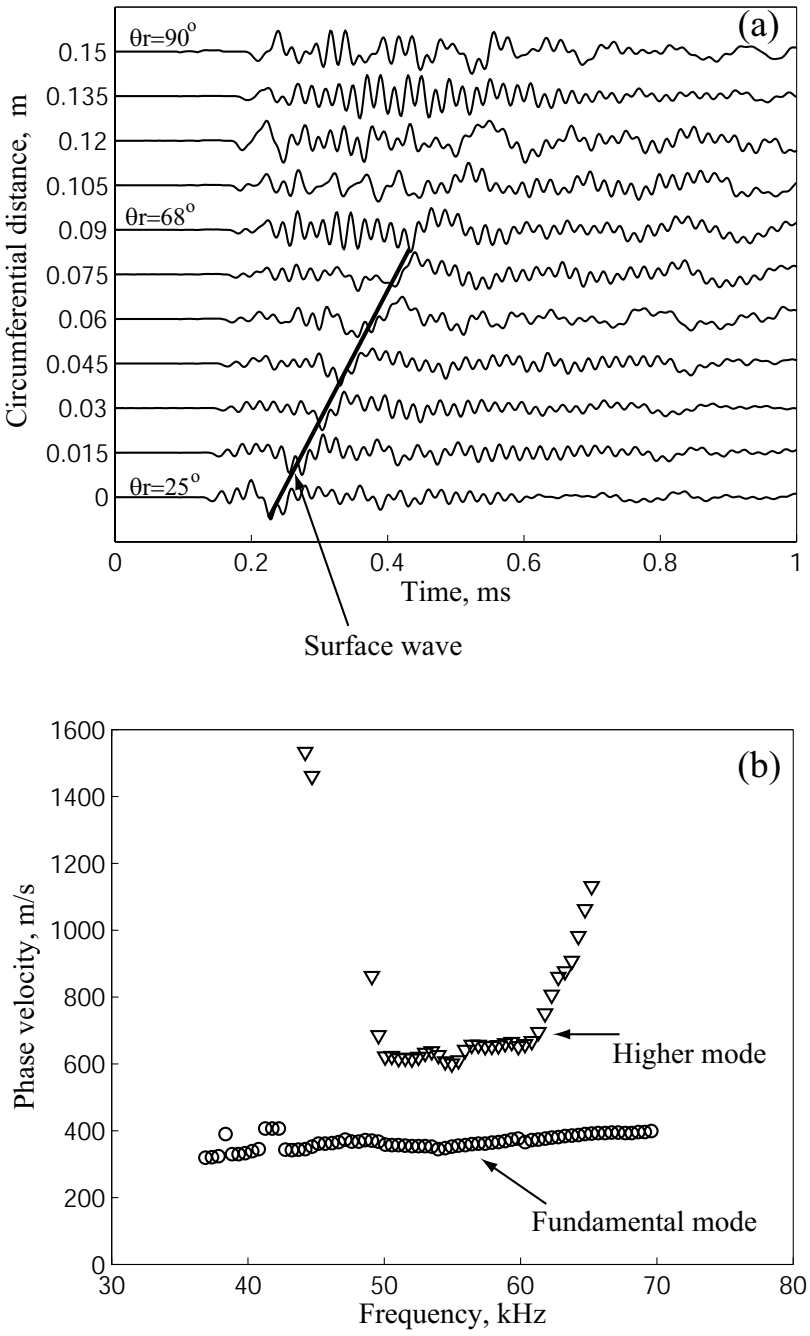

Figure 6.5: Acceleration time histories (a) and surface phase velocity (b) measured in a sound pine pole using ultrasonic testing

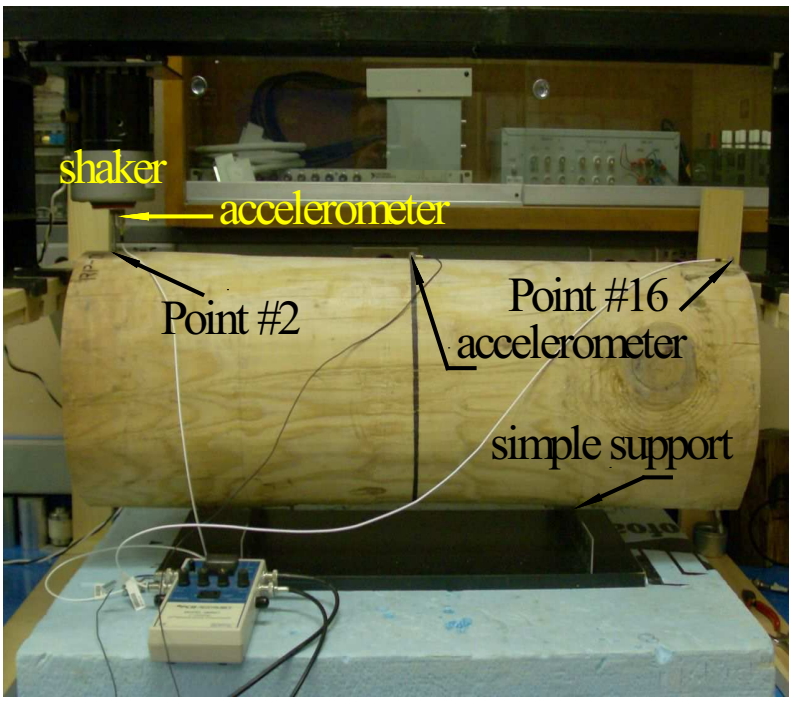

Figure 6.6: Experimental modal analysis for the fundamental vibration mode in bending

the vertical direction. The shaker is located at the left end of the pole (point #1). Two piezoelectric accelerometers are used to measured the excitation and the response on 16 points spaced 5 cm along the pole length.

Figure 6.7(a) shows typical frequency response functions (H_{1-16} and H_{16-1}). The frequency response function H_{1-16} corresponds to the response at point #16 when the shaker is located at the point #1. Similarly, H_{16-1} represents the response measured on point #1 when the shaker is located at point #16. The response of the wood pole is linear because $H_{1-16} = H_{16-1}$.

A resonant frequency of $f = 819.6$ Hz is clearly observed from the FRF (Fig. 6.7(a)). A damping ratio of 1% is determined by the band-width method. The mode shape corresponding to this resonant frequency is presented in Fig. 6.7(b). It is obtained from the magnitude and phase angle information at the resonant frequency measured at different positions along the pole length. The measured fundamental mode in bending is almost symmetrical with nodes located approximately at $L/4$ from the ends as predicted by the theoretical solution for an elastic material.

The elastic moduli E_r and E_t are estimated from ultrasonic testing in the cross-section of a wood pole by using the Vp-COM method (Section 4.6). The elastic moduli in the radial and tangential directions are $E_r = 1.09$ GPa and $E_t = 0.91$ GPa, respectively.

A 3D cylindrical orthotropic model by finite elements of the wood pole is performed to determine the elastic modulus in the longitudinal direction E_l. This modulus (E_l) is selected such that the fundamental resonant frequency in bending is the same to the experimental value.

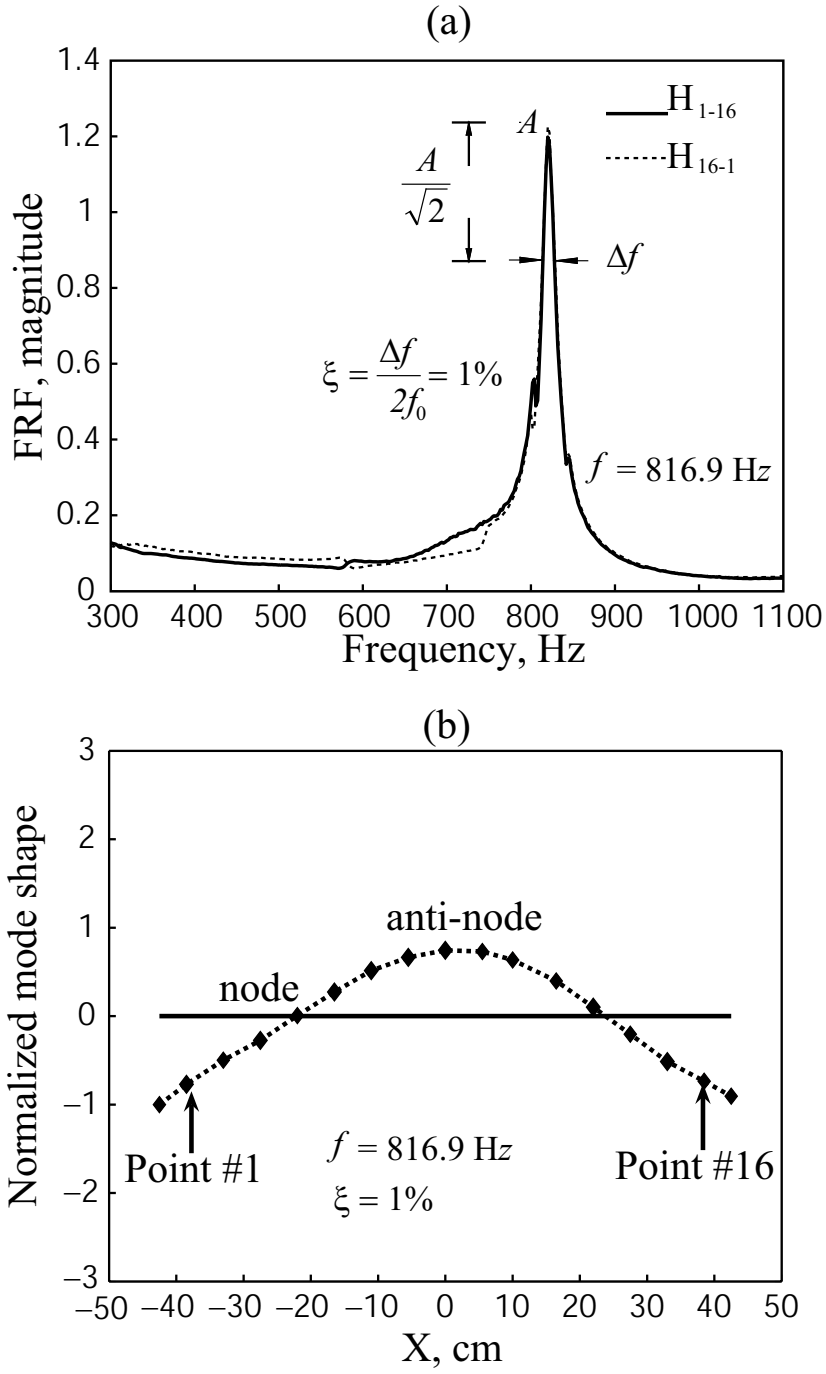

Figure 6.7: Frequency response function (a) and the fundamental vibration mode in bending (b)

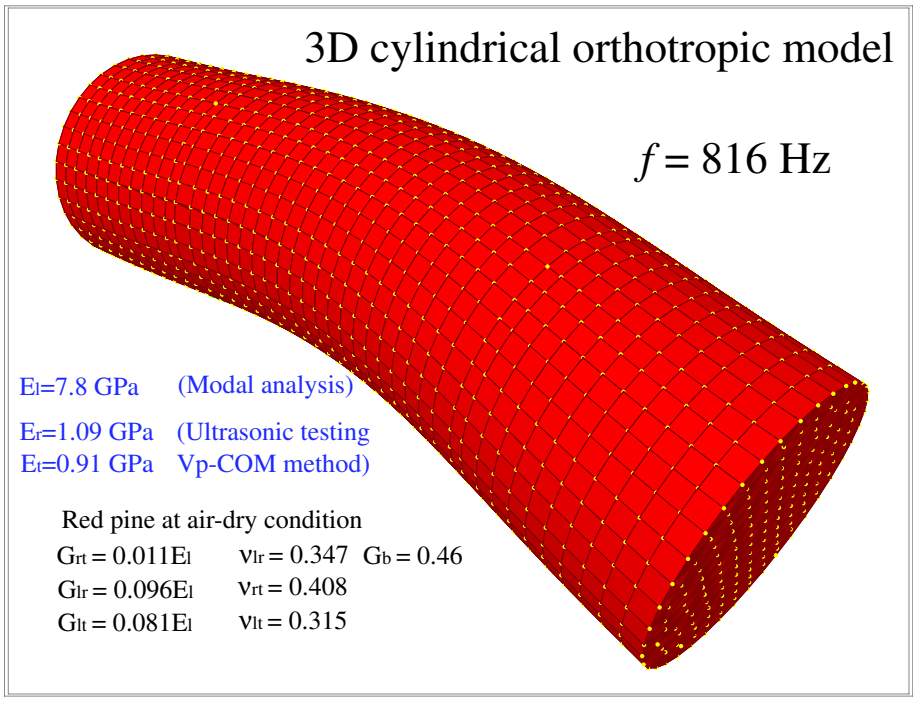

Figure 6.8: 3D cylindrical orthotropic model of a rep pine pole

Figure 6.8 shows the flexural vibration mode obtained from the 3D model. The elastic modulus in the longitudinal direction is $E_l = 7.8GPa$.

The mean value of elastic modulus suggested in the literature for red pine is 9.45 GPa with a coefficient of variation $COV = 0.22$ (Table 3.2). The elastic modulus estimated is equal to the mean value minus 0.8σ ($\sigma = 2.1$ GPa).

6.2.7 Ultrasonic source

The measured displacement response of an ultrasonic transmitter subjected to a one-cycle sinusoidal wave of 50 kHz is used as excitation for the numerical simulations. The response of the transmitter is measured using a piezoelectric accelerometer with flat response up to 70 kHz (0.94 dB of deviation at 60 kHz). The acceleration time history is integrated to obtain the velocity and displacement time histories as shown in Fig. 6.9.

6.2.8 Numerical model validation

The same nomenclature used for ultrasonic testing (Chapter 5) is used in the numerical simulations. The receivers located at $\theta_r = \pm 90$, $\theta_r = \pm 135$, and $\theta_r = 180$ correspond to the positions respect the source in the cross-section where the dynamic responses are computed.

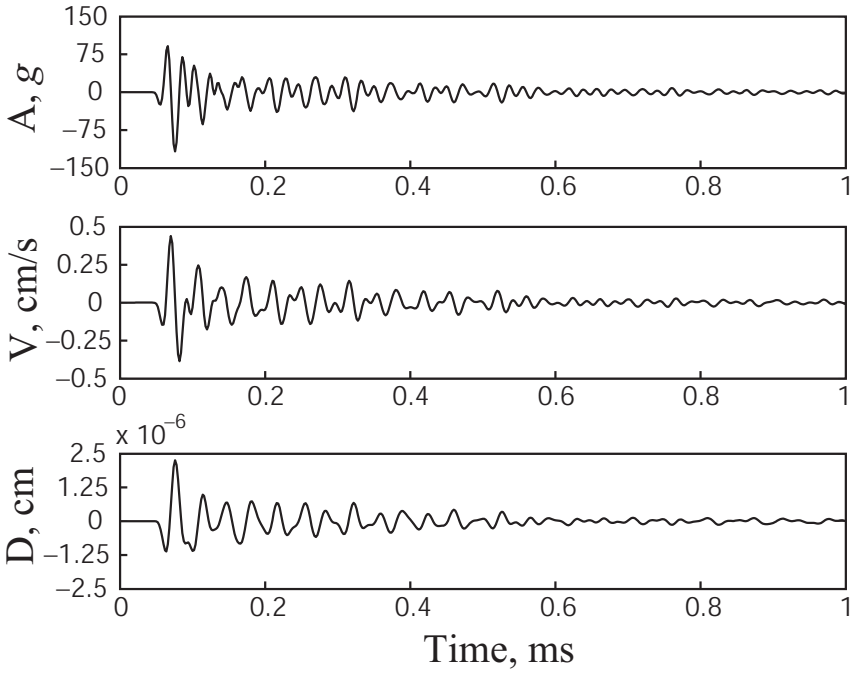

Figure 6.9: Dynamic excitation given as acceleration, velocity, and displacement time histories

The numerical model of a cross-section of the red pine pole RP-01 is illustrated in Fig. 6.10. The source is located at the top of the section and applied in vertical direction. The acceleration time histories are computed for the receivers located at $\theta_r = 90°$, $\theta_r = 135°$, and $\theta_r = 180°$. The diameter of the pole is 26.6 cm and the simulation is performed for a temperature of 20 $°C$ and moisture content of 12%.

Figure 6.11(a) shows the measured and computed velocities V_p for the receivers located at $\theta_r = 90°$, $\theta_r = 135°$, and $\theta_r = 180°$. The computed velocities V_p are obtained from the finite element (FEA) and the Vp-COM method results. The maximum difference between the computed (FEA) and the measured velocities V_p is 6%. The computed V_p values using FEA and the Vp-COM method show a maximum difference of 2%.

The measured and computed FRFs (20-60 kHz) are presented in Fig. 6.11(b). In general, the FRF computed from FEA shows the correct frequency content. The ratio of the FRF area (computed/measured) is 0.98. The calibrated numerical model can be used not only for determining velocities V_p but also for performing full-waveform analysis of wave propagation in a cross-section of wood poles.

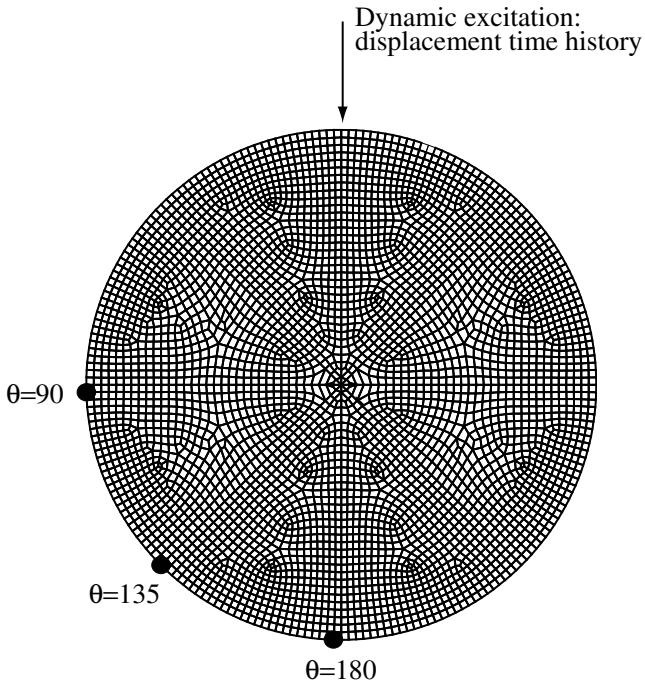

Figure 6.10: Numerical model of a cross-section of the red pine pole RP-01 ($\phi = 26.6$ cm, $MC = 12\%$, $T = 20\ ^{\circ}C$)

6.3 Numerical Results

Numerical results of condition assessment for cross-sections of new and decayed red pine poles are presented in this section. The cross-section for the new red pine pole is analyzed without and with a centric hole.

6.3.1 New red pine pole

The condition assessment for the cross-section of a simulated new red pine pole is presented in Figs. 6.12 and 6.13. The condition assessment is based on the P-wave velocity curve, the elastic moduli E_r and E_t, and the impulse response and frequency response functions. The pole has a diameter of 30 cm. The elastic moduli in the longitudinal, radial and tangential directions are 7.8, 1.09 and 0.91 GPa, respectively. The Poisson's ratios and mass density correspond to the red pine specie in air-dry condition (Tables 3.1 and 3.4). The source is located at the cardinal point A; and the receivers, at $\theta_r = 90^{\circ}$, $\theta_r = 135^{\circ}$, and $\theta_r = 180^{\circ}$. The response for the receiver located at $\theta_r = -90^{\circ}$ is the same that the response for the receiver located at $\theta_r = 90^{\circ}$ by symmetry. Likewise, the same response is obtained for the receivers located at $\theta_r = \pm 135^{\circ}$.

The P-wave velocity curve (Fig. 6.12(c)) is linear with respect to the receiver location angle with $V_{p(\theta_r=180)} > V_{p(\theta_r=135)} > V_{p(\theta_r=90)}$. In this plot, representative curves for the mean value

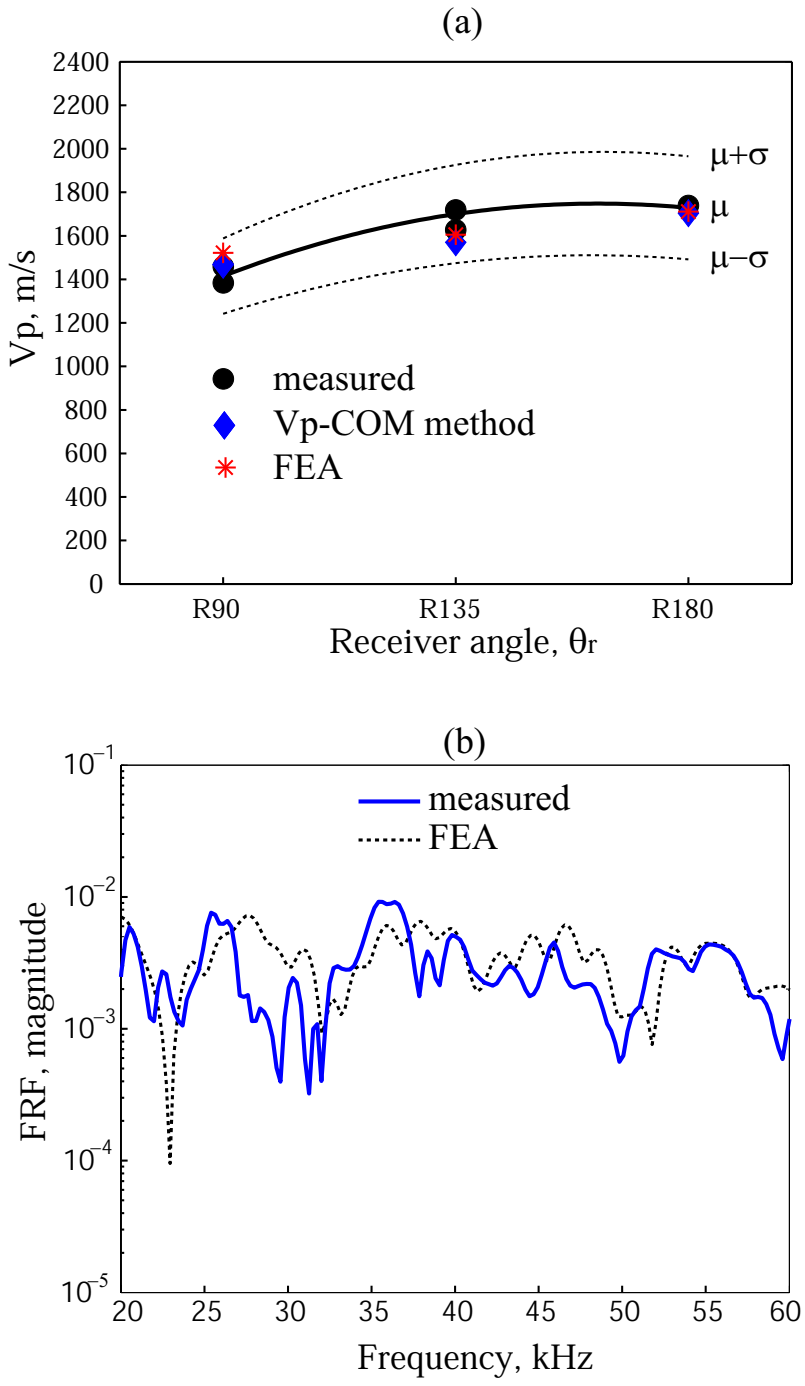

Figure 6.11: Numerical model validation: velocity V_p (a), frequency response function magnitude (b)

and mean value plus/minus one standard deviation of the velocity V_p for new red pine poles are also shown. These curves are obtained from numerical simulations using the Vp-COM method adjusted with measured values of velocities V_p in cross-sections of new red pine poles.

The P-wave arrival times at $\theta_r = 90°$, $\theta_r = 135°$, and $\theta_r = 180°$ are used to determine the elastic moduli E_r and E_t by solving the inverse problem of P-wave propagation using the Vp-COM method (Section 4.6). Figure 6.12(d) shows the mean square relative error for arrival times as function of the elastic moduli. The x-axis represents the elastic modulus E_r; each curve corresponds to an elastic ratio E_r/E_t. The estimated elastic moduli are $E_r = 1.1$ and $E_t = E_r/1.18 = 0.93$ GPa, which are 1% and 2% longer than the theoretical values. The computed arrival times using the Vp-COM method and the estimated elastic modulus E_r and E_t are in agrement with the theoretical ones as shown in Fig. 6.12(e).

The IRFs for the receivers located at $\theta_r = 90°$, $\theta_r = 135°$, and $\theta_r = 180°$ are illustrated in Fig. 6.12(f). The delay observed in the IRF corresponds with the arrival of the compressional wave. On the other hand, the arrival of a second wavefront observed at $\theta_r = 180°$ corresponds to a reflection introduced by the convex geometry. This effect is less noticeable for the receivers at $\theta_r = \pm 135°$.

The FRFs for the receivers located at $\theta_r = 90°$, $\theta_r = 135°$, and $\theta_r = 180°$ are presented in Figs. 6.13(a), 6.13(b), and 6.13(c), respectively. The FRFs are computed in the frequency range 20-70 kHz. Figures 6.13(d), 6.13(e), and 6.13(f) present the transmission factors for the receivers located at $\theta = \pm 90°$, $\theta = \pm 135°$, and $\theta = 180°$, respectively. The transmission factor between the receiver and the transmitter is computed as the area of the FRF divided by the frequency bandwidth ($\Delta f = 70 - 20 = 50$ kHz). In these figures, the mean value and mean value plus/minus one standard deviation as function of the pole diameter are also illustrated. These curves are obtained from numerical simulations (7 values) and measurements (30 values) in new red pine poles. The computed transmission factors are close to the expected values.

6.3.2 New red pine pole with a centric hole

The condition assessment for the cross-section of a simulated new red pine pole with a centric hole is presented in Figs. 6.14 and 6.15. The mechanical properties and geometry are the same used in the previous simulation. The diameter of the hole is 6 cm representing 4% of the section area (pole diameter equal to 30 cm). The numerical model, the source, and receiver locations are shown in Figs. 6.14(a) and 6.14(b).

The P-wave velocity curve is linear respect the receiver angle as shown in Fig. 6.14(c). For the receiver located at $\theta_r = 180°$, the P-wave velocity is 9% smaller than the corresponding value without a hole ($\hat{V_p}/V_p = 0.91$). The main effect of a centric hole on the P-wave veloc-

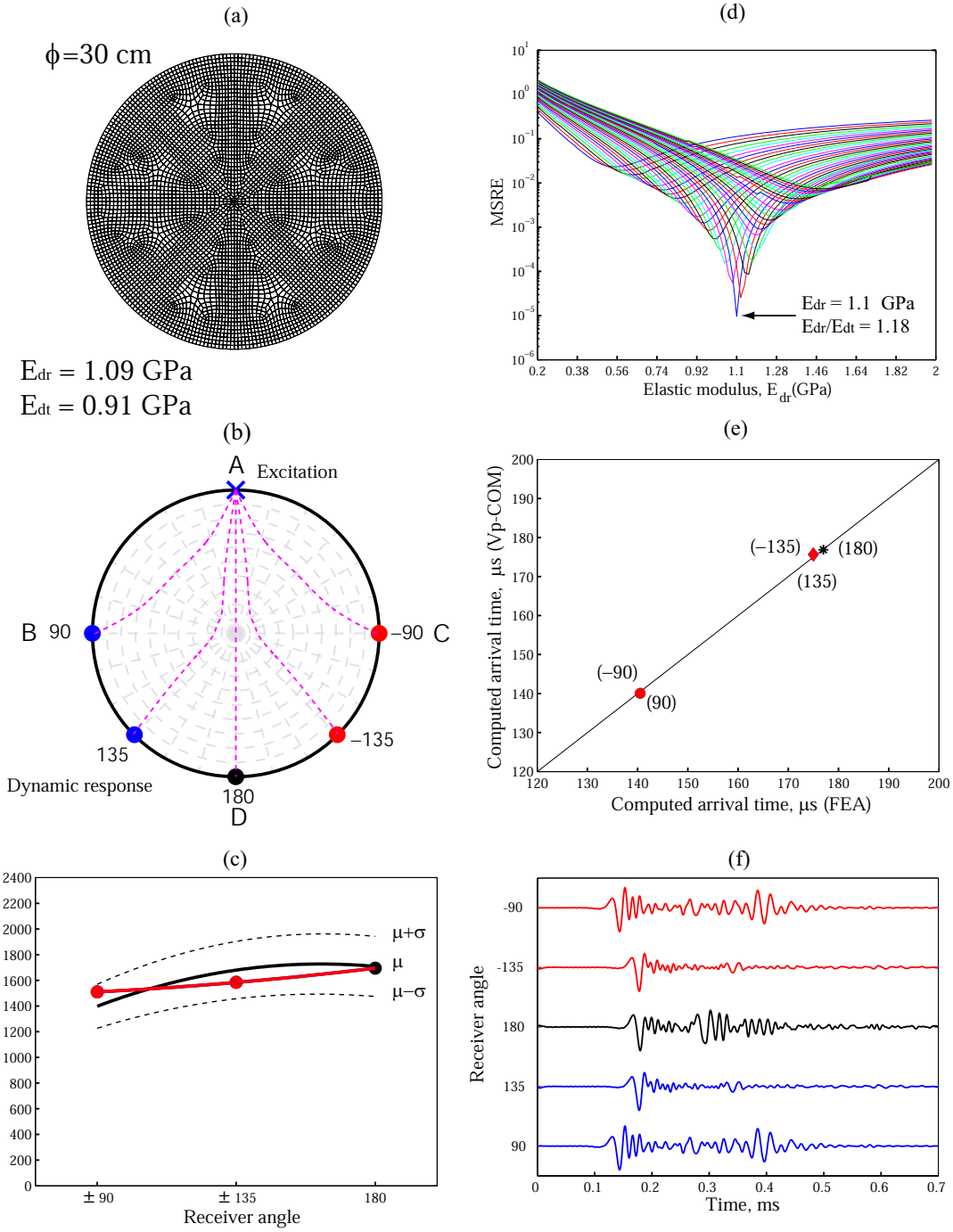

Figure 6.12: Numerical simulation results of ultrasonic testing in a red pine pole cross-section ($\phi = 30$ cm, $MC = 12\%$, $T = 20\ ^{\circ}C$): finite element model (a), source and receiver locations (b), velocities V_p (c), elastic moduli E_r and E_t (d), arrival times (e), and impulse response functions (f)

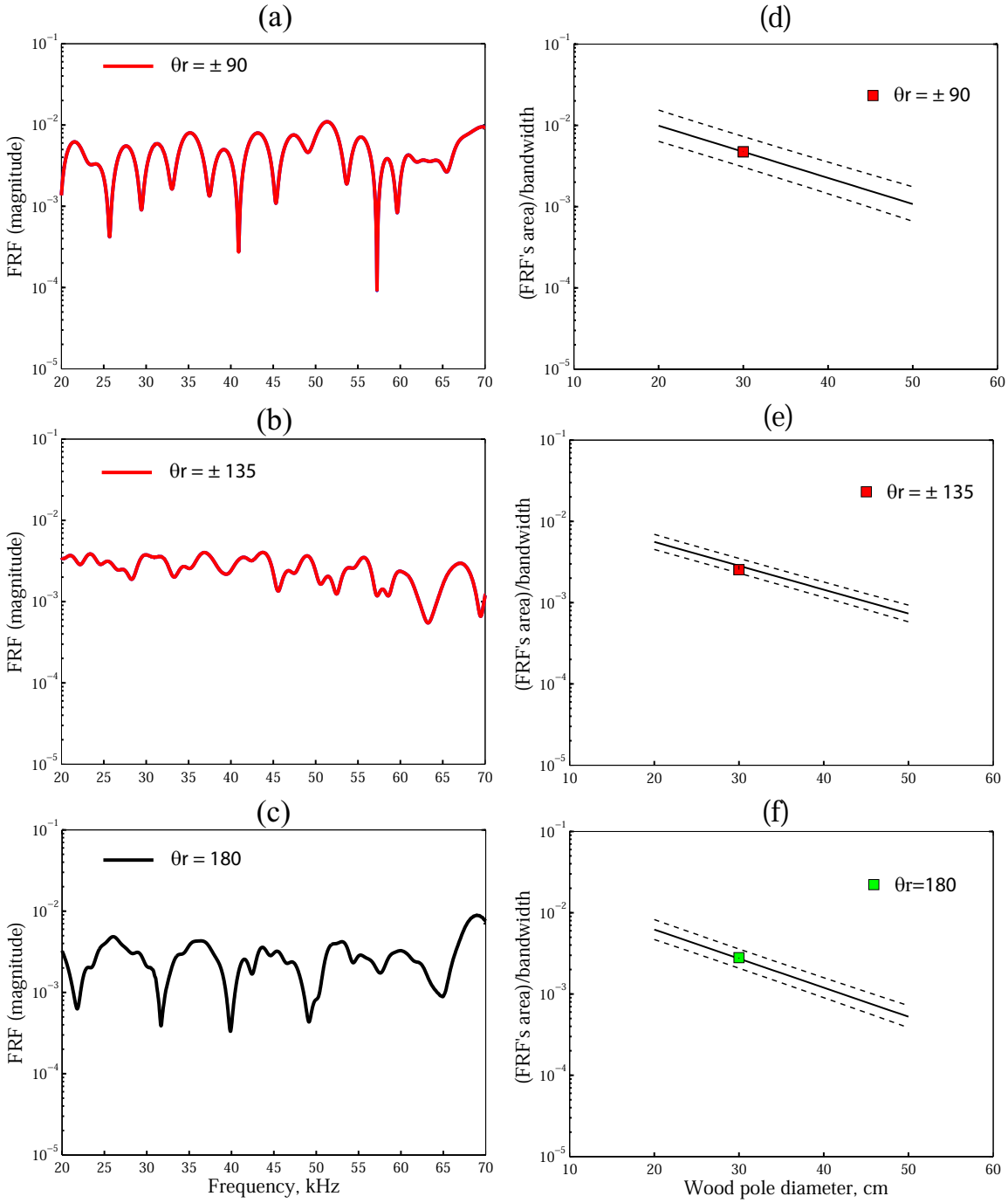

Figure 6.13: Numerical simulation results of ultrasonic testing in a red pine pole cross-section ($\phi = 30$ cm, $MC = 12\%$, $T = 20\ ^{\circ}C$): FRFs for the receivers located at 90° (a), 135° (b), and 180° (c); wave transmission factors for the receivers located at 90° (d), 135° (e), and 180° (f)

ity field is that $V_{p(\theta=180)} < V_{p(\theta=135)}$. Although the P-wave velocities are between the mean value plus/minus one standard deviation, the presence of a centric hole changes the cylindrical orthotropic behaviuor found in cross-sections of sound wood poles.

The equivalent elastic modulus E_r computed using the Vp-COM method is reduced in 18% respect to the value obtained without a hole. The modulus ratio is approximately equal to the square velocity ratio, or $\hat{E_p}/E_r = (\hat{V_p}/V_p)^2$. The variation in the elastic modulus E_t is only 4% (Fig 6.14(d)). The computed arrival times using the estimated elastic moduli and the theoretical values (with a hole) are shown in Fig. 6.14(e). An equivalent solid section (no hole) with $E_r = 0.9$ GPa and $E_t = 0.95$ GPa presents similar arrival times as the same section with a hole ($E_r = 1.09$ GPa and $E_t = 0.91$ GPa).

The arrival of the compressional waves for the receivers located at $\theta_r = \pm 90°$, $\theta_r = \pm 135°$, and $\theta_r = 180°$ are clearly shown in the IRFs presented in Fig. 6.14(f). The arrival of other wavefronts due to the convex geometry as well as to the surface waves are also observed.

The FRFs for the receiver located at $\theta_r = 90°$, $\theta_r = 135°$, and $\theta_r = 180°$ are presented in Figs. 6.15(a), 6.15(b), and 6.15(c); and the transmission factors, in Figs. 6.15(d), 6.15(e), and 6.15(f). The transmission factors are reduced by 13, 43, and 30% for the receivers located at $\theta_r = 90°$, $\theta_r = 135°$, and $\theta_r = 180°$, respectively. The transmission factors are smaller because of destructive interference and wave reflections produced by the presence of a centric hole.

Numerical simulations are performed varying the pole diameter (ϕ_{pole}), the hole diameter (ϕ_{hole}), and the elastic ratio E_r/E_t. The pole diameters used for the simulations are $\phi_{pole} = 20$, 30, 40, and 50 cm, with hole diameters of $\phi_{hole} = 6$, 9, and 12 cm. The elastic ratios are $E_r/E_t = 1.2$ and $E_r/E_t = 2$. The dissimilarity index of the velocity V_p for the receiver located at $\theta_r = 180°$ is computed for each simulation. The variation in the dissimilarity index of the velocity V_p with respect to the condition without a hole ($\Delta(DIV_{(180)})$) is presented as function of the ratio ϕ_{hole}/ϕ_{pole} in Fig. 6.16. A linear relationship is observed respect to the elastic ratio E_r/E_t. The dissimilarity index of velocity V_p for a centric hole increases with the increase of the ratios E_r/E_t and ϕ_{hole}/ϕ_{pole}.

6.3.3 Decayed red pine pole

The RP-010 is an aged red pine pole with a diameter of 22.1 cm and 100 cm of length. Evidence of decay is not observed from a visual inspection. However, results of ultrasonic testing performed in a cross-section of the pole show that the section is decayed. Details of the ultrasonic tests are presented in the next chapter (Section 7.4.5). The tested section is cut to verify the results obtained using the proposed new methodology based on ultrasonic testing. The results of the pole condition assessment are in agreement with the decay areas observed in the tested

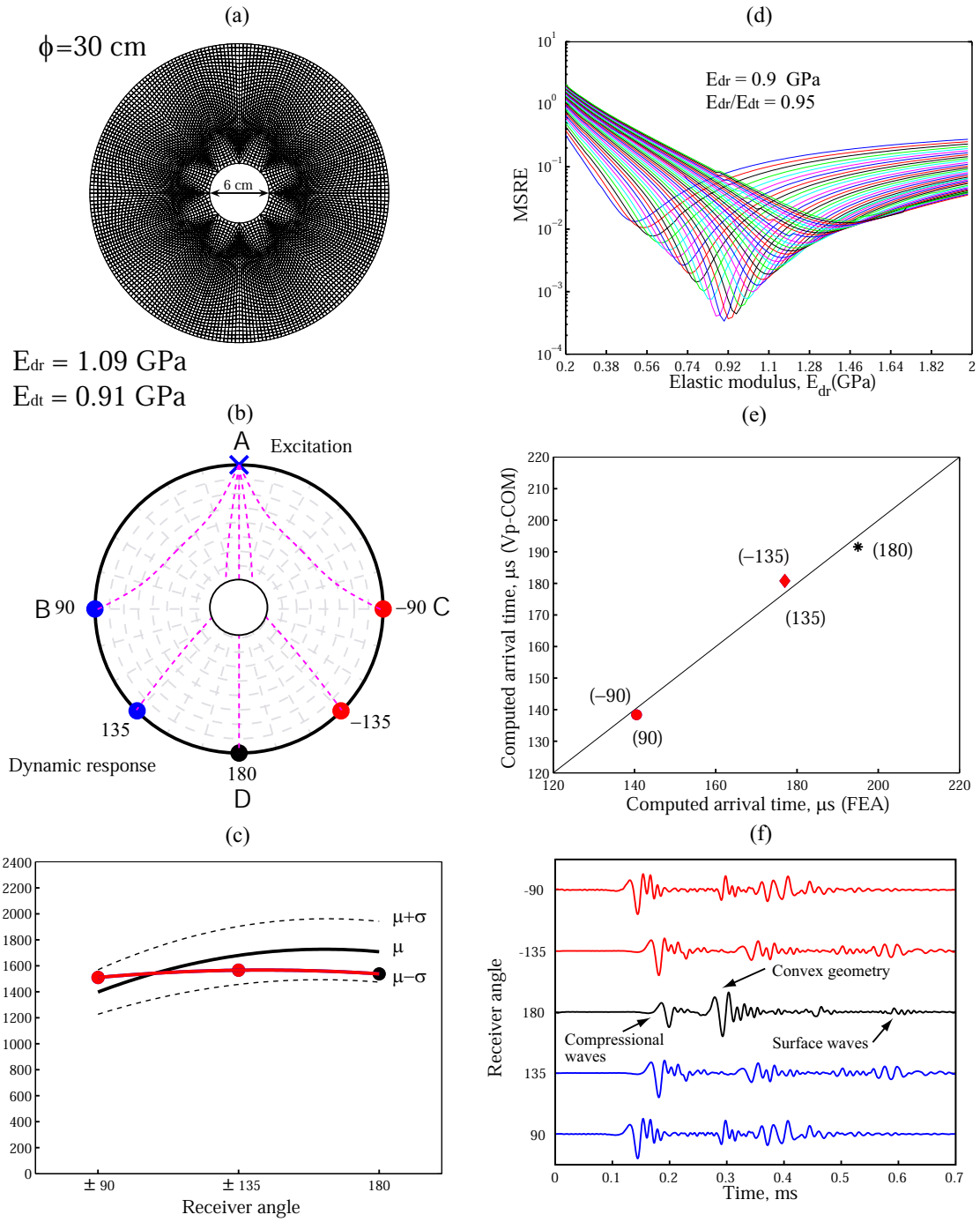

Figure 6.14: Numerical simulation results of ultrasonic testing in a red pine pole cross-section with a centric hole ($\phi = 30$ cm, $\phi_{hole} = 6$ cm, $MC = 12\%$, $T = 20\ ^{\circ}C$): finite element model (a), source and receiver locations (b), velocities V_p (c), elastic moduli E_r and E_t (d), arrival times (e), and impulse response functions (f)

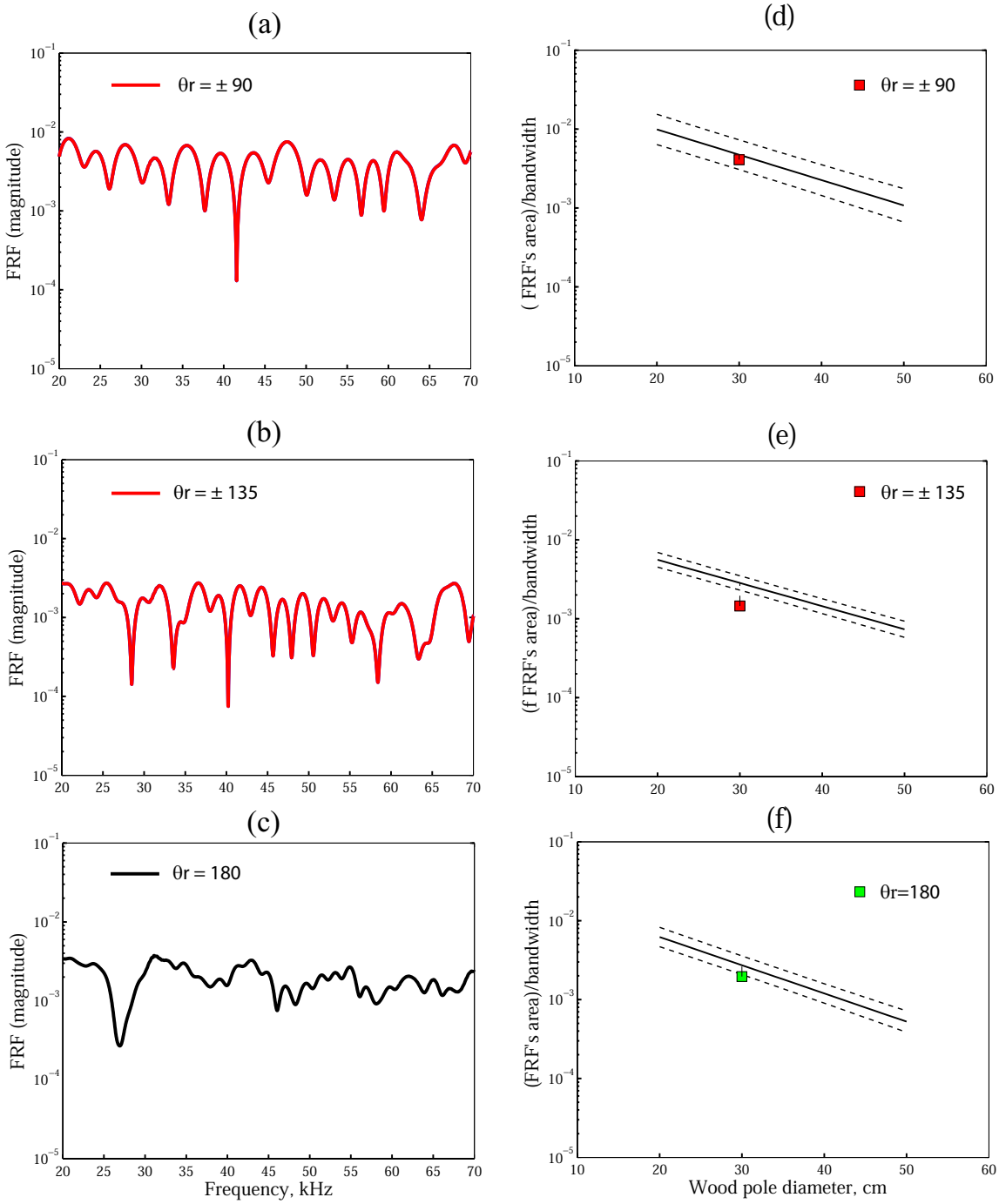

Figure 6.15: Numerical simulation results of ultrasonic testing in a red pine pole cross-section with a centric hole ($\phi = 30$ cm, $\phi_{hole} = 6$ cm, $MC = 12\%$, $T = 20\ ^{\circ}C$): FRFs for the receivers located at 90° (a), 135° (b), and 180° (c); wave transmission factors for the receivers located at 90° (d), 135° (e), and 180° (f)

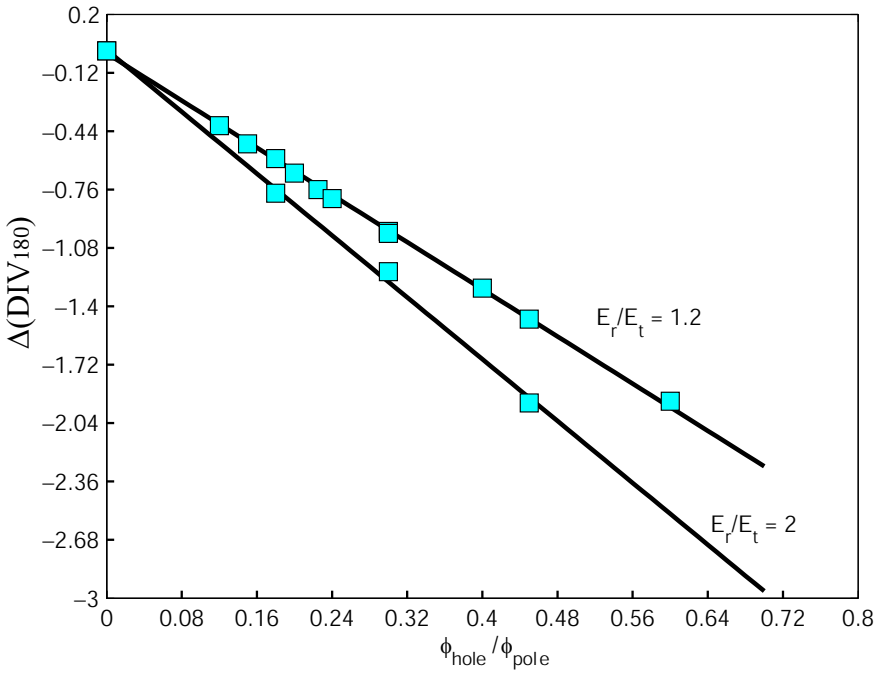

Figure 6.16: Effect of a centric hole on the dissimilarity index of the velocity V_p

section.

Penetrometer tests are performed (resistance to penetration of a metallic cone [92]) in the cross-section of a new red pine pole as well as in the tested section of the RP-010 as shown in Figs. 6.17(a) and 6.17(b). The penetrometer test is used to estimate the elastic moduli for the tested section as function of the corresponding values of a new red pine pole. A metallic cone of 2.2 cm of base and 4.3 cm of length is dropped from a height of 5.31 cm. The cone penetration is measured at different positions in the cross-section. The histograms of the cone penetration for new, aged, and decayed red pine woods are presented in Fig. 6.18. The mean sample of the cone penetration for new, aged, and decayed red pine woods are 0.25, 0.29, and 0.52 cm. The coefficient of variations are 0.23, 0.20, and 0.22, respectively.

The potential energy of a elastic spring is $U_s = k \cdot q^2/2$, where k is a measure of the stiffness of the spring and q is the displacement. Doing an analogy with a linear spring and assuming the same strain energy, the cone penetration is used to estimate the elastic ratio between two penetration tests as

$$\frac{E_a}{E_b} \approx (\frac{q_b}{q_a})^2 \tag{6.1}$$

where $E_a =$ elastic modulus for wood condition "a",

q_a = cone penetration for wood condition "a",
E_b = elastic modulus for wood condition "b", and
q_b = cone penetration for wood condition "b".

For the cases of the aged and decayed red pine poles, the estimated elastic ratios are $E_{aged}/E_{new} \approx 0.63$ and $E_{decayed}/E_{new} \approx 0.20$.

The numerical model is shown in Fig. 6.19(a). Two decayed areas are defined which represent 8% (area I) and 18% (area II) of the total section area. The mass density is estimated from samples taken of the areas I and II. The area I has a reduction in stiffness and mass density of 80% and 10% with respect to the corresponding values for a new pole. The area II has the same reduction in stiffness but with 20% of reduction in mass density. The apparent sound area (aged wood) is modeled with 37% of reduction in stiffness according the results obtained from the penetrometer tests. Two cavities are located next to the decayed areas I and II. The decay areas and the cavities represent 30% of the total area of the section. As before, the source is represented by the displacement response of an ultrasonic transmitter subjected to a one-cycle sinusoidal wave of 50 kHz (Fig. 6.9). The source is applied at point A in vertical direction. The dynamic response is computed for the receivers located at $\theta_r = \pm 90^\circ$, $\theta_r = \pm 135^\circ$, and $\theta_r = 180^\circ$. Figure 6.19(b) shows the source and receivers locations in the cross-section.

The velocity V_p decreases with the receiver location angle; thus, $V_p(180) < V_p(135) < V_p(90)$ as shown in Fig. 6.19(c). The dissimilarity index for the receiver at $\theta_r = 180^\circ$ is $DIV_{(180)} = -2.4$. Figure 6.19(d) shows the mean square relative error for the arrival times as function of the elastic moduli. The equivalent elastic moduli are $E_r = 0.43$ GPa and $E_t = E_r/0.57 = 0.75$ GPa. E_t is greater than E_r, which is not an expected result for a sound wood pole. The dissimilarity indexes for the elastic modulus E_r is $DIE_{\theta_r} = -3.13$. The computed arrival times using the Vp-COM method for an equivalent section are in agreement with the computed values for the tested section using FEA as shown in Fig. 6.19(e).

The arrival times of the compressional waves are clearly observed from the IRFs shown in Fig. 6.19(f). However, the waves generated by the convex geometry are attenuated, particularly for the receivers located at $\theta_r = \pm 135^\circ$ and $\theta_r = 180^\circ$.

The FRFs for the receivers located at $\theta_r = \pm 90^\circ$, $\theta_r = \pm 135^\circ$, and $\theta_r = 180^\circ$ are presented in Figs. 6.20(a), 6.20(b), and 6.20(c); and the transmission factors, in Figs. 6.20(d), 6.20(e), and 6.20(f). The dissimilarity indexes are $DIA_{(90)} = -1.91$, $DIA_{(-90)} = -1.84$, $DIA_{(135)} = -4.4$, $DIA_{(-135)} = -4.34$, and $DIA_{(180)} = -3.44$.

(a)

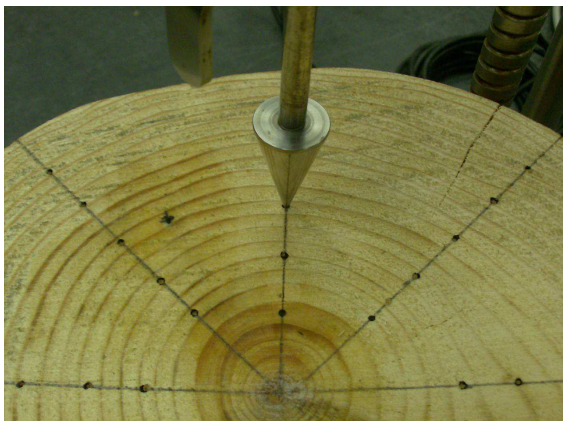

(b)

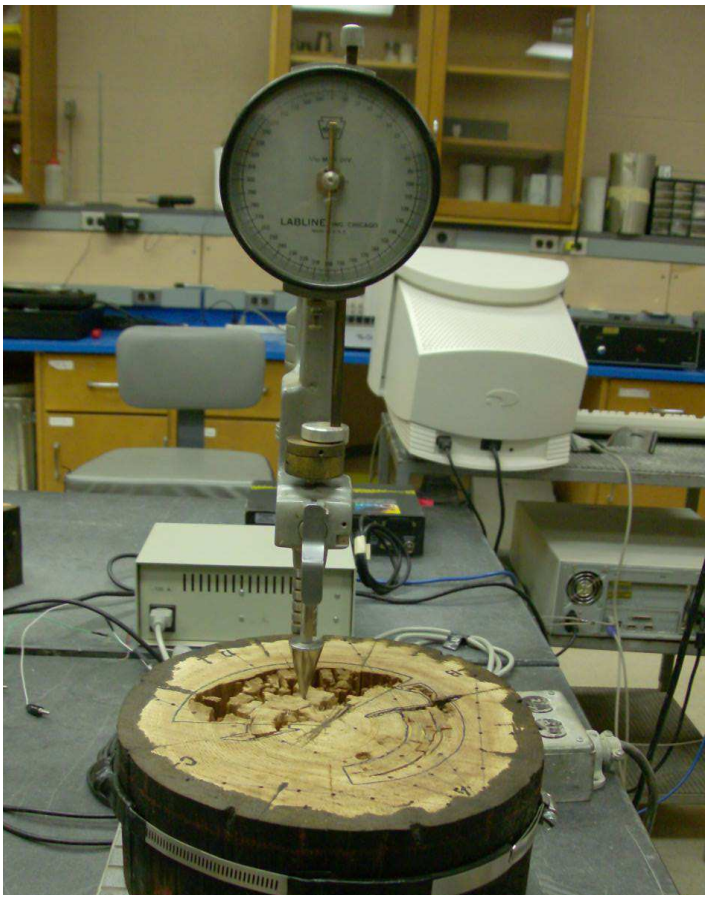

Figure 6.17: Penetrometer tests for new (a), aged and decayed (b) red pine poles

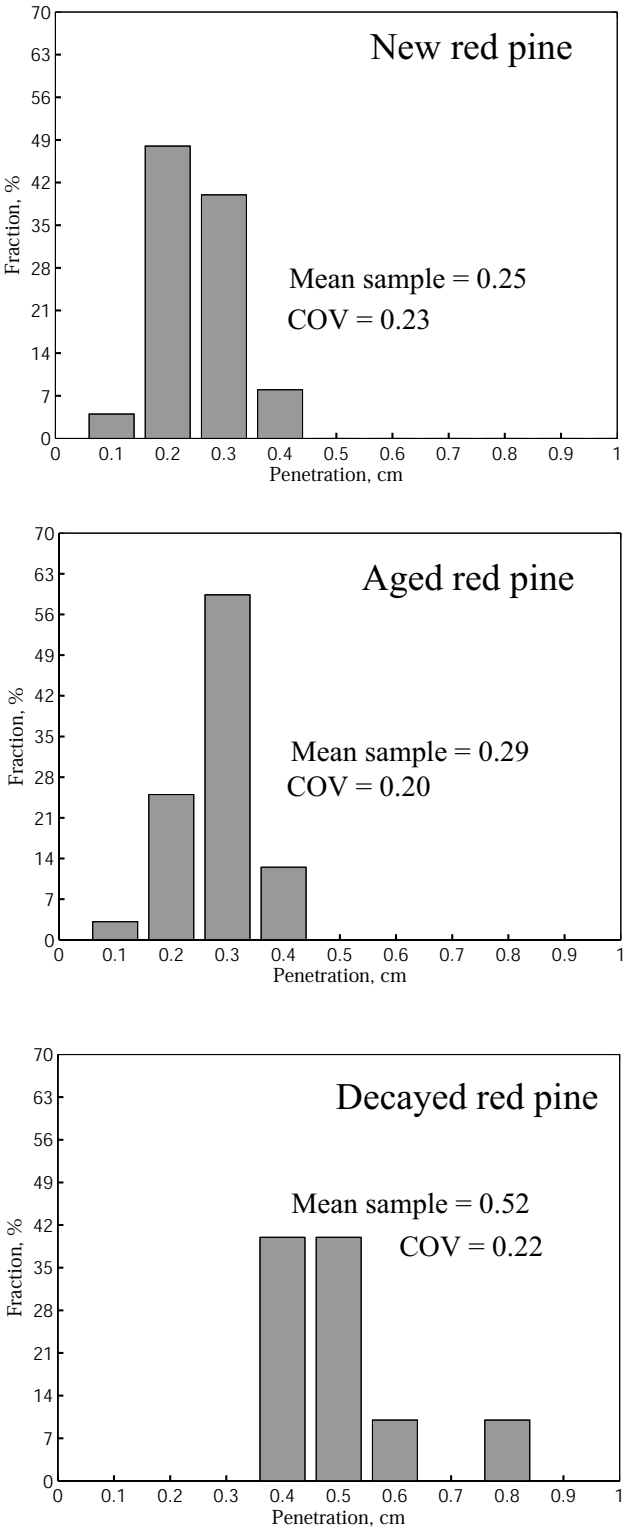

Figure 6.18: Histogram of cone penetration for new (25 values), aged (30 values), and decayed (10 values) rep pine poles

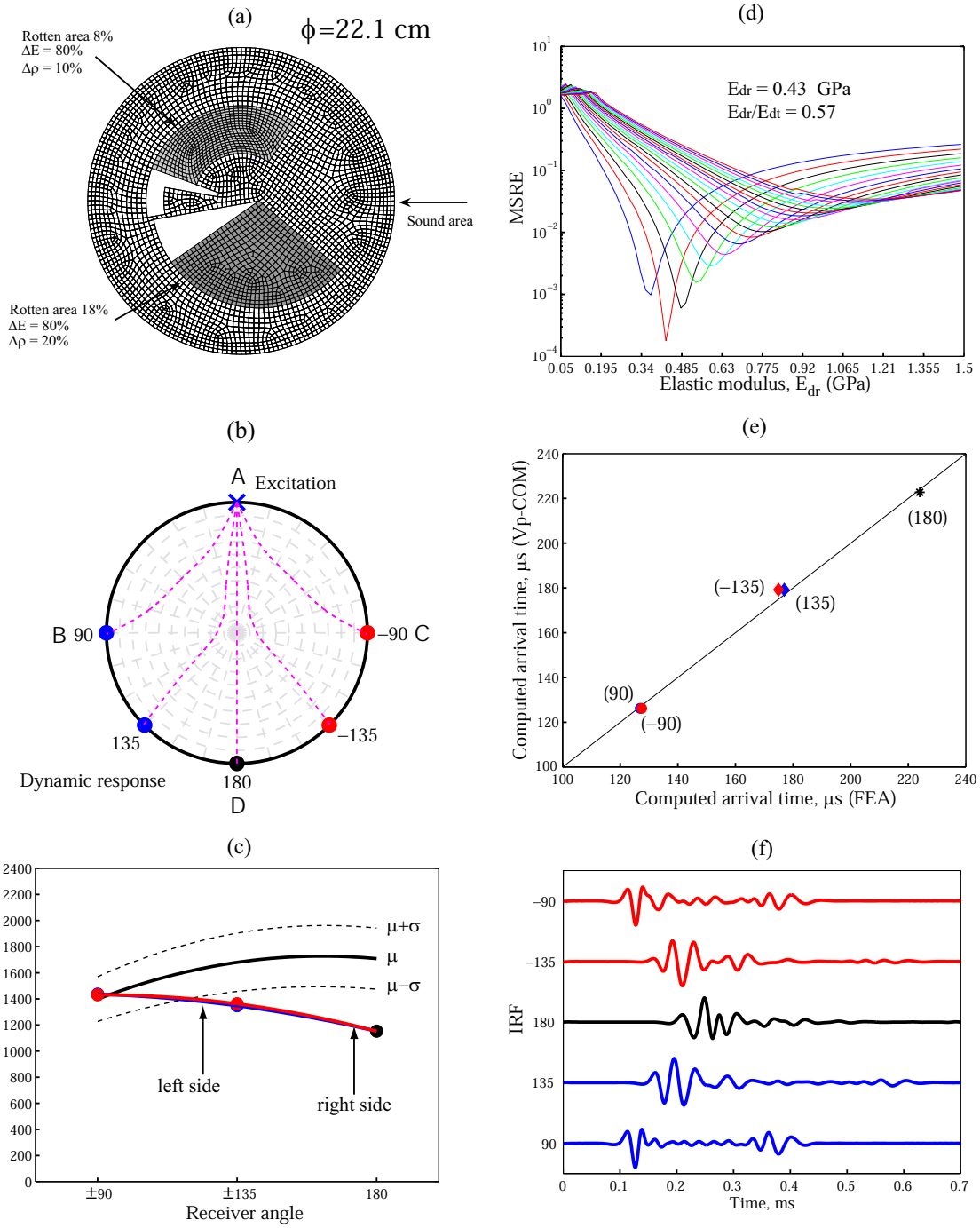

Figure 6.19: Numerical simulation results in a cross-section of the red pine pole RP-010 (ϕ = 22.1 cm, $MC = 5\%$, $T = 20\ ^{\circ}C$): RP-010 ultrasonic test (a), source and receiver locations (b), velocities V_p (c), elastic moduli E_r and E_t (d), arrival times (e), and impulse response functions (f)

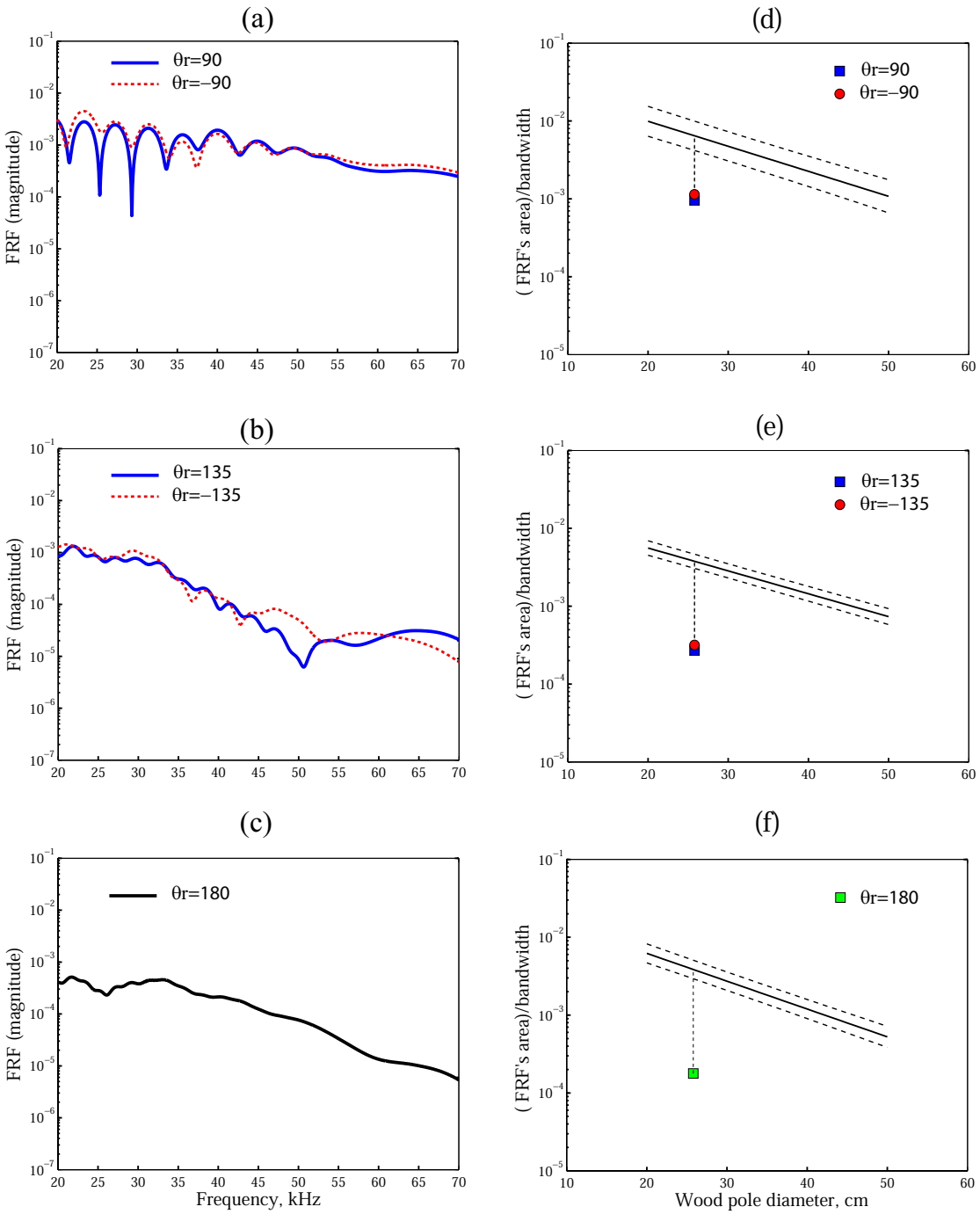

Figure 6.20: Numerical simulation results in a cross-section of the red pine pole RP-010 (ϕ = 22.1 cm, $MC = 5\%$, $T = 20\ ^{\circ}C$): FRFs for the receivers located at 90° (a), 135° (b), and 180° (c); wave transmission factors for the receivers located at 90° (d), 135° (e), and 180° (f)

6.4 Chapter Summary

A numerical model by finite elements is presented to study the propagation of ultrasonic waves in a cross-section of a red pine pole. The strain in the longitudinal direction is an order of magnitude smaller than the strain in the radial direction because of the high anisotropy of the wood; therefore, plain strain conditions can be assumed. The numerical model is validated with results of ultrasonic testing in a new red pine pole. The maximum difference between the calculated and the measured velocity V_p is 9%. The calibrated numerical model can be used to study the effect of cavities and decayed areas in the propagation of ultrasonic waves.

Experimental modal analysis can be used to estimate the elastic modulus in the longitudinal direction of a wood pole specimen; whereas, the radial and tangential elastic moduli can be estimated using ultrasonic tests and the Vp-COM method.

A Rayleigh damping model adjusted with measured values of damping ratio can be used to model wave attenuation in wood pole cross-sections. The damping model is inversely proportional to frequency (mass-proportional damping). The difference between the measured and the calculated transmission factors for the receiver located at $\theta_r = 180^\circ$ is 2%. For the receivers located at $\theta_r = 90^\circ$ and $\theta_r = 135^\circ$, the maximum difference is less than 20%.

A centric hole of 6 cm diameter can be detected by using ultrasonic tests with a transmitter of 50 kHz as nominal frequency. The presence of a centric hole changes the cylindrical orthotropic behaviuor of sound wood pole cross-sections. The Velocity V_p for the receiver located at $\theta_r = 180^\circ$ is smaller than the velocity V_p at $\theta_r = 135^\circ$. For the receiver located at $\theta_r = 180^\circ$, the Velocity V_p, the equivalent elastic modulus E_r, and the transmission factor are reduced by 9%, 18%, and 30%, respectively. The dissimilarity index of the velocity V_p increases with the increase of the ratios E_r/E_t and ϕ_{hole}/ϕ_{pole}.

Penetrometer tests are used to estimate the elastic moduli of an aged/decayed red pine pole from the elastic moduli of a new red pine pole. The difference between the computed (using the estimated elastic moduli) and the measured velocity V_p is less than 18%.

Chapter 7

Experimental Results

7.1 Chapter Overview

Ultrasonic measurements based on full-waveform can be affected by the coupling between the transducers and the wood pole. Therefore, repetition of measurements are needed to determine the accuracy of the results. In this section, variations of the velocity V_p and the transmission factor are presented for different conditions keeping the same coupling, and for assembling and disassembling the UT-Pole device. The effect of moisture content on the velocity V_p, the condition assessment of new and decayed red pine poles, and the effect of a centric and an eccentric cavities in the condition assessment are also shown. A blind test is performed in an aged red pine pole. The wood pole is cut transversally at the tested section after the ultrasonic tests have been carried out. The results of the condition assessment are compared with the observed wood condition in the tested section. In the proposed methodology, using wave velocity and attenuation, it is possible to determine the position of a decayed circle in the cross-section of a wood pole. This determination requires the use of four or eight transmitters located around the wood pole and the raypaths corresponding to five receiver locations for each transmitter

7.2 Red Pine Pole Specimens

Ultrasonic tests are preformed in four new (sound) and two aged red pine pole specimens. One of the aged pole is visibly decayed. No evidence of decay is observed for the other aged pole. Table 7.1 shows the wood pole designation, the diameter, the length, and the weight of the specimen. The diameter of the specimens varies from 21.3 to 34.7 cm.; and the length, from 80.7 to 100 cm.

Theoretically, the wavelength (λ) should be equal or smaller than the anomaly size to be

Table 7.1: Red pine pole specimens used for ultrasonic tests

Wood pole	Diameter (cm)	Length (cm)	Weight (kg)	Remarks
RP-01	26.3	85.8	25.2	new
RP-02	22.6	80.7	16.6	new
RP-03	31.6	100.0	39.2	new
RP-04	34.7	102.4	49.2	new
RP-002A	21.5	93.1	12.5	rotten
RP-010	25.8	100	18.1	aged (blind test)
RP-03	30.6	100.0	39.2	new (centric hole)
RP-03	32.0	100.0	39.2	new (eccentric hole)

detected (ϕ_{hole}); however, it is a good practice to have $\phi_{hole} \geq 1.5\lambda$ [15]. A typical wave velocity for wood in the radial direction is $V_p = 2000$ m/s. For a transmitter with nominal frequency of $f_0 = 50$ kHz, the suggested minimum anomaly size is $Z = 1.5(V_p/f_0) = 6$ cm. A centric and an eccentric holes of 6.3 cm are made in the wood pole specimen RP-03 which has a diameter of 31.6 cm. The hole represents 4% of the wood pole section area.

7.3 Accuracy of the Measurements

Uncertainties on measurements of P-wave velocity and transmission factor are presented as histograms. Measurement uncertainties occur because of numerical errors (sampling rate, ratio noise/signal) and variations on the setting of the transmitter and receiver (coupling condition, direction, and inclination).

The measurements are divided in two groups. The group (1) corresponds to measurements performed keeping the same coupling but swapping the transmitter and the receiver. Whereas in group (2), the location of the transmitter and the receiver are the same but the UT-Pole device is assembled and disassembled between measurements.

Figure 7.1 shows histogram of the deviation on measurements of the velocity V_p. The X-axis represents the velocity deviation with respect to a reference value. The velocity deviation is computed as $(V_p/\bar{V}_p - 1)\cdot 100$, where V_p is the measured velocity and $\bar{V}_p$ is the mean sample value of the measured velocities V_p. The Y-axis is the fraction of the total number of measurements given as percentage. A total of 32 samples are used for the histogram for velocities V_p including

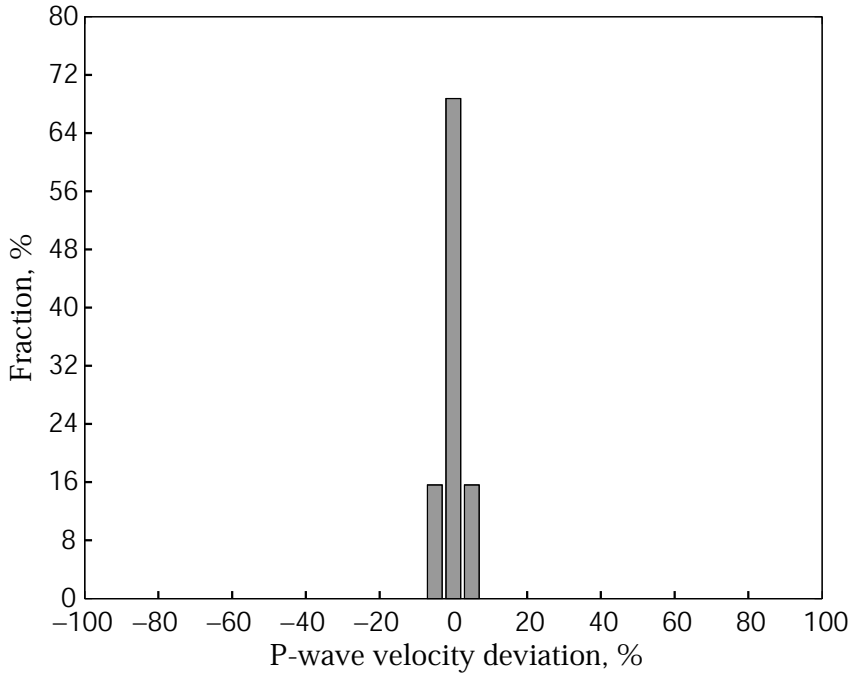

Figure 7.1: Histogram of the velocity V_p deviation (32 samples)

the two groups. A maximum deviation less than 2.5% for the velocity V_p is obtained for 70% of the measurements, whereas 30% of the measurements showed a deviation between 2.5% and 5% in the calculation of the velocity V_p.

Figures 7.2(a) and 7.2(b) show histogram of the transmission factor for groups 1 and 2, respectively. For group 1 (58 samples), 70% of the transmission factors have a deviation less than 5%; and 30%, show a deviation between 5% and 15%. For the case of group 2 (36 samples), a larger dispersion for the measurement of the transmission factor is observed. A deviation less than 15% is obtained for 47% of the measurements, whereas the maximum deviation for 94% of the measurements is less than 45%. The deviation in the transmission factor for group 2 is greater than group 1 because the direction and inclination of the transducers are not exactly the same for different assemblies of the system.

7.4 Condition Assessment

Results of condition assessment for red pine pole specimens RP-03 (without and with a hole), RP-002A, and RP-010 are presented next. The results for the specimens RP-01, RP-02, and RP-04 are presented in Appendix B.

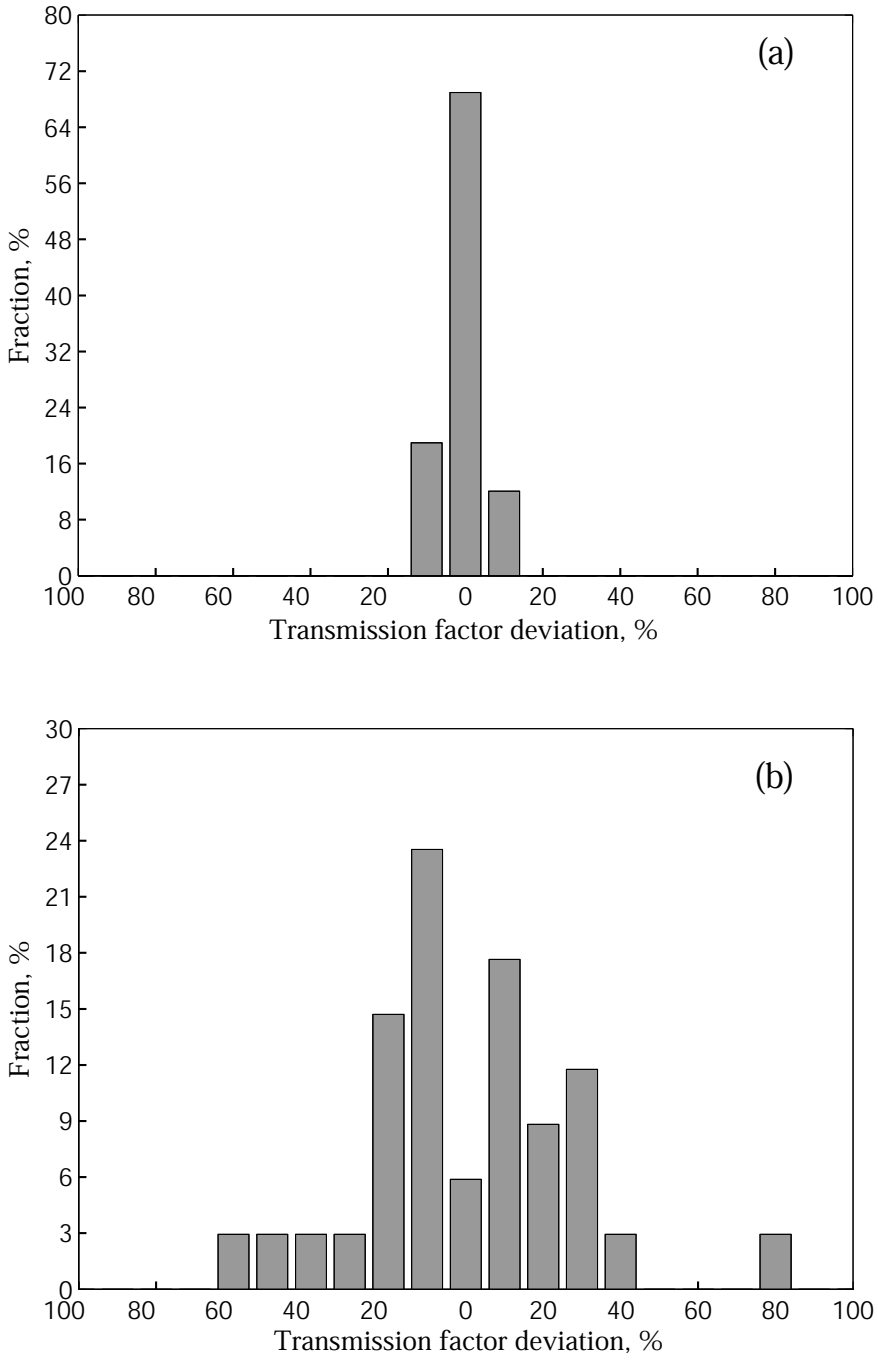

Figure 7.2: Histogram of transmission factor deviation: (a) interchanging transmitter/receiver transducers (58 samples), and (b) assembling and disassembling the UT-Pole device (36 samples)

7.4.1 Sound red pine pole RP-03

The tested cross-section has a diameter of 31.6 cm and is located at 50 cm from the bottom of the specimen RP-03. The first set of ultrasonic tests on the red pine pole specimens are performed during the summer (June, 2008). The temperature and the relative humidity in the laboratory are monitored during a full month (August, 2008). The temperature in this period is almost constant and equal to 20 $^{\circ}C$. However, the relative humidity fluctuates between 40 and 69% for the same period of time. Moisture content can be estimated from the temperature and the relative humidity as shown in Fig. 3.2. The estimated moisture content is between 8 and 13% for the measured range of relative humidity and temperature. Values of $MC = 12\%$ and $T = 20\ ^{\circ}C$ are assumed for the red pine pole specimens.

A second set of ultrasonic tests is carried out in the winter (November, 2008). New radial cracks and increase of the existing ones are observed with respect to the first set of ultrasonic (June, 2008) as shown in Figs. 7.3(a) and 7.3(b). The radial crack close to the receiver located at $\theta_r = 135^{\circ}$ increased 1.5 mm in width (50%) and 3.5 cm in depth (175%). Figure 7.3(c) shows the velocity V_p as function of the receiver location angle for the two sets of measurements. The velocity V_p increased for the measurements taken on November because of the decrease of moisture content. The maximum increase of the velocity V_p for the receivers located at $\theta_r = 180^{\circ}$, $\theta_r = 135^{\circ}$, and $\theta_r = 90^{\circ}$ are 7%, 10%, and 8%, respectively.

The change in MC can be estimated from the variation of the velocity V_p by using eqn. (4.31). For a temperature of 20 $^{\circ}C$, a value of $MC = 5\%$ is obtained for an increase of 8% in the velocity V_p. Figure 7.4(a) shows ultrasonic testing results for a cross-section of the red pine RP-03. The transmitter is located at point A; and the receivers, at $\theta_r = \pm 90^{\circ}$, $\theta_r = \pm 135^{\circ}$, and $\theta_r = 180^{\circ}$ respect to the transmitter position (Fig. 7.4(b)).

The measured velocities for the receivers located at $\theta_r = \pm 90^{\circ}$, $\theta_r = \pm 135^{\circ}$, and $\theta_r = 180^{\circ}$ are presented in Fig. 7.4(c). The measured velocities are similar to the expected values. The minimum dissimilarity index for the velocity V_p is $DIV_{(-90)} = -0.27$.

The Vp-COM method assumes that the pole cross-section is cylindrically orthotropic and a homogeneous material. Therefore, the inverse process gives the elastic moduli of an equivalent homogeneous wood cross-section with the pith at the centre. The mean square relative error for the arrival time is presented in Fig. 7.4(d). The equivalent elastic moduli are $\tilde{E}_r = 1.51$ GPa and $\tilde{E}_t = 1.7/\tilde{E}_r = 0.89$ GPa. The measured and computed values of arrival times are plotted in Fig. 7.4(e). The maximum difference between the arrival times computed from the Vp-COM method and the measured values is 10%. This difference is likely because wood is not completely a homogeneous material, the cross-section is not completely circular, and the pith is not located exactly at the geometry centre of the section.

The IRFs of the system transmitter-pole-receiver for the receivers located at $\theta_r = \pm 90^{\circ}$,

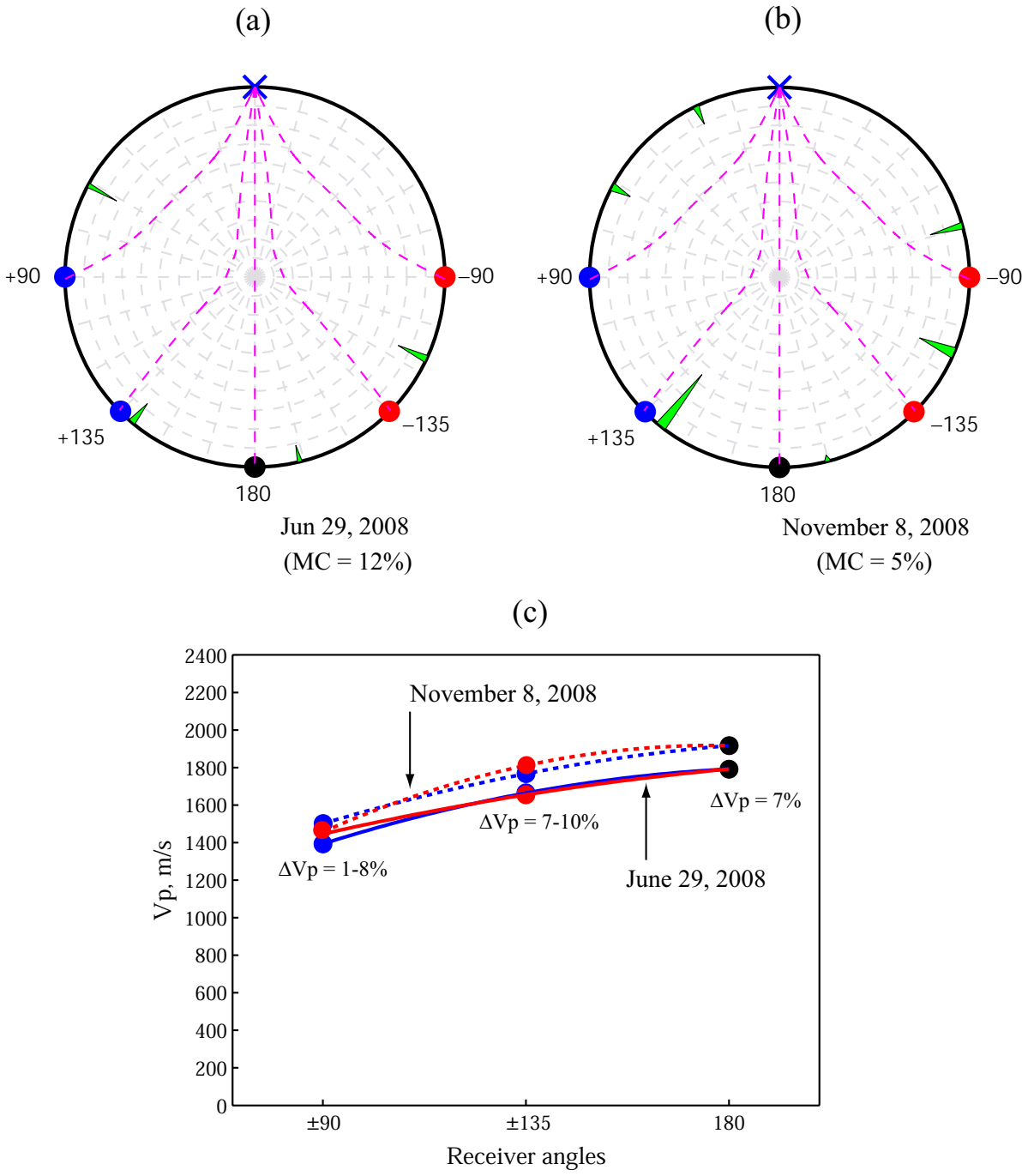

Figure 7.3: Effect of moisture content in the velocity V_p

$\theta_r = \pm 135°$, and $\theta_r = 180°$ is illustrated in Fig. 7.4(f). The IRFs show the first arrival of the compressional wave at each receiver location as well as other wavefront arrivals produced by the convex geometry of the section.

The FRFs for the receivers at $\theta_r = \pm 90°$, $\theta_r = \pm 135°$, and $\theta_r = 180°$ are presented in Figs. 7.5(a), 7.5(b), and 7.5(c), respectively. Four main peaks are observed for the frequencies of 28.4, 51, 52.3, and 65.6 kHz. The transmission factor at each receiver location is within the mean value plus/minus one standard deviation as shown in Figs. 7.5(d), 7.5(e), and 7.5(f).

The transmitter is also placed on the points B, C, and D (Fig. 7.5(b)). The results for each location are presented in Appendix C. The condition assessment of the cross-section including the results for the transmitter positions on A, B, C, and D is presented in Fig. 7.6. The inversion of these four independent ultrasonic tests generates different equivalent elastic moduli in the radial direction E_r as well as equivalent elastic ratios E_r/E_t. Figure 7.6(a) shows the tested cross-section with the locations of the points A, B, C, and D. The range for the equivalent elastic modulus is $\tilde{E}_r = 1.48 - 1.51$ GPa; and for the equivalent elastic ratio, $\tilde{E}_r/\tilde{E}_t = 1.63 - 1.79$. The mean value of the elastic ratio obtained for this section is 15% smaller than the value reported in the literature for red pine [2].

Figure 7.6(b) presents the histogram of the overall dissimilarity index (ODI_{θ_r}). A 58% of the computed ODI_{θ_r} are between -0.25 and 0.25; 35%, between 0.25 and 0.75; and 7%, between 0.75 and 1.25. The overall dissimilarity index represents the number of standard deviation respect to the expected value for sound wood poles. An acceptable criterion for sound condition of a wood pole is to select a value of dissimilarity index α_d such that $P[ODI \geq \alpha_d] = 0.95$. For a normal distribution, $\alpha_d = -1.6$. The Ultrasonic test results using the new methodology show that the wood pole is healthy with a behaviour as expected for new red pine poles.

7.4.2 Sound red pine pole RP-03 with a centric hole

A hole of 6.24 cm diameter and 37.5 cm length is drilled at the bottom of the RP-03 as shown in Fig. 7.7(a). The tested cross-section has a diameter of 30.6 cm and is located at 20 cm from the bottom of the specimen. The hole coincides with the pith position of the wood located at $x = -0.7$ cm and $y = -0.3$ cm from the centre of the section (Fig. 7.7(b)).

The velocity V_p curves are presented in Fig. 7.7(c). The velocity V_p curve left side shows that $V_{p90} > V_{p180} > V_{p135}$. Whereas for the right side, the relationship is $V_{p135} > V_{p90} > V_{p180}$. Both patterns differ from the expected one for a sound wood pole ($V_{p180} > V_{p135} > V_{p90}$). The dissimilarity indexes of the velocity V_p for the receivers located at $\theta_r = 135°$ and $\theta_r = 180°$ are $DIV_{(135)} = -2.17$ and $DIV_{(180)} = -1.44$. Thus the velocity V_p at $\theta_r = 135°$ is equal to the expected value minus 2.17 standard deviations. Likewise, the velocity V_p at $\theta_r = 180°$ is the

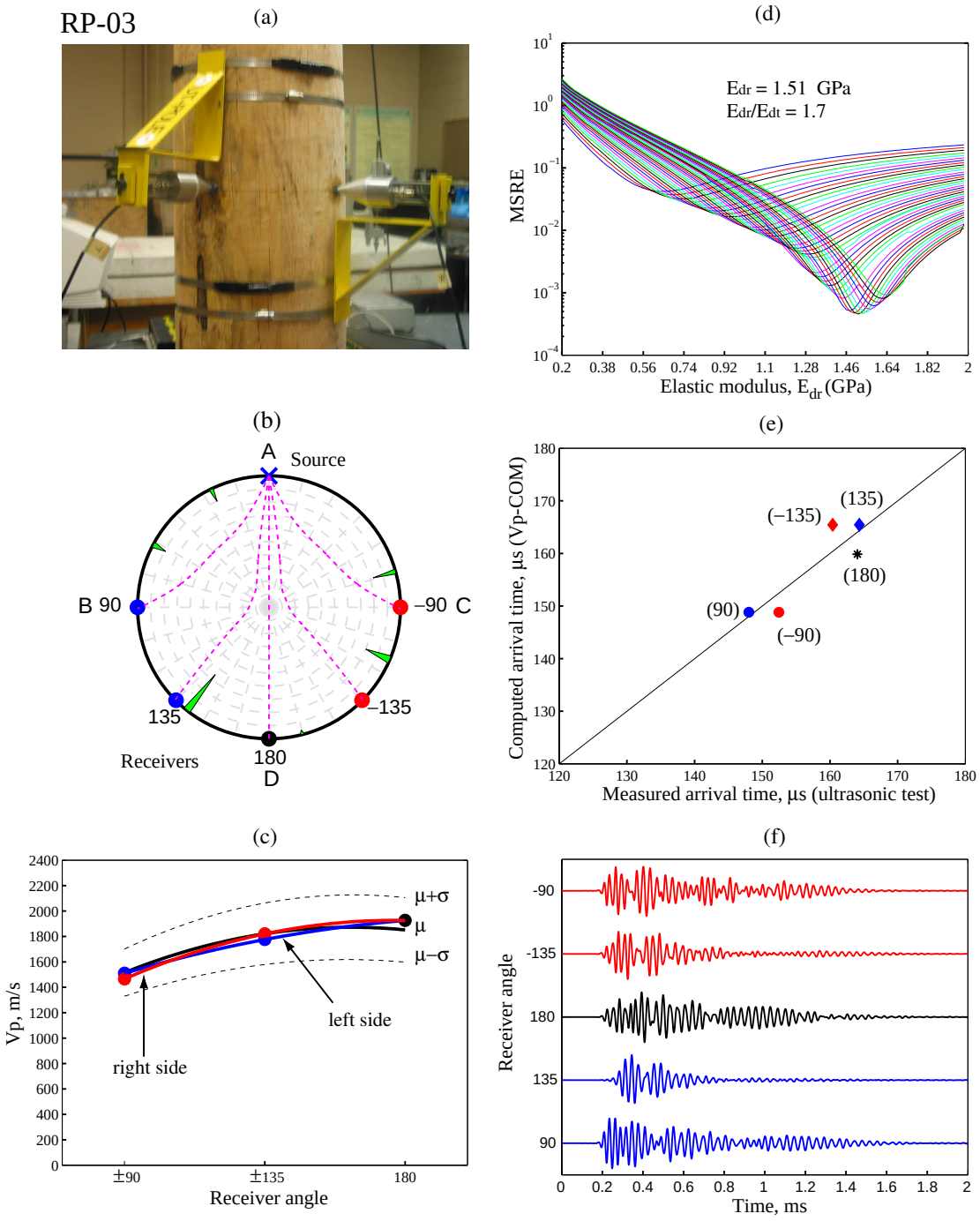

Figure 7.4: Experimental results of ultrasonic testing in red pine pole RP-03 ($\phi = 31.6$ cm, $MC = 5\%$, $T = 20\ ^{\circ}C$): (a) ultrasonic test, (b) source and receiver locations, (c) velocities V_p, (d) elastic moduli E_r and E_t, (e) arrival times, and (f) IRFs

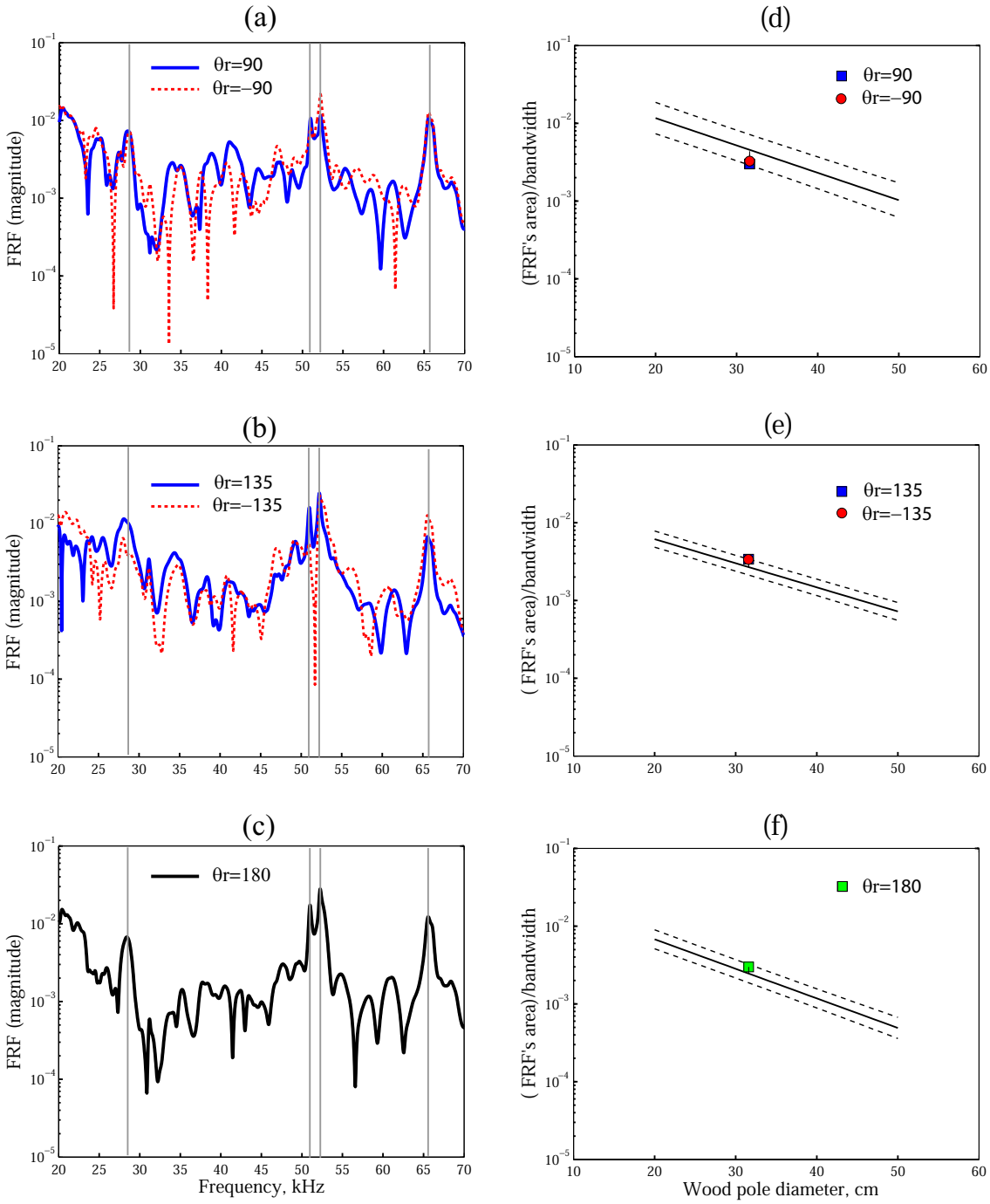

Figure 7.5: Experimental results of ultrasonic testing in red pine pole RP-03: FRFs for the receivers located at $\theta_r = \pm 90^\circ$ (a), $\theta_r = \pm 135^\circ$ (b), and $\theta_r = 180^\circ$ (c); transmission factors for the receivers located at $\theta_r = \pm 90^\circ$ (d), $\theta_r = \pm 135^\circ$ (e), and $\theta_r = 180^\circ$ (f)

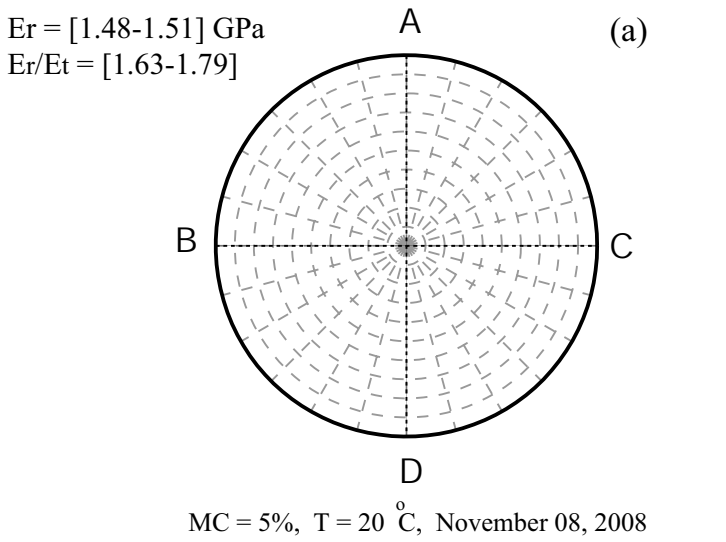

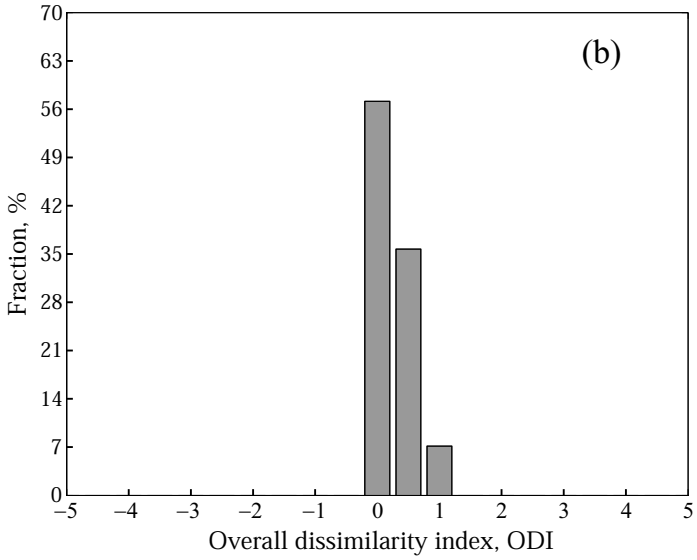

Figure 7.6: Condition assessment of red pine pole RP-03 (sound pole): elastic moduli and cross-section analysis (a), overall dissimilarity index histogram (b)

expected value minus 2.17 standard deviations. If the velocity V_p is normally distributed; then $[P(V_p \leq (\mu_{V_p} - 1.44\sigma_{V_p})] = 0.0745$ and $[P(V_p \leq (\mu_{V_p} - 2.17\sigma_{V_p})] = 0.0146$. The low probability associated with these velocity values is a direct indication of the presence of a weak area in the pole.

The equivalent elastic moduli are $\tilde{E}_r = 0.74$ GPa and $\tilde{E}_t = 0.74/0.84 = 0.88$ GPa (Fig. 7.7(d)). These values show that the orthotropic condition of this section is different to the expected conditions for a sound red pine pole ($E_r > E_t$). The equivalent elastic modulus $\tilde{E}_r$ is 51% smaller than the corresponding value without the hole. The equivalent elastic modulus $\tilde{E}_t$ with and without the hole are practically the same. The comparison between the measured and computed arrival time of the compressional wave at each receiver location is presented in Fig. 7.7(e)). The major dispersion between the measured and computed arrival times occur for the receivers located at $\theta_r = \pm 135^\circ$ (30%). It is likely because the raypaths for the receivers located at $\theta_r = \pm 135^\circ$ are more disturbed for the reflections of a hole at the centre than for the receiver located at $\theta_r = 180^\circ$. From numerical simulations, the raypath for the receiver located at $\theta_r = 180^\circ$ surrounds the centric hole and continues its propagation in the radial direction.

The impulse response functions of the system transmitter-pole-receiver for the receiver located at $\theta_r = \pm 90^\circ$, $\theta_r = \pm 135^\circ$, and $\theta_r = 180^\circ$ are presented in Fig. 7.7(f). The first arrival of the compressional wave is not well-defined for the receivers located at $\theta_r = -135^\circ$ and $\theta_r = 180^\circ$ because of the hole and pith locations.

The FRFs for the receivers located at $\theta_r = \pm 90^\circ$, $\theta_r = \pm 135^\circ$, and $\theta_r = 180^\circ$ are presented in Figs. 7.8(a), 7.8(b), and 7.8(c), respectively. Three main peaks are clearly observed at the frequencies of 51, 52.3, and 65.6 kHz. For the receiver located at $\theta_r = 180^\circ$ (Fig. 7.8(c)), the amplitudes at these frequencies are attenuated with respect to the cross-section without the hole by factors of 11, 6, and 3, respectively. The corresponding wavelengths assuming the same velocities V_p of the sound red pine pole RP-03 without the hole vary from 3.0 to 3.8 cm ($\lambda/\phi_{hole} = 0.5 - 0.6$). The frequency of 28.4 kHz ($\lambda/\phi_{hole} = 1.1$ cm) is attenuated by a factor of 9. The transmission factors in the frequency range from 20 to 70 kHz for the receivers located at $\theta_r = 135^\circ$, $\theta_r = 180^\circ$, and $\theta_r = -135^\circ$ are 30% of the corresponding values for the cross-section without the hole (Figs. 7.8(d), 7.8(e), and 7.8(f)). The measured transmission factors are 15% smaller than the repetition variability obtained for 95% of the measurements (Fig. 7.2(b)).

The results for the transmitter locations on the points B, C, and D are presented in Appendix D. The condition assessment of the cross-section for the transmitter located on the points A, B, C, and D is presented in Fig. 7.9. Figure 7.9(a) shows the cross-section where an anomaly has been identified at the centre from the analysis of the results. The ranges of the equivalent elastic modulus and the equivalent elastic ratio are $\tilde{E}_r = 0.74 - 1.05$ GPa and $\tilde{E}_r/\tilde{E}_t = 0.84 - 1.11$. Figure 7.9(b) presents the histogram of the overall dissimilarity index (ODI). The measurements

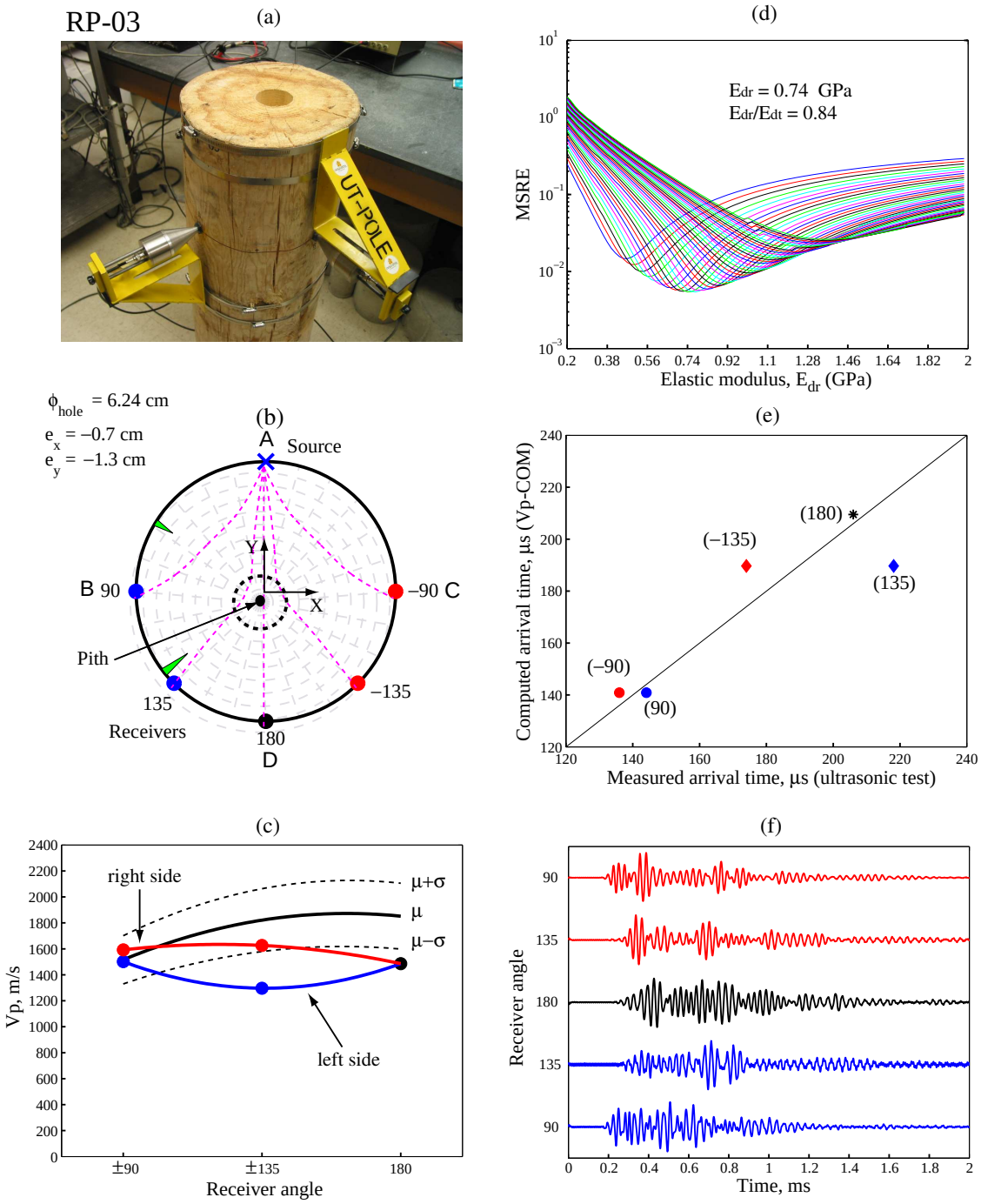

Figure 7.7: Experimental results of ultrasonic testing in red pine pole RP-03 with a centric hole ($\phi = 31.6$ cm, $\phi_{hole} = 6.24$ cm, $MC = 5\%$, $T = 20\,^{\circ}C$): (a) ultrasonic test, (b) source and receiver locations, (c) velocities V_p, (d) elastic moduli E_r and E_t, (e) arrival times, and (f) IRFs

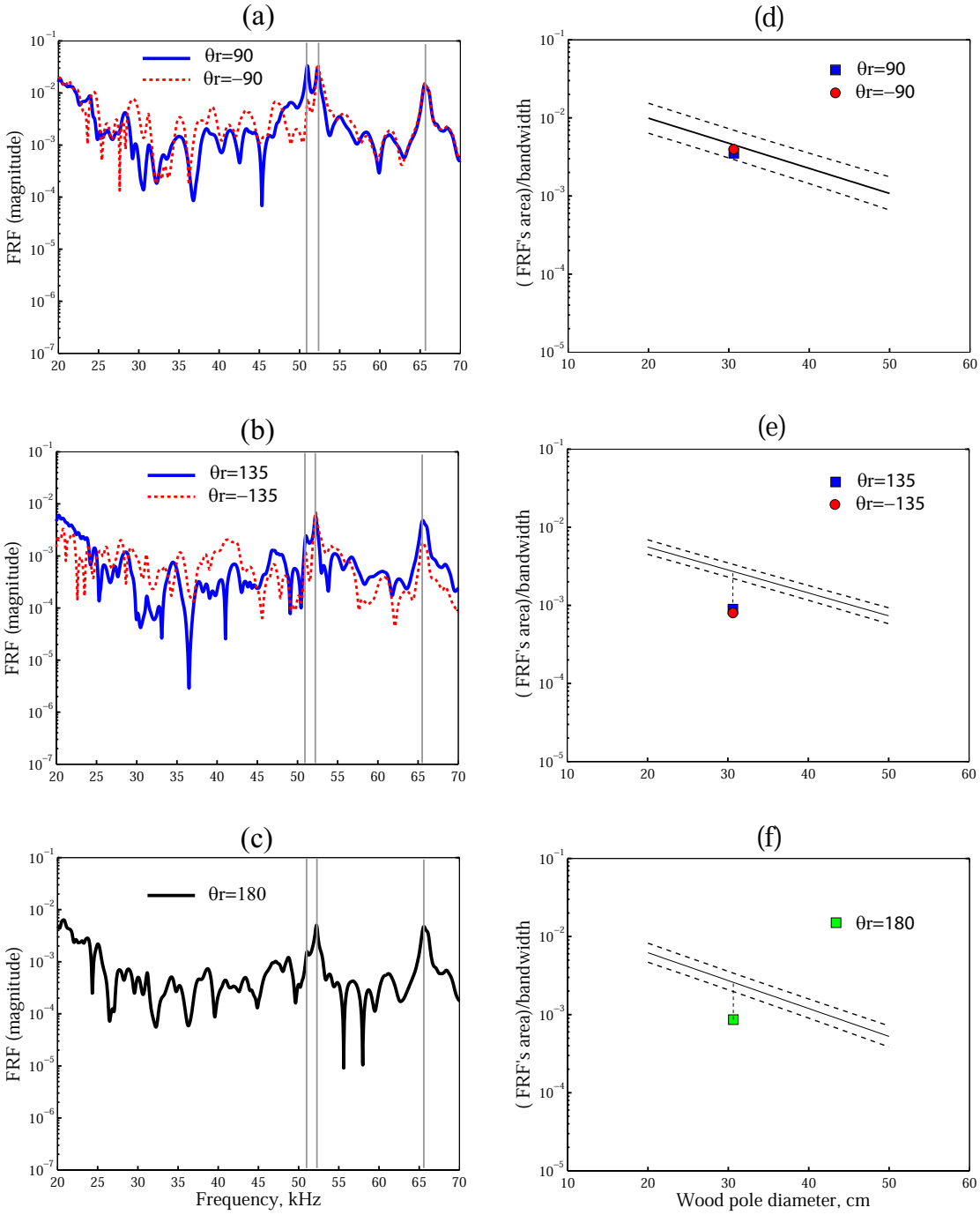

Figure 7.8: Experimental results of ultrasonic testing in red pine pole RP-03 with a centric hole: FRFs for the receivers located at $\theta_r = \pm 90^\circ$ (a), $\theta_r = \pm 135^\circ$ (b), and $\theta_r = 180^\circ$ (c); transmission factors for the receivers located at $\theta_r = \pm 90^\circ$ (d), $\theta_r = \pm 135^\circ$ (e), and $\theta_r = 180^\circ$ (f)

show that 30% of the ODIs are smaller than -2; and 65% are smaller than -1.5.

Figure 7.9(c) shows the variation of the dissimilarity index of the velocity V_p for the receiver located at $\theta_r = 180^\circ$ as function of the hole and pole diameters. The relationships are obtained from numerical simulations for values of $E_r/E_t = 1.2$ and $E_r/E_t = 2$. The mean value for the change in the dissimilarity index of the velocity V_p for the receiver at $\theta_r = 180^\circ$ is $\Delta(DIV_{(180)}) = -1.04$. For $\phi_{pole} = 30.62$ cm and $E_r/E_t = 2$ ($E_r/E_t = 1.7 for the sound pole$, Fig. 7.4(d)), the hole diameter is estimated as 7.52 cm (Fig. 7.9(c)). This value is 20% greater than the diameter of the hole in the cross-section. The difference is likely because the hole has an eccentricity of 5% respect to the diameter of the section, whereas a centric hole is assumed for the numerical simulations. Ultrasonic test results using the new methodology show that the tested section has an anomaly at or close to the centre of the section.

7.4.3 Sound red pine pole RP-03 with an eccentric hole

An eccentric hole of 6.3 cm diameter and 37.5 cm length is drilled at the top of the RP-03 as shown in Fig. 7.10(a). The tested cross-section has a diameter of 30.6 cm and is located at 20 cm from the top of the specimen. The eccentric hole is located at $x = 0.7$ cm and $y = 8.3$ cm from the centre of the section (Fig. 7.10(b)). The wood pith is located at $x = 2.3$ cm and $y = -0.38$ cm from the centre of the section; therefore, the geometric centre, the wood pith, and the hole are not coincident. The velocity V_p curves are presented in Fig. 7.10(c). The velocity V_p curve left side show that $V_{p180} > V_{p90} > V_{p135}$. The curve is concave likewise to the obtained one for the hole at the centre. The relationship between velocities is as expected for the right side ($V_{p180} > V_{p135} > V_{p90}$), but the velocities V_p are 16% smaller than the values for the cross-section without the hole. This behaviour is likely because the wood pith is displaced 2.3 cm to the right of the section (Fig. 7.10(b)). The dissimilarity indexes of the velocity V_p for different receivers are $DIV_{(90)} = 0.2$, $DIV_{(-90)} = -1.2$, $DIV_{(135)} = -1.2$, $DIV_{(-135)} = -1.4$ and $DIV_{(180)} = -1.6$.

The equivalent elastic moduli are $\tilde{E}_r = 1.06$ GPa and $\tilde{E}_t = 1.06/1.36 = 0.78$ GPa (Fig. 7.10(d)). The equivalent elastic moduli $\tilde{E}_r$ and $\tilde{E}_t$ are 30% and 12% smaller than the corresponding values without the hole. The comparison between the measured and computed (using the Vp-COM method) arrival times at each receiver location are presented in Fig. 7.10(e). The major dispersion is found for the receiver located at $\theta_r = \pm 90^\circ$ (27%). It is likely because the reflections generated close to the source have a greater affect on the raypaths to the receivers located at $\theta_r = \pm 90^\circ$.

The impulse response functions of the system transmitter-pole-receiver at different locations are presented in Fig. 7.10(f). The first arrival of the compressional wave is more attenuated for the receivers located at $\theta_r = \pm 135^\circ$ and $\theta_r = 180^\circ$ because of the reflections close to the source.

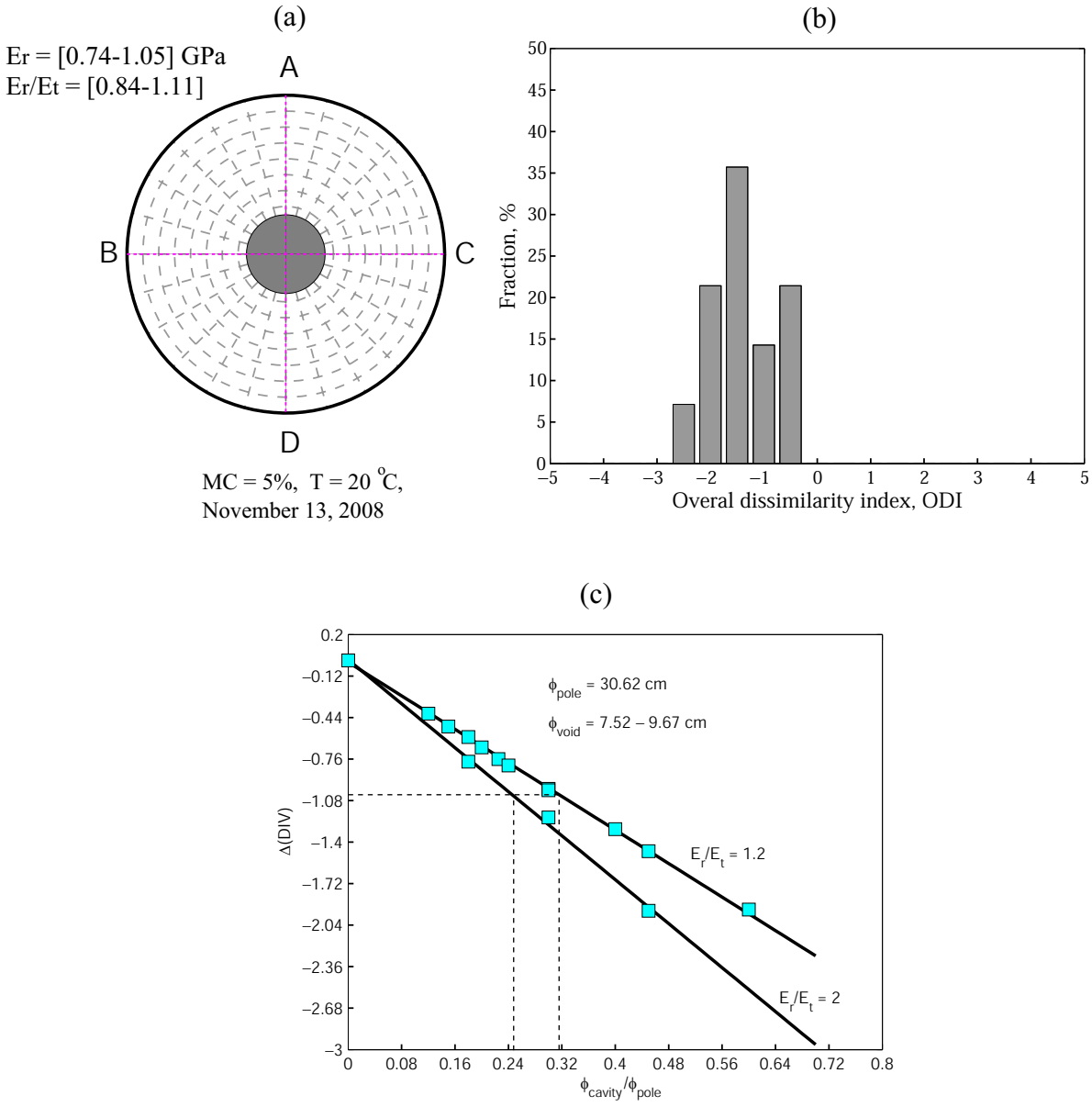

Figure 7.9: Condition assessment of red pine pole RP-03 with a centric hole: elastic moduli and cross-section analysis (a), overall dissimilarity index histogram (b), hole diameter estimation (c)

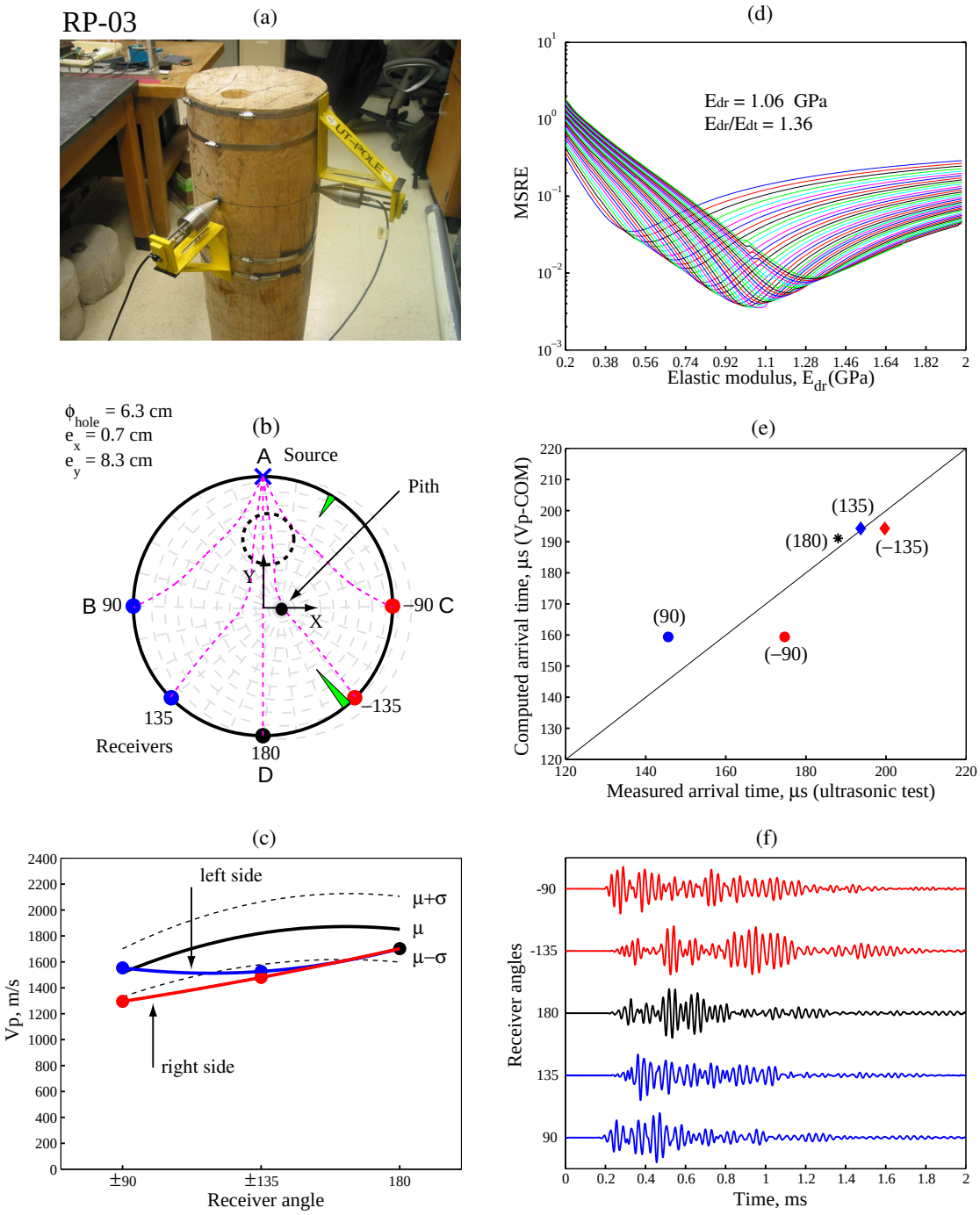

Figure 7.10: Experimental results of ultrasonic testing in red pine pole RP-03 with an eccentric hole ($\phi = 31.6$ cm, $\phi_{hole} = 6.24$ cm, $MC = 5\%$, $T = 20\ ^{\circ}C$): (a) ultrasonic test, (b) source and receiver locations, (c) velocities V_p, (d) elastic moduli E_r and E_t, (e) arrival times, and (f) IRFs

The FRFs are shown in 7.11(a), 7.11(b), and 7.11(c). Two main peaks are observed at the frequencies of 51, and 52.3 kHz. The amplitudes for these frequencies at $\theta_r = 180^\circ$ are attenuated with respect to the cross-section without the hole by un factor of 7. The frequency of 65.4 kHz appears attenuated respect to the cross-section without the hole. The transmission factors in the frequency range from 20 to 70 kHz for the receivers located at $\theta_r = -90^\circ$, $\theta_r = -135^\circ$, and $\theta_r = 180^\circ$ are 28% of the corresponding values for the cross-section without the hole (Figs. 7.8(d), 7.8(e), and 7.8(f)).

The results for the transmitter locations on points B, C, and D are presented in Appendix E. Figure 7.12(a) shows the predicted location and estimated size of the anomaly; whereas Fig. 7.12(b) presents the histograms of the overall dissimilarity index. The ranges of the equivalent elastic modulus and the equivalent elastic ratio are $E_r = 1.06 - 1.57$ GPa and $E_r/E_t = 1.36 - 1.78$. Thirty percent of the ODIs are smaller or equal than -1.

A second set of measurements are performed for the transmitter locations on A', B', C', and D' as shown in Fig. 7.12(c). The new transmitter position system is the original rotated 45° counterclockwise. The location of the anomaly is also identified from the second set of measurements when the transmitter is located on B' and D'. The ranges of the equivalent elastic modulus and the equivalent elastic ratio are $E_r = 1.49 - 1.65$ GPa and $E_r/E_t = 1.59 - 1.77$. These values are similar to the computed values without the hole. It is because the eccentric hole only affects the raypaths at $\theta_r = -135$ when the transmitter is on B' and at $\theta_r = -35$ when the transmitter is on D'. For this case, only 7.4% of the ODIs are smaller or equal than -1.

Ultrasonic test results using the new methodology show that the tested section has an eccentric anomaly located between the point A and the centre of the section. The eccentric anomaly is better identified when the transmitter and receiver locations for $\theta_r = 180^\circ$ define a ray that passes through the anomaly.

7.4.4 Decayed red pine pole RP-002A

The red pine pole RP-002A has a diameter of 21.3 cm and a length of 93.1 cm. The wood presents a condition of advanced decay by looking at the ends of the specimen. The tested section is located at the middle of the pole. The ultrasonic testing and the transmitter and receivers locations are shown in Figs. 7.13(a) and 7.13(b).

The velocity V_p curves are presented in Fig. 7.13(c). The velocities V_p for the receivers at $\theta_r = \pm 135^\circ$ and $\theta_r = 180^\circ$ are smaller than 50% of the expected values for a new red pine pole. On the other hand, the relationship of the velocity V_p curve left side is $V_{p135} > V_{p90} > V_{p180}$. This type of relationship is characteristic of decay close to the receiver located at $\theta_r = 135^\circ$. Another important aspect is that the velocity V_p at $\theta_r = -90^\circ$ is 12% smaller than the expected value.

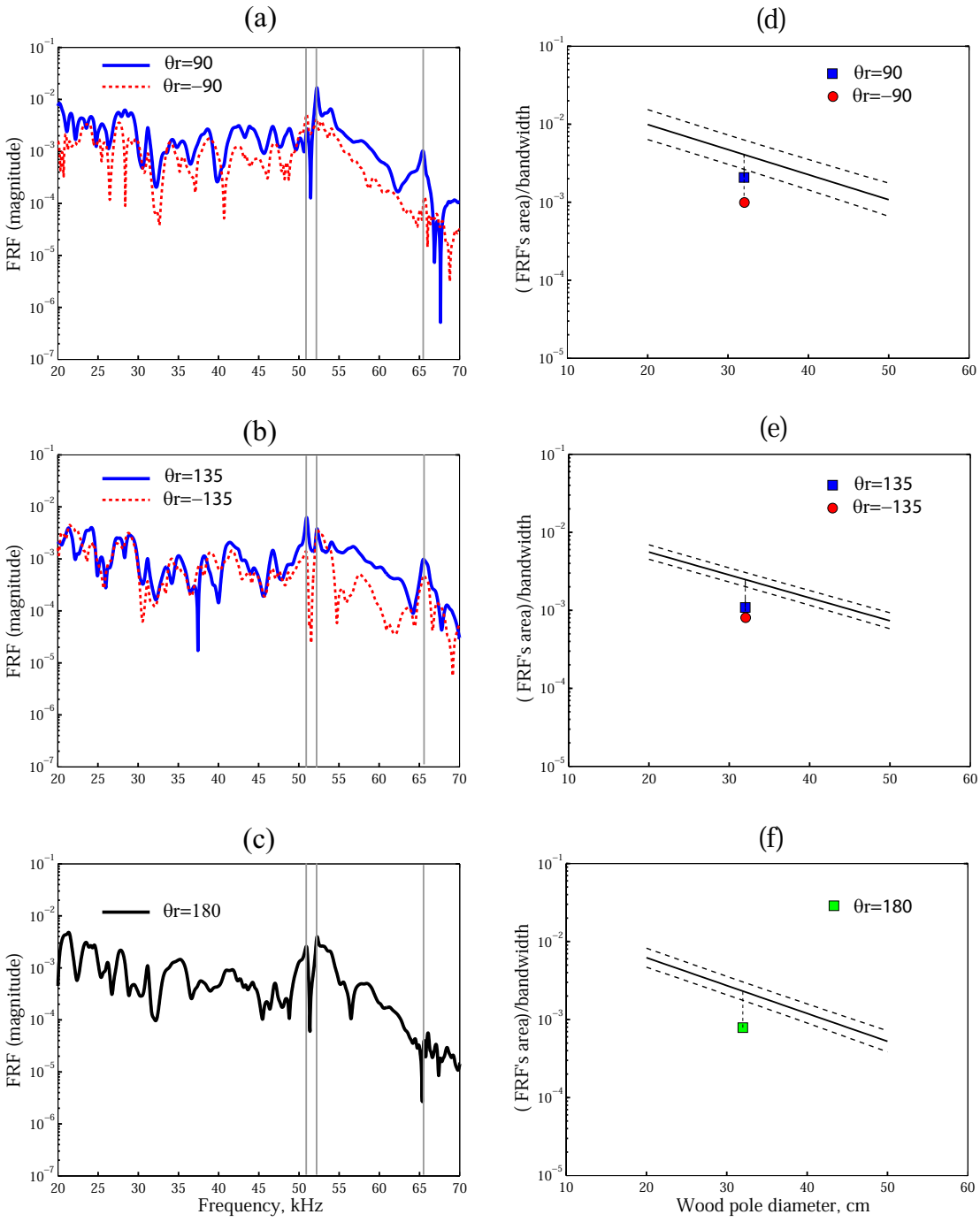

Figure 7.11: Experimental results of ultrasonic testing in red pine pole RP-03 with an eccentric hole: FRFs for the receivers located at $\theta_r = \pm 90°$ (a), $\theta_r = \pm 135°$ (b), and $\theta_r = 180°$ (c); transmission factors for the receivers located at $\theta_r = \pm 90°$ (d), $\theta_r = \pm 135°$ (e), and $\theta_r = 180°$ (f)

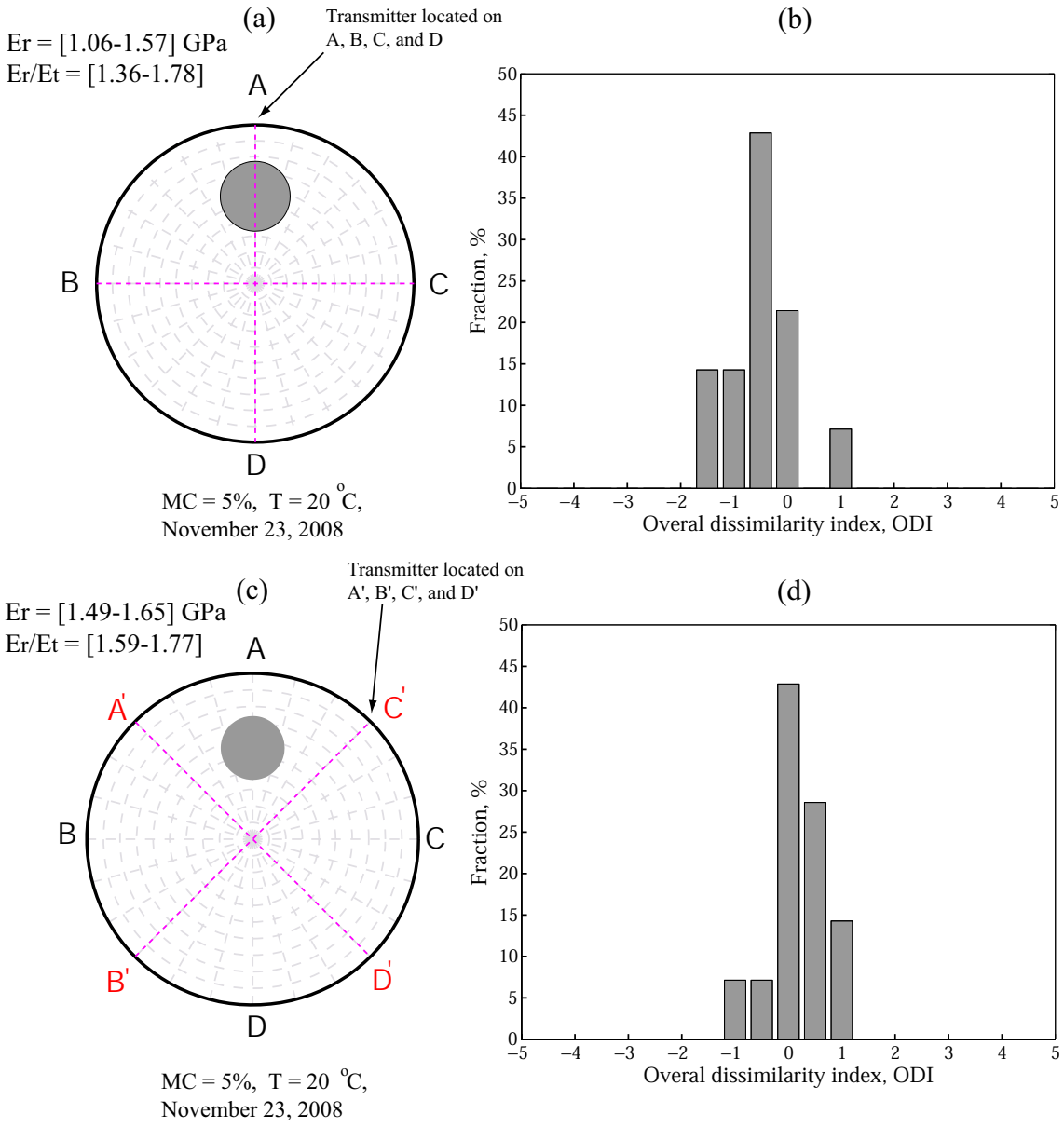

Figure 7.12: Condition assessment of red pine pole RP-03 with an eccentric hole: elastic moduli and cross-section analysis (a) and (c), overall dissimilarity index histogram (b) and (d)

From these results, the decay areas are predicted to be close to the receivers at $\theta_r = \pm 135^\circ$, and at the centre of the section or close to the receiver at $\theta_r = 180^\circ$. An additional set of measurements with the transmitter located on points B or C can determine whether the centre of the section is decayed or not.

The equivalent elastic moduli using the Vp-COM method are $\tilde{E}_r = 0.19$ GPa and $\tilde{E}_t = 0.19/0.49 = 0.39$ GPa (Fig. 7.13(d)). Not only is the elastic modulus $\tilde{E}_r$ equal to 12% of the expected value, but also the ratio $\tilde{E}_r/\tilde{E}_t < 1$. The comparison between the measured and computed (using the Vp-COM method) arrival times of compressional waves at each receiver location is presented in Fig. 7.13(d). The major differences between the measured and computed arrival times are found for the receivers located at $\theta_r = 90^\circ$ and $\theta_r = -135^\circ$. The first arrival of the compressional wave is not well-defined for all the receivers but the receiver at $\theta_r = -90^\circ$ as shown in Fig. 7.13(f).

The FRFs for the receivers located at $\theta_r = \pm 90^\circ$, $\theta_r = \pm 135^\circ$, and $\theta_r = 180^\circ$ are shown in Figs. 7.14(a), 7.14(b), and 7.14(c), respectively. The transmission factor for the receiver at $\theta_r = 90$ is more than 20 times smaller than the transmission factor at $\theta_r = -90^\circ$ (Fig. 7.14(d)). A main peak at the frequency of 57.4 kHz is clear observed for the receivers located at $\theta_r = \pm 90^\circ$ and $\theta_r = \pm 135^\circ$. This frequency is more attenuated at $\theta_r = 90^\circ$ and $\theta_r = -135^\circ$. For the receiver at $\theta_r = 180^\circ$, the frequency of 57.4 kHz is not well-defined. These results are in agreement with the measured velocities V_p. The transmission factors for the receivers located at $\theta_r = \pm 135^\circ$ and $\theta_r = 180^\circ$ are 42 and 37 times smaller than the corresponding expected values for a new red pine pole as shown in Figs. 7.14(e) and 7.14(f). These levels of transmission factors are clear indication of decay. From these results, the decayed areas are located at the centre of the section and toward the receiver at $\theta_r = 90^\circ$. Ultrasonic tests for other transmitter positions can be used to confirm the decayed area locations.

7.4.5 Red pine RP-010 (Blind test)

The wood condition of the poles previously analyzed are known (sound with ad without a hole or decayed red pine poles), but the wood condition of the red pine pole RP-010 is unknown; therefore, it is a blind test (no decay observed at the ends of the specimen). The pole specimen RP-010 has a diameter of 22.1 cm and a length of 100 cm. The tested section is located at the middle of the pole. The ultrasonic test and locations of the transmitter and receivers are shown in Figs. 7.15(a) and 7.15(b). The transmitter is located on the point A. Radial cracks greater than 2 mm are not observed on the wood pole surface. There is external evidence that the wood pole was treated with preservative.

The P-wave velocity curves are presented in Fig. 7.15(c). The velocities V_p for the receivers

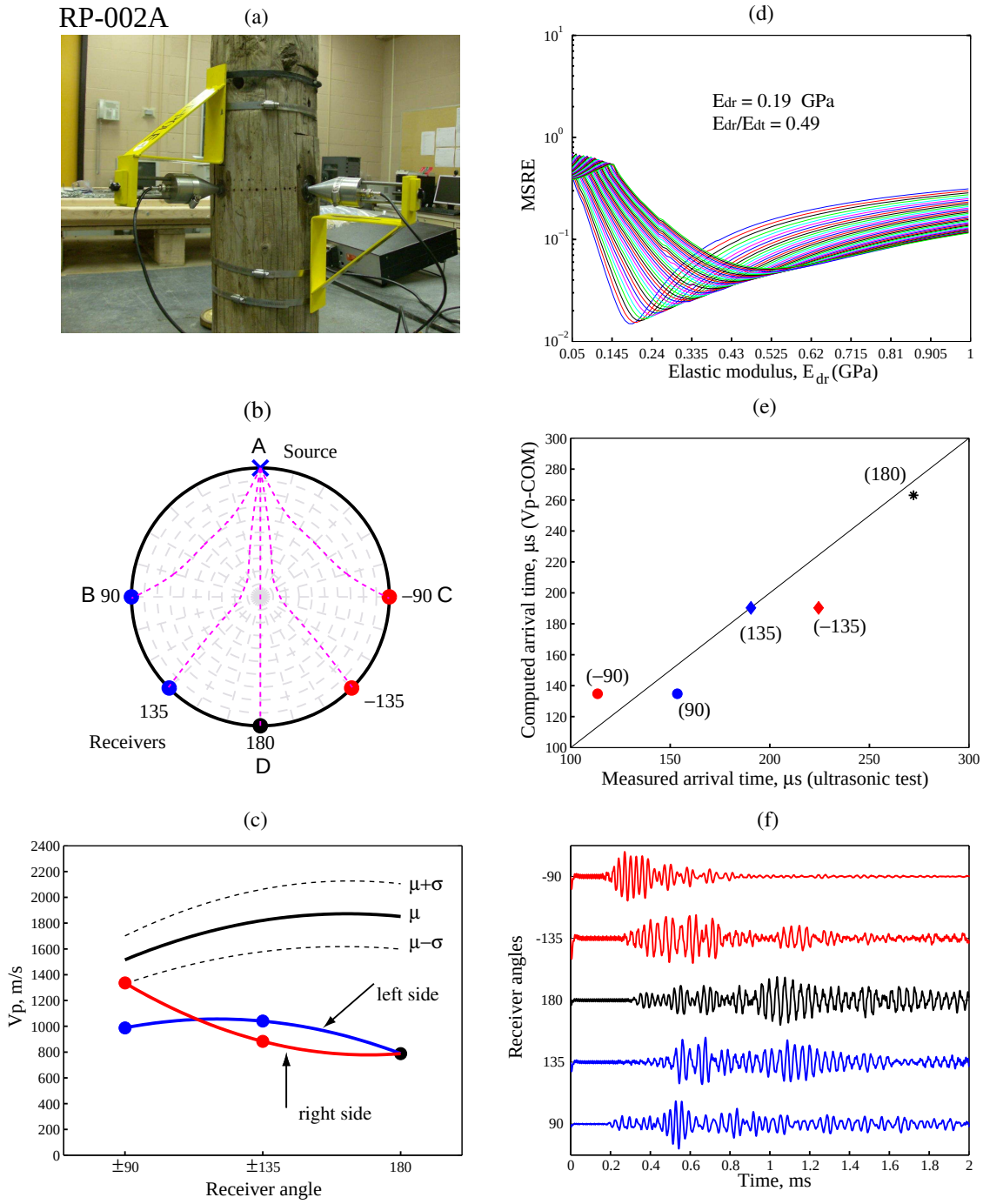

Figure 7.13: Experimental results of ultrasonic testing in red pine pole RP-002A ($\phi = 21.3$ cm, $MC = 5\%$, $T = 20\ ^{\circ}C$): (a) ultrasonic test, (b) source and receiver locations, (c) velocities V_p, (d) elastic moduli E_r and E_t, (e) arrival times, and (f) IRFs

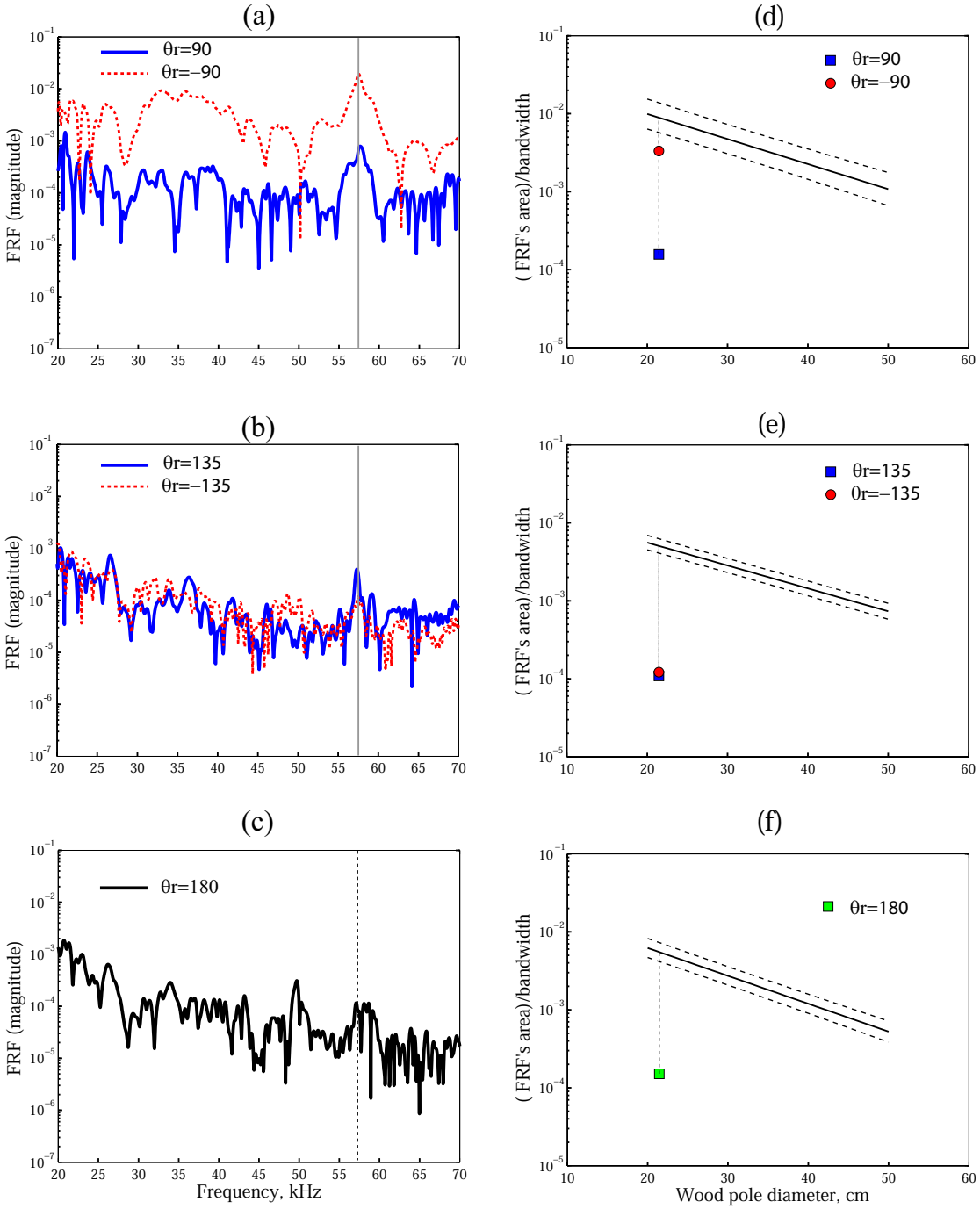

Figure 7.14: Experimental results of ultrasonic testing in red pine pole RP-002A: FRFs for the receivers located at $\theta_r = \pm 90^\circ$ (a), $\theta_r = \pm 135^\circ$ (b), and $\theta_r = 180^\circ$ (c); transmission factors for the receivers located at $\theta_r = \pm 90^\circ$ (d), $\theta_r = \pm 135^\circ$ (e), and $\theta_r = 180^\circ$ (f)

at $\theta_r = \pm 135^\circ$ and $\theta_r = 180^\circ$ are smaller than 50% of the expected values for a new red pine pole. The velocity V_p curves, left and right sides, follow the relationship $V_{p90} < V_{p135} < V_{p180}$. The velocities V_p for the receivers at $\theta_r = 90^\circ$ and $\theta_r = 135^\circ$ are smaller than the corresponding values at $\theta_r = -90^\circ$ and $\theta_r = -135^\circ$. This condition means that the left side of the section defined by the points A, B, and D is more deteriorated than the right side.

The equivalent elastic moduli using the Vp-COM method are $\tilde{E}_r = 0.29$ GPa and $\tilde{E}_t = 0.29/0.69 = 0.42$ GPa (Fig. 7.15(d)). The arrival times for the receivers at $\theta_r = 90^\circ$, $\theta_r = 135^\circ$, and $\theta_r = 180^\circ$ are used to solve the inverse problem because the velocities V_p are smaller. When the arrival times of all the receivers are included to solve the inverse problem, the new equivalent elastic moduli are $\tilde{E}_r = 0.26$ GPa and $\tilde{E}_t = 0.52$ GPa. The equivalent elastic modulus $\tilde{E}_r$ is smaller than 20% of the expected value for a new red pine, and the equivalent elastic ratio is smaller than 1 ($\tilde{E}_r/\tilde{E}_t < 0.69$). The comparison between the measured and computed (using the Vp-COM method) arrival time of the compressional wave at each receiver location is presented in Fig. 7.15(d). The major difference between the measured and computed arrival times is found for the receiver located at $\theta_r = 135^\circ$.

The first arrival of the compressional wave is not well-defined for the receivers located at $\theta_r = 90^\circ$, $\theta_r = \pm 135^\circ$, and $\theta_r = 180^\circ$ as shown from the IRFs in Fig. 7.15(f). The effect is more remarkable for the receivers located at $\theta_r = 135^\circ$ and $\theta_r = 180^\circ$. The IRF looks as expected for the receiver located at $\theta_r = -90^\circ$. These results are in agreement with the velocities V_p shown in Fig. 7.15(c).

The FRFs for the receivers located at $\theta_r = \pm 90^\circ$, $\theta_r = \pm 135^\circ$, and $\theta_r = 180^\circ$ are shown in Figs. 7.15(a), 7.15(b), and 7.15(c), respectively. The transmission factors for the receivers located at $\theta_r = 90^\circ$ and $\theta_r = 135^\circ$ are smaller than the corresponding values at $\theta_r = -90^\circ$ and $\theta_r = -135^\circ$. These results are also in agreement with the measured velocities V_p. A main peak at the frequency of 57.4 kHz is clear observed for the receivers located at $\theta_r = -90^\circ$, $\theta_r = \pm 135^\circ$, and $\theta_r = 180^\circ$. This frequency appears attenuated for the receiver at $\theta_r = 90^\circ$. The transmission factors are shown in Figs. 7.15(d), 7.15(e), and 7.15(f). For the receivers located at $\theta_r = 90^\circ$, $\theta_r = 135^\circ$, $\theta_r = 180^\circ$, $\theta_r = -135^\circ$, and $\theta_r = -90^\circ$, the transmission factors are 15, 42, 38, 16, and 2.2, respectively. The smaller transmission factor occurs at $\theta_r = 135^\circ$; and the larger one, at $\theta_r = -90^\circ$. These results are in agreement with the measured velocities V_P.

Ultrasonic test evaluations for the transmitter located on the points B, C, and D, are carried out. The results are presented in Appendix F. Figure 7.17(a) shows the decayed area locations inside the pole identified from ultrasonic testing; and in Fig. 7.17(b), the histogram of the overall dissimilarity index. The decayed areas are identified from the dissimilarity indexes of the different raypaths for the transmitter locations on the points A, B, C, and D around the pole surface. The deterioration is concentrated between the centre of the section and the pole surface and is

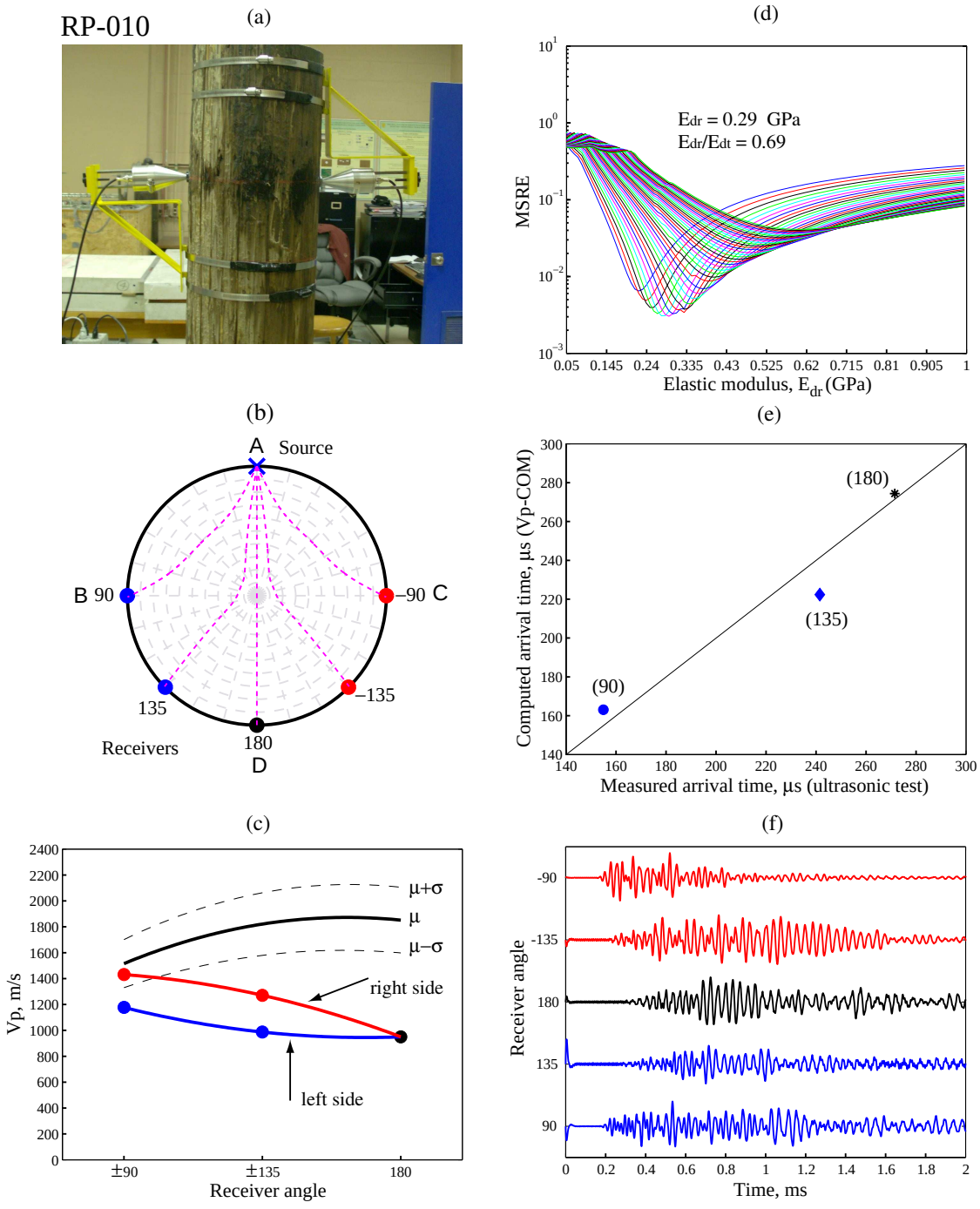

Figure 7.15: Experimental results of ultrasonic testing in red pine pole RP-010 ($\phi = 22.1$ cm, $MC = 5\%$, $T = 20\ ^{\circ}C$): (a) ultrasonic test, (b) source and receiver locations, (c) velocities V_p, (d) elastic moduli E_r and E_t, (e) arrival times, and (f) IRFs

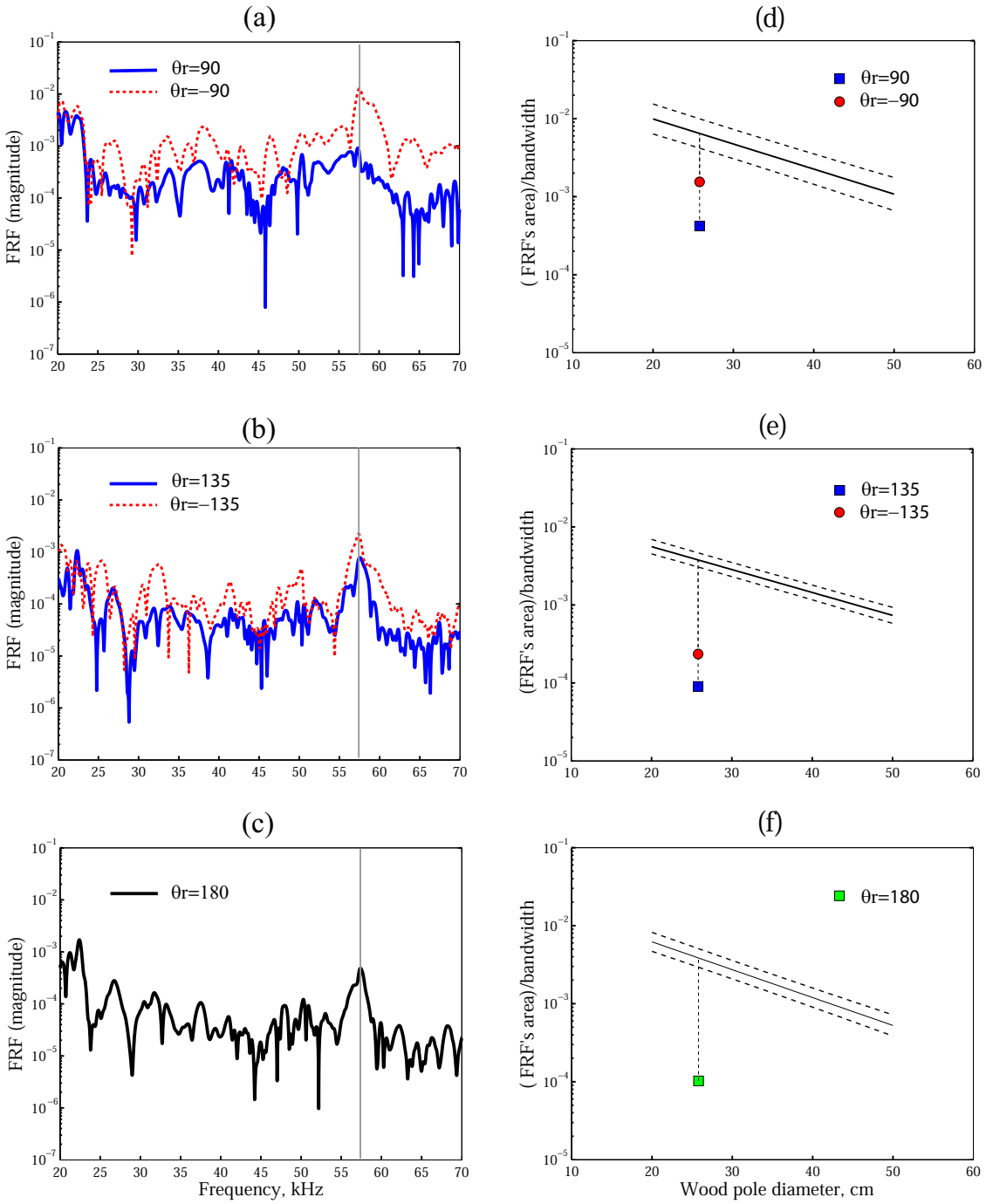

Figure 7.16: Experimental results of ultrasonic testing in red pine pole RP-010: FRFs for the receivers located at $\theta_r = \pm 90^\circ$ (a), $\theta_r = \pm 135^\circ$ (b), and $\theta_r = 180^\circ$ (c); transmission factors for the receivers located at $\theta_r = \pm 90^\circ$ (d), $\theta_r = \pm 135^\circ$ (e), and $\theta_r = 180^\circ$ (f)

greater towards the receivers located at $\theta_r = 90^\circ$ and $\theta_r = 180^\circ$. The ranges of the equivalent elastic modulus and equivalent elastic ratio are $\tilde{E}_r = 0.26 - 0.78$ GPa and $\tilde{E}_r/\tilde{E}_t = 0.51 - 1.44$. Fourteen independent overall dissimilarity indexes are determined from all the measurements. Eighty five percent of them are smaller or equal than -2.5.

After the ultrasonic tests are analyzed, the wood pole is cut transversally. Figure 7.17(c) shows the wood pole section where can be clearly detected two major areas of decay. One of decayed area is located between the points A and B with a major deterioration close to B. This decayed area represents 10% of the section area. The second decayed area is located between the points B and D and between D and C. This decayed area represents 20% of the section area. The wood between the points A and C looks in good condition. A preservative penetration of 1.5 cm is clearly observed, and the wood pith has an eccentricity of 4% of the pole diameter measured from the centre of the section. The deterioration pattern is in agreement with the obtained one from ultrasonic testing. Numerical simulations of this section are presented in Sub-section 6.3.3.

7.5 Chapter Summary

P-wave velocity measurements on cross-sections of a wood pole are very consistent when the same coupling is used but interchanging the transmitter and the receiver, or when the UT-Pole device is assembled and disassembled. A maximum deviation less than 2.5% for the velocity V_p is obtained for 70% of the measurements, whereas 30% of the measurements showed a deviation between 2.5% and 5% in the calculation of the velocity V_p. Hence, a variation in the velocity V_p of 5% could be measured precisely with the UT-Pole device.

The transmission factors are different when the transducers are interchanged (same coupling) or the UT-Pole device is assembled and disassembled again. When the transducer are interchanged, 70% of the measurements have a deviation less than 5%; and 30%, show a deviation between 5% and 15%. For the second case, 42% of the measurements have a maximum deviation of 15%; whereas a maximum deviation of 45% is obtained for 94% of the measurements. The deviation in the transmission factor for group 2 is greater than group 1 because the direction and inclination of the transducers are not exactly the same for different assemblies of the system.

The velocity V_p is related with moisture content and temperature by eqn. (4.31). Therefore, changes in moisture content can be determined from changes in the velocity V_p for the same wood specie.

The velocity V_p for a sound wood pole cross-section follows the relationship $V_{p180} > V_{p135} > V_{p90}$. This relationship is modified when the wood pole has a hole or presents decayed areas.

The Vp-COM method assumes that the pole cross-section is cylindrically orthotropic and a homogeneous material. Therefore, the inverse process gives the elastic moduli of an equivalent

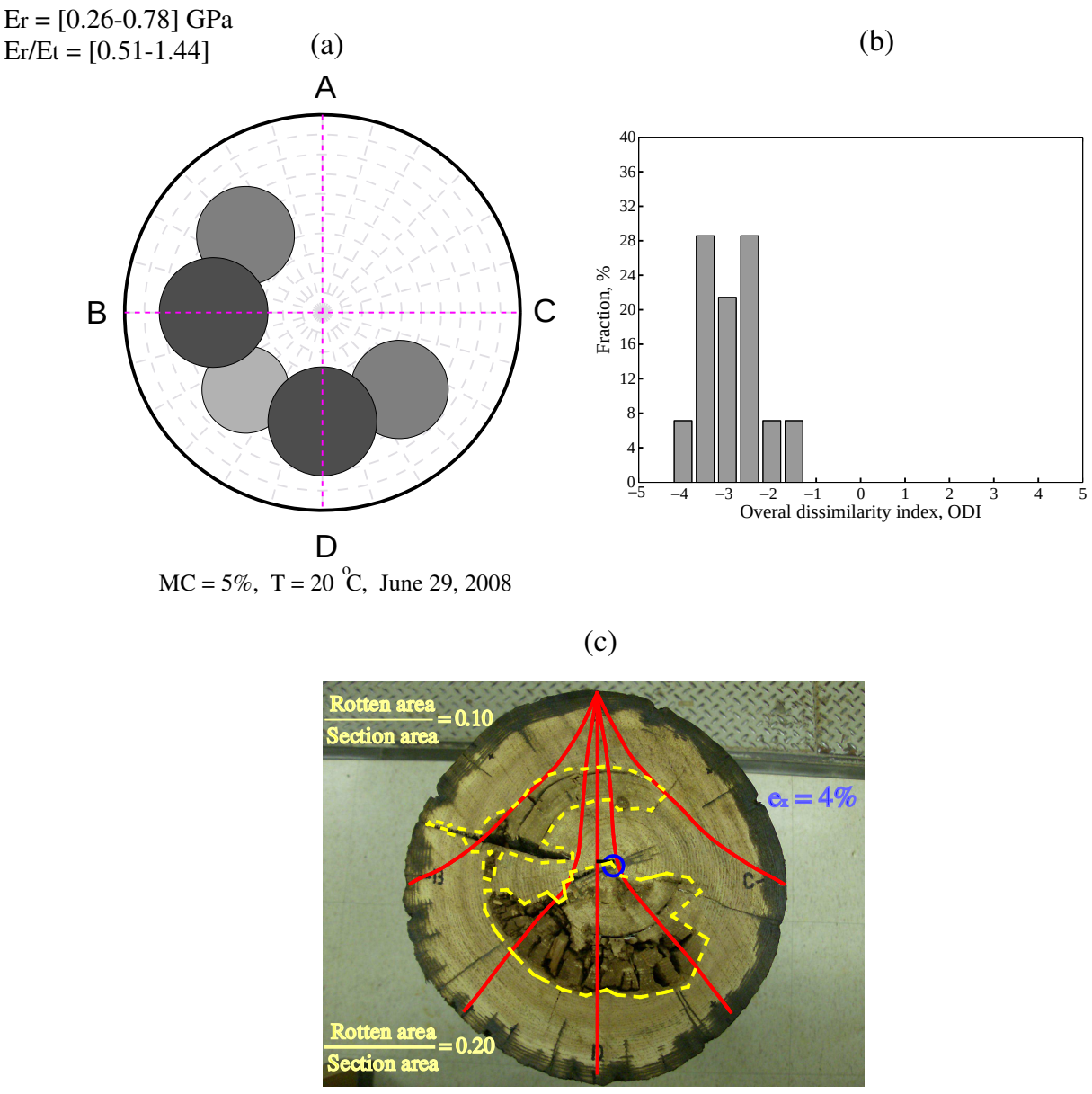

Figure 7.17: Condition assessment of red pine pole RP-010: elastic moduli and cross-section analysis (a), overall dissimilarity index histogram (b), tested section (c)

homogeneous wood cross-section with the pith at the centre.

The impulse response functions show the first arrival of the compressional wave at each receiver location as well as other wavefront arrivals produced by the convex geometry of the cross-section. The first arrival of the compressional wave is not well-defined when the wood is decayed.

The transmission factor is a ratio between the vibration energies of the receiver and the source for a given frequency bandwidth. The transmission factor decreases in decayed sections because the wave attenuation is greater. The transmission factors decreases also by the presence of a hole because of destructive interference and wave reflections. The transmission factor is the reciprocal of the attenuation factor.

The overall dissimilarity index represents the number of standard deviation respect to the expected value for sound wood poles. An acceptable criterion for sound condition of a wood pole is to select a value of dissimilarity index α_d such that $P[ODI \geq \alpha_d] = 0.95$. For a normal distribution, $\alpha_d = -1.6$. The decayed areas are predicted from the dissimilarity indexes for the transmitter locations on different points around the pole surface.

The new methodology based on ultrasonic testing can be successfully used for condition assessment of wood poles. The new methodology could detect a centric and a eccentric hole of 6.3 cm diameter in the cross-section of a sound red pine pole.

The velocity V_p and the transmission factor for the receiver located at $\theta_1 80^\circ$ are decreased in 23% and 70% by the centric hole, respectively. For an eccentric hole, the same value is obtained for the transmission factor but 12% of decreasing for the velocity V_p. The eccentric hole is better identified when the transmitter and receiver locations for $\theta_r = 180^\circ$ define a ray that passes through the anomaly. The new methodology could also detect successfully decayed areas inside of a wood pole. For a decay of 30% of the cross-section, the velocity V_p and the transmission factor decreased 51% and 96%, respectively. The predicted areas of decay from the ultrasonic measurements are in good agreement with the actual decay observed from dissecting the pole sections.

Chapter 8

Conclusions and Recommendations

A new methodology for condition assessment of wood poles using ultrasonic testing is presented. This methodology includes advances in the areas of ultrasonic wave propagation in a cylindrical orthotropic medium, signal processing, numerical simulations, statistical analysis, and ultrasonic transducer characterization. The proposed methodology can detect centric or eccentric holes larger than of 6 cm diameter in wood poles. The location of decayed areas in a cross-section of wood poles is also successfully determined by the new methodology.

A new specialized software (WPNDTool-Box) for data and signal processing in time and in frequency domains is developed in MatLab. The software contains different modules with all the required functions for pre-processing, processing, and post-processing time signals from ultrasonic testing.

Experimental and numerical results show that the complex exponential method (CEM) can be successfully used for dynamic characterization of ultrasonic transmitters subjected to different electrical excitation pulses. Dynamic parameters such as amplitude, resonant frequency, damping ratio, and phase angle are obtained for each vibration mode of the transmitter. The CEM is a parametric method, so it is not affected by the spectral leakage problem that exists in the Fourier analysis.

The effects of different excitation pulses on the response of an ultrasonic transmitter are studied experimentally and numerically. The lowest response of the ultrasonic transmitter at the nominal frequency is obtained for the linear-exponential pulse, which is commonly used in commercial systems. This result is in agreement with the theoretical evaluation of the spectral energy functions. The linear-exponential pulse has the widest frequency content. For one-cycle electrical pulses at the nominal frequency of the transmitter, the square pulse produced the largest response. The spectral ratios at the maximum amplitudes for the square pulse and the sinusoidal, triangle, and sawtooth pulses are 1.9, 3.0, and 5.2, respectively. These results are in agreement

with the ratios computed from the theoretical spectra of these pulses. When the number of cycles is increased to three, the maximum response of the ultrasonic transmitter is increased almost by a factor of three. Thus, the use of three-cycle pulses is beneficial when testing high-attenuation materials.

The source characterization of ultrasonic transmitters can be used for full-waveform analysis in ultrasonic testing. The results from finite element numerical simulations of wave propagation in an aluminum bar and laboratory experiments are in good agreement. This characterization allows the use of ultrasonic testing beyond common practice applications to measure velocity dispersion curves in laboratory specimens.

A simplified method of analysis for 2D-wave propagation in a cylindrical orthotropic medium is presented. The new method called Vp-COM is based on the closed-form solution of a plane wave propagating in an orthotropic medium. The Vp-COM method is validated using wave propagation results from finite element analysis. The method is used to compute the probability density function of the P-wave velocity (V_p) in a cross-section of a wooden pole for different receiver locations along the circumference. Uncertainties in the elastic and mechanical properties are defined by the user; and there is not limitation on the number of simulations. The second application of the Vp-COM method is the estimation of the elastic moduli in the radial and tangential directions of wooden poles. This estimation is done by solving the inverse problem given the velocities V_p measured from ultrasonic testing. The inverted elastic moduli are used for condition assessment and health monitoring of wooden poles.

A finite-element numerical model is presented to study ultrasonic wave propagation in cross-sections of red pine poles considering the wood as a cylindrical orthotropic material. The strain level in the longitudinal direction is an order of magnitude smaller than the strain in the radial direction because of the high anisotropy of the wood; therefore, plain strain conditions is assumed. The numerical model is validated using ultrasonic tests performed in new red pine pole sections. The calibrated model is used for the understanding of ultrasonic wave propagation in cross-sections of wood poles including holes and decayed areas.

The UT-Pole device is designed and built for ultrasonic testing in cross-sections of wood poles. The UT-Pole device is easy to install and versatile. It can be used at any distance from the ground level, and it is practically isolated from the cross-section being tested. P-wave velocity measurements are consistent for a given measurement or even after swapping the transmitter and receiver or after re-assembling the UT-Poly system. A maximum deviation less than 2.5% for the velocity V_p is obtained for 70% of the measurements, whereas 30% of the measurements showed a deviation between 2.5% and 5% in the calculation of the velocity V_p.

The velocity V_p is related with moisture content and temperature by eqn. (4.31). Therefore, changes in moisture content can be determined from changes in the velocity V_p for the same

wood specie.

Experimental modal analysis can be used to estimate the elastic modulus in the longitudinal direction of a wood pole specimen; whereas, the radial and tangential elastic moduli can be estimated using ultrasonic tests in conjunction with the Vp-COM method.

A Rayleigh damping model adjusted with measured values of damping ratio can be used to model wave attenuation in wood pole cross-sections. The obtained damping model is inversely proportional to frequency (mass-proportional damping). The difference between the measured and the calculated attenuation factors for the receiver located at $\theta_r = 180^\circ$ is 2%. For the receivers located at $\theta_r = 90^\circ$ and $\theta_r = 135^\circ$, the maximum difference is less than 20%.

A centric hole of 6.3 cm diameter can be detected by using ultrasonic tests with a transmitter of 50 kHz. The presence of a centric hole changes the expected behaviuor of sound wood pole cross-sections ($V_{p180} > V_{p135} > V_{p90}$). The Velocity V_p for the receiver located at $\theta_r = 180^\circ$ is smaller than the corresponding value at $\theta_r = 135^\circ$. The velocity V_p and the transmission factor for the receiver located at $\theta_1 80^\circ$ are decreased in 23% and 70% by the centric hole, respectively. For an eccentric hole, the same value is obtained for the transmission factor but 12% of decreasing for the velocity V_p. The eccentric hole is better identified when the transmitter and receiver locations for $\theta_r = 180^\circ$ define a ray that passes through the anomaly.

Penetrometer tests can be used to estimate the elastic moduli of an aged/decayed red pine pole from the elastic moduli of a new red pine pole. The difference between the computed (using the estimated elastic moduli) and the measured velocity V_p is less than 18%.

The transmission factors are different when the transducers are interchanged (same coupling) or the UT-Pole device is assembled and disassembled again. When the transducer are interchanged, 70% of the measurements have a deviation less than 5%; and 30%, show a deviation between 5% and 15%. For the second case, 42% of the measurements have a maximum deviation of 15%; whereas a maximum deviation of 45% is obtained for 94% of the measurements. The deviation in the transmission factor for group 2 is greater than group 1 because the direction and inclination of the transducers are not exactly the same for different assemblies of the system.

The transmission factor decreases in decayed sections because the wave attenuation is greater, and decreases by the presence of a hole because of destructive interference and wave reflections.

The impulse response functions show the first arrival of the compressional wave at each receiver location as well as other wavefront arrivals produced by the convex geometry of the cross-section. The first arrival of the compressional wave is not well-defined when the wood is decayed.

The overall dissimilarity index (ODI) representing the deviation of the measurements respect to the expected behaviour of a sound pole is successfully used for the condition assessment of wood poles. The ODI at each receiver location is a function of the characterization features and

the corresponding statistical parameters. An acceptable criterion for sound condition of a wood pole is to select a value α_d such that $P[ODI \geq \alpha_d = 0.95]$. For a normal distribution, $\alpha_d = -1.6$. The decayed areas are predicted from the dissimilarity indexes for the transmitter locations on different points around the pole surface.

For a decay of 30% of the cross-section, the velocity V_p and the transmission factor decreased 51% and 96%, respectively. The observed deterioration pattern is in agreement with the obtained one from ultrasonic testing.

The following recommendations are addressed as topics for future research:

- Improvement of the UT-Pole device by (a) reducing the transducer size, (b) making a belt structure to supporting eight ultrasonic transducers around the pole, and (c) using wireless technology.

- Use of modular neural network (MNN) for the direct calculation of the first arrival of compressional waves, the elastic moduli, and the dissimilarity indexes as function of moisture content and temperature.

- Statistical characterization of P-wave velocity, mass density, and transmission factor for most common wood species used as utility poles in Canada (red pine, lodgepole pine, and Western red cedar).

- Evaluation of an empirical relationship between the elastic moduli obtained from ultrasonic tests (E_r and E_t) and the rupture modulus obtained from bending tests (MOR).

APPENDICES

Appendix A

Vp-COM: Matlab code

```
%
%
%  Vp-COM is a simplified method for P-wave propagation in
%  the cross-section of a wood pole.
%  Wood is modeled as cylindrical orthotropic material
%  under plain strain conditions. Vp-COM is based on the
%  closed form solution of plane wave propagation in an
%  orthotropic medium represented in cartesian coordinates.
%
%  Fernando Tallavo, 2009
%
%
%

clc
clear all
prompt={'Fs: factor for static El','Fd: factor for dynamic Ed',...
        'Number of rays or receiver angles','Time (us)','Diameter (cm)',...
        'MC, %','T, in Celsius'};
name='P-wave velocity in cilindrical orthotropic medium';
defaultanswer={'1.1','1.2','90 135 180','0','26.6','12','20'};
try
answer=inputdlg(prompt,name,1,defaultanswer);
Fs=cell2mat(answer(1,:));
Fs=str2num(Fs);
Fd=cell2mat(answer(2,:));
Fd=str2num(Fd);
Na=cell2mat(answer(3,:));
Na=str2num(Na);
AT=cell2mat(answer(4,:));
```

```
AT=str2num(AT);
Diameter=cell2mat(answer(5,:));
Diameter=str2num(Diameter);
MC=cell2mat(answer(6,:));
MC=str2num(MC);
T0=cell2mat(answer(7,:));
T0=str2num(T0);
catch
    return
end
 Na_l=length(Na);
Delta_g=0.05; % Delta angle
R_a=Diameter/2;
  a1=R_a*sqrt(2*(1-cos(Na*pi/180)));
  Phi_a=acos(a1./(2*R_a));
  Angle_a=90-Phi_a*180/pi;
q=menu('Wood specie','Western red cedar','Douglas-fir','Western larch',...
       'Red pine','Lodgepole pine','User');
if q==1
    Ind=2;
elseif q==2;
    Ind=3;
elseif q==3;
    Ind=4;
elseif q==4;
    Ind=6;
elseif q==5;
    Ind=8;
elseif q==6;
    Ind=10;
end
Mp=[25
    25
    24
    28
    24
    24
    25
    25];
WP=['EWC'
    'WRC'
    'DOF'
    'WEL'
```

```
    'TAM'
    'RPI'
    'JPI'
    'LPI'
    'ISO'];
E_l=[4.38
8.27
13.5
14.3
9.38
9.45
10.20
10.90
13.5*0.068];
E_l=E_l*1.0003414e9*Fd*Fs;
E_l_FSP=[3.55
7.24
11.10
11.40
8.55
7.38
8.07
8.76
13.5*0.068];
E_l_FSP=E_l_FSP*1.0003414e9*Fd*Fs;
Gs=[0.30
0.34
0.49
0.58
0.51
0.46
0.44
0.41
0.49];
Gs_FSP=[0.30
0.31
0.45
0.55
0.48
0.41
0.42
0.40
0.49];
```

```
if q<=5
     R_t=(1-(T0-20)*(0.0129*MC+0.04)/100);
E_l(Ind)=E_l(Ind)*(E_l(Ind)/E_l_FSP(Ind))^((12-MC)/(Mp(Ind)-12));
E_l(Ind)=E_l(Ind)*R_t;
Rho=1000*Gs_FSP(Ind)*(1+MC/100)/(1-(30-MC)/30*0.265*Gs_FSP(Ind));
else
end
R_lr=[0.07
0.081
0.068
0.079
0.086
0.088
0.085
0.102
1.0];
R_ls=[0.050
0.055
0.05
0.065
0.057
0.044
0.052
0.068
1.0];
E_r=R_lr.*E_l;
E_s=R_ls.*E_l;
R_sr=E_r./E_s;
u_lr=[0.337
0.378
0.292
0.355
0.3375
0.347
0.3375
0.316
0];
u_rl=(E_r./E_l).*u_lr;
u_rs=[0.458
0.484
0.390
0.389
0.4330
```

```
0.408
0.4330
0.469
0];
u_sr=(E_s./E_r).*u_rs;
u_ls=[0.340
0.296
0.449
0.276
0.3372
0.315
0.3372
0.347
0];
u_sl=(E_s./E_l).*u_ls;
R_G_lr=[0.0713
0.087
0.064
0.063
0.069
0.096
0.071
0.049
0.5/1.1];
R_G_rs=[0.018
0.005
0.007
0.007
0.008
0.011
0.007
0.005
0.5/1.1];
R_G_ls=[0.0700
0.086
0.078
0.069
0.063
0.081
0.067
0.046
0.5/1.1];
G_lr=R_G_lr.*E_l;
```

```
G_rs=R_G_rs.*E_l;
G_ls=R_G_ls.*E_l;
if Ind==10
prompt={'E_l (GPa)',...
        'Gs',...
        'R_lr (Er/El)',...
        'R_lt (Et/El)',...
        'RG_rt (G/El)',...
        'u_lr',...
        'u_rt',...
        'u_lt'};
name='P-wave velocity in a cilindrical orthotropic material';
defaultanswer={'7.80','0.46','0.1397','0.1167','0.011','0.347','0.408','0.315'};
answer=inputdlg(prompt,name,1,defaultanswer);
E_lt=cell2mat(answer(1,:));
E_l(10)=str2num(E_lt)*1.0003414e9;
Gst=cell2mat(answer(2,:));
Gs(10)=str2num(Gst);
R_lrt=cell2mat(answer(3,:));
R_lr(10)=str2num(R_lrt);
R_lst=cell2mat(answer(4,:));
R_ls(10)=str2num(R_lst);
R_G_rst=cell2mat(answer(5,:));
R_G_rs(10)=str2num(R_G_rst);
u_lrt=cell2mat(answer(6,:));
u_lr(10)=str2num(u_lrt);
u_rst=cell2mat(answer(7,:));
u_rs(10)=str2num(u_rst);
u_lst=cell2mat(answer(8,:));
u_ls(10)=str2num(u_lst);
E_r(10)=R_lr(10)*E_l(10);
E_s(10)=R_ls(10)*E_l(10);
R_sr(10)=E_r(10)/E_s(10);
u_rl(10)=(E_r(10)/E_l(10)).*u_lr(10);
u_sr(10)=(E_s(10)/E_r(10)).*u_rs(10);
u_sl(10)=(E_s(10)/E_l(10)).*u_ls(10);
G_rs(10)=R_G_rs(10)*E_l(10);
Rho=Gs(10)*1000;
else
end
%
D=E_r(Ind)*E_l(Ind)-u_lr(Ind)^2*E_r(Ind)^2-u_rs(Ind)^2*E_s(Ind)*E_l(Ind) ...
-2*u_rs(Ind)*u_lr(Ind)*u_ls(Ind)*E_s(Ind)*E_r(Ind)-u_ls(Ind)^2*E_s(Ind)*E_r(Ind);
```

```
C11=((E_l(Ind)-u_lr(Ind)^2*E_r(Ind))*E_r(Ind)*E_s(Ind))/D;
C12=((u_rs(Ind)*E_l(Ind)+u_lr(Ind)*u_ls(Ind)*E_r(Ind))*E_r(Ind)*E_s(Ind))/D;
C22=((E_l(Ind)-u_ls(Ind)^2*E_s(Ind))*E_r(Ind)^2)/D;
C33=G_rs(Ind);
Su=0;
for kq=1:Na_l
i=0;
x0=0;
y0=1;
%
x0_s=0;
y0_s=1;
%
%
% ========================================================================
% ========================================================================
%
%
Lj=Angle_a(kq)*pi/180;
%
if Lj==pi/2
    ax=-cos(Lj);
    ay=-sin(Lj);
m2=sin(Lj)/cos(Lj);
    x2=0;
    y2=-1;
Theta1=abs(atan(y2/x2));
if y2>0
Theta2=pi/2-Theta1;
else
Theta2=pi/2+Theta1;
end
M_d=Theta2*180/pi;
Bx=1;
By=0;
a_x(1)=ax*Bx+ay*By;
a_y(1)=ay*Bx-ax*By;
R1(1)=a_x(1)^2+a_y(1)^2;
Gamma_11=C11*a_x(1)^2+(C33)*a_y(1)^2;
Gamma_12=(C33+C12)*a_x(1)*a_y(1);
Gamma_22=C22*a_y(1)^2+(C33)*a_x(1)^2;
V_ph1=sqrt((Gamma_11+Gamma_22+sqrt((Gamma_11-Gamma_22)^2+4*Gamma_12^2))/(2*Rho));
V_ph2=sqrt((Gamma_11+Gamma_22-sqrt((Gamma_11-Gamma_22)^2+4*Gamma_12^2))/(2*Rho));
```

```
if V_ph1>V_ph2
    Vp_2(1)=V_ph1;
    Vs_2(1)=V_ph2;
else
    Vp_2(1)=V_ph2
    Vs_2(1)=V_ph1;
end
x1_2=0;
y1_2=-1;
%
%
% 88888888888888888888888888888888888888888888888888888888888888888888888888888888
%
%
else  % If Lj
ax=-cos(Lj);              % director cosine
ay=-sin(Lj);              % director cosine
m2=sin(Lj)/cos(Lj);
if Lj==pi/2
    x2=0;
    y2=-1;
elseif Lj==0;
      x2=0;
      y2=1;
else
x2=-(2*m2)/(1+m2^2);
y2=m2*x2+1;
end
Theta1=abs(atan(y2/x2));
if y2>0
Theta2=pi/2-Theta1;
else
Theta2=pi/2+Theta1;
end
M_d=Theta2*180/pi;
for j=1:Delta_g:M_d+1
    i=i+1;
Bx=cos((j-1)*pi/180);
By=cos(pi/2-(j-1)*pi/180);
a_x(i)=ax*Bx+ay*By;
a_y(i)=ay*Bx-ax*By;
R1(i)=a_x(i)^2+a_y(i)^2;
Gamma_11=C11*a_x(i)^2+(C33)*a_y(i)^2;
```

```
Gamma_12=(C33+C12)*a_x(i)*a_y(i);
Gamma_22=C22*a_y(i)^2+(C33)*a_x(i)^2;
V_ph1=sqrt((Gamma_11+Gamma_22+sqrt((Gamma_11-Gamma_22)^2+4*Gamma_12^2))/(2*Rho));
V_ph2=sqrt((Gamma_11+Gamma_22-sqrt((Gamma_11-Gamma_22)^2+4*Gamma_12^2))/(2*Rho));
if V_ph1>V_ph2
    Vp(i)=V_ph1;
    Vs(i)=V_ph2;
else
    Vp(i)=V_ph2;
    Vs(i)=V_ph1;
end
if abs(a_y(i))<1e-10;
 U_x_p(i)=1;
 U_y_p(i)=0;
 U_x_s(i)=0;
 U_y_s(i)=1;
elseif abs(a_x(i))<1e-10;
 U_x_p(i)=0;
 U_y_p(i)=1;
 U_x_s(i)=1;
 U_y_s(i)=0;
else
U_x_p(i)=1;
U_y_p(i)=(Rho*Vp(i)^2-Gamma_11)/Gamma_12;
U_x_s(i)=1;
U_y_s(i)=(Rho*Vs(i)^2-Gamma_11)/Gamma_12;
end
alpha_x_p(i)=U_x_p(i)/sqrt(U_x_p(i)^2+U_y_p(i)^2);
alpha_y_p(i)=U_y_p(i)/sqrt(U_x_p(i)^2+U_y_p(i)^2);
alpha_x_s(i)=U_x_s(i)/sqrt(U_x_s(i)^2+U_y_s(i)^2);
alpha_y_s(i)=U_y_s(i)/sqrt(U_x_s(i)^2+U_y_s(i)^2);
alphax_p(i)=Bx*alpha_x_p(i)-By*alpha_y_p(i);
alphay_p(i)=Bx*alpha_y_p(i)+By*alpha_x_p(i);
alphax_s(i)=(Bx*alpha_x_s(i)-By*alpha_y_s(i));
alphay_s(i)=(Bx*alpha_y_s(i)+By*alpha_x_s(i));
Angle(i)=j-1;
m(i)=sin(acos(alphax_p(i)))/alphax_p(i);
m1(i)=-cos((j)*pi/180)/sin((j)*pi/180);
m_s(i)=-sin(acos(alphax_s(i)))/cos(acos(alphax_s(i)));
m1_s(i)=cos((j)*pi/180)/sin((j)*pi/180);
x1(i)=(m(i)*x0-y0)/(m(i)-m1(i));
y1(i)=m(i)*(x1(i)-x0)+y0;
x1_s(i)=(m_s(i)*x0_s-y0_s)/(m_s(i)-m1_s(i));
```

```
y1_s(i)=m_s(i)*(x1_s(i)-x0_s)+y0_s;
x0=x1(i);
y0=y1(i);
x0_s=x1_s(i);
y0_s=y1_s(i);
end
%
X_Vp=Vp.*cos(Angle*pi/180);
Y_Vp=Vp.*sin(Angle*pi/180);
X_Vs=Vs.*cos(Angle*pi/180);
Y_Vs=Vs.*sin(Angle*pi/180);
R=sqrt(x1.^2+y1.^2);
I1=find(R<=1);
x1_2=x1(I1);
y1_2=y1(I1);
Vp_2=Vp(I1);
R2=sqrt(x1_s.^2+y1_s.^2);
I2=find(R2<=1);
x1_2s=x1_s(I2);
y1_2s=y1_s(I2);
%Vs_2=Vs(I2);
Vs_2=Vs(I1);
if length(Na)<=3
displa=(diff([0, x1_2]).^2+diff([1, y1_2]).^2).^0.5;
displa=displa*Diameter/2;
Time_q=((displa)/100)./Vp_2(1:length(displa));
Time_q=Time_q;
eval(['figure(' num2str(kq) ')'])
%subplot(2,1,1)
plot(Angle(1:length(Vp_2)),Vp_2,'-b')
hold on
plot(Angle(1:length(Vs_2)),Vs_2,'-r')
hold off
xlabel('Position angle, degree')
ylabel('Wave velocity, m/s')
eval(['title(' '''' 'Receiver angle ' num2str(Na(kq)) ', degree' '''' ')'])
legend('P-wave velociy','Shear wave velocity')
legend boxoff
else
end
end
%
%
```

```
% ========================================================================
% ========================================================================
%
%
figure(4)
if kq==1
set(gca,'DataAspectRatio',[1,1,1])
hold on
for k=1:10
R=0.1*k;
[x_cir,y_cir]=Circle_s(R);
plot(x_cir,y_cir,'--','color',[0.88 0.87 0.89]);
end
for k=0:10:180
Theta=k*pi/180;
Sig=1;
[x_lin,y_lin]=Line_s(Theta,Sig);
plot(x_lin,y_lin,'--','color',[0.88 0.87 0.89]);
plot(x_lin,y_lin,'--','color',[0.88 0.87 0.89]);
end
for k=180:10:360
Theta=k*pi/180;
Sig=-1;
[x_lin,y_lin]=Line_s(Theta,Sig);
plot(x_lin,y_lin,'--','color',[0.88 0.87 0.89]);
plot(x_lin,y_lin,'--','color',[0.88 0.87 0.89]);
end
else
end
[Xv,Yv] = scircle1(0,0.0,1);
plot(Xv,Yv,'--k')
x1_2=[0, x1_2];
y1_2=[1, y1_2];
if AT==0
disp2=(diff(x1_2).^2+diff(y1_2).^2).^0.5;
Time=(disp2*Diameter/200)./Vp_2(1:length(disp2));
Lt=length(Time);
Time=cumsum(Time);
Time_f(kq)=Time(Lt);
if length(Na)<=3
disp('Angle')
disp(Na(kq))
disp('Time')
```

```
disp(Time_f(kq)*1e6)
else
end
D_CR(kq)=sum(disp2)*Diameter/2;
theta_a=(Na(kq)-90)*pi/180;
D_DR(kq)=Diameter/2*sqrt(2)*sqrt(1+sin(theta_a));
if D_CR(kq)<D_DR(kq)
    D_CR(kq)=D_DR(kq);
    Time_f(kq)=(D_DR(kq)/100)/mean(Vp_2);
else
end
Vp_LR(kq)=D_DR(kq)/Time_f(kq)/100;
Vp_CR(kq)=D_CR(kq)/Time_f(kq)/100;
Time_f(kq)*1e6;
Vp_LR(kq)=round(Vp_LR(kq));
Vp_CR(kq)=round(Vp_CR(kq));
Vp_mean(kq)=round(mean(Vp_2));
Vp_max(kq)=round(max(Vp_2));
Vp_min(kq)=round(min(Vp_2));
try
Vs_max(i)=max(Vs_2);
Vs_min(i)=min(Vs_2);
Vs_mean(i)=mean(Vs_2);
catch
end
plot([0 x2],[1 y2],'--m')
plot([0 -x2],[1 y2],'--m')
if Lj~=pi/2
plot([x1_2(:)],[y1_2(:)],'-b');
plot([-x1_2(:)],[y1_2(:)],'-b');
else
end
eval(['text(x2*1.4,y2*1.1,' '''' num2str(Vp_CR(kq)) ' m/s' '''' '),'])
xlabel('X')
ylabel('Y')
axis([-1 1 -1 1])
axis off
else
disp2=(diff(x1_2).^2+diff(y1_2).^2).^0.5;
Time=(disp2*Diameter/200)./Vp_2(1:length(disp2))*1e6;
Time=cumsum(Time);
Jp=find(Time>AT);
try
```

```
 Dr=cumsum(disp2);
 T_a=atan(y1_2(Jp(1))/x1_2(Jp(1)));
 Ax1=x1_2(Jp(1)+1);
 Ay1=y1_2(Jp(1)+1);
 x_0=Ax1;
 y_0=Ay1;
plot(x_0,y_0,'ob');
plot(-x_0,y_0,'ob');
catch
end
xlabel('X')
ylabel('Y')
axis([-1 1 -1 1])
axis off
end
xq=[0 x1_2]';
yq=[1 y1_2]';
Sd=0;
for k=2:length(xq);
Sd=Sd+sqrt((xq(k)-xq(k-1))^2+(yq(k)-yq(k-1))^2);
end
clear x1_2 y1_2 x1 y1
clear a_x a_y Vp Vs U_x_p U_y_p
clear U_x_s U_y_s alpha_x_p alpha_y_p
clear alpha_x_s alpha_y_s Angle m m1
clear m_s m1_s R1
clear x1_s y1_s X_Vp Y_Vp X_Vs Y_Vs
clear Vp_2 R2 I1 I2
clear x1_2s y1_2s alphax_p alphay_p alphax_s alphay_s
clear disp2 Time Dr disp2 Time_q Vp_3 displa
end
hold off
```

Appendix B

Red pine poles RP-01, RP-02, and RP-04

Pole RP-01, source located on A

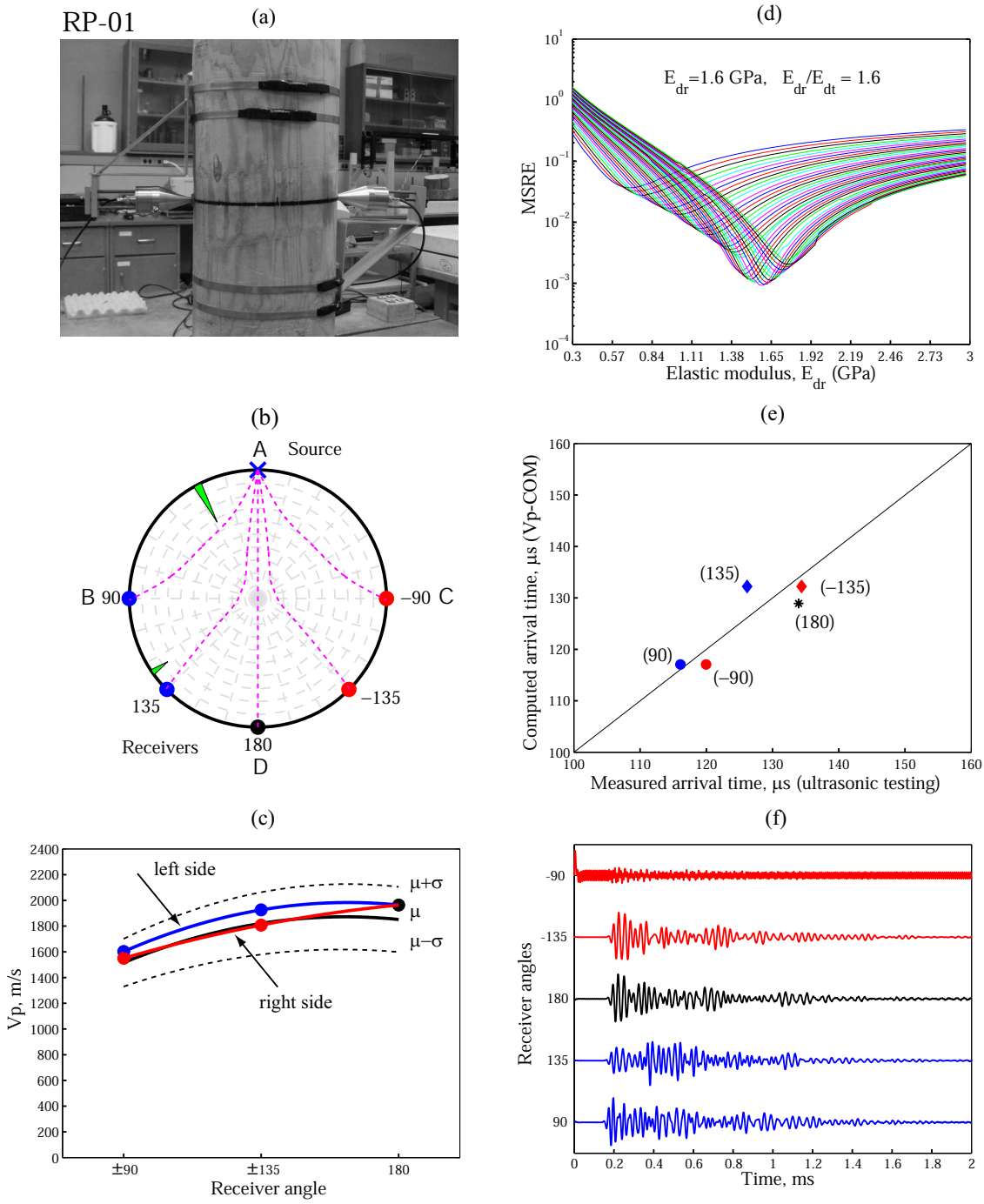

Figure B.1: Experimental results of ultrasonic testing in red pine pole RP-01 ($\phi = 31.6$ cm, $MC = 5\%$, $T = 20\ ^{\circ}C$, source on B): (a) ultrasonic test, (b) source and receiver locations, (c) V_p velocities, (d) elastic moduli E_r and E_t, (e) arrival times, and (f) IRFs

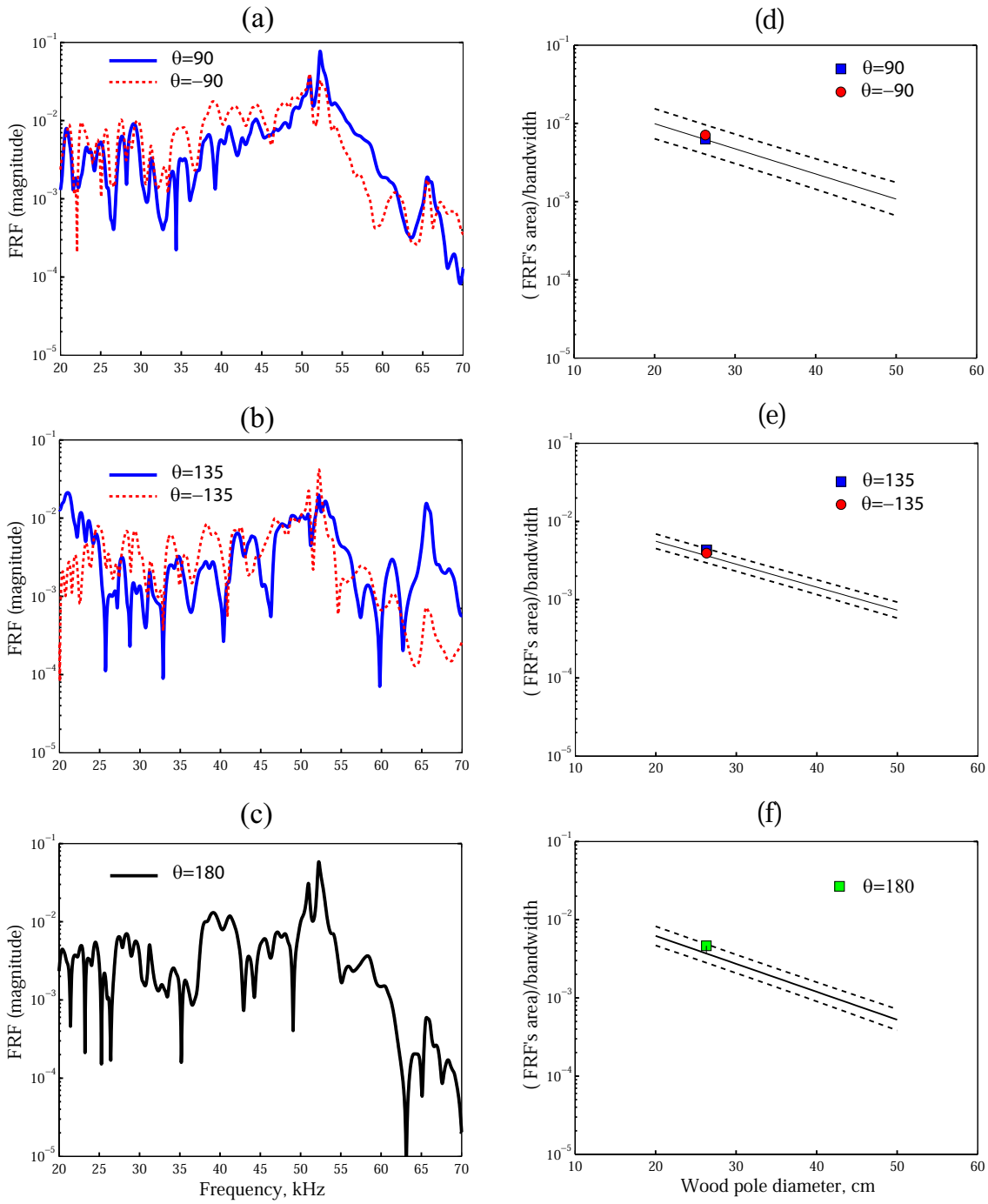

Figure B.2: Experimental results of ultrasonic testing in red pine pole RP-01: FRF for the receivers located at $\theta_r = \pm 90^\circ$ (a), $\theta_r = \pm 135^\circ$ (b), and $\theta_r = 180^\circ$ (c); wave attenuation for the receivers located at $\theta_r = \pm 90^\circ$ (d), $\theta_r = \pm 135^\circ$ (e), and $\theta_r = 180^\circ$ (f)

Pole RP-02, source located on A

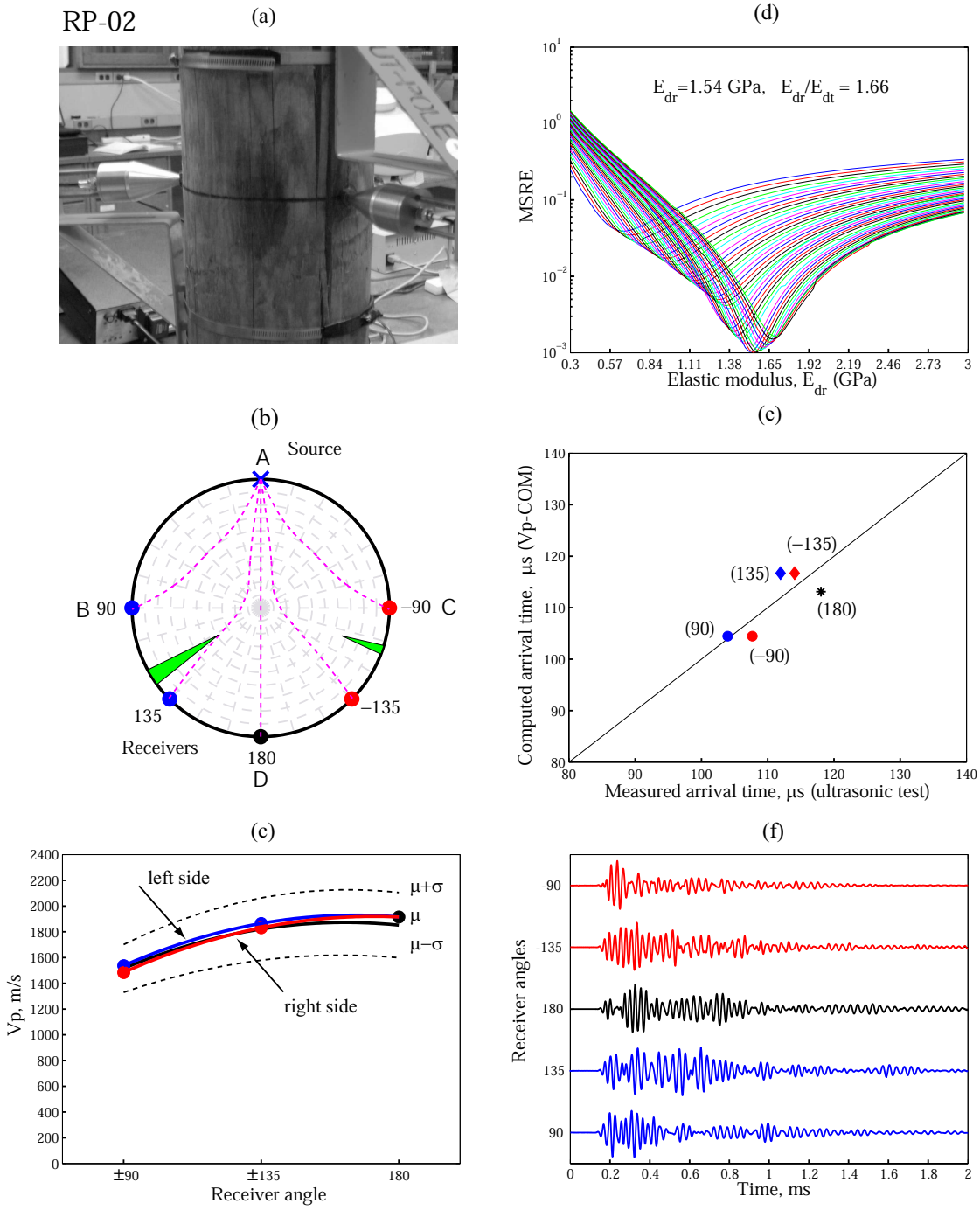

Figure B.3: Experimental results of ultrasonic testing in red pine pole RP-02 ($\phi = 31.6$ cm, $MC = 5\%$, $T = 20\ ^{\circ}C$, source on C): (a) ultrasonic test, (b) source and receiver locations, (c) V_p velocities, (d) elastic moduli E_r and E_t, (e) arrival times, and (f) IRFs

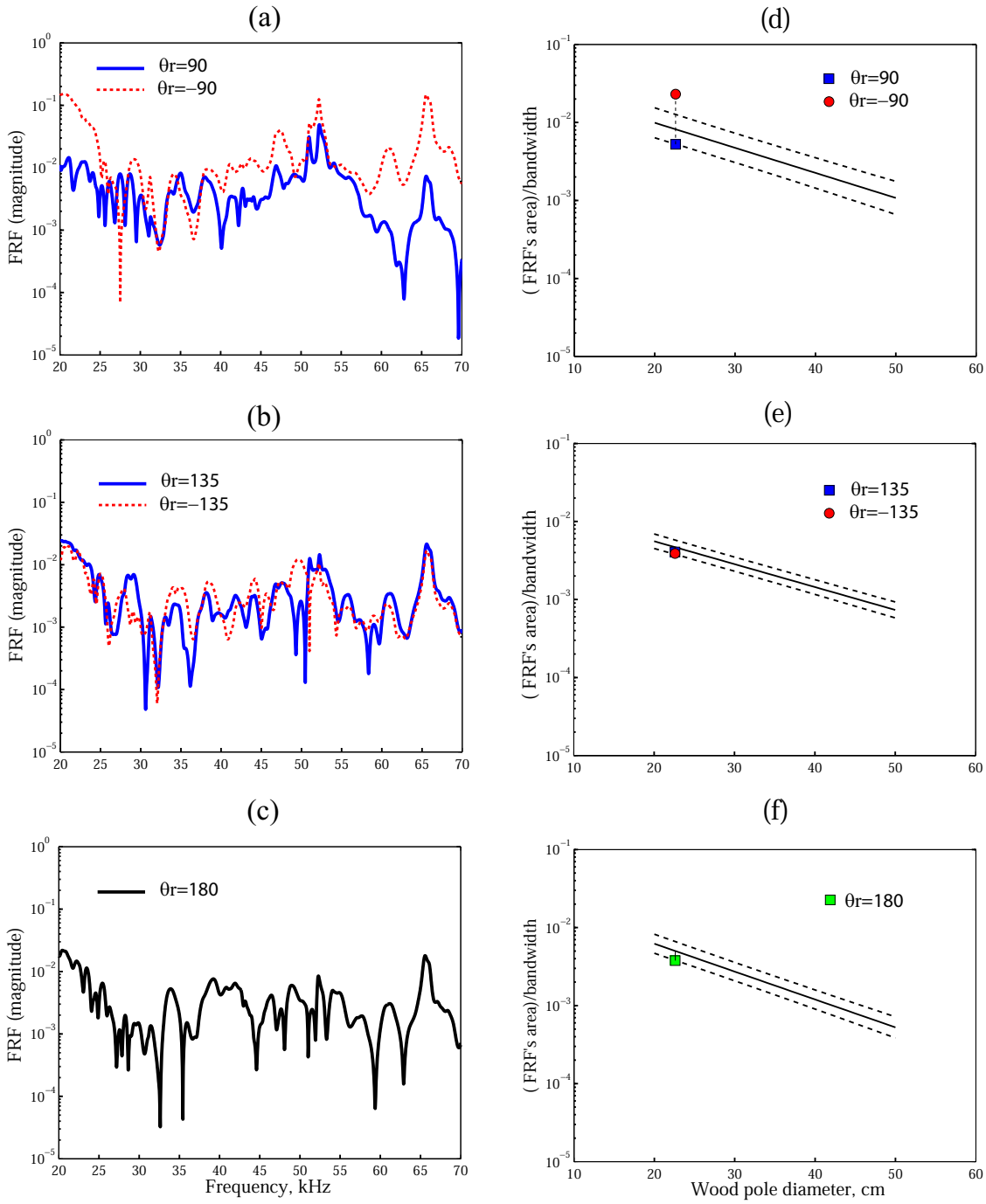

Figure B.4: Experimental results of ultrasonic testing in red pine pole RP-02: FRF for the receivers located at $\theta_r = \pm 90^\circ$ (a), $\theta_r = \pm 135^\circ$ (b), and $\theta_r = 180^\circ$ (c); wave attenuation for the receivers located at $\theta_r = \pm 90^\circ$ (d), $\theta_r = \pm 135^\circ$ (e), and $\theta_r = 180^\circ$ (f)

Pole RP-04, source located on A

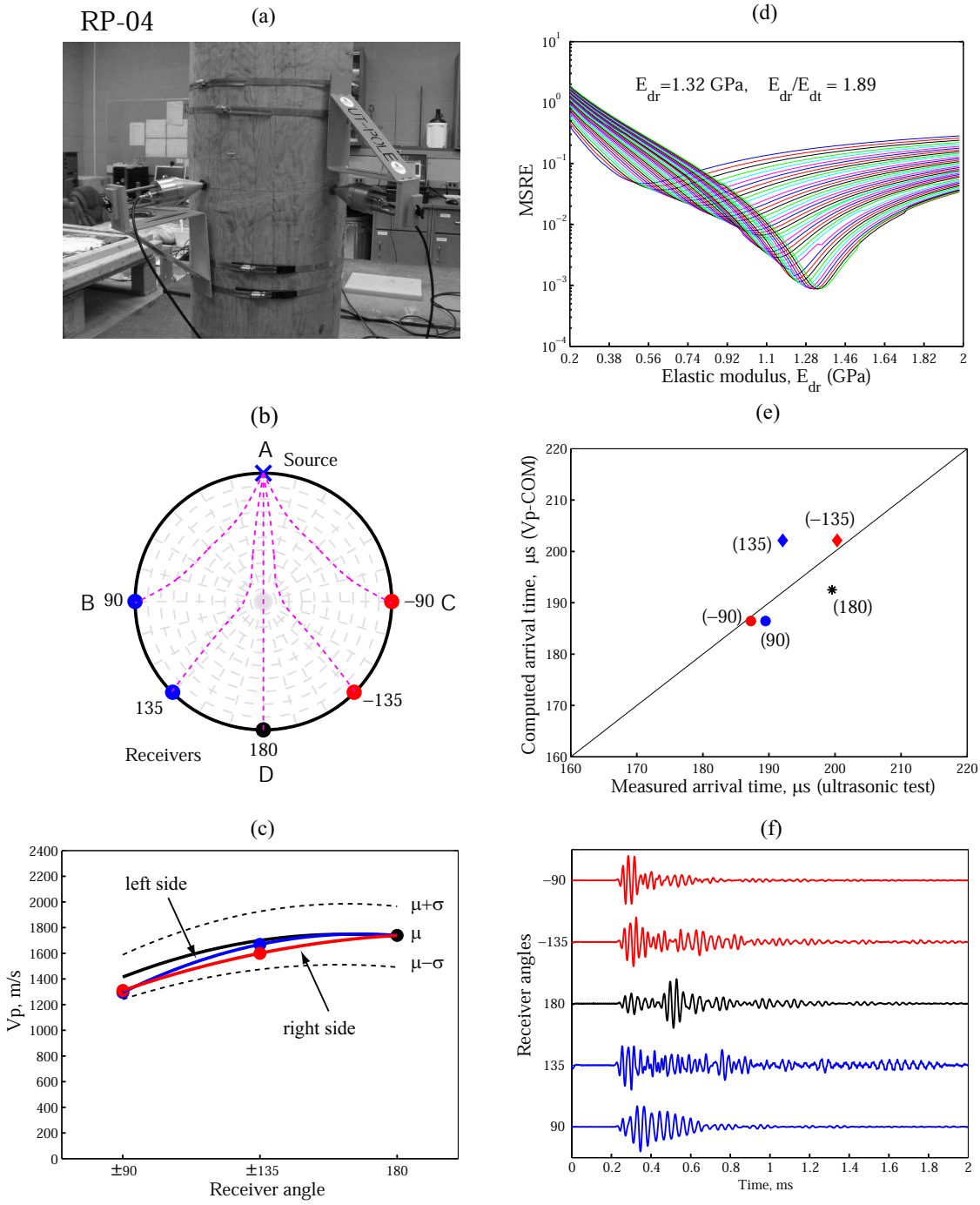

Figure B.5: Experimental results of ultrasonic testing in red pine pole RP-04 ($\phi = 31.6$ cm, $MC = 12\%$, $T = 20\ ^{\circ}C$, source on D): (a) ultrasonic test, (b) source and receiver locations, (c) V_p velocities, (d) elastic moduli E_r and E_t, (e) arrival times, and (f) IRFs

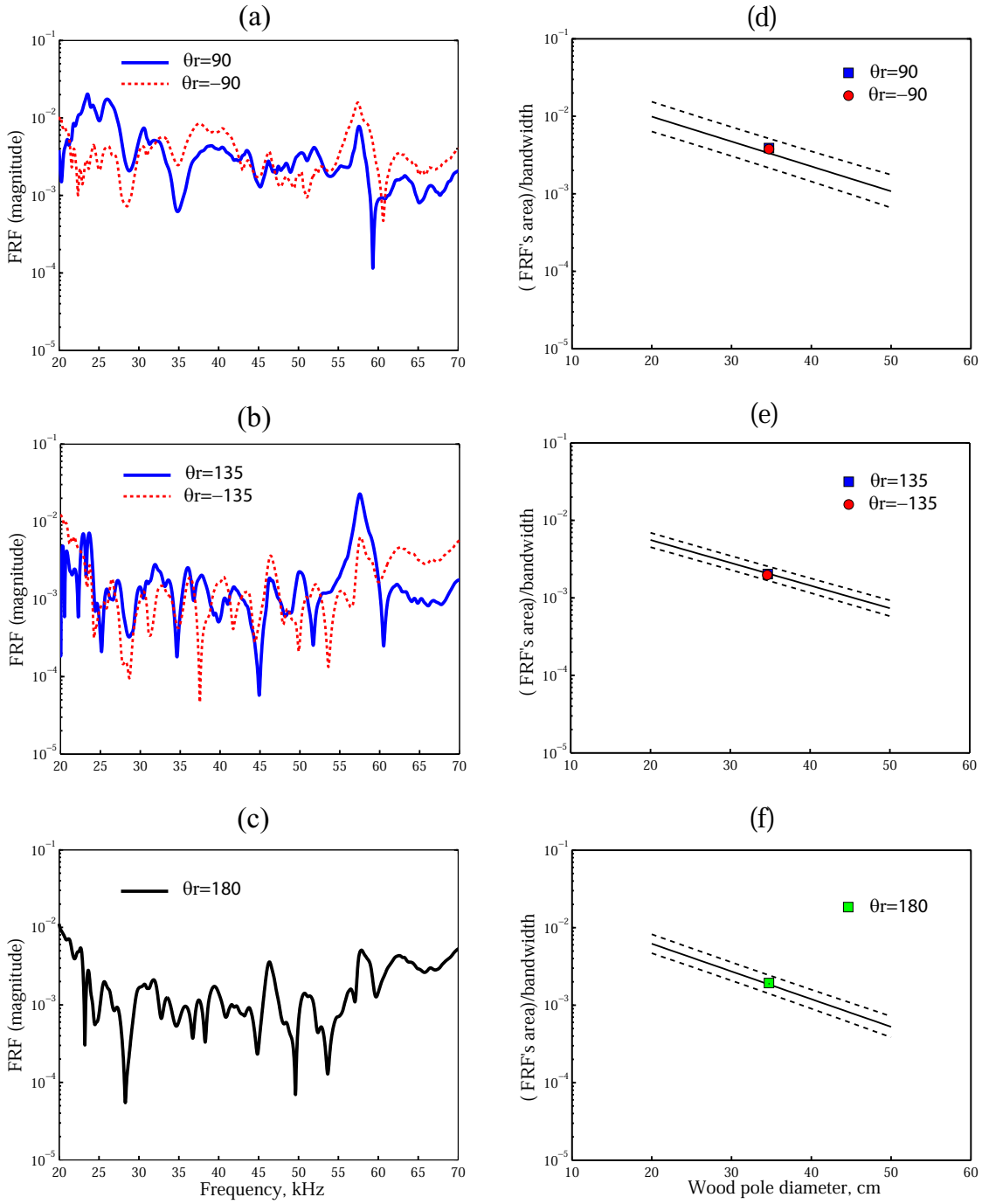

Figure B.6: Experimental results of ultrasonic testing in red pine pole RP-04: FRF for the receivers located at $\theta_r = \pm 90^\circ$ (a), $\theta_r = \pm 135^\circ$ (b), and $\theta_r = 180^\circ$ (c); wave attenuation for the receivers located at $\theta_r = \pm 90^\circ$ (d), $\theta_r = \pm 135^\circ$ (e), and $\theta_r = 180^\circ$ (f)

Appendix C

Red pine pole RP-03

Source located on B

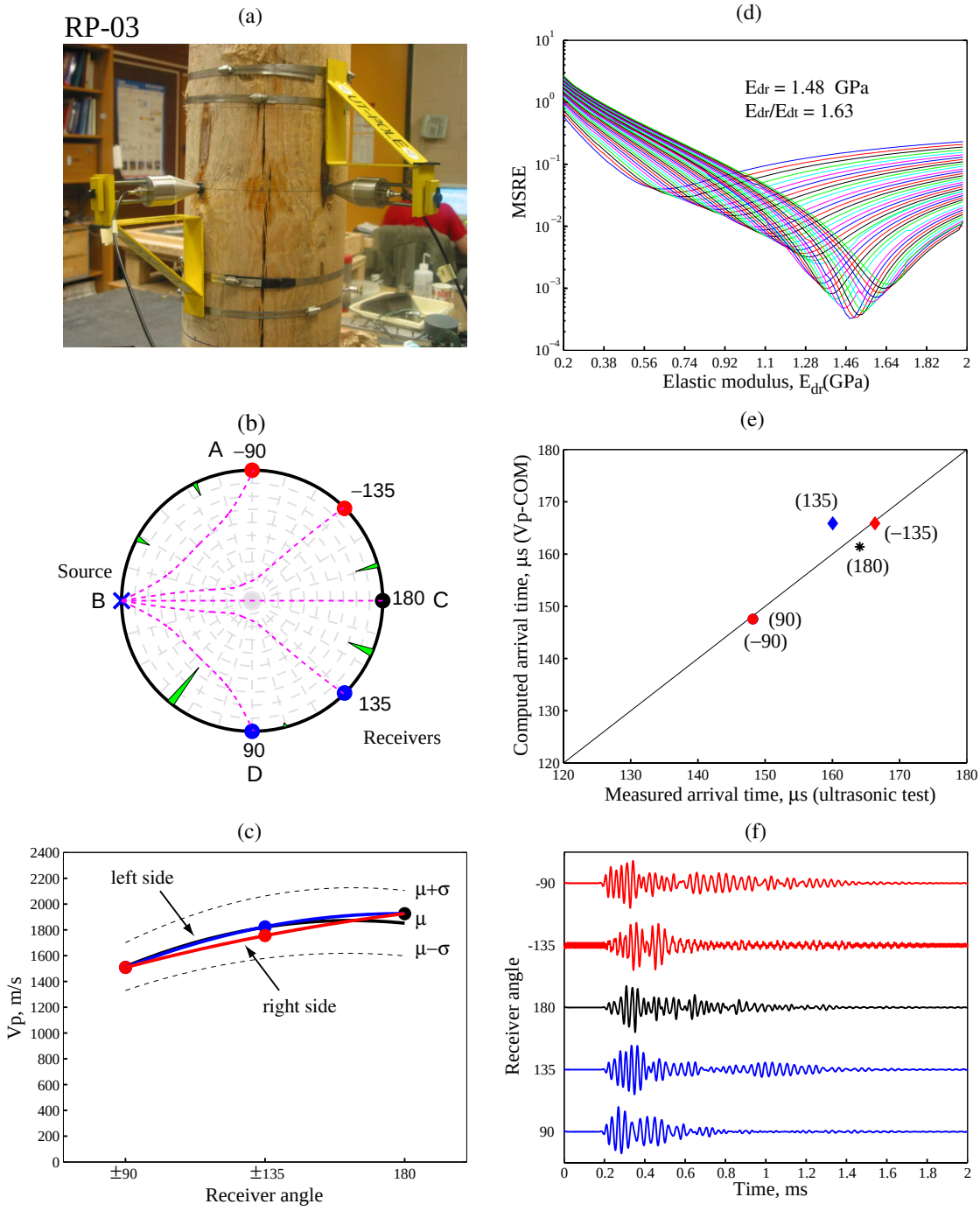

Figure C.1: Experimental results of ultrasonic testing in red pine pole RP-03 ($\phi = 31.6$ cm, $MC = 5\%$, $T = 20\ ^{\circ}C$): (a) ultrasonic test, (b) source and receiver locations, (c) V_p velocities, (d) elastic moduli E_r and E_t, (e) arrival times, and (f) IRFs

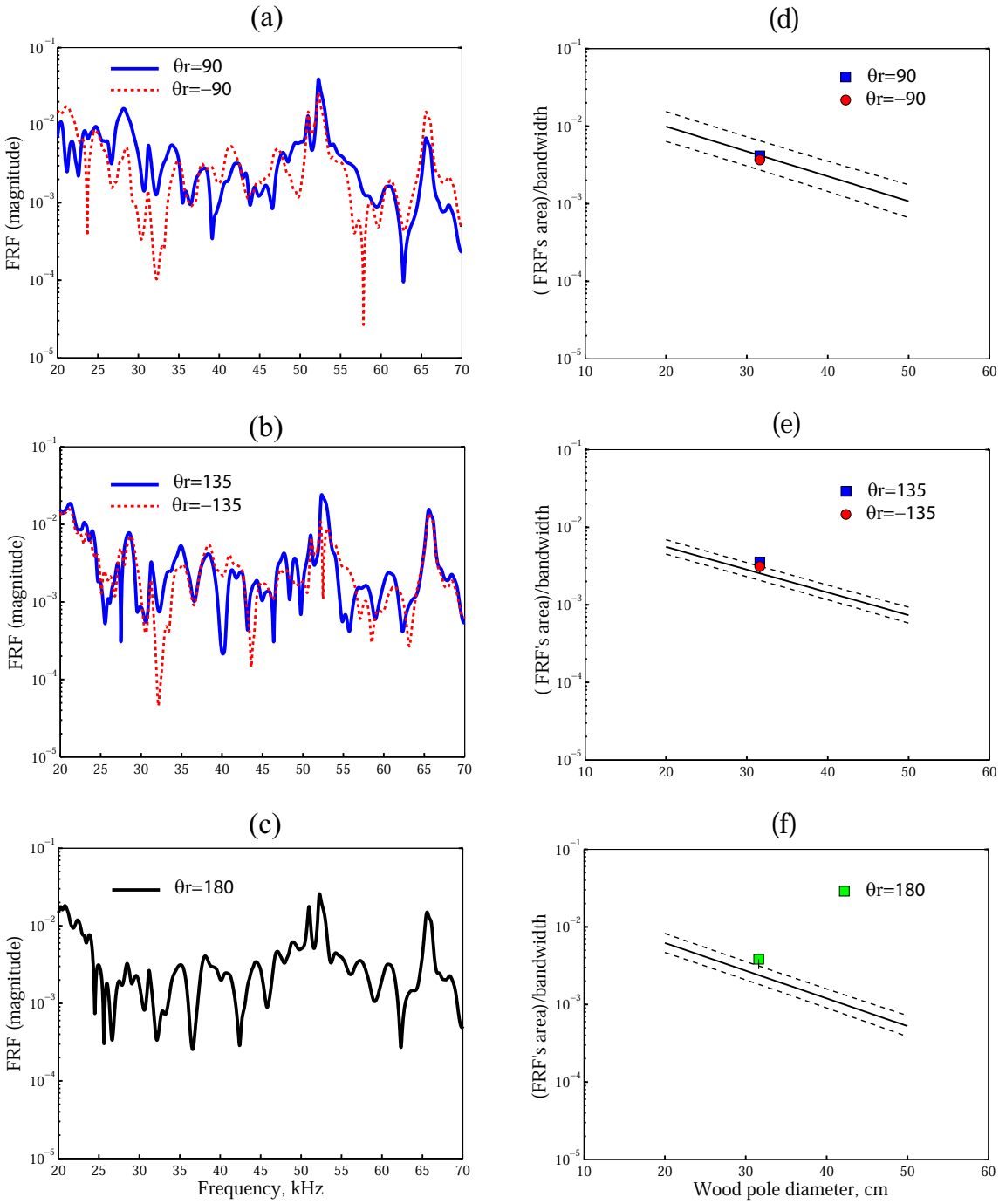

Figure C.2: Experimental results of ultrasonic testing in red pine pole RP-03: FRF for the receivers located at $\theta_r = \pm 90^\circ$ (a), $\theta_r = \pm 135^\circ$ (b), and $\theta_r = 180^\circ$ (c); wave attenuation for the receivers located at $\theta_r = \pm 90^\circ$ (d), $\theta_r = \pm 135^\circ$ (e), and $\theta_r = 180^\circ$ (f)

Source located on C

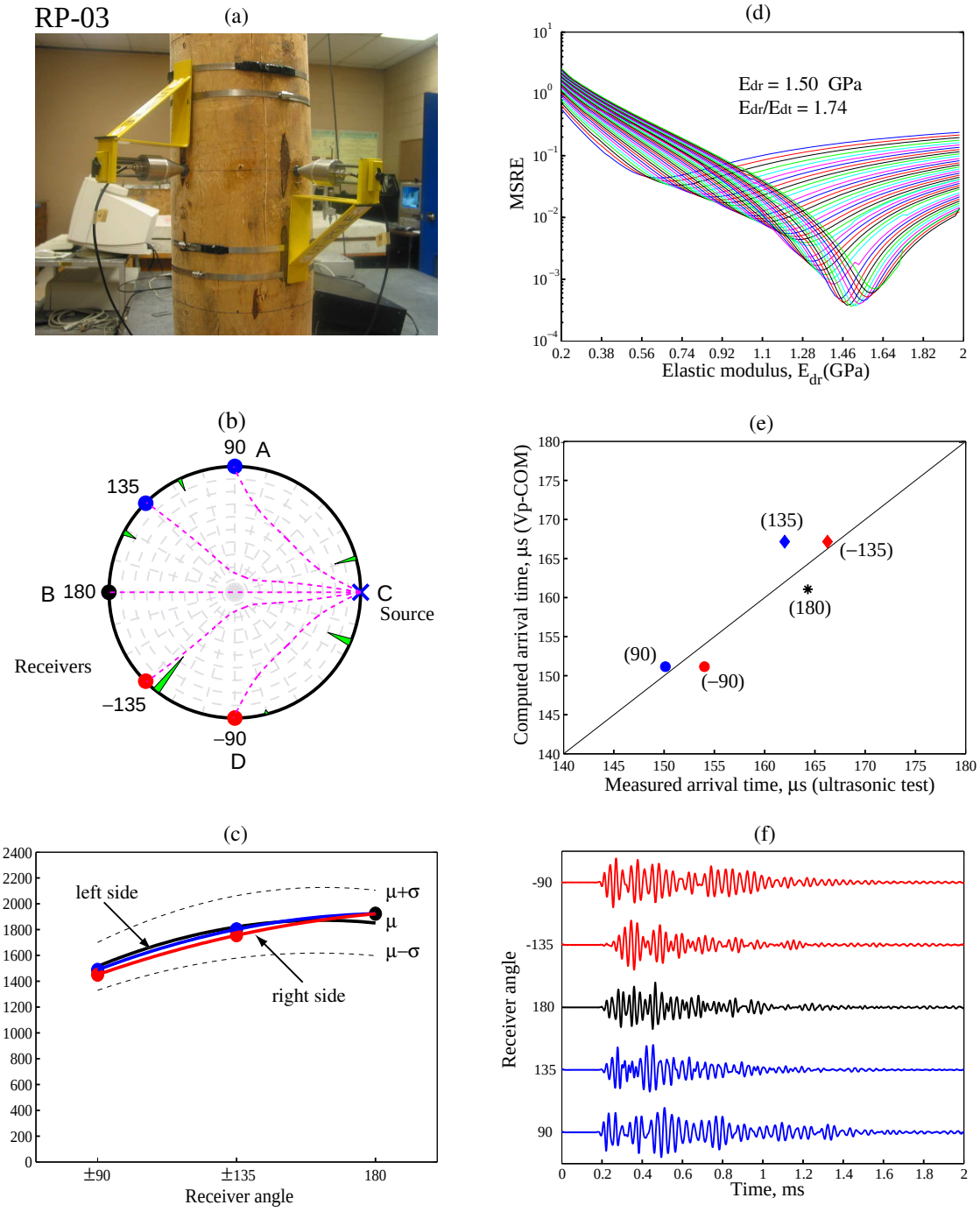

Figure C.3: Experimental results of ultrasonic testing in red pine pole RP-03 ($\phi = 31.6$ cm, $MC = 5\%$, $T = 20\ ^{\circ}C$): (a) ultrasonic test, (b) source and receiver locations, (c) V_p velocities, (d) elastic moduli E_r and E_t, (e) arrival times, and (f) IRFs

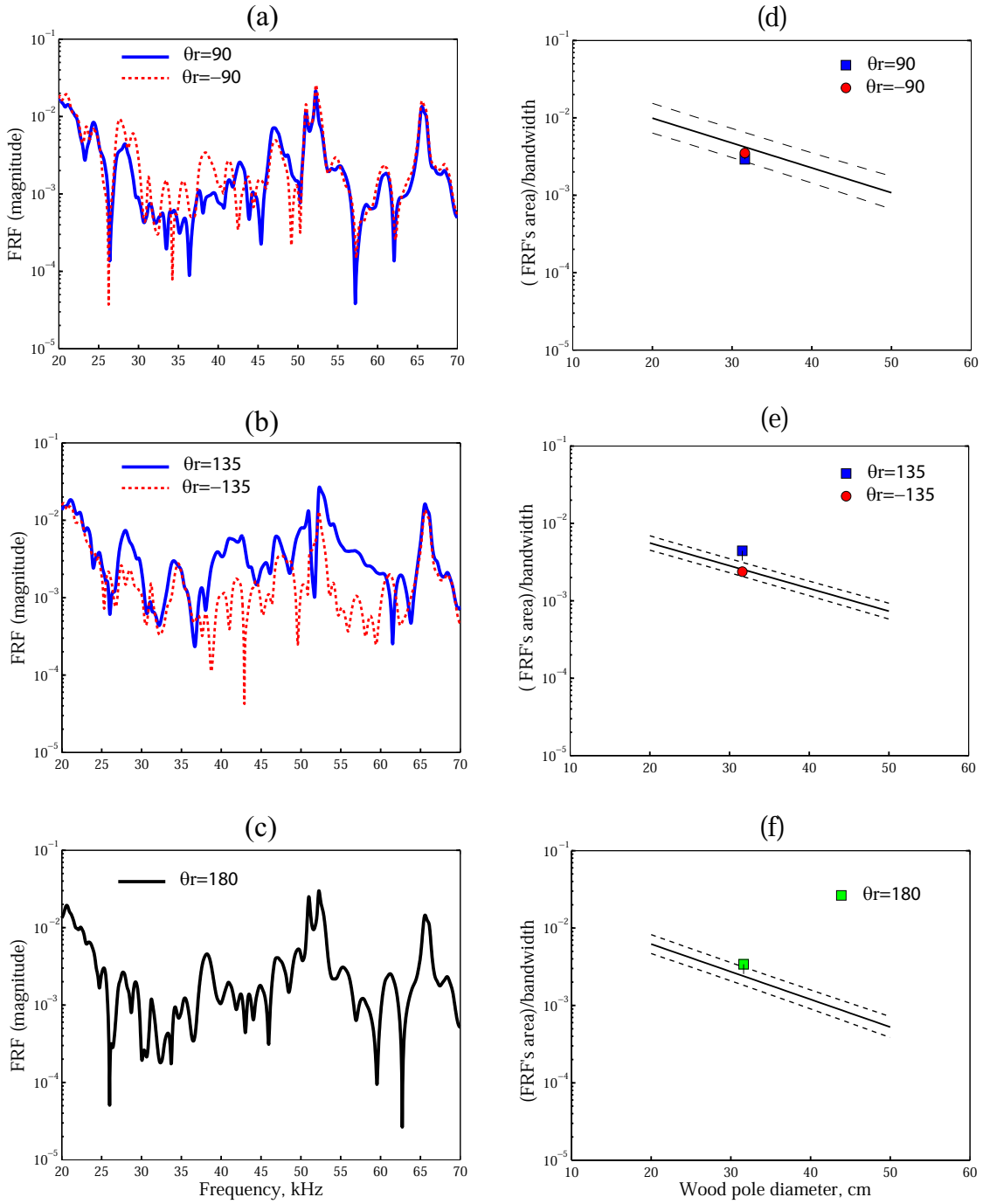

Figure C.4: Experimental results of ultrasonic testing in red pine pole RP-03: FRF for the receivers located at $\theta_r = \pm 90^\circ$ (a), $\theta_r = \pm 135^\circ$ (b), and $\theta_r = 180^\circ$ (c); wave attenuation for the receivers located at $\theta_r = \pm 90^\circ$ (d), $\theta_r = \pm 135^\circ$ (e), and $\theta_r = 180^\circ$ (f)

Source located on D

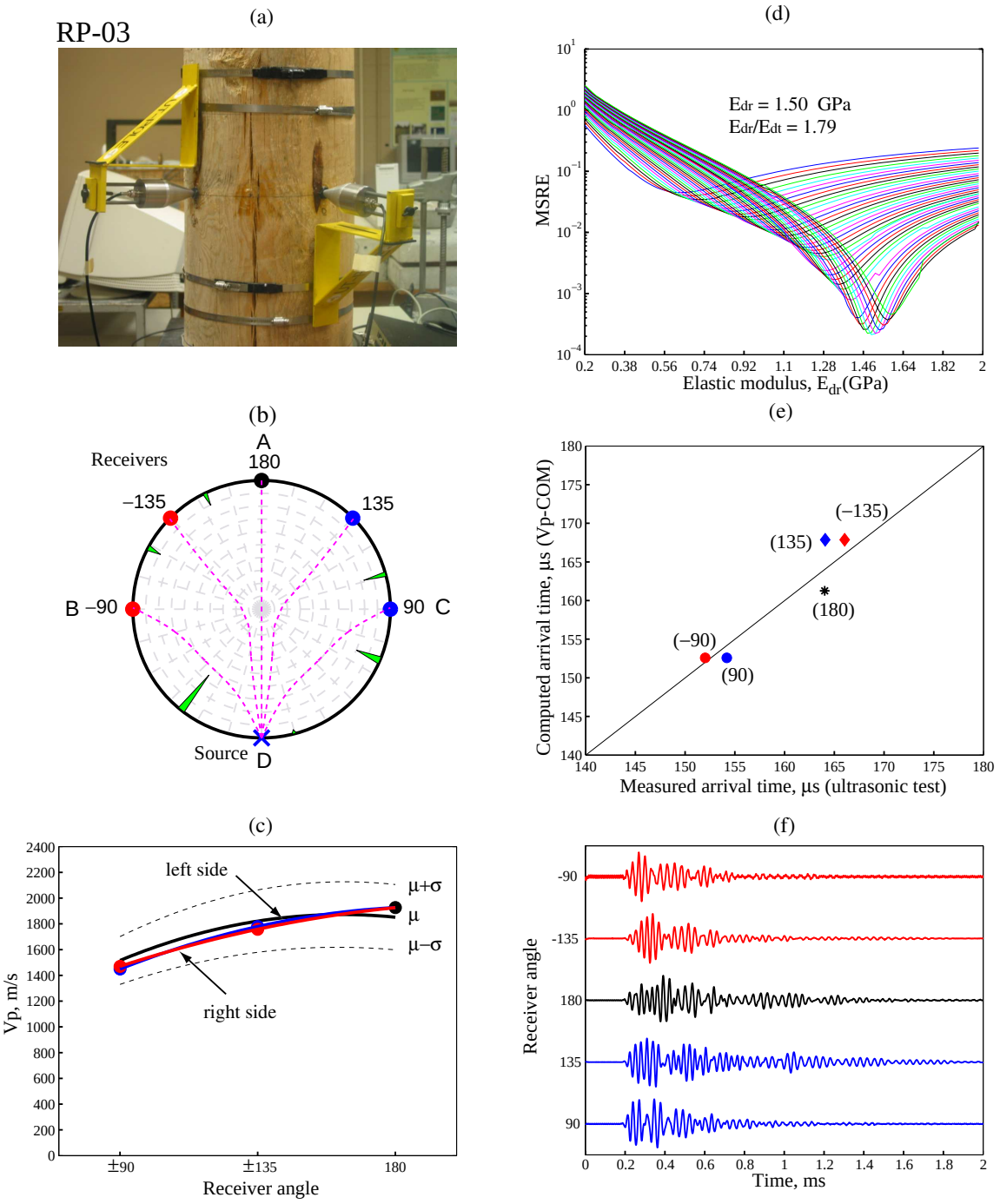

Figure C.5: Experimental results of ultrasonic testing in red pine pole RP-03 ($\phi = 31.6$ cm, $MC = 5\%$, $T = 20\ ^{\circ}C$): (a) ultrasonic test, (b) source and receiver locations, (c) V_p velocities, (d) elastic moduli E_r and E_t, (e) arrival times, and (f) IRFs

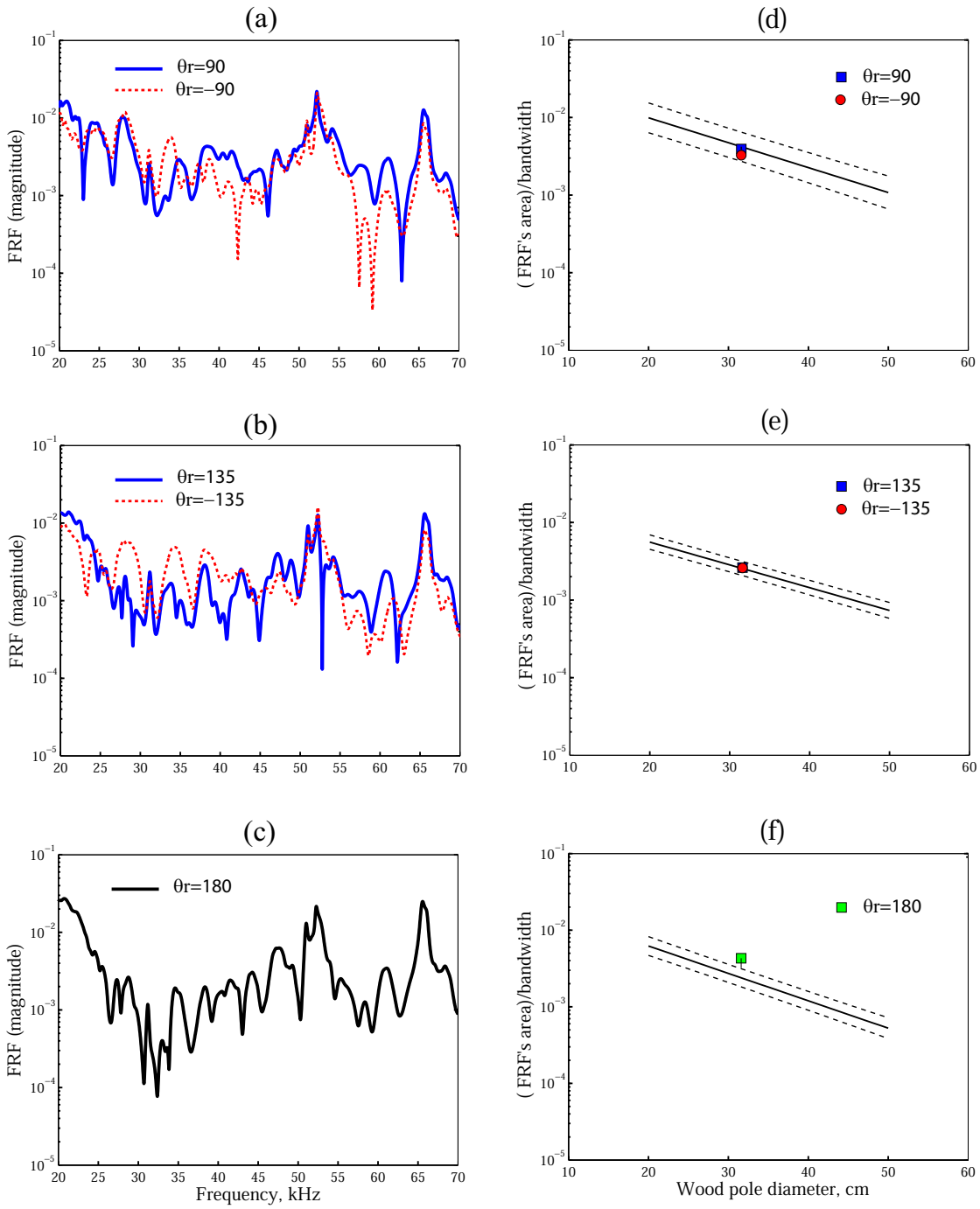

Figure C.6: Experimental results of ultrasonic testing in red pine pole RP-03: FRF for the receivers located at $\theta_r = \pm 90^\circ$ (a), $\theta_r = \pm 135^\circ$ (b), and $\theta_r = 180^\circ$ (c); wave attenuation for the receivers located at $\theta_r = \pm 90^\circ$ (d), $\theta_r = \pm 135^\circ$ (e), and $\theta_r = 180^\circ$ (f)

Appendix D

Red pine pole RP-03 with a centric hole

Source located on B

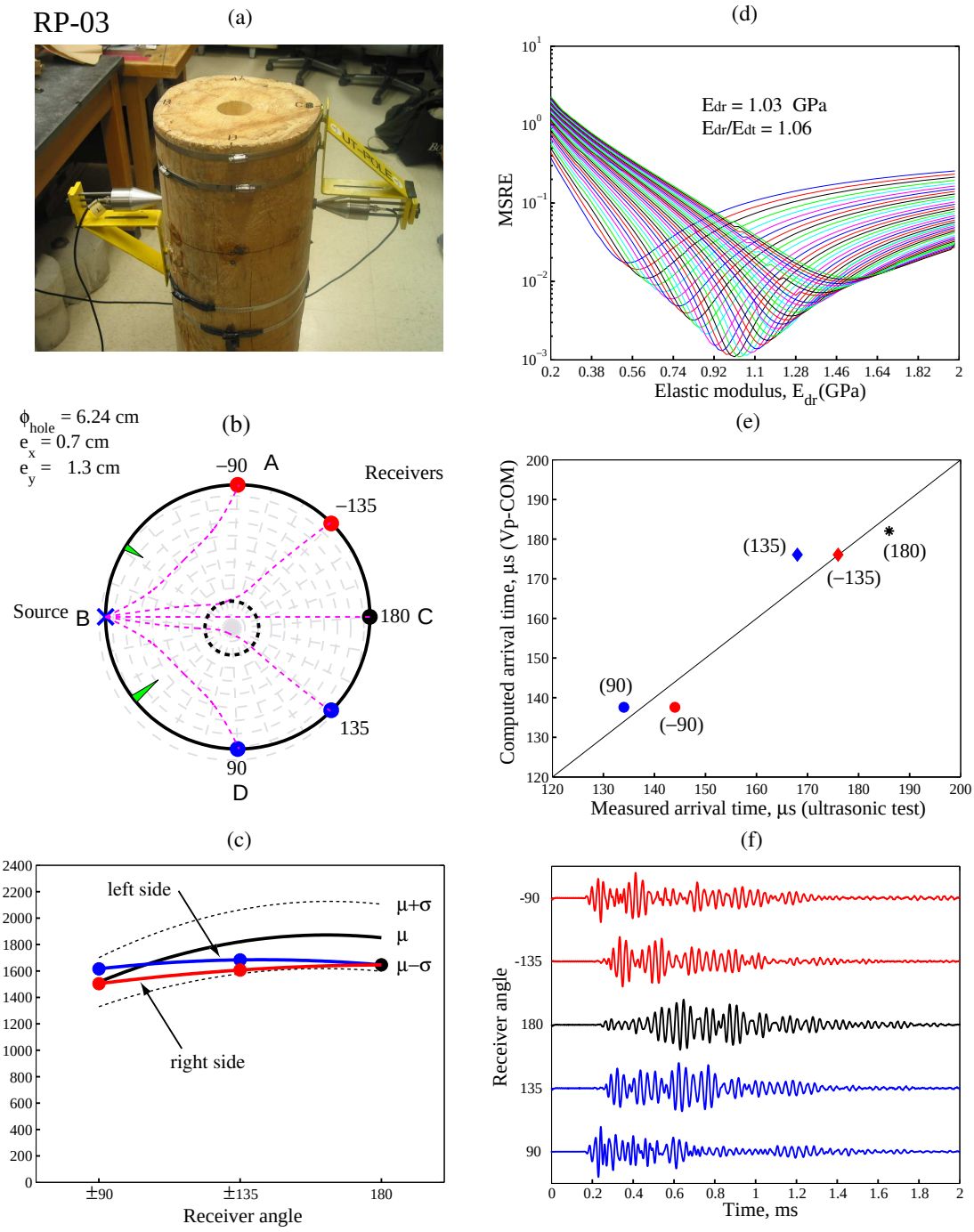

Figure D.1: Experimental results of ultrasonic testing in red pine pole RP-03 with a centric void ($\phi = 31.6$ cm, $\phi_{void} = 6.24$ cm, $MC = 5\%$, $T = 20\ ^{\circ}C$): (a) ultrasonic test, (b) source and receiver locations, (c) V_p velocities, (d) elastic moduli E_r and E_t, (e) arrival times, and (f) IRFs

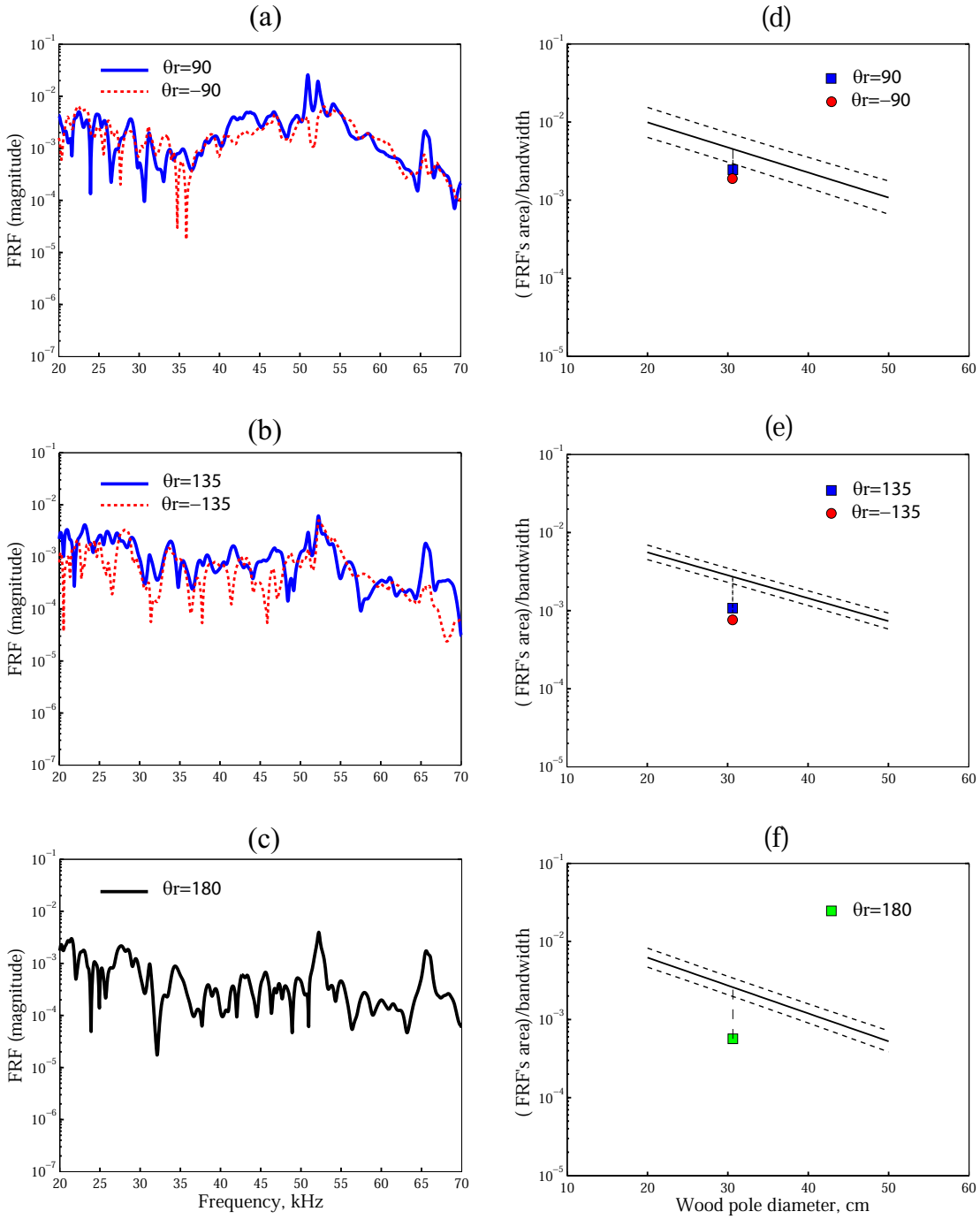

Figure D.2: Experimental results of ultrasonic testing in red pine pole RP-03 with a centric void: FRF for the receivers located at $\theta_r = \pm 90^\circ$ (a), $\theta_r = \pm 135^\circ$ (b), and $\theta_r = 180^\circ$ (c); wave attenuation for the receivers located at $\theta_r = \pm 90^\circ$ (d), $\theta_r = \pm 135^\circ$ (e), and $\theta_r = 180^\circ$ (f)

Source located on C

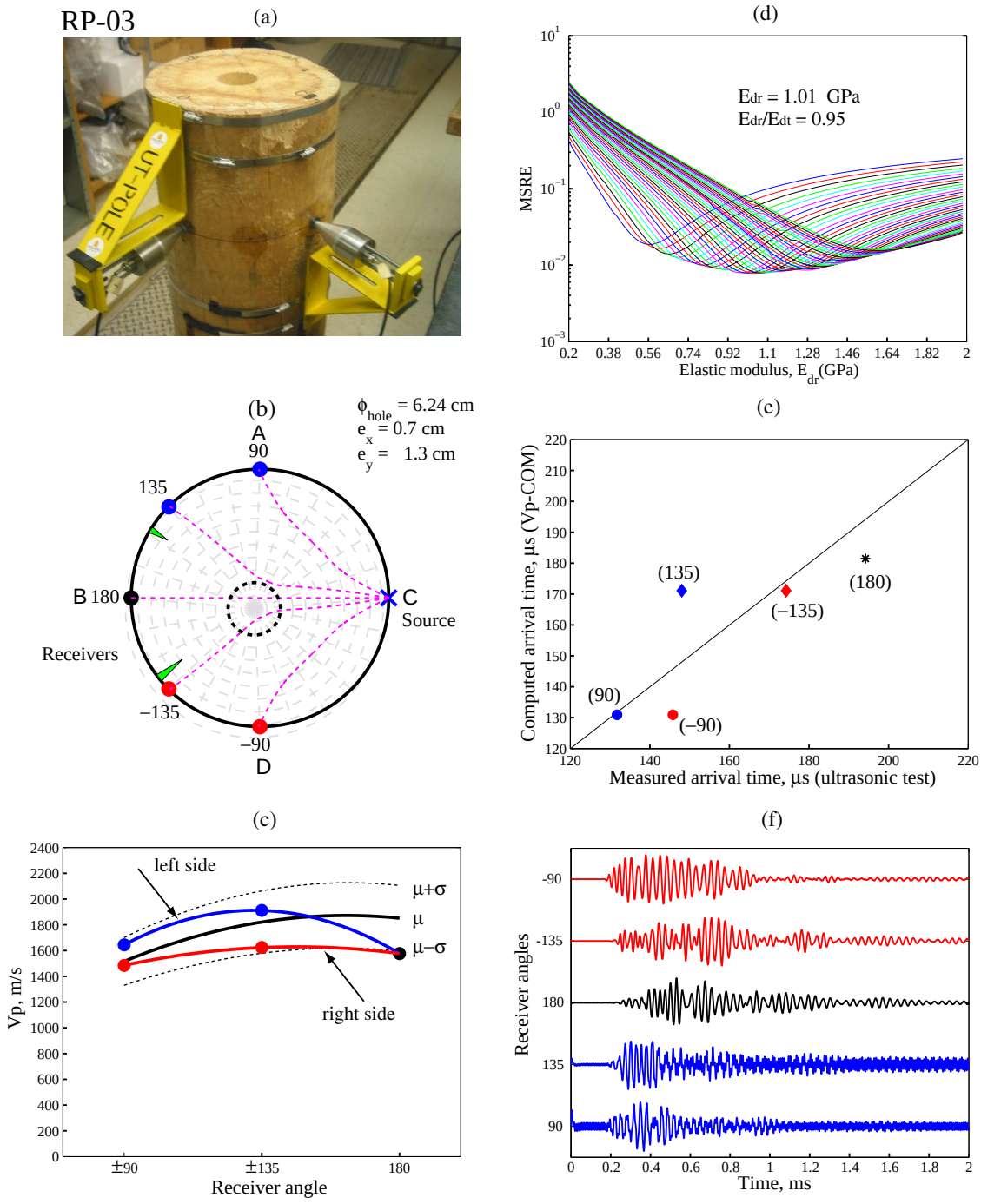

Figure D.3: Experimental results of ultrasonic testing in red pine pole RP-03 with a centric void ($\phi = 31.6$ cm, $\phi_{void} = 6.24$ cm, $MC = 5\%$, $T = 20\ ^{\circ}C$): (a) ultrasonic test, (b) source and receiver locations, (c) V_p velocities, (d) elastic moduli E_r and E_t, (e) arrival times, and (f) IRFs

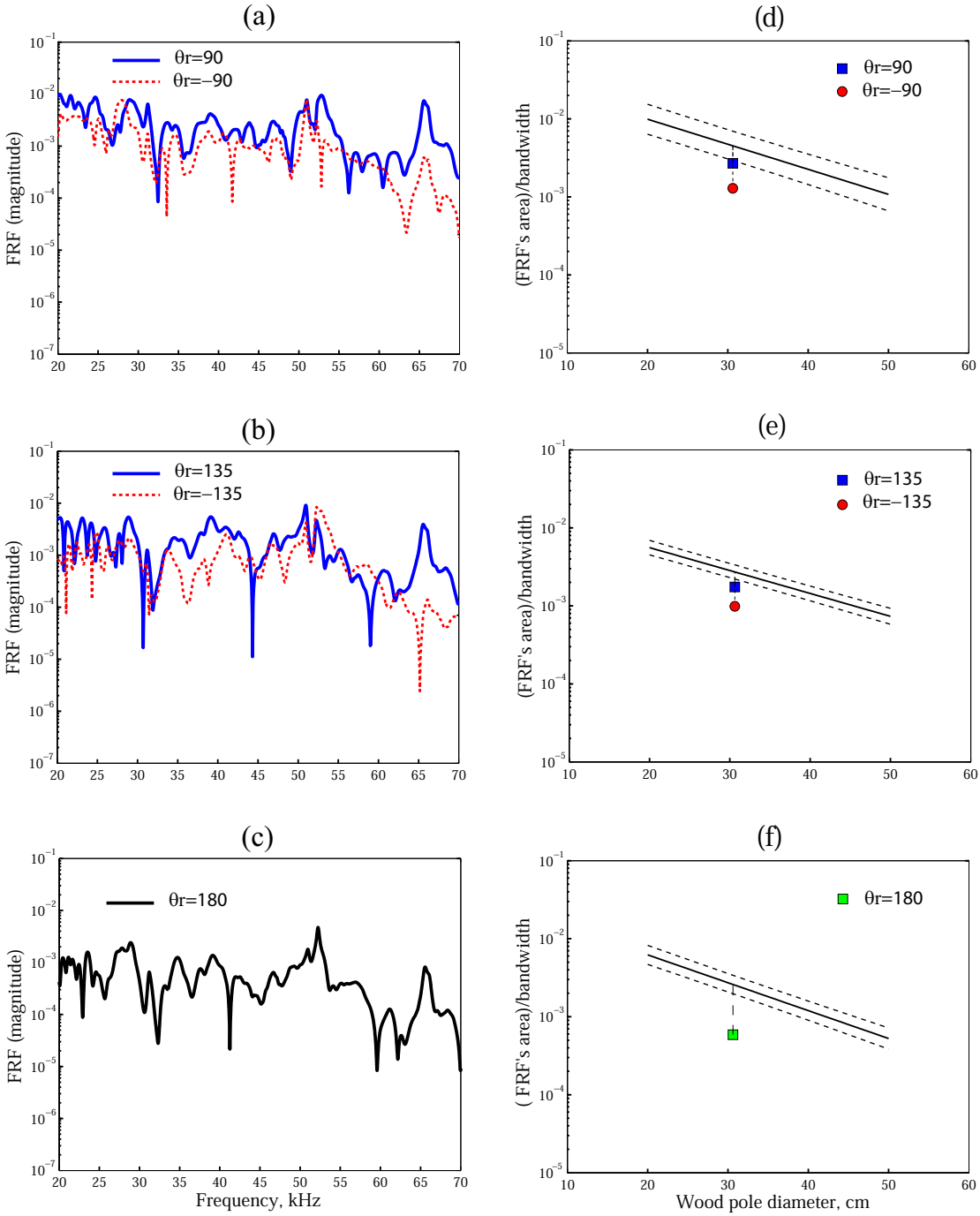

Figure D.4: Experimental results of ultrasonic testing in red pine pole RP-03 with a centric void: FRF for the receivers located at $\theta_r = \pm 90^\circ$ (a), $\theta_r = \pm 135^\circ$ (b), and $\theta_r = 180^\circ$ (c); wave attenuation for the receivers located at $\theta_r = \pm 90^\circ$ (d), $\theta_r = \pm 135^\circ$ (e), and $\theta_r = 180^\circ$ (f)

Source located on D

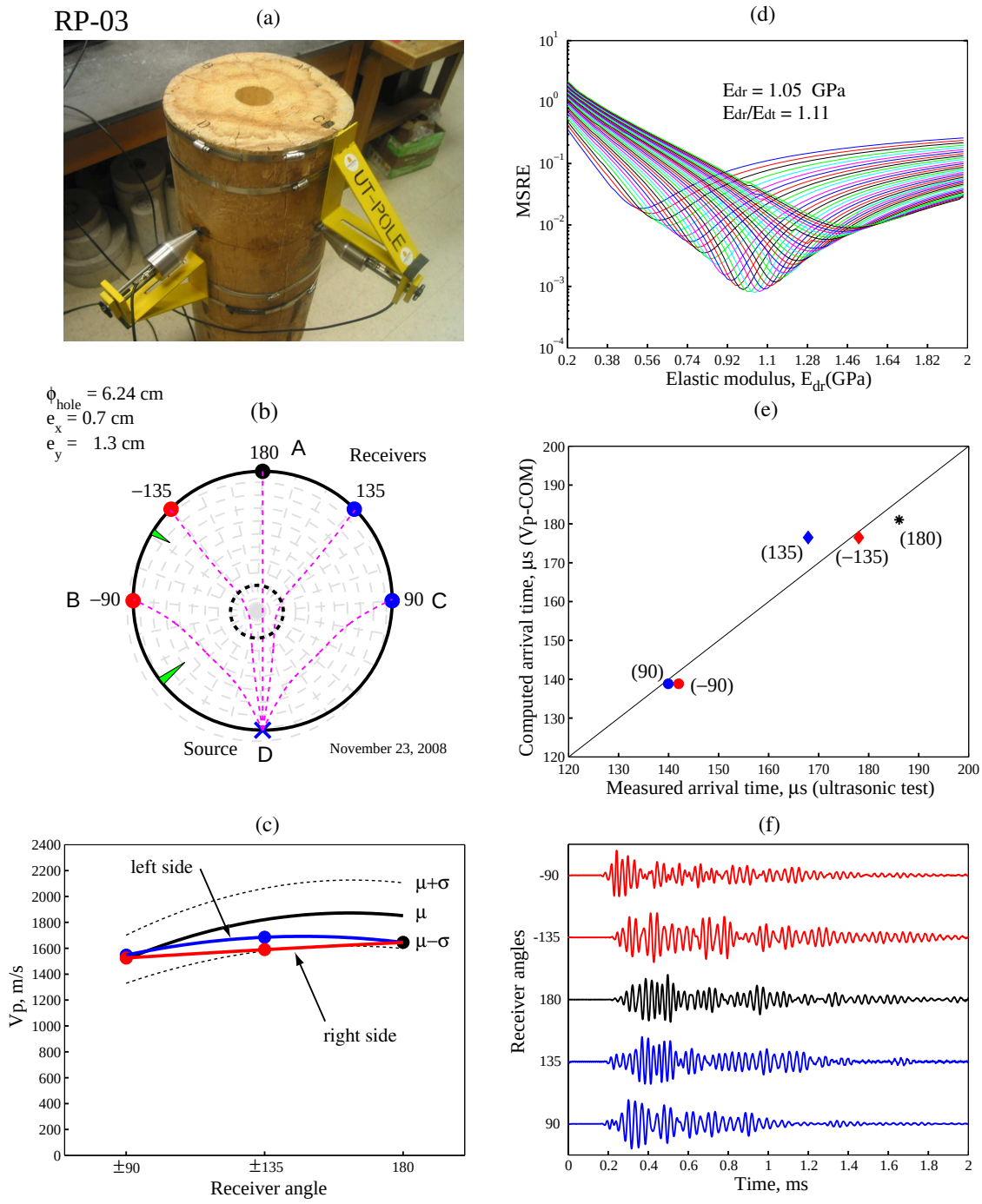

Figure D.5: Experimental results of ultrasonic testing in red pine pole RP-03 with a centric void ($\phi = 31.6$ cm, $\phi_{void} = 6.24$ cm, $MC = 5\%$, $T = 20\ ^{\circ}C$): (a) ultrasonic test, (b) source and receiver locations, (c) V_p velocities, (d) elastic moduli E_r and E_t, (e) arrival times, and (f) IRFs

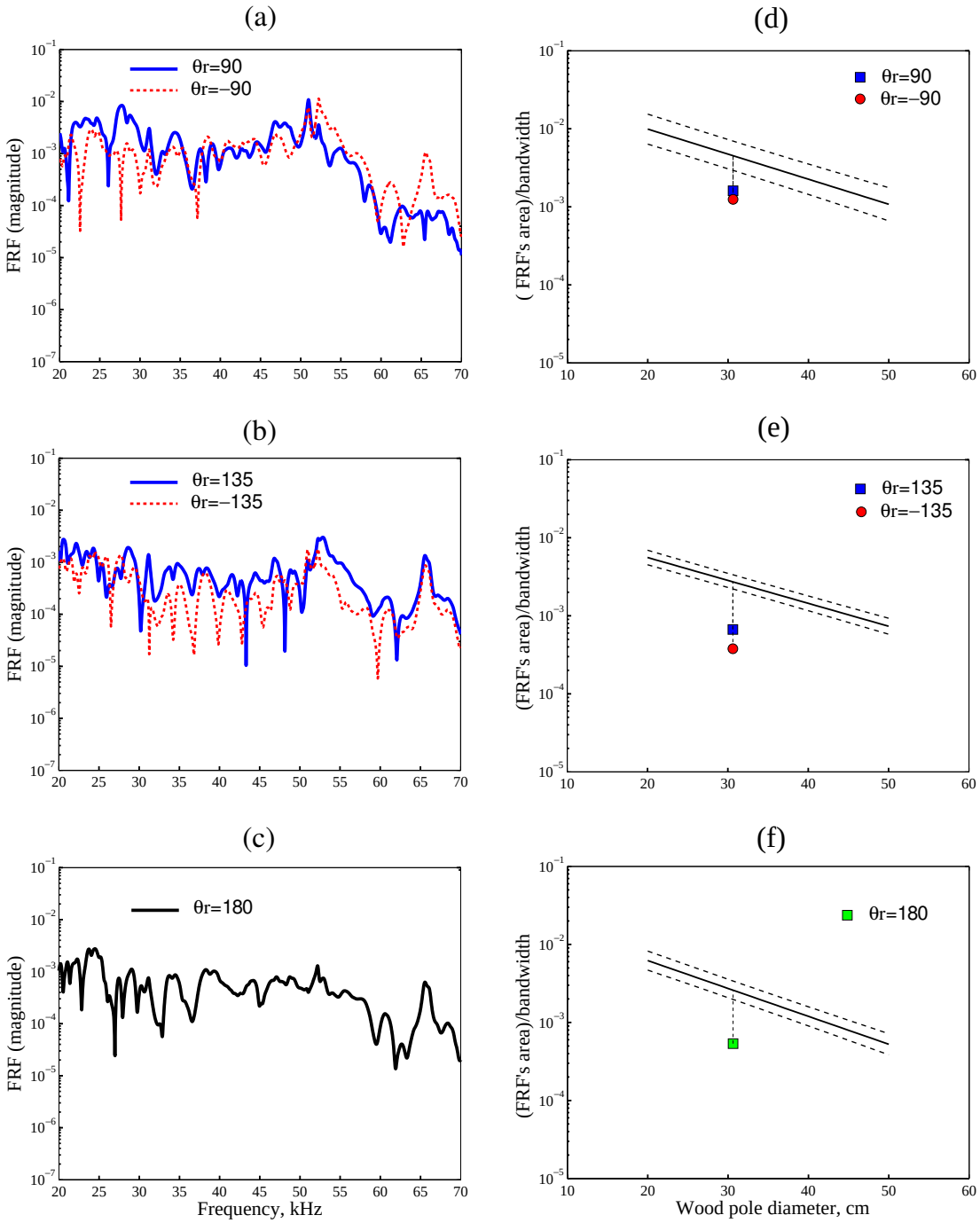

Figure D.6: Experimental results of ultrasonic testing in red pine pole RP-03 with a centric void: FRF for the receivers located at $\theta_r = \pm 90^\circ$ (a), $\theta_r = \pm 135^\circ$ (b), and $\theta_r = 180^\circ$ (c); wave attenuation for the receivers located at $\theta_r = \pm 90^\circ$ (d), $\theta_r = \pm 135^\circ$ (e), and $\theta_r = 180^\circ$ (f)

Appendix E

Red pine pole RP-03 with an eccentric hole

Source located on B

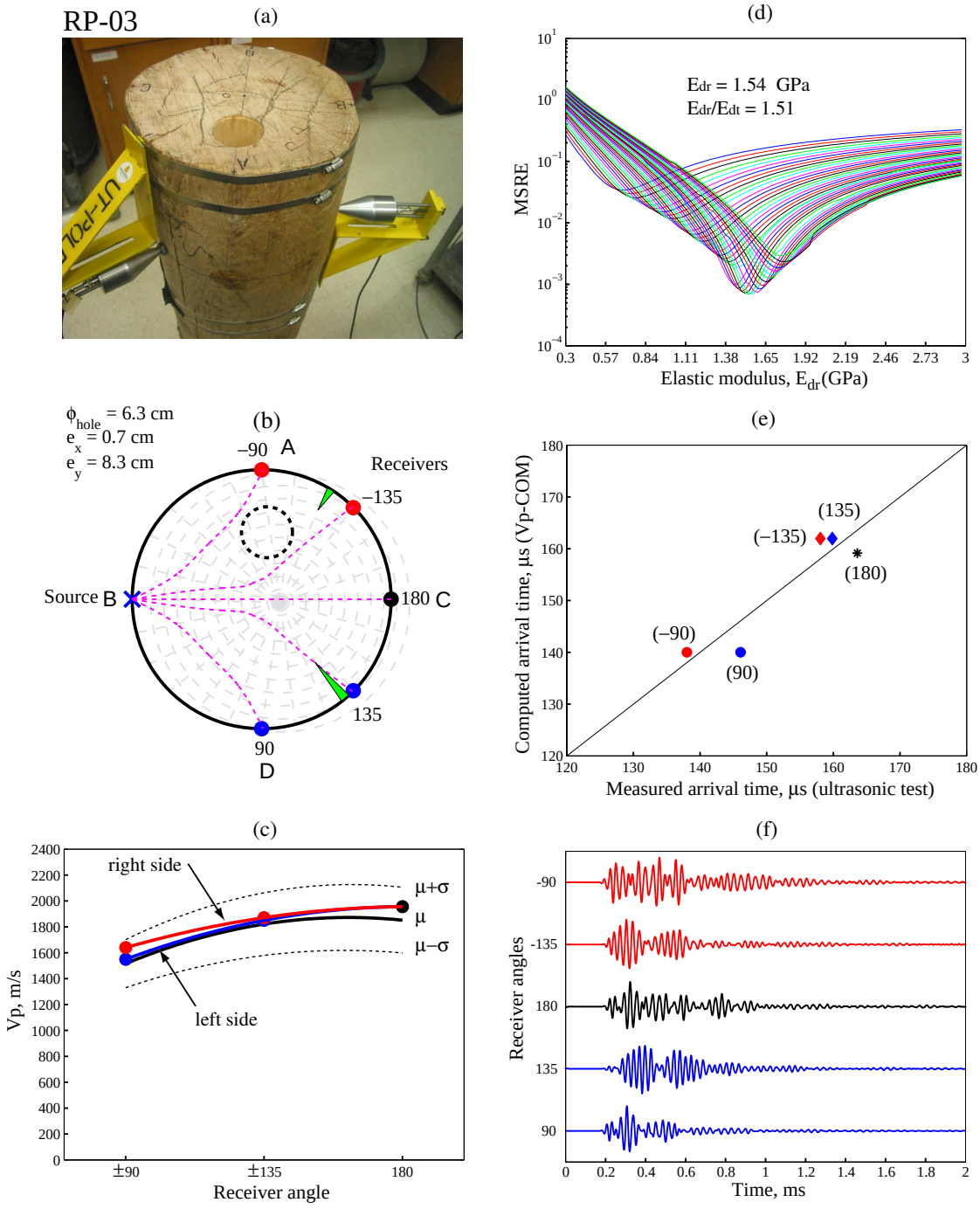

Figure E.1: Experimental results of ultrasonic testing in red pine pole RP-03 with an eccentric void ($\phi = 31.6$ cm, $\phi_{void} = 6.24$ cm, $MC = 5\%$, $T = 20\ ^{\circ}C$): (a) ultrasonic test, (b) source and receiver locations, (c) V_p velocities, (d) elastic moduli E_r and E_t, (e) arrival times, and (f) IRFs

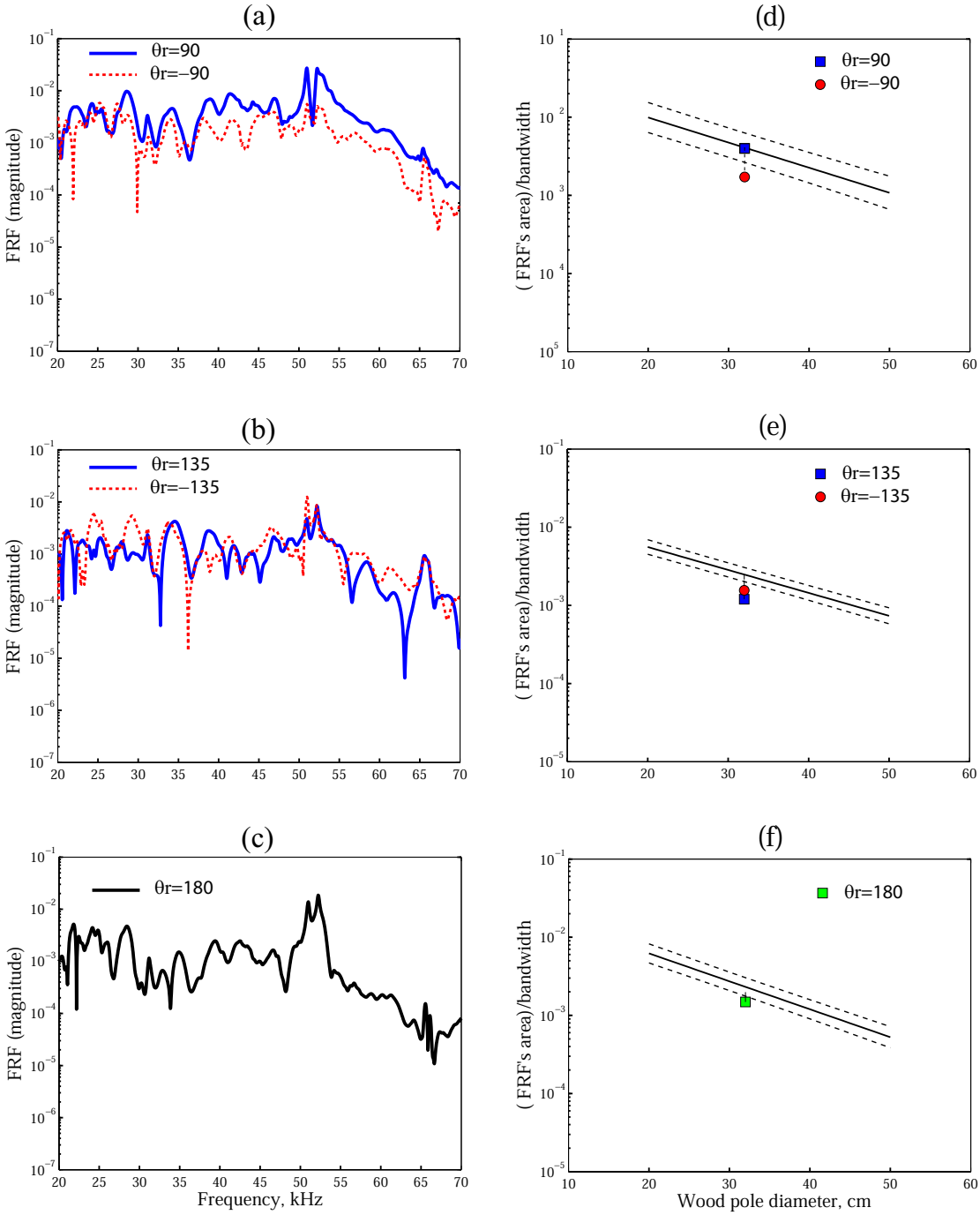

Figure E.2: Experimental results of ultrasonic testing in red pine pole RP-03 with an eccentric void: FRF for the receivers located at $\theta_r = \pm 90^\circ$ (a), $\theta_r = \pm 135^\circ$ (b), and $\theta_r = 180^\circ$ (c); wave attenuation for the receivers located at $\theta_r = \pm 90^\circ$ (d), $\theta_r = \pm 135^\circ$ (e), and $\theta_r = 180^\circ$ (f)

Source located on C

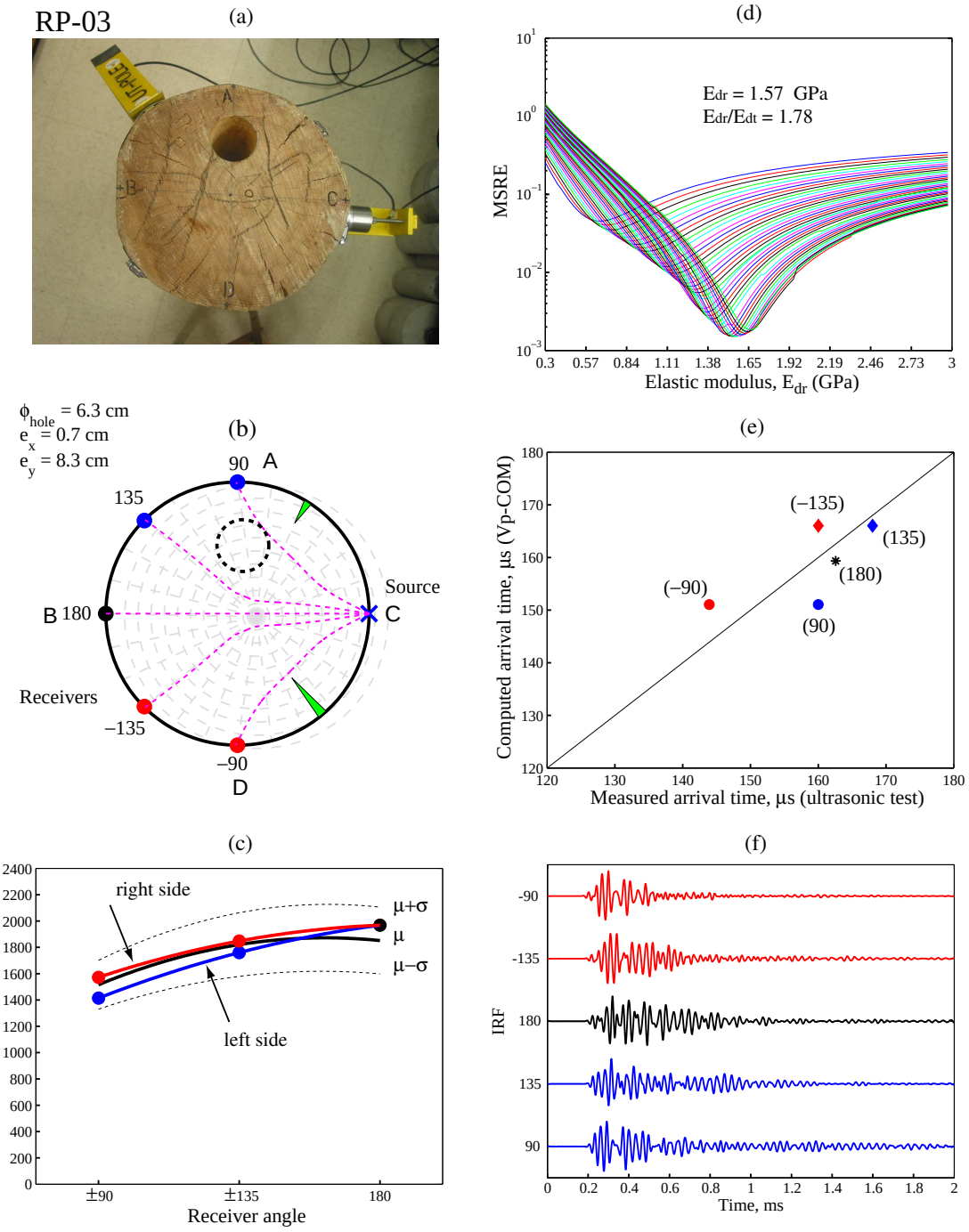

Figure E.3: Experimental results of ultrasonic testing in red pine pole RP-03 with an eccentric void ($\phi = 31.6$ cm, $\phi_{void} = 6.24$ cm, $MC = 5\%$, $T = 20\ ^{\circ}C$): (a) ultrasonic test, (b) source and receiver locations, (c) V_p velocities, (d) elastic moduli E_r and E_t, (e) arrival times, and (f) IRFs

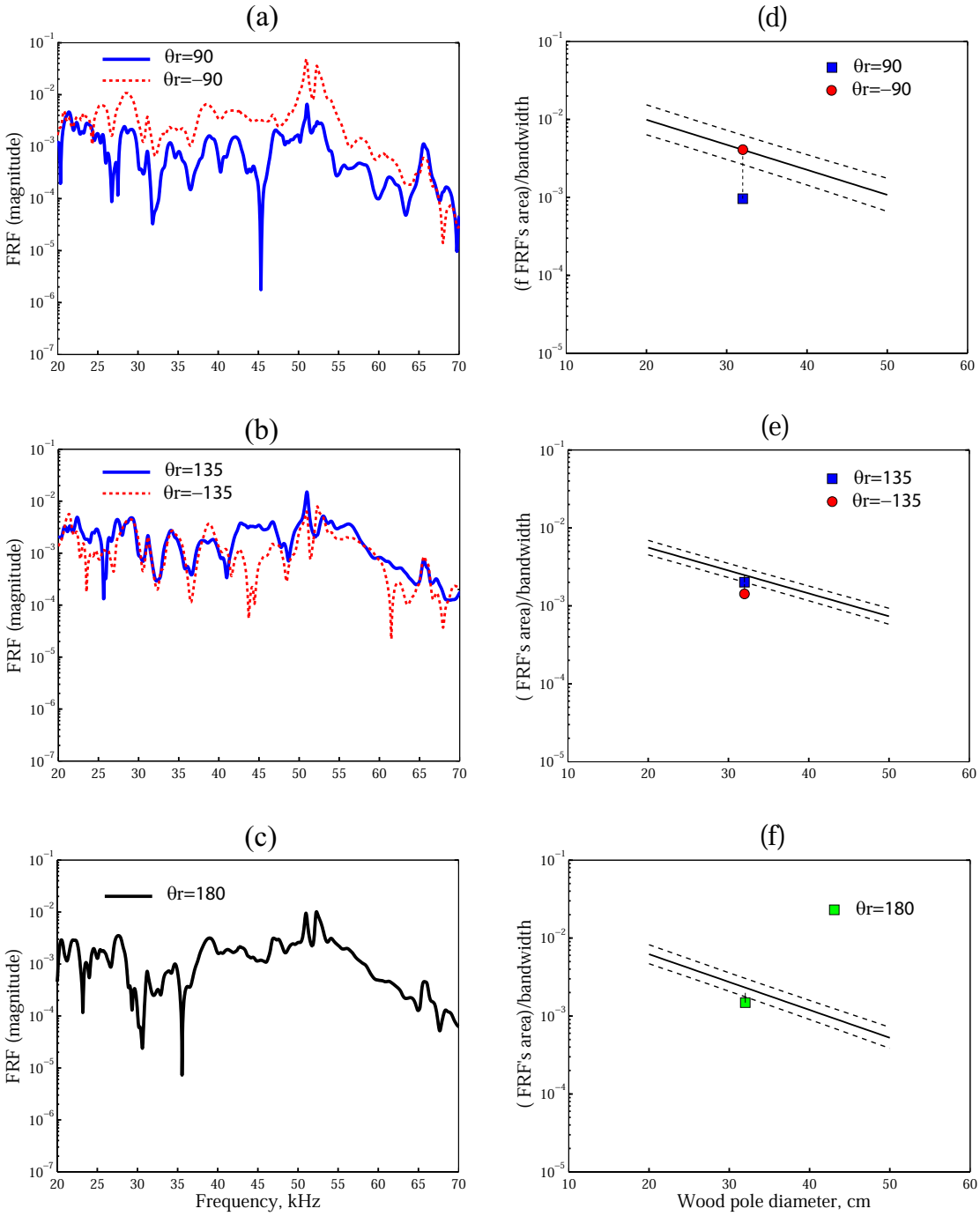

Figure E.4: Experimental results of ultrasonic testing in red pine pole RP-03 with an eccentric void: FRF for the receivers located at $\theta_r = \pm 90^\circ$ (a), $\theta_r = \pm 135^\circ$ (b), and $\theta_r = 180^\circ$ (c); wave attenuation for the receivers located at $\theta_r = \pm 90^\circ$ (d), $\theta_r = \pm 135^\circ$ (e), and $\theta_r = 180^\circ$ (f)

Source located on D

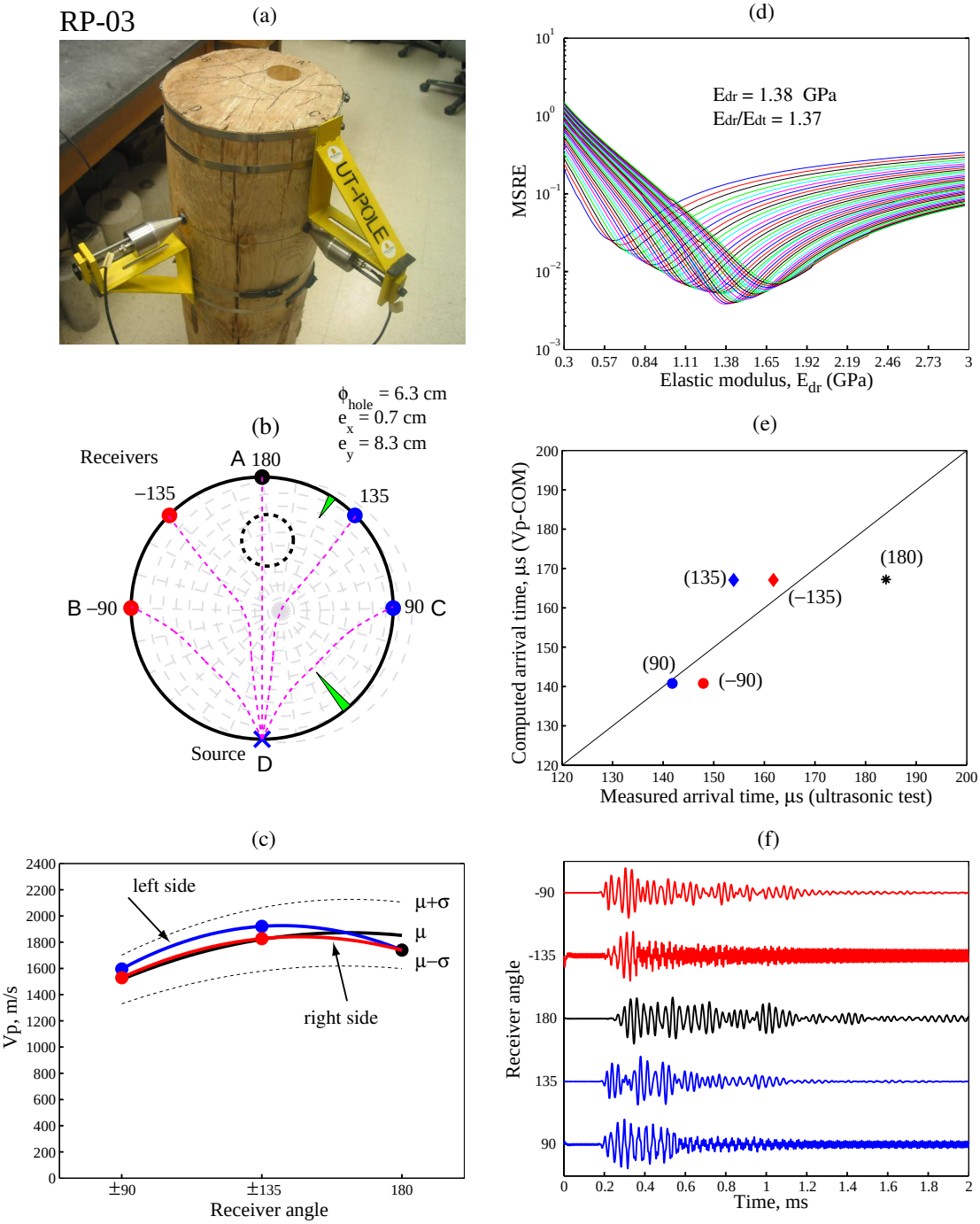

Figure E.5: Experimental results of ultrasonic testing in red pine pole RP-03 with an eccentric void ($\phi = 31.6$ cm, $\phi_{void} = 6.24$ cm, $MC = 5\%$, $T = 20\ ^{\circ}C$): (a) ultrasonic test, (b) source and receiver locations, (c) V_p velocities, (d) elastic moduli E_r and E_t, (e) arrival times, and (f) IRFs

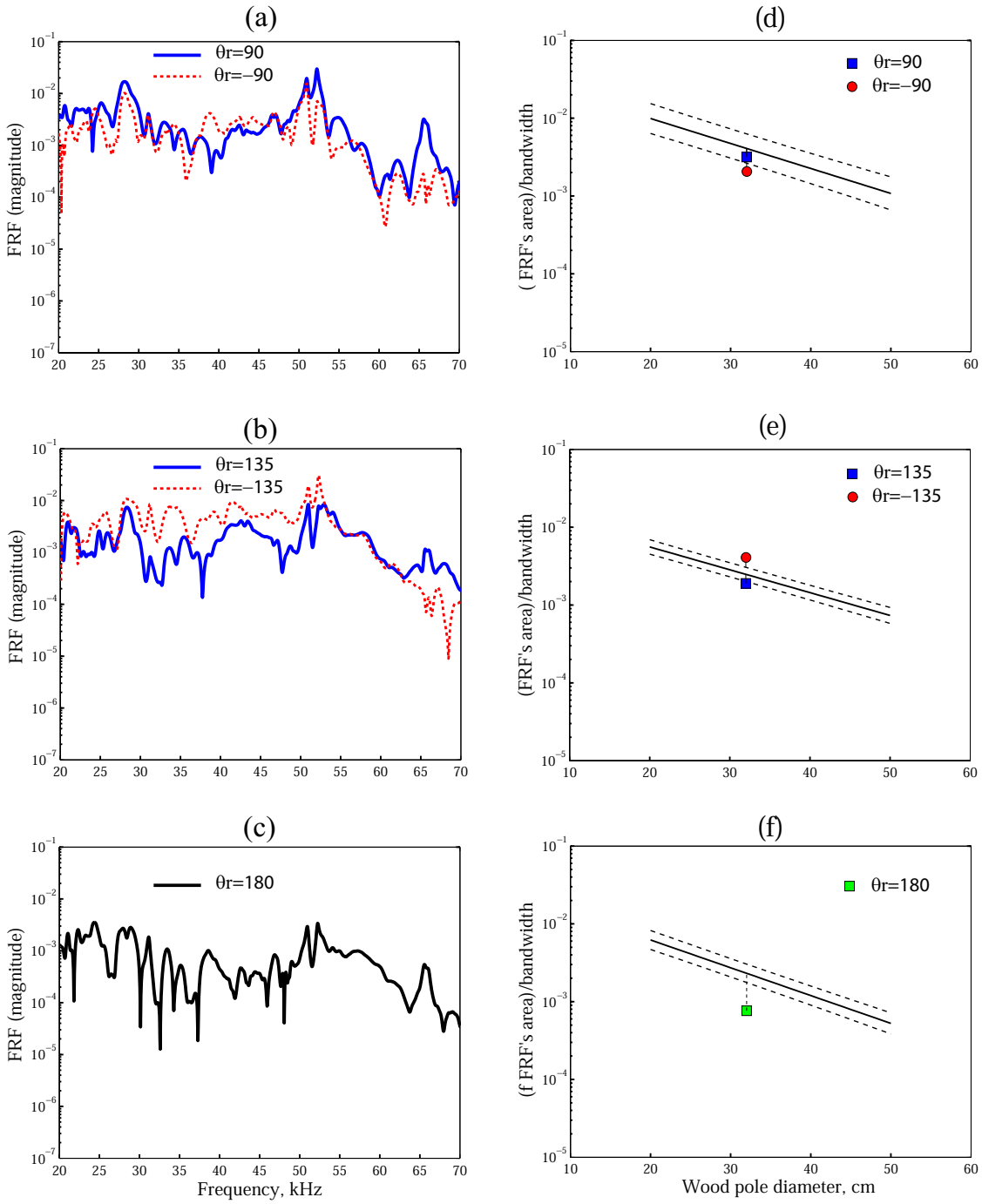

Figure E.6: Experimental results of ultrasonic testing in red pine pole RP-03 with an eccentric void: FRF for the receivers located at $\theta_r = \pm 90^\circ$ (a), $\theta_r = \pm 135^\circ$ (b), and $\theta_r = 180^\circ$ (c); wave attenuation for the receivers located at $\theta_r = \pm 90^\circ$ (d), $\theta_r = \pm 135^\circ$ (e), and $\theta_r = 180^\circ$ (f)

Appendix F

Red pine pole RP-010

Source located on B

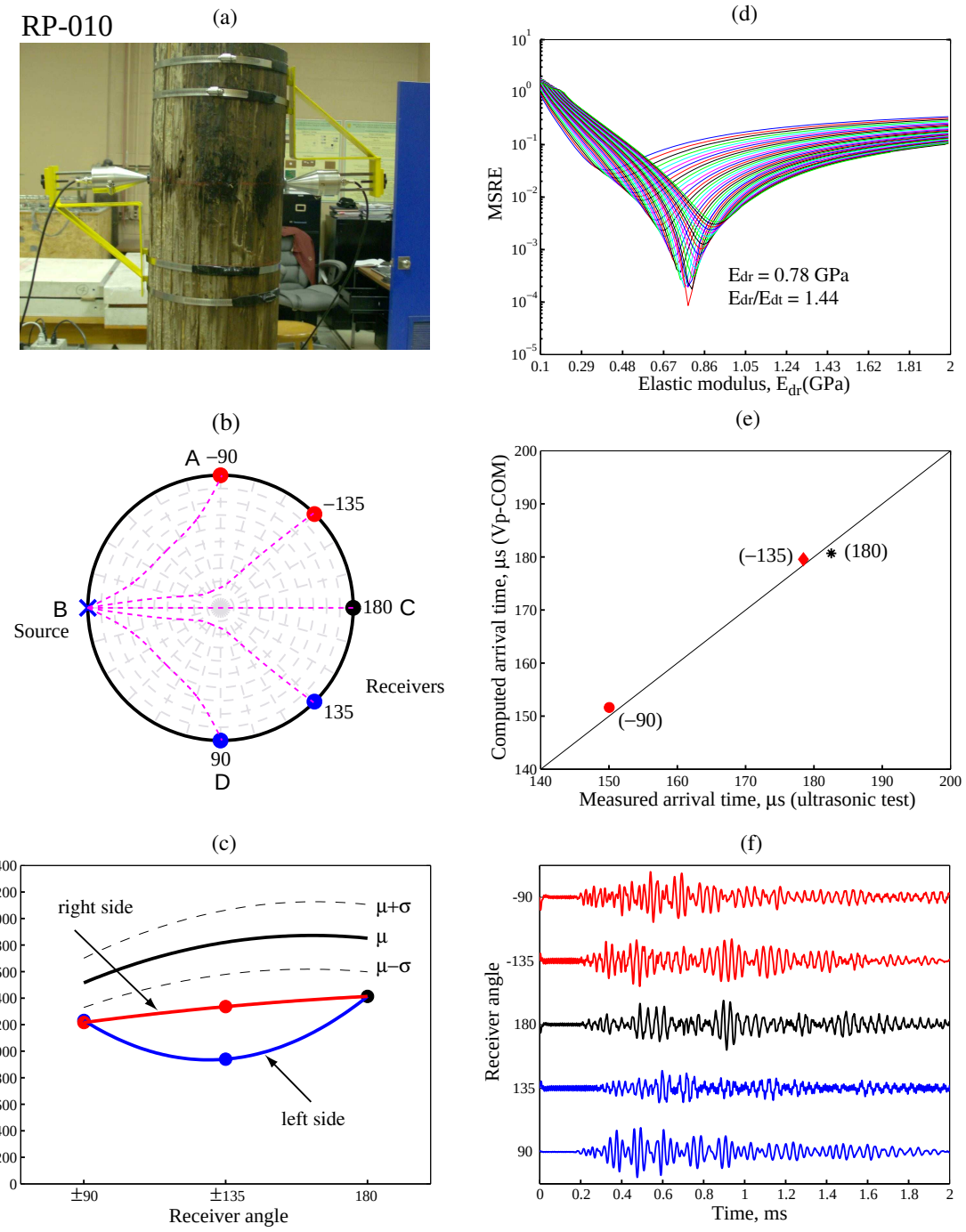

Figure F.1: Experimental results of ultrasonic testing in red pine pole RP-010 ($\phi = 22.1$ cm, $MC = 5\%$, $T = 20\ ^{\circ}C$): (a) ultrasonic test, (b) source and receiver locations, (c) V_p velocities, (d) elastic moduli E_r and E_t, (e) arrival times, and (f) IRFs

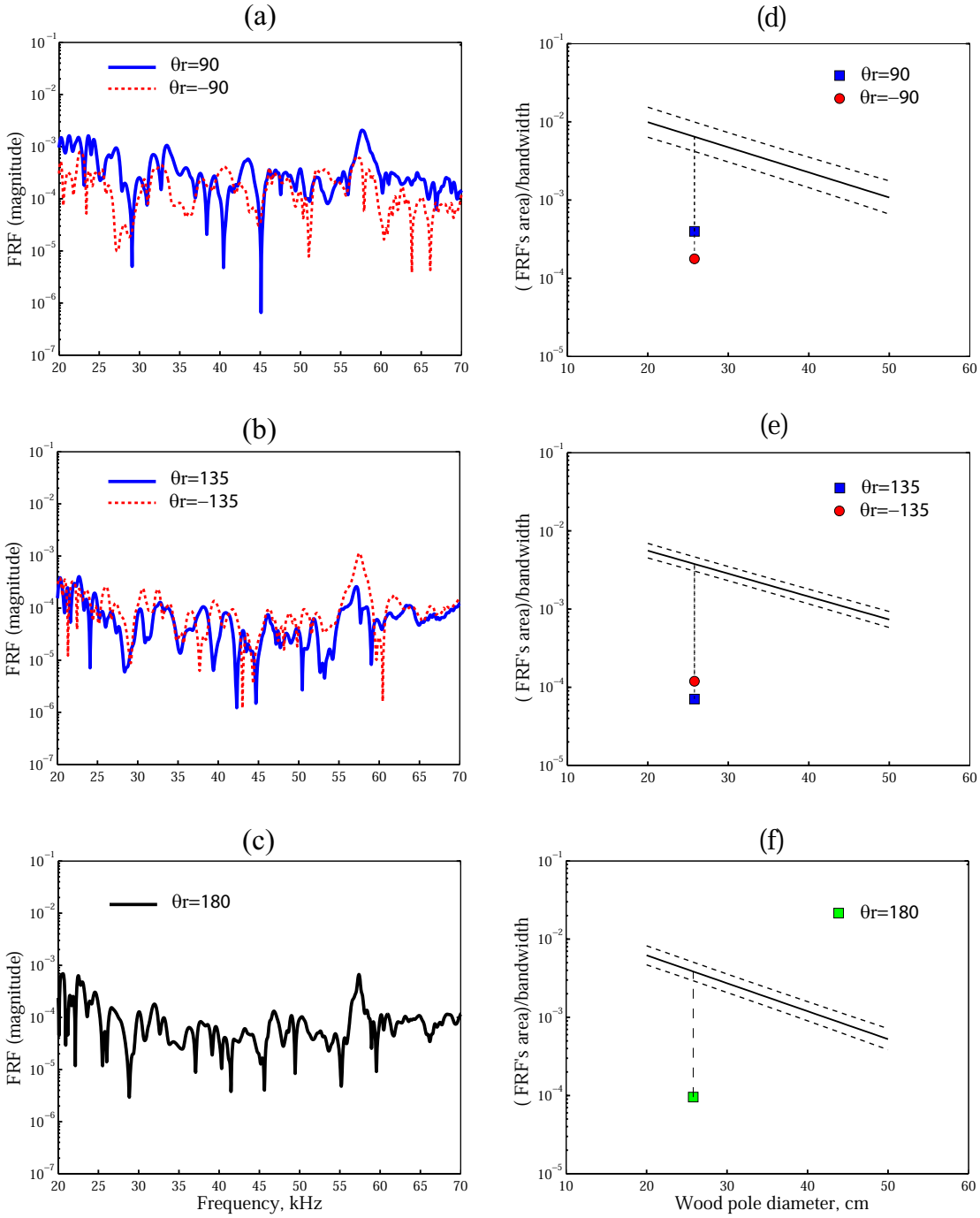

Figure F.2: Experimental results of ultrasonic testing in red pine pole RP-010: FRF for the receivers located at $\theta_r = \pm 90^\circ$ (a), $\theta_r = \pm 135^\circ$ (b), and $\theta_r = 180^\circ$ (c); wave attenuation for the receivers located at $\theta_r = \pm 90^\circ$ (d), $\theta_r = \pm 135^\circ$ (e), and $\theta_r = 180^\circ$ (f)

Source located on C

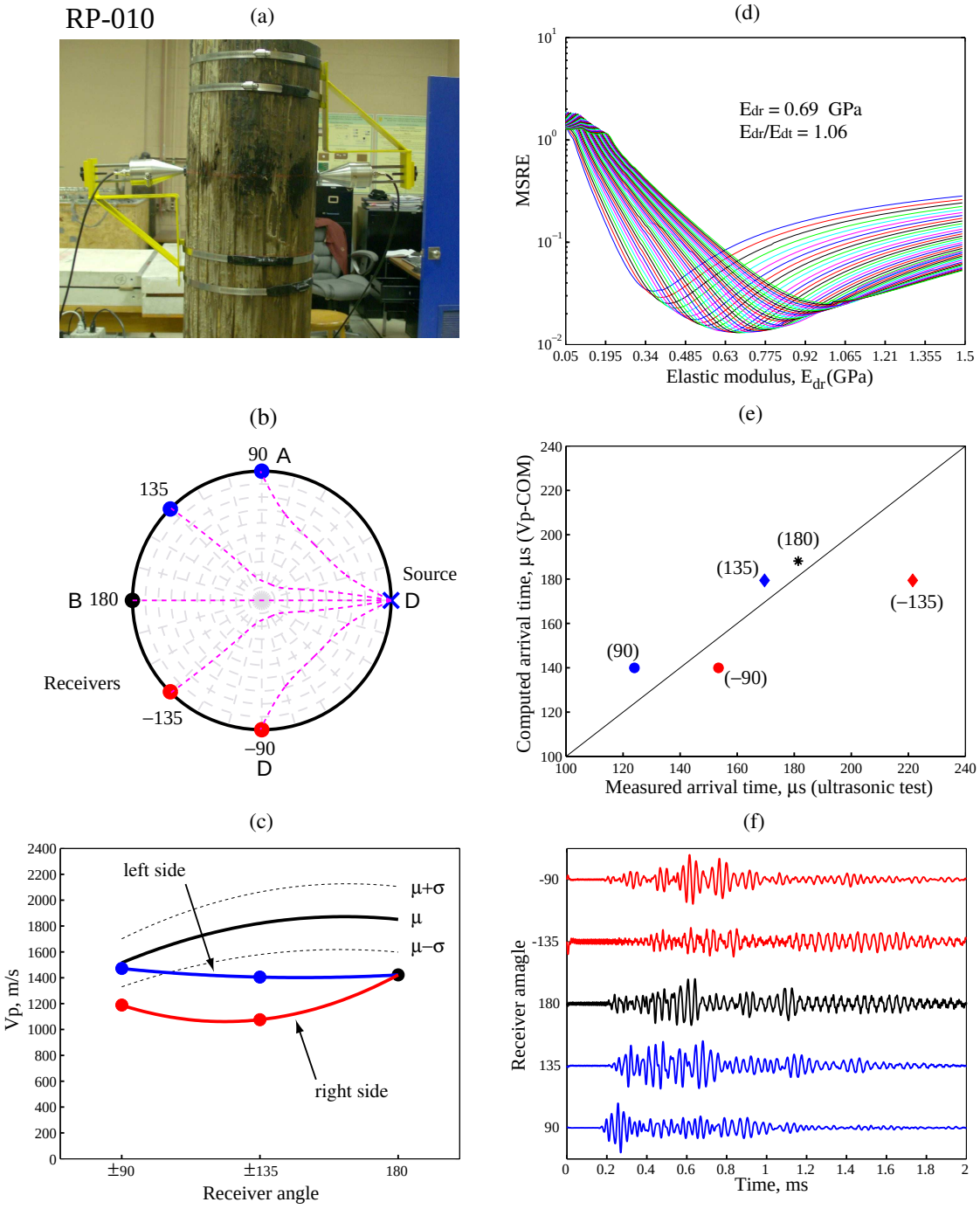

Figure F.3: Experimental results of ultrasonic testing in red pine pole RP-010 ($\phi = 22.1$ cm, $MC = 5\%$, $T = 20\ ^{\circ}C$): (a) ultrasonic test, (b) source and receiver locations, (c) V_p velocities, (d) elastic moduli E_r and E_t, (e) arrival times, and (f) IRFs

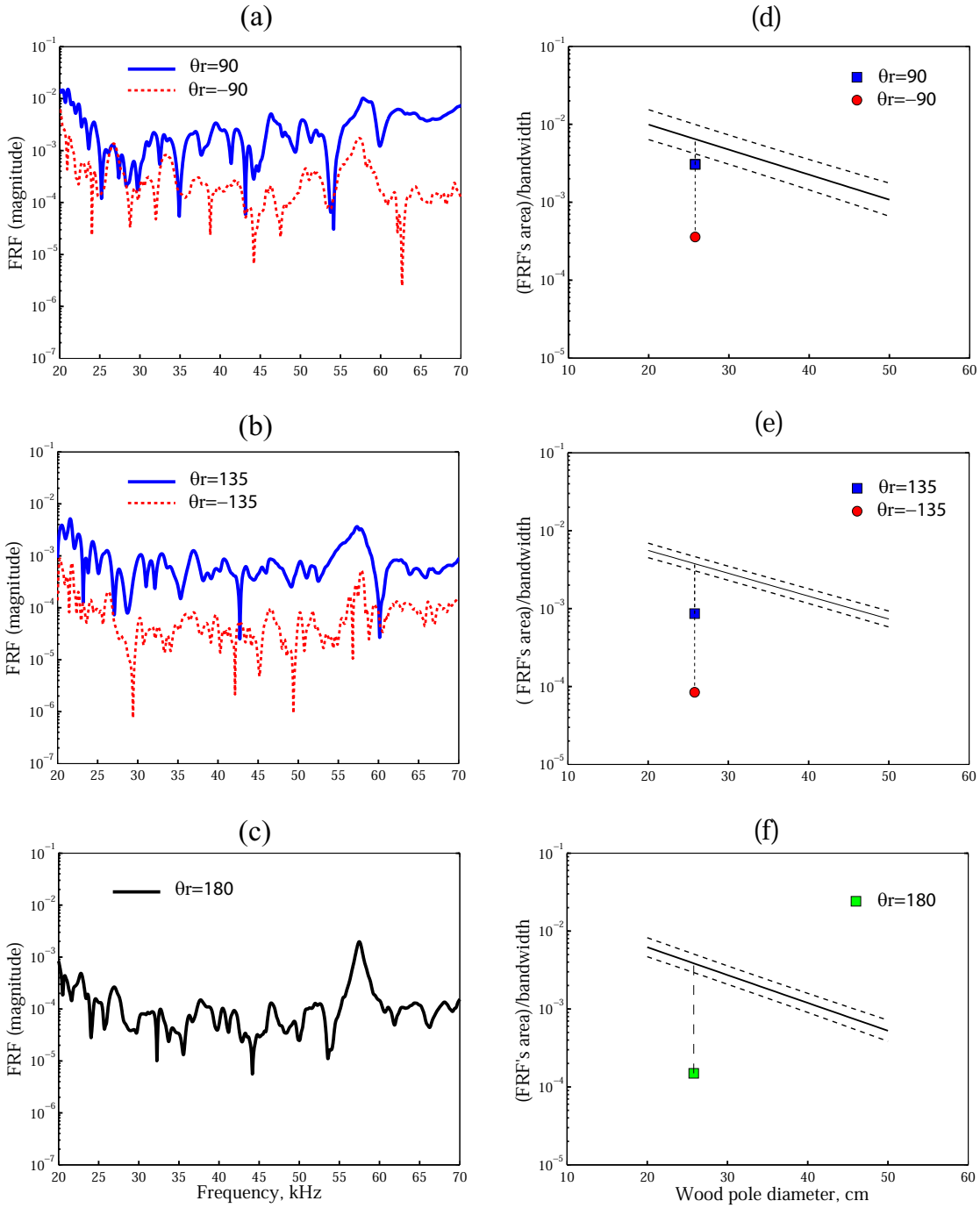

Figure F.4: Experimental results of ultrasonic testing in red pine pole RP-010: FRF for the receivers located at $\theta_r = \pm 90^\circ$ (a), $\theta_r = \pm 135^\circ$ (b), and $\theta_r = 180^\circ$ (c); wave attenuation for the receivers located at $\theta_r = \pm 90^\circ$ (d), $\theta_r = \pm 135^\circ$ (e), and $\theta_r = 180^\circ$ (f)

Source located on D

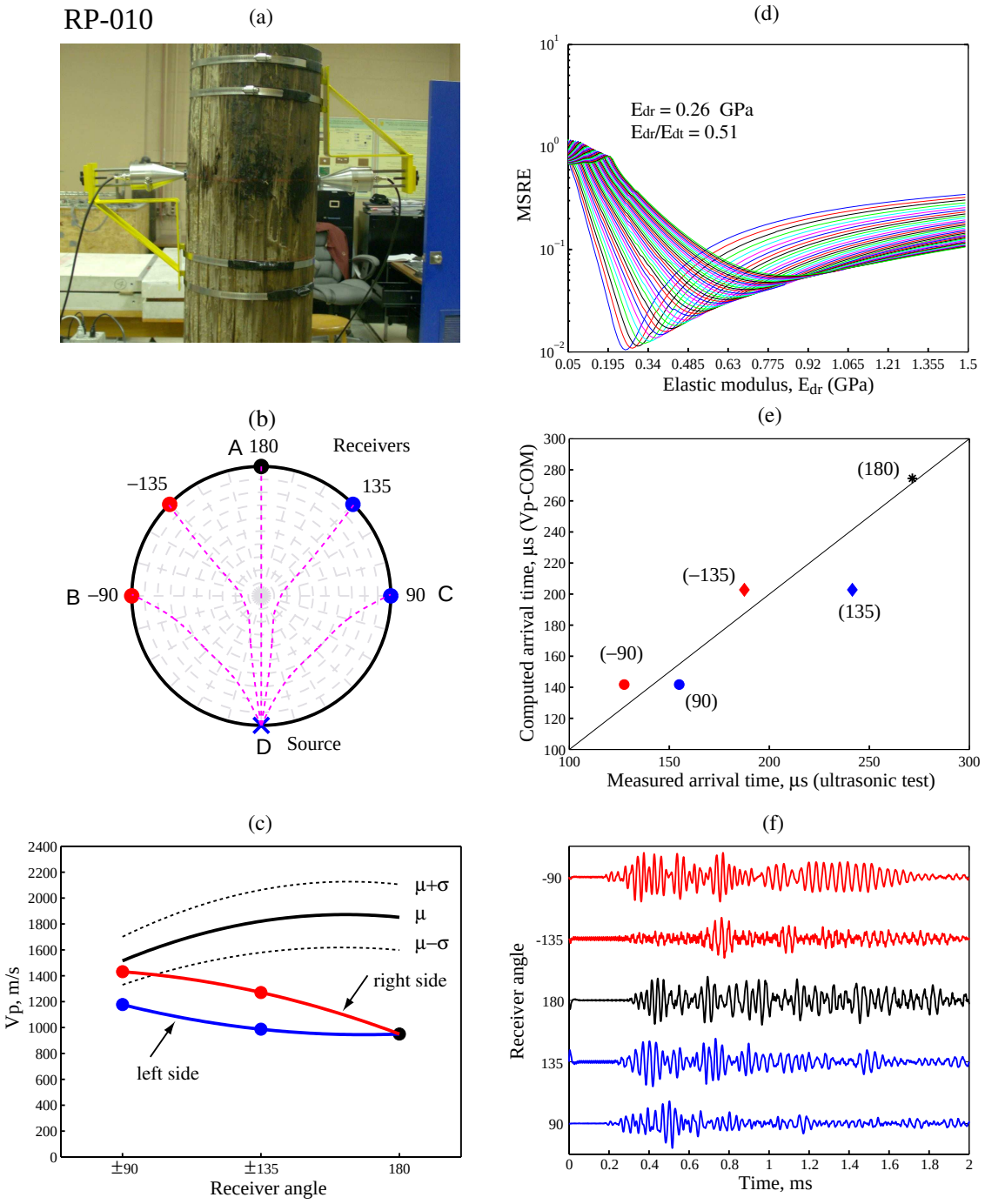

Figure F.5: Experimental results of ultrasonic testing in red pine pole RP-010 ($\phi = 22.1$ cm, $MC = 5\%$, $T = 20\ ^{\circ}C$): (a) ultrasonic test, (b) source and receiver locations, (c) V_p velocities, (d) elastic moduli E_r and E_t, (e) arrival times, and (f) IRFs

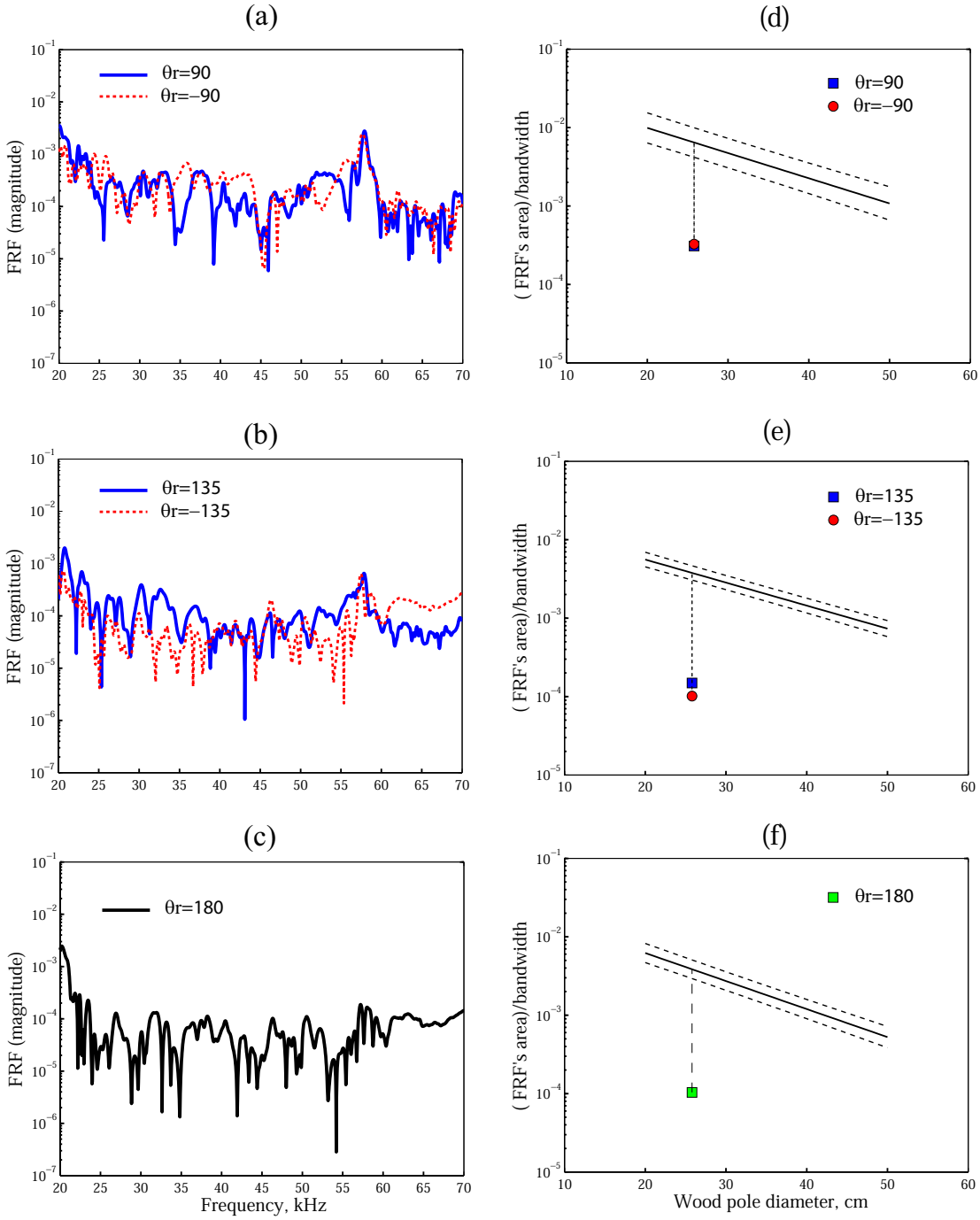

Figure F.6: Experimental results of ultrasonic testing in red pine pole RP-010: FRF for the receivers located at $\theta_r = \pm 90^\circ$ (a), $\theta_r = \pm 135^\circ$ (b), and $\theta_r = 180^\circ$ (c); wave attenuation for the receivers located at $\theta_r = \pm 90^\circ$ (d), $\theta_r = \pm 135^\circ$ (e), and $\theta_r = 180^\circ$ (f)

References

[1] A. W. Porter, *Canadian Woods: Their Properties and Uses*. University of Toronto. Press Toronto Buffalo London in cooperation with Canadian Forestry Service, Enviroment Canada and the Canadian Goverment Publishing Center and Services Canada. Third edition, 1981, ch. 4, pp. 71–96.

[2] D. W. Green, J. E. Winandy, and D. E. Kretschmann, *Mechanical Properties of Wood*. Forest Products Laboratory. Wood handbook-Wood as an engineering material. Gen. Tech. Rep. FPL-GTR-113. Madison, WI: U.S. Department of Agriculture, Forest Service, Forest Products Laboratory, 1999, ch. 4, pp. 1–45.

[3] W. Simpson and A. TenWolde, *Physical Properties and Moisture Relations of Wood*. Forest Products Laboratory. Wood handbook-Wood as an engineering material. Gen. Tech. Rep. FPL-GTR-113. Madison, WI: U.S. Department of Agriculture, Forest Service, Forest Products Laboratory, 1999, ch. 3, pp. 1–25.

[4] W. W. P. Institute, "Pressure treated wood proves to be the most cost efficient building material," Western Wood Preservers Institute, Tech. Rep., 2003.

[5] W. R. Lovelace, "The wood pole 2005: Design considerations, service benefits, and economic reward," Hi-Line Engineering, LLC, Tech. Rep., 2005.

[6] IESO, "Ontario transmission system," IESO Power to Ontario, On Demand, Tech. Rep., 2005.

[7] D. Hayward, "Wood poles: How long do they last? 30...45...60...100 years? it makes a difference!" Wood pole new letter, vol. 20, Tech. Rep., 1996.

[8] R. W. Wolfe, *Round Timbers and Ties*. Forest Products Laboratory. Wood handbook. Wood as an engineering material. Gen. Tech. Rep. FPL GTR 113. Madison, WI: U.S. Department of Agriculture, Forest Service, Forest Products Laboratory, 1999, ch. 18, pp. 1–9.

[9] M. D. Pandey, *Engineering Risk and Reliability*. University of Waterloo, 2005.

[10] R. C. DeGroot and T. H. Lauret, "Durability of preservative- treated wood utility poles in guam," United States Department of Agriculture Forest Service. Forest Products Laboratory Research. Paper FPL 472, Tech. Rep., 1986.

[11] U. S. D. of Agriculture. Rural Utilities Service, "Pole inspection and maintenance," Bulleting 1730B-12, Tech. Rep., 1996.

[12] R. Birtz, "Conventional methods for the inspection of poles," in *Wood Pole Maintenance Workshop, North Carolina State University, April 27*, 1977.

[13] ——, "Reliability of the various groundline pole inspection methods and proper application of fumigants," in *7th Wood Pole Institute, Colorado State University*, 1981.

[14] Vector, "2004 Asset management plan," Vector - New Zealand electricity company, Tech. Rep., 2004.

[15] N. R. Center, "Non-destructive testing," 2007. [Online]. Available: http://www.ndt-ed.org/EducationResources/CommunityCollege/NDTIntro/cc_intro001.htm

[16] J. Bodig and B. Jayne, *Mechanics of Wood and Wood Composites.* Van Nostrand Reinhold Company, 1982.

[17] F. Divos and T. Tanaka, "Relation between static and dynamic modulus of elasticity of wood," *Acta Silv. Lign. Hung.*, vol. 1, pp. 105–110, 2005.

[18] K. Hardie, "A review of strength testing as a measure of biodeterioration of wood and wood based materials," Int Biodet Bull 16:4156, Tech. Rep., 1980.

[19] S. Gray, "A deflection test for monitoring decay in miniature beam," Document IRG/WP/2269. International Research Group on Wood Preservation, Tech. Rep., 1986.

[20] L. Machek, H. Militz, and A. R. Sierra, "A dynamic approach to assess the modulus of elasticity in wood decay testing," Document IRG/WP/98-20139. International Research Group on Wood Preservation, Tech. Rep., 1998.

[21] V. W. K. Ho, "Strength assessment of wood crossarms using image processing techniques," Master's thesis, University of Waterloo. Ontario, Canada, 2005.

[22] F. J. McCarthy, "Condition assessment of wooden cross arms in 230 kv transmission structures," Master's thesis, University of Waterloo. Ontario, Canada, 2005.

[23] R. J. Ross and M. O. Hunt, "Stress wave timing nondestructive evaluation tools for inspecting historic structures a guide for use and interpretation," United States Department of Agriculture, Tech. Rep., 2000.

[24] K. C. Schad, D. L. Schmoldt, and R. J. Ross, "Non-destructive methods for detecting defects in softwood logs," United States Department of Agriculture Forest Service Forest Products Laboratory Research. Paper FPL-RP-546, Tech. Rep., 1996.

[25] G. Nicolotti, L. Socco, R. Martinis, A. Godio, and L. Sambuelli, "Application and comparison of three tomographic techniques for detection of decay in trees," *Journal of Arboriculture*, vol. 29(2), pp. 66–78, 2003.

[26] D. E. Franklin, M. W. Murphy, and R. A. Palylyc, "Apparatus and method for testing wooden poles," Canadian Patent 1 249 664, Jan. 31, 1989.

[27] X. Yang, Y. Ishimaru, I. Iida, and H. Urakami, "Application of modal analysis by transfer function to nondestructive testing of wood: Determination of localized defects in wood by the shape of the flexural vibration wave," *Wood Science*, vol. 48, pp. 283–288, 2002.

[28] J. Bodig, "The process of nde research for wood and wood composites," *12th International Symposium on Nondestructive Testing of Wood*, vol. 6 No. 03, pp. 1–18, 2001.

[29] R. F. Pellering, R. C. deGroot, and G. R. Esenther, "Non-destructive stress wave measurements of decay and termite attack in experimental wood units," *Proceeding, 5th Nondestructive testing of wood. Washington State University*, pp. 319–353, 1985.

[30] X. Wang, F. Divos, C. Pilon, B. K. Brashaw, R. R. J., and R. F. Pellerin, "Assessment of decay in standing timber using stress wave timing nondestructive evaluation tools a guide for use and interpretation," United States Department of Agriculture, Tech. Rep., 2004.

[31] U. B. Halabe, G. M. Bidigalu, H. V. GangaRao, and R. J. Ross, "Non-destructive evaluation of green wood using stress wave and transverse vibration techniques," *Materials Evaluation*, vol. 55, pp. 1013–1018, 1995.

[32] R. Anthony and J. Bodig, "Non-destructive evaluation of timber structures for reliable performance," *Proceedings, 2d Pacific Timber Engineering Conference. Auckland, New Zealand.*, 1989.

[33] J. Axmon and M. Hansson, "Non-destructive detection of decay in spruces using acoustic signals: Evaluation of circumferential modes," Lund Institute of Technology. Signal

Processing Report SPR-45 ISSN 1100-8105 ISRN LUTEDX TETT-8045-SE, Tech. Rep., 1999.

[34] C. J. Santamarina and D. Frata, *Introduction to Discrete Signals and Inverse Problems in Civil Engineering*. ASCE PRESS, 1998.

[35] S. Rust, "A new tomographic device for the non - destructive testing of trees," *12th International Symposium on Nondestructive Testing of Wood*, vol. Vol. 6 No. 03, 2001.

[36] J. L. Sandoz, "Ultrasonic solid wood evaluation in industrial applications," *NDTnet*, vol. 1 (12), pp. 1–7, 1996.

[37] R. Emerson, D. Pollock, D. Mclean, K. Fridley, R. Pellerin, and R. Ross, "Ultrasonic inspection of large bridge timbers," *Forest Products Journal*, vol. 52, No. 9, pp. 88–95, 2002.

[38] R. Martinis, L. V. Socco, L. N. Sambuelli, G. Olivier, and V. Schmitt, "Tomographie ultrasonore pour les arbres sur pied," *INRA, EDP Sciences DOi: 10.1051/forest: 2004007*, vol. 61, pp. 157–162, 2004.

[39] P. Gaydecki, *Foundations of Digital Signal Processing: Theory, Algorithms and Hardware Design*. IET. Institution of Electrical Engineers, 2004.

[40] R. N. Bracewell, *The Fourier Transform & Its Applications*. McGraw-Hill, 2000.

[41] A. V. Oppenheim, R. W. Schafer, and J. R. Buck, *Discrete - Time Signal Processing*. Prentice Hall, 1998.

[42] N. B. Jones, *Digital Signal Processing: Chapter I Introduction and Background*, N. B. Jones, Ed. Peter Peregrinus LTD, 1982.

[43] D. J. Ewins, *Modal Testing: Theory and Practice*. John Wiley & Sons INC, 1991.

[44] R. W. Clough and J. Penzien, *Dynamics of Structures*. Computers & Structures, Inc., 2003, Third Edition.

[45] D. J. Ewins, *Modal Analysis as a Tool for Studying Structural Vibration*. Academic Press, 1986, ch. 8, pp. 217–261.

[46] S. L. Marple, *Digital Spectral Analysis with Applications*. Prentice Hall, 1987.

[47] M. R. Osborne and G. K. Smyth, "A modified Prony algorithm for fitting sums of exponential functions," *SIAM Journal of Scientific Computing*, vol. 16, pp. 119–138, 1995.

[48] V. Slivinskas and V. Simonyte, "Estimation of parameters of impulse responses of mechanical systems by modified Prony method," *Mechatronic Systems and Materials*, vol. 113, pp. 190–194, 2006.

[49] A. Bracale, P. , Caramia, and G. Carpinelli, "Adaptive Prony method for waveform distortion detection in power systems," *Electrical Power and Energy Systems*, vol. 29, pp. 371–379, 2007.

[50] V. Garoosi and H. Jansen, "Development and evaluation of the piecewise Prony method for evoked potential analysis," *IEEE Transactions on Biomedical Engineering*, vol. 47, pp. 1549–1554, 2000.

[51] S. Braun and K. J. Hammond, *Parametric Methods*. Academic Press, 1986, ch. 5, pp. 103–138.

[52] K. C. Rajendra, "An introduction to wood drying," 2007. [Online]. Available: http://www.forestrynepal.org/article/rajendra-kc/2411

[53] W. T. Simpson, "Specific gravity, moisture content, and density relationship for wood," United States Department of Agriculture. Forest Products Laboratory. General Technical Report FPL-GTR-76, Tech. Rep., 1993.

[54] R. J. Ross, J. I. Zerbe, X. Wang, D. W. Green, and R. F. Pellerin, "Stress wave nondestructive evaluation of douglas-fir peeler cores," *Forest Products Journal*, vol. 55-No. 3, pp. 90–94, 2005.

[55] F. F. Wangaard, *The Mechanical Porperties of Wood*. John Wiley & Sons, INC, 1959.

[56] V. Bucur and F. Feeney, "Attenuation of ultrasound in solid wood," *Ultrasonics*, vol. 30, pp. 76–81, 1992.

[57] U. Halabe, "Assessment of defects and mechanical properties of wood members using ultrasonic frequency analysis," *Materials Evaluation*, vol. 54(4), pp. 314–322, 1996.

[58] D. Roylance, "Constitutive equations," Department of Materials Science and Engineering Massachusetts Institute of Technology Cambridge, MA 02139, Tech. Rep., 2000.

[59] G. Rose, "The mechanical behaviour of pinewood under dynamic constant stress depending on kind and amount of load, moisture content and temperature," *Holz als Roh - und Werkstoff (in German)*, vol. 23(7), pp. 271–284, 1965.

[60] J. Bodig, "Moisture effects on structural use of wood," in *Structural use of Wood in Adverse Environments*, 1982.

[61] V. S. Mujumdar, "Strength of slender timber columns in a cooling tower environment," in *Structural use of Wood in Adverse Environments*, 1982.

[62] R. B. Miller, *Structure of Wood*. Forest Products Laboratory. Wood handbookWood as an engineering material. Gen. Tech. Rep. FPLGTR113. Madison, WI: U.S. Department of Agriculture, Forest Service, Forest Products Laboratory. 463 p., 1999, ch. 2, pp. 1–5.

[63] M. C. Russell and T. Anton, *Use of Wood in Buildings and Bridges*. Forest Products Laboratory. Wood handbookWood as an engineering material. Gen. Tech. Rep. FPLGTR113. Madison, WI: U.S. Department of Agriculture, Forest Service, Forest Products Laboratory., 1999, ch. 16, pp. 1–15.

[64] W. W. P. Institute, "Factors which affect the service life of your poles," Western Wood Preservers Institute, Tech. Rep., 1997.

[65] S. Przewloka, "Comparison of rapid decay testing methodologies for the screening of new wood preservatives," Fores and Wood Products Research and Development Corporation. Report Number PG04.5015, Tech. Rep., 2004.

[66] C. A. Clausen and S. N. Kartal, "Accelerated detection of brown-rot decay: Comparison of soil block test, chemical analysis, mechanical properties, and immunodetection," *Forest Products Society, Forest Prod. J. 53(11/12):90-94.*, 2003.

[67] T. E. MacLain, H. W. Spurlock, M. J. A., and W. B. Wallin, "The flexural properties of eastern oak pallet lumber," Virginia Polytechnic Institute and State University. Department of Forest Products. Bulletin No. 6, Tech. Rep., 1986.

[68] C. E. Langum, "Characterization of pacific northwest softwoods for wood composites production," Ph.D. dissertation, Washington State University. Department of Civil and Environmental Engineering, 2007.

[69] M. Pandey, V. Ho, S. Bedi, and S. Woodward, "Development of a condition assessment model for transmission line in-service wood crossarms," *Canadian Journal of Civil Engineering*, vol. 32, pp. 480–489, 2005.

[70] R. F. S. Hearmon, *An introduction to Applied Anisotropic Elasticity*. Oxford university Press, 1961.

[71] R. G. Payton, *Elastic Wave Propagation in Transversely Isotropic Media*. Martinus Nijhoff, 1982.

[72] O. C. Zienkiewicz and R. L. Taylor, *The Finite Element Method Volume 1: The Basis*. Butterworth Heinemann, 2000.

[73] ANSYS, *Release 11.0 Documentation for ANSYS*, ANSYS, Inc, 2005.

[74] G. W. Brodland, *Finite Element Analysis*. University of Waterloo, Ontario, Canada, 2002.

[75] S. Braun and K. Hammond, *Additional Techniques*. Academic Press, 1986, ch. 6, pp. 141–171.

[76] M. Paz, *Structural Dynamics Theory and Computation*. Van Nostrand Reinhold Company, 1985.

[77] P. C. A. Lee, R. Huang, X. Li, and W.-H. Shih, "Vibrations and static responses of axsymmetric bimorph disks of piezoelectric ceramics," *IEE Transactions on Ultrasonics, Ferroelectrics, and Frequency Control*, vol. 47, pp. 706–715, 2000.

[78] R. C. NDT, "Acoustic properties of metals," 2008. [Online]. Available: http://www.ndt-ed.org/EducationResources/CommunityCollege/Ultrasonics/Reference%20Information/UT/ut_matlprop_metals.htm

[79] T. Irvine, *Damping Properties of Materials*, revision c ed., tomirvine@aol.com, 2004.

[80] SAP2000, "Integrated finite element analysis and design of structures analysis reference," Computers and Structures, Inc. Berkeley, California, USA, Tech. Rep., 1998.

[81] M. Chen, "Current technologies and trends of aluminum design," Master's thesis, Massachusetts Institute of Technoligy, 2003.

[82] Z. Khan, G. Cascante, and M. H. El Naggar, "Measurement of dynamic properties of a cemented sand using ultrasonic waves," *Submitted to the Canadian Geotechnical Journal*, 2009.

[83] R. G. Payton, "Wave fronts in wood," *Q. Jl Mech. Appl. Math, Oxford University Press*, vol. 56 (4), pp. 527–536, 2003.

[84] S. Schubert, D. Gsell, P. Niemz, and J. Dual, "Numerical simulation of elastic wave propagation in the radial-tangential plane of wooden trunks with and without fungal decay," *3th Workshop "NDT in Progress"*, 2005.

[85] F. Tallavo, "New methodology forstructural condition assessment of wood poles using ultrasonic testing," Ph.D. dissertation, University of Waterloo, Ontario, Canada, 2009.

[86] N. Ryden, "Surface wave testing of pavements," Ph.D. dissertation, Department of Engineering Geology Lund Institute of Technology, Lund University, 2004.

[87] J. Bodij and J. R. Goodman, "Prediction of elastic parameters of wood." *Wood Science*, vol. 5(4), pp. 249–264, 1972.

[88] A. P. Jessome, "Strength and related properties of woods grown in canada." Eastern Forest Products Laboratory, Ottawa, ON., Tech. Rep., 1977.

[89] B. A. Bendtsen, F. Freese, and R. L. Ethington, "A forest sampling method for wood strength," *For. Prod. Journal*, vol. 20 (11), pp. 38–47, 1970.

[90] C. T. Nguyen, "Ee c245 - me c218 introduction to mems design. lecture 18: Equivalent circuits & energy conserving transducers," Dept. of Electrical Engineering & Computer Sciences. University of Californy at Berkeley, Tech. Rep., 2007.

[91] X. Wang, R. Ross, and P. Carter, "Acoustic evaluation of standing trees - recent research development," *International symposium on Nondestructive Testing of Wood*, pp. 455–465, 2005.

[92] A. S. for Testing and Materials, *ASTM D217-02 Standard Test Methods for Cone Penetration of Lubricating Grease*, 2007.